



**UNIVERSITÀ
DEGLI STUDI
DI TRIESTE**

Università degli Studi di Trieste

XXXVI CICLO DEL DOTTORATO DI RICERCA IN
FISICA

Chemical evolution of neutron capture elements in different environments

SETTORE SCIENTIFICO-DISCIPLINARE: ASTRONOMIA E ASTROFISICA

DOTTORANDA:

Marta Molero

COORDINATORE:

Prof. Francesco Longo

SUPERVISORE:

Prof.ssa Francesca Matteucci

Anno Accademico 2022-2023



**UNIVERSITÀ
DEGLI STUDI
DI TRIESTE**

Università degli Studi di Trieste

XXXVI CICLO DEL DOTTORATO DI RICERCA IN
FISICA

Chemical evolution of neutron capture elements in different environments

SETTORE SCIENTIFICO-DISCIPLINARE: ASTRONOMIA E ASTROFISICA

DOTTORANDA:

Marta Molero

COORDINATORE:

Prof. Francesco Longo

SUPERVISORE:

**Prof.ssa Francesca
Matteucci**

Anno Accademico 2022-2023

Abstract

THE majority of elements beyond the Fe peak are produced by neutron capture processes which can be rapid (r-process) or slow (s-process) relative to the β -decay in nuclei. Understanding which are the astrophysical formation sites of these two processes has become one of the major challenges in the field of the chemical evolution of galaxies. The s-process mainly takes place in low-intermediate mass stars during the asymptotic giant branch (AGB) phase and in rotating massive stars, with the latter being particularly relevant at low metallicities. On the other hand, the r-process sites are still under debate, with possible main producer candidates being merging of compact objects (neutron stars or neutron star-black hole) or peculiar supernovae (magneto-rotational supernovae, MR-SNe). In particular, merging neutron stars (MNS) have been supposed to be powerful sources of r-process matter and this has been proved thanks to the observation of the kilonova AT2017gfo, following the gravitational wave event GW170817. However, although observations point towards MNS as the major astrophysical r-process sites, chemical evolution simulations still struggle to reproduce the abundance pattern of the [Eu/Fe] vs. [Fe/H] (with Eu being a typical r-process element) if MNS are the only producers of r-process material and realistic timescales for merging are assumed.

In this Thesis, we aim to investigate the origin of neutron capture elements by studying their evolution in time and space in the interstellar medium (ISM) of galaxies of different morphological types, i.e. dwarf spheroidal, ultra-faint dwarf, external irregular, elliptical and spiral galaxies, as well as in the Milky Way. The study of the chemical evolution of galaxies is performed by means of detailed chemical evolution models that predict the evolution of 40 chemical species, from H to Fe and the neutron capture elements Y, Zr, Ba, La, Ce, Eu, Mo, Nd and Pr. The adopted models include gas infall and outflow as well as the chemical enrichment from low-intermediate mass stars, novae, supernovae of all types (including MR-SNe) and MNS.

In the first part of the Thesis, we compute rates of MNS in external galaxies of different morphological types as well as cosmic MNS rates assuming different cosmological scenarios. Our aim is to provide predictions of kilonova rates for future observations both a low and high redshift. In the adopted models, the MNS rates are computed by adopting either a constant and short total time delay for merging (10 Myr) or a distribution function of such delays. The production of r-process elements either by MNS or core-collapse supernovae is taken into account in detail. We test our models by comparing results for spiral galaxies with the observed MNS rate in the Milky Way and with the observed abundance pattern of the $[\text{Eu}/\text{Fe}]$ vs. $[\text{Fe}/\text{H}]$, as well as the solar abundances of both Eu and Fe. In order to get a more complete picture of the cosmic MNS rates evolution, we also investigate how these quantities evolve on larger scales. We test our models with the observed cosmic stellar mass density and compare our results with the cosmic rate of short gamma-ray bursts. In particular, we find that spiral galaxies are the major contributors to the cosmic MNS rate at all redshifts in hierarchical scenarios while in a pure luminosity evolution scenario spirals are the major contributors locally, whereas ellipticals dominate at high redshift. Moreover, the cosmic rate of short gamma-ray bursts is well reproduced only if the distribution function of delays is adopted in a hierarchical scenario.

Then, we focus our study on dwarf galaxies by studying the evolution of the Eu and Ba abundances in Local Group dwarf spheroidal and ultra-faint dwarf galaxies and compare our results with new sets of homogeneous abundances. In this work, we investigate several production scenarios for r-process elements, including both MNS and MR-SNe. For MNS we test yields derived from the spectra of the kilonova AT2017gfo which followed the neutron stars merger GW170817, while for MR-SNe we adopt different sets of nucleosynthesis yields. Our simulations show that if r-process material is produced only by a quick source, it is possible to reproduce the $[\text{Eu}/\text{Fe}]$ vs. $[\text{Fe}/\text{H}]$ observed abundance pattern, but those models fail in reproducing the $[\text{Ba}/\text{Fe}]$ vs. $[\text{Fe}/\text{H}]$ one. If r-process elements are produced only with longer delays then the opposite happens. Finally, if both a quick source and a delayed one are adopted, such as MR-SNe and MNS with a delay time distribution respectively, the $[\text{Eu}/\text{Fe}]$ is successfully reproduced, but models still struggle in reproducing the $[\text{Ba}/\text{Fe}]$. We also investigate the ultra-faint dwarf galaxy Reticulum II, which stands out among all the other galaxies because of its peculiar Eu and Ba abundances data, which are concentrated at low metallicities and also show strong enhancements. We are able to reproduce such a pattern only if both the Eu and the r-process fraction of Ba are produced on short and constant time delays during a single merging event (or MR-SNe explosion).

The origin of neutron capture elements is then studied in the Milky Way disc, by analysing both their abundance patterns and radial gradients. We adopt a detailed two-infall chemical evolution model for the Galaxy, including state-of-the-art nucleosynthesis prescriptions for neutron capture elements. In particular, we consider r-process nucleosynthesis from MNS, MR-SNe and s-process synthesis from low-intermediate mass stars and rotating massive stars. We also include the processes which mainly influence the formation of abundance gradients: the inside-out scenario and a variable star formation efficiency. Predictions

of our model are compared with data from the sixth data release of the *Gaia*-ESO survey, from which we consider 62 open clusters with age ≥ 0.1 Gyr and ~ 1300 Milky Way disc field stars. We confirm that the [Eu/Fe] vs. [Fe/H] diagram is reproduced by adopting both prompt and delayed sources, with the prompt source dominating the Eu production. Including rotation in massive stars significantly contributes to the first peak s-process elements, even if constant initial rotational velocities are assumed, but MNS and MR-SNe are necessary to match the observations. Regarding the radial gradients, our predicted [Fe/H] gradient slope agrees with observations from *Gaia*-ESO and other high-resolution spectroscopic surveys. However, the predicted [Eu/H] radial gradient slope is steeper than the observed one, regardless of how quick the production of Eu is, prompting discussions on different Galaxy-formation scenarios and stellar radial migration effects. Finally, elements in the second s-process peak as well as Nd and Pr, exhibit a plateau at low-Galactocentric distances, likely due to the enhanced enrichment from LIMS in the inner regions.

The formation and chemical evolution of the Galactic bulge is also discussed, with a great focus on the stellar metallicity distribution function (MDF). Following previous literature results, we investigate the bimodality of the bulge MDF suggested by both old and more recent APOGEE data. The MDF is characterized by two populations, one metal poor (MP) and the other metal rich (MR). We investigate the possibility that the MP population is formed *in situ* in a gas-rich environment characterized by violent and fast star formation, while the MR population is made both by stars which formed *in situ* and by stars which are accreted from the innermost part of the Galactic disc region, being their motions strongly affected by the bar's gravitational perturbation. We investigate different percentages of stars which might come from the inner disc, in order to reproduce the bimodality of the MDF and the main α -elements abundance patterns. Finally, we study how the neutron capture element Ce may be affected by the stellar accretion phenomenon.

In the final part of the Thesis, we present the first of two papers which will be devoted to the study of the evolution of neutron capture elements in early-type galaxies. In the first paper, which is presented in this Thesis, we focus on studying the formation and evolution of elliptical galaxies and how they suppress star formation and maintain it quenched. We adopt a chemical evolution model for elliptical galaxies where the SN rates are computed in detail as well as stellar nucleosynthesis. The main novelty of this model is the inclusion of the AGN feedback, besides that of SNe and stellar winds. The AGN feedback is computed by considering a Bondi-Eddington limited accretion onto the central supermassive black hole. In particular, we study the evolution of early-type galaxies with different initial infall of gas mass (between $10^{10} - 5 \times 10^{12} M_{\odot}$). The evolutionary scenario that we consider is the following: ellipticals are formed by infall of gas in a primordial dark matter halo and its evolution is influenced by infall and outflow of gas as well as by stellar nucleosynthesis. The system goes through an early intense burst of SF, which is then quenched when strong galactic winds are produced and the galaxy evolves passively afterwards. This happens when the thermal energy of the gas in the ISM exceeds its binding energy. We study both the case in which the gas is thermalized only by stellar winds and SNe of all types,

and the case in which AGN feedback also contributes to the thermal energy of the gas. We successfully reproduce several observational features, such as the $[\alpha/\text{Fe}]$ ratios increasing with galaxy mass, mass-metallicity, $M_{\text{BH}}-\sigma$ and $M_{\text{BH}} - M_*$ relations. We show that stellar feedback, in particular from Type Ia SNe, is necessary since it has a main role in maintaining quenched the star formation after the occurrence of the main galactic wind episode, especially in low-mass ellipticals. For larger systems, the contribution from AGN to the thermal energy of the gas appears to be necessary. However, the effect of the AGN on the development of the main galactic wind is negligible, unless an unreasonable high AGN efficiency or an extremely low stellar feedback is assumed.

Contents

List of Abbreviations	ix
List of Figures	xii
List of Tables	xix
1 Introduction	1
1.1 The origin of elements	2
1.1.1 Stellar evolution and nucleosynthesis of elements up to the Iron group	3
1.1.2 Nucleosynthesis of elements beyond the Iron group	4
Merging neutron stars	7
Magneto-rotational driven supernovae	9
1.2 Chemical evolution of galaxies	11
1.2.1 Chemical evolution models	11
Galaxies of different morphological type and the time-delay model	12
1.3 Previous results	14
1.4 Structure of the Thesis	16
2 Chemical Evolution Models	17
2.1 Fundamental ingredients	18
2.1.1 Initial conditions	18
2.1.2 Birthrate function	18
The star formation rate	19
The initial mass function	19
2.1.3 Stellar yields	20
2.1.4 Gas flows	22
2.2 Chemical evolution equations	23
2.3 The rate of merging neutron stars	24
2.3.1 The delay time distribution for MNS	25
2.4 Delay time distribution for Type Ia SNe	28

3	External Galaxies and the Cosmic Merging Neutron Stars Rate	29
3.1	Introduction	30
3.2	The model	31
3.3	Simulations for galaxies of different morphological type	34
3.3.1	Predicted MNS rate	35
3.3.2	Predicted [Eu/Fe] vs [Fe/H] pattern in spiral galaxies	38
3.3.3	Predicted [Eu/Fe] vs [Fe/H] patterns for ellipticals and irregulars	42
3.4	Cosmic rates	43
3.4.1	Cosmic stellar mass density	45
3.4.2	Cosmic merging neutron stars rate	46
3.4.3	Comparison with the SGRB redshift distribution	51
3.4.4	Predicted number of Kilonovae detections for future surveys	51
3.5	Conclusions	54
4	Dwarf Spheroidal and Ultra Faint Dwarf Galaxies	57
4.1	Introduction	58
4.2	Observational Data	59
4.3	The Model	59
4.4	Nucleosynthesis prescriptions	60
4.4.1	Eu and Ba yields	60
4.5	Results	62
4.5.1	Sculptor and Fornax	65
	Results for Eu in Sculptor and Fornax	69
	Results for Ba in Sculptor and Fornax	71
4.5.2	Reticulum II	74
	Results for Eu in Reticulum II	77
	Results for Ba in Reticulum II	78
	A single r-process event	80
4.6	Conclusions	82
5	Milky Way - The Disc	85
5.1	Introduction	86
5.2	Observational Data	87
5.2.1	The data samples	88
	The sample of open clusters	88
	The sample of field stars	88
5.3	The Model	89
5.4	Nucleosynthesis Prescriptions	90
5.4.1	Heavy elements production	90
5.5	Results	92
5.5.1	Abundance ratios vs. metallicity trends	93
	Europium	93
	s-process elements	95
	Mixed-process elements	97
	Comparison with previous studies	101
5.5.2	Gradients	102
	Present day radial abundance gradients	102

	Time evolution of the radial abundance gradients	105
5.6	Conclusions	110
6	Milky Way - The Bulge	115
6.1	Introduction	116
6.2	Observational data	118
6.3	The model	118
6.4	Results without the bar	120
	6.4.1 Metallicity distribution function	120
	6.4.2 Abundance patterns	124
6.5	Results with accreted stars	126
6.6	Conclusions	128
7	Elliptical Galaxies - The AGN Feedback	131
7.1	Introduction	132
7.2	The model	134
	7.2.1 Basic equations	134
	7.2.2 Nucleosynthesis prescriptions	135
	7.2.3 Energy prescriptions	135
	Gas thermal energy	135
	Gas binding energy	136
	Galaxy binding energy	137
7.3	Results	137
	7.3.1 $[\alpha/\text{Fe}]$ ratio and mass-metallicity relations	138
	7.3.2 Energies with no AGN feedback	139
7.4	Black hole accretion and AGN feedback	143
	7.4.1 Black hole masses and luminosities	145
	7.4.2 Energies with AGN feedback	146
7.5	Conclusions	150
	7.5.1 Models without AGN feedback	151
	7.5.2 Models with AGN feedback	152
8	Final Remarks	155
8.1	Summary and conclusions	156
	8.1.1 External galaxies and the cosmic merging neutron stars rate	156
	8.1.2 Dwarf spheroidal and ultra-faint dwarf galaxies	157
	8.1.3 Milky Way - the disc	159
	8.1.4 Milky Way - the bulge	161
	8.1.5 Elliptical galaxies - the AGN feedback	161
8.2	Future prospects	164

List of Abbreviations

AGB	Asymptotic Giant Branch
AGN	Active Galactic Nuclei
BH	Black Hole
CC-SNe	Core-Collapse Supernovae
CE	Common Envelope
CMNSR	Cosmic Merging Neutron Star Rate
CSFR	Cosmic Star Formation Rate
CSMD	Cosmic Stellar Mass Density
DD	Double Degenerate
DE	Density Evolution
DM	Dark Matter
DNS	Double Neutron Stars
dSph	dwarf Spheroidal
DTD	Delay Time Distribution
GW	Gravitational Wave
IMF	Initial Mass Function
ISM	Inter Stellar Medium
IGRB	long Gamma Ray Burst
LIMS	Low Intermediate Mass Star
MDF	Metallicity Distribution Function
MNS	Merging Neutron Star
MP	Metal Poor
MR	Metal Rich
MR-SNe	Magneto Rotationally Driven Supernovae
MW	Milky Way
NS	Neutron Star
OC	Open Cluster
PLE	Pure Luminosity Evolution
SD	Single Degenerate
SF	Star Formation

SFR	Star Formation Rate
sGRB	short Gamma Ray Burst
SNe	Supernovae
UFD	Ultra Faint Dwarf
WD	White Dwarf

List of Figures

1.1	From Arcones et al. (2023). Solar System abundances as a function of the mass number A ($A = Z + N$, where Z is the number of protons and N the number of neutrons) normalized to $\log(N(Si)) = 6$.	2
1.2	Left panel: from Iben (1967); paths in the HR diagram for stars of different initial masses. Luminosity is in solar units, $L_{\odot} = 3.86 \times 10^{33}$ erg/s and surface temperature is in K. Right panel: from Arcones et al. (2023), composition and burning stages in a massive star before CC-SN.	4
1.3	Courtesy of M. Jacobi; Path of nuclear fusion, s-process, i-process, ν p-process, γ -process, and r-process in the nuclear chart.	6
1.4	Adapted from Tauris et al. (2017). Illustration of the formation of a double neutron stars system. Acronyms used in this figure are - ZAMS: zero-age main sequence; RLO: Roche-lobe overflow; He-star: helium star; SN: supernova; NS: neutron star; HMXB: high-mass X-ray binary; CE: common envelope; BH: black hole.	8
1.5	From Reichert et al. (2021). Integrated nucleosynthetic yields for models with various magnetic fields and rotation: model 35OC-Rs is the one with the strongest magnetic field, model 35OC-RRw is the one with the weakest magnetic field, model 35OC-RO has the same magnetic field of the progenitor (from Woosley et al., 2006b) and model 35OC-Rw has intermediate magnetic field but the fastest rotation.	10
1.6	The Hubble sequence of galaxies.	12
1.7	Adapted from Peterken et al. (2021). The star formation history of the Universe separated into its contributions from galaxies of different morphological type (indicated by colours). Each color is also stratified by present-day stellar mass (darkest to lightest shades for most to least massive galaxies).	13

1.8	From Matteucci (2012). Predicted $[\alpha/\text{Fe}]$ vs. $[\text{Fe}/\text{H}]$ abundance patterns for the solar neighborhood (dotted line), for the Galactic Bulge (dashed line) and for the Large Magellanic Cloud (solid line).	14
2.1	Left panel: Salpeter (1955), Scalo (1986), Yoshii et al. (1987), Kroupa et al. (1993) and Chabrier (2003) IMFs. Right panel: same as left panel but with each IMFs divided by the Salpeter one to allow a better comparison of the different mass distributions.	20
2.2	Delay time distributions for MNS computed for the three different values of β . A normalization factor of 1 has been assumed.	27
3.1	Predicted SFRs for galaxies of different morphological type as a function of time. Red dashed, green solid and blue dotted lines represent elliptical, spiral and irregular galaxies, respectively. Present time data are taken from Chomiuk et al. (2011) (green circle) and Rubele et al. (2015) (blue circle) for the Galaxy and for the Small Magellanic Cloud, respectively.	32
3.2	Predicted rate of MNS in spiral galaxies as a function of time for the four different DTDs derived by S19 corresponding to four different values of β ($-1.5, -0.9, 0.0, 0.9$) and for a constant total delay time equal to 10 Myr.	38
3.3	Predicted MNS rates for galaxies of different morphological type as a function of time. Left panel: case of a total delay time for all neutron stars binary systems equal to 10 Myr; right panel: case of a DTD for MNS with $\beta = -0.9$	39
3.4	Upper panel: results of models (1-5)A with Eu production from both CC-SNe and MNS; bottom panel: results of models (1-5)B with no Eu production from CC-SNe. Observational data used: 428 MW halo stars from JINABase and 374 MW thin disk stars from Battistini et al. (2016).	40
3.5	$[\alpha/\text{Fe}]$ vs $[\text{Fe}/\text{H}]$ predicted patterns in spiral galaxies for O, Mg, S and Ca. The observational data used are those of the MW and are from Cayrel et al. (2004) (purple upside-down triangles), Reddy et al. (2003) (red triangles), Gratton et al. (2003) (green stars), Reddy et al. (2006) (orange points), Ramya et al. (2012) (black crosses), Caffau et al. (2005) (purple diamonds) and (n.d.[b]) (green upside-down triangles).	41
3.6	$[\text{Eu}/\text{Mg}]$ vs $[\text{Fe}/\text{H}]$ as reproduced by models (1-5)A. Observational data are a collection of 412 MW halo stars from JINABase and 216 thin disk stars from a Venn et al., 2004).	42
3.7	Predicted $[\text{Eu}/\text{Fe}]$ vs. $[\text{Fe}/\text{H}]$ by models 1S(a-b), 1I(a-b) and 1E(a-b) in which a DTD with $\beta = -0.9$ has been assumed. Panel (a): results of models with Eu from CC-SNe; panel (b): results of models with no Eu from CC-SNe.	43
3.8	Predicted $[\alpha/\text{Fe}]$ vs. $[\text{Fe}/\text{H}]$ patterns in galaxies with different SF histories for O, Mg, S and Ca for the same models of Figure ??	44

3.9	Cosmic stellar mass density as a function of redshift for the three different cosmological scenario of galaxy formation. Observational data are a collection from Madau et al. (2014).	46
3.10	Contributions to the CMNSR from galaxies of different morphological type for the PLE, DE and alternative scenarios, in the case of a total delay time of 10 Myr (left panels) and in the case of a DTD with $\beta = -0.9$ (right panels).	48
3.11	CMNSR as a function of the redshift for the three different scenarios (PLE, DE and alternative) in the case of a total delay time of 10 Myr (upper panel) and in the case of a DTD with $\beta = -0.9$ (lower panel).	49
3.12	Redshift distributions of SGRB as found by Ghirlanda et al. (2016) (their case 'a', orange dashed line; their case 'c', red dashed line) against our predicted redshift distribution of MNS rate in the three different cosmological scenarios (PLE, DE and alternative), in the case of assuming a total delay time of 10 Myr (upper panel) and in the case of a DTD for MNS with $\beta = -0.9$ (lower panel)).	52
4.1	Results for Sculptor dSph. Panel (a): predicted SF history as a function of time; panel (b) predicted [Mg/Fe] vs. [Fe/H] pattern together with observational data; panel (c) predicted rates of Type Ia SNe (turquoise), Type II SNe (green), MNS with a constant delay time for merging (red) and MNS with a DTD (light blue); panel (d) comparison between predicted and observed MDE	67
4.2	Same as Figure 4.1 but for Fornax.	68
4.3	Results of models with different nucleosynthesis prescriptions for the [Eu/Fe] vs. [Fe/H] pattern for Sculptor dSph. Details of models are in Tables 4.4 and 4.5.	72
4.4	Same as Figure 4.3 but for Fornax. Note that in panel (d) the light green curve refers to the case in which the MR-SNe are producing r-process material only for metallicities higher than 10^{-3} . See text for details.	73
4.5	Results of models for the evolution of [Ba/Fe] and [Ba/Eu] vs. [Fe/H] for Sculptor dSph. For all models s-process Ba production comes from LIMS. Details of models are in Tables 4.4 and 4.5.	75
4.6	Same as Figure 4.5 but for Fornax.	76
4.7	Same as Figures 4.1 and 4.2 but for Reticulum II.	77
4.8	Same as Figures 4.3 and 4.4, but for Reticulum II.	79
4.9	Same as Figures 4.5 and 4.6 but for Reticulum II.	81
4.10	Results of models C54, C65 and C76 for Reticulum II for [Eu/Fe] and [Ba/Fe] vs [Fe/H] in the case of 1 event of MNS in the first Gyr.	82

5.1	Upper panel: time evolution of the SFR as predicted by our models at various Galactocentric distances. Right corner plot: predicted SFR in the solar neighborhood compared to present day estimates (Guesten et al., 1982; Prantzos et al., 2018); lower panel: predicted Type Ia SNe, Type II SNe and MNS rates compared to present day observations from Cappellaro et al. (1999a) (for SNe) and estimate from Abbott et al. (2021) (for MNS).	93
5.2	Predicted [Eu/Fe] vs [Fe/H] abundance patterns for the outer ($R_{GC} = 12$ kpc), local ($R_{GC} = 8$ kpc) and inner disc ($R_{GC} = 6$ kpc). The curves refer to the predictions of model R-150 (see Table 5.1) and are color coded by the age of the stars created by the chemical evolution code. The grey small dots refer to the sample of field stars.	94
5.3	[Y/Fe] and [Ba/Fe] vs. [Fe/H] for our sample of field stars (in grey) and OCs (magenta, green and blue dots) at all Galactocentric distances.	95
5.4	Predicted abundance patterns for [Y/Fe] and [Ba/Fe] vs. [Fe/H] for outer ($R_{GC} = 12$ kpc), local ($R_{GC} = 8$ kpc) and inner ($R_{GC} = 6$ kpc) disc regions. We assume that only massive stars and LIMS are Y and Ba producers. The three lines in each plot corresponds to different initial rotational velocities of massive stars (see legend and Table 5.1).	97
5.5	Predictions from model R-150 for the s-process elements abundance patterns vs. [Fe/H] for outer ($R_{GC} = 12$ kpc), local ($R_{GC} = 8$ kpc) and inner ($R_{GC} = 6$ kpc) disc regions. The channels considered for the production of the s-process components are: massive stars with initial rotational velocities of 150 km/s and LIMS. The channels for the r-process components are: MR-SNe and MNS with a DTD. The curves are color coded by the age of the stars created by the chemical evolution code.	98
5.6	Predictions from model R-150 for the mixed-process elements abundance patterns vs. [Fe/H] for outer ($R_{GC} = 12$ kpc), local ($R_{GC} = 8$ kpc) and inner ($R_{GC} = 6$ kpc) disc regions. The curves are color coded by the age of stars created by the chemical evolution code.	100
5.7	Prediction of the present day slope of the [Fe/H] and [Eu/H] gradients from our models with variable (olive line) and constant (dashed turquoise line) SF efficiency compared to the the one of the restricted ($Age \leq 3$ Gyr) OC sample (upper panel) and the Cepheid sample (lower panel) with data from Luck et al. (2011) (grey diamonds) and Genovali et al. (2015) (grey stars). For the [Eu/H] we show also models with Eu produced only by MR-SNe (purple line) and Eu produced only by MNS with a constant and short delay time for merging (teal line). The grey lines represent the linear fit of the observational data.	104

5.8	Left panels: Time evolution of the radial [Fe/H] and [Eu/H] gradients as predicted by model R-150. The OC sample is divided in three age bins: young ($\text{Age} < 1 \text{ Gyr}$), intermediate ($1 < \text{Age} < 3 \text{ Gyr}$) and old ($\text{Age} > 3 \text{ Gyr}$). Solid lines are the results for the [Fe/H] gradient as predicted by our model at 0.5 Gyr, 2 Gyr and 5 Gyr. Right panels: time evolution of the [Fe/H] and [Eu/H] as predicted by model R-150 for different Galactocentric distances. Vertical dotted lines indicate the ages considered to compute the gradients.	106
5.9	Same as Figure 5.8 but for 1 st peak s-process elements.	108
5.10	Same as Figure 5.8 but for 2 nd peak s-process elements.	109
5.11	Same as Figure 5.8 but for mixed-process elements.	111
6.1	Probability distributions of initial rotational velocities (IRV) for massive stars as a function of the metallicity (Z).	120
6.2	MDFs as predicted by models M19-0, M19-150 and M19-300 obtained with the prescriptions of Matteucci et al. (2009) best model with yields of rotating massive stars with initial velocity equal to 0 km/s (left panel), 150 km/s (middle panel) and 300 km/s (right panel).	122
6.3	MDFs predicted with a Chabrier IMF and a stop in the SF lasting 250 Myr. The MDFs differ for the different initial rotational velocities adopted. Models C-0A, C-150 and C-300 in the first row, with constant initial rotational velocities and models D-1-, D-2A and D-3A characterized by a diistribution of the initial rotational velocities (see Table 6.1).	123
6.4	MDFs predicted by models C-0(A-D) (first row), D-2(A-D) (second row) and D-3(A-D) (third row) characterized by a different duration of the SF stop.	123
6.5	SFR, [Fe/H] and surface number density of stars as a function of time predicted by models C-0(A, C, D).	124
6.6	Predicted [Mg/Fe], [O/Fe], [Al/Fe] and [Si/Fe] vs. [Fe/H] trends for models C-0(A-D), D-2(A-D) and D-3(A-D).	125
6.7	Predicted [Mg/Fe], [O/Fe], [Al/Fe] and [Si/Fe] vs. [Fe/H] trends with yields set for massive stars from Kobayashi et al. (2006) and different IMFs.	126
6.8	Same as Figure 6.6 but for Ce. The purple dashed line correspond to model DIS2 but with reduced yields from LIMS.	127
6.9	MDF of the Galactic bulge predicted by models C-0(A-C) with no stop in the SF (first row, model C-0B), 150 Myr of stop (second row, model C-0C) and 250 Myr (third row, model C-0A) and with different fractions of stars contributing to the bar.	129

- 7.1 Upper panels: Predicted abundances ratios in the ISM as functions of $[\text{Fe}/\text{H}]$ for O, Mg, S, Zn and Ca for an elliptical galaxy with infall gas mass of $M_i = 10^{11}M_\odot$ (left). Predicted $[\text{O}/\text{Fe}]$ abundance ratio in the ISM as a function of $[\text{Fe}/\text{H}]$ for galaxies with $10^{10}M_\odot$ (dashed line), $10^{11}M_\odot$ (solid line) and $10^{12}M_\odot$ (dash-dotted line) initial infall masses (right). Lower panels: Line-strength indices predicted by the model using Tantalo et al. (1998) calibrations together with observational data for both $\langle \text{Fe} \rangle$ (left panel) and Mg_2 (right panel). Black dots are the galaxies in the catalogue and the lines are the linear fit to the data (black line) and to the model (cyan line). The shaded area represents the 1σ uncertainties, while the black dotted lines are the boundaries of the 95% confident region. 140
- 7.2 Energy balance as a function of time for simulated elliptical galaxies with initial infall mass of $10^{10} M_\odot$, $10^{11} M_\odot$, $10^{12} M_\odot$ and $5 \times 10^{12} M_\odot$. For each panel, the blue solid line represents the thermal energy of the gas $E_{\text{gas}}^{\text{th}}$, the green dashed line its binding energy, $E_{\text{gas}}^{\text{b}}$, and the grey dash-dotted line the binding energy of the galaxy, $E_{\text{gal}}^{\text{b}}$ 141
- 7.3 Energies for an elliptical galaxies with initial infall mass of $10^{11} M_\odot$. Left panel: contribution to the gas thermal energy by Type II SNe ($E_{\text{II}}^{\text{th}}$), Type Ia SNe ($E_{\text{Ia}}^{\text{th}}$) and stellar wind (E_{W}^{th} , E_{σ}^{th}). Central panel: contribution to the total gas binding energy from the gravitational energy of the gas due to luminous matter, W_{L} , and the gravitational energy of the gas due to the interaction between luminous and dark matter, W_{LD} . Right panel: same as central panel, but for the galaxy binding energy. 142
- 7.4 Comparison between the thermal energy of the gas, $E_{\text{gas}}^{\text{th}}$ (blue solid line), and its binding energy, $E_{\text{gas}}^{\text{b}}$ (green dotted line), for a galaxy of initial mass $M_i = 10^{11} M_\odot$, for different values of the efficiency of energy transfer from Type Ia SNe. 143
- 7.5 Evolution of the accretion rate, bolometric luminosity and BH mass for an elliptical galaxy of initial infall mass $5 \times 10^{12} M_\odot$. Left panel: evolution of the accretion rate as a function of time. In grey dotted line is reported the Bondi accretion rate, in grey dash-dotted line is reported the Eddington accretion rate and in cyan continuous line the resulting accretion according to equation 7.21. Central panel: bolometric luminosity evolution as a function of time. Right panel: the BH mass evolution as a function of time, with the vertical grey dotted lines indicating the mass reached by the BH after 1 Gyr. The grey continuous line represent the evolution of the mass of gas inside the galaxy. 146

7.6	Comparison between our model predictions and observational data from Gültekin (2010) for the M_{BH} vs σ relation (left panel) and for the M_{BH} vs M_* relation with observational data from Marconi et al. (2003) (right panel). In both panel, the solid black line is the best fit of the observational data and the cyan and red stars are the predictions of our model for galaxies of initial infall mass equal to 10^{10} , 10^{11} , 10^{12} and $5 \times 10^{12} M_{\odot}$ and for an absorption coefficient ξ equal to 3×10^{-14} and 3×10^{-2} , respectively.	147
7.7	Energy balance as a function of time for simulated elliptical galaxies with initial infall mass of $5 \times 10^{12} M_{\odot}$ and for different values of the absorption coefficient ξ . For each panel, the blue solid line represents the thermal energy of the gas $E_{\text{gas}}^{\text{th}}$, the green dashed line its binding energy, $E_{\text{gas}}^{\text{b}}$, and the grey dash-dotted line the binding energy of the galaxy, $E_{\text{gal}}^{\text{b}}$	148
7.8	Contributions to the gas thermal energy by Type II SNe ($E_{\text{II}}^{\text{th}}$), Type Ia SNe ($E_{\text{Ia}}^{\text{th}}$), stellar wind (E_{W}^{th} , E_{σ}^{th}) and AGN feedback ($E_{\text{AGN}}^{\text{th}}$), for different values of the absorption coefficient ξ	149
7.9	Evolution of the SFR for a galaxy with initial infall mass of $5 \times 10^{12} M_{\odot}$ and for different values of the absorption coefficient.	150
8.1	Observed [Eu/Fe], [Ba/Fe] and [Sr/Fe] vs. [Fe/H] of Reticulum II (black dots) and Tucana III (purple dots) compared to those of other UFDs (colored points) and the MW halo (grey dots). Data are a collection from SAGA database (Suda et al., 2008; Suda et al., 2011; Yamada et al., 2013; Suda et al., 2017).	164

List of Tables

- 3.1 Parameters used for the chemical evolution models of spiral, irregular and elliptical galaxies. In the first column it is reported the morphological type of the galaxy, in the second, third, fourth and fifth column the infall mass M_{infall} , the star formation efficiency ν , the infall timescale τ_{infall} , the effective radius R_{eff} , and the wind parameter ω_i , respectively. 32
- 3.2 All the models for galaxies of different morphological type with Eu production from CC-SNe. In the 1st column the name of the model, in the 2nd column the galaxy type, in the 3rd column the production of Eu from CC-SNe, in the 4th column the DTD used for SNeIa, in the 5th column the occurrence probability of SNeIa (α_{Ia}), which has been tuned to obtain the estimated current rate of SNeIa, in the 6th column the DTD used for MNS, in the 7th column the occurrence probabilities of MNS (α_{MNS}) which has been tuned in order to obtain for spiral galaxies the estimated rate of MNS in the MW, in the 8th column the yield of Eu from MNS and in the 9th column the predicted rates of MNS. 36
- 3.3 All the models for galaxies of different morphological type with no Eu production from CC-SNe. In the 1st column the name of the model, in the 2nd column the galaxy type, in the 3rd column the production of Eu from CC-SNe, in the 4th column the DTD used for Type Ia SNe, in the 5th column the occurrence probability of Type Ia SNe (α_{Ia}), which has been tuned to obtain the estimated current rate of Type Ia SNe, in the 6th column the DTD used for MNS, in the 7th column the occurrence probabilities of MNS (α_{MNS}) which has been tuned in order to obtain for spiral galaxies the estimated rate of MNS in the MW, in the 8th column the yield of Eu from MNS and in the 9th column the predicted rates of MNS. 37

3.4	Parameters used for the evolution of the number density for galaxies of different morphological type. In the 1 st column it is reported the type of galaxy, in the 2 nd column the adopted number density at redshift $z = 0$ and in the 3 rd column the parameter γ_k . These parameters are the same as those adopted in Gioannini et al. (2017)	45
3.5	CMNSR for galaxies of different morphological type and in the three different cosmological scenarios (PLE, DE and alternative). In the 1 st column it is reported the DTD for MNS used, in the 2 nd column it is reported the total CMNSR, in the 3 rd , 4 rd and 5 th columns are reported the contribution to the total CMNSR from spirals, ellipticals and irregulars galaxies, respectively. By the end of the Table we also report the observed rates of MNS as predicted by Abbott et al. (2017) and by Kalogera et al. (2004).	50
3.6	Predicted Kilonovae rates ($\text{yr}^{-1}\text{Gpc}^{-3}$) for LSST and VST surveys in the case of a DTD with $\beta = -0.9$. In the 1 st it is specified the type of galaxy, in the 2 nd column the cosmological scenario, in the 4 th and 5 th columns the predicted Kilonovae detections for LSST and VST surveys, respectively.	53
3.7	Predicted Kilonovae rates ($\text{yr}^{-1}\text{Gpc}^{-3}$) for LSST and VST surveys in the case of a constant total delay time of 10 Myr. In the 1 st it is specified the type of galaxy, in the 2 nd column the cosmological scenario, in the 4 th and 5 th columns the predicted Kilonovae detections for LSST and VST surveys, respectively.	53
4.1	Yields of Sr, Eu and Ba from MNS adopted in this work. Yields of Sr are those measured by Watson et al. (2019) while those of Eu and Ba have been obtained as described in the text.	61
4.2	Yields of r-process elements from MR-SNe adopted in this work.	62
4.3	Yields of Eu and r-process Ba of Cescutti et al. (2006) for massive stars in the mass range $12 - 30 M_{\odot}$.	62
4.4	Summary table of the nucleosynthesis prescriptions adopted by different models. In the 1 st column in is reported the name of the model, in the 2 nd column it is specified if there is production from MNS, in the 3 rd it is specified if we adopted a DTD for MNS, in the 4 th column it is reported the adopted yield of Eu from MNS, in the 5 th column the yield of Ba from MNS, in the 6 th it is specified if there is production from MR-SNe, in the 7 th column it is reported the yield of both Eu and Ba from MR-SNe, in the 8 th column the percentage of stars in the $(10 - 80)M_{\odot}$ mass range which explode as MR-SNe and in the last column the range of metallicities in which the MR-SNe channel is active for the Eu and/or Ba production.	63
4.5	Table 4.4 continue.	64

4.6	Input parameters of the chemical evolution model for specific dSphs and UFDs. In the 1 st column it is reported the name of the galaxy, in the 2 nd column the infall mass, in the 3 rd column the efficiency of star formation, in the 4 th column the infall timescale, in the 5 th column the wind parameter and in the last three columns the number, time and duration of the bursts of star formation, respectively. The first three galaxies are discussed at length in the main text, while results for the others are presented as Supplementary Material of Molero et al. (2021a) in the online version of the journal.	66
5.1	Nucleosynthesis prescriptions. In the 1 st column we report the name of the model, in the 2 nd the initial rotational velocities for massive stars. In the 3 rd , 4 th and 5 th columns we list whether LIMS, MR-SNe and MNS channels are active or not, respectively. We point out that in the case of model 'R-150 MNS' MNS are assumed to merge with a short and constant time delay of 10 Myr instead that with a DTD.	92
5.2	Slopes of the [Fe/H] and [Eu/H] gradients of the reduced (Age \leq 3 Gyr) OC sample and as predicted by our model for the all, inner ($R_{GC} < 11.2$ kpc) and outer ($R_{GC} > 11.2$ kpc) radial region. For comparison we show also the one obtained from the Cepheid sample of Luck et al. (2011) and Genovali et al. (2015). In the case of Eu we show predictions also of models in which Eu is produced either by MR-SNe or by MNS with a constant and short delay time for merging.	103
5.3	Slopes of the [El/H] gradients predicted by our model at Age = 0.5, 2 and 5 Gyr.	107
6.1	Input parameters for the chemical evolution models. In the first column we specify the name of the model, in the second we indicate the initial rotational velocity of massive stars, in the third column it is specified the duration of the stop in the SF and in the last column the adopted IMF.	121
7.1	Parameters of the model. We adopted different values for the star formation efficiency ν , the infall timescale τ and the effective radius R_e (columns 2, 3 and 4, respectively) for the different infall masses M_i (column 1). In column 5, 6 and 7 we report the predicted final stellar mass M_{*f} , the predicted time for the onset of the galactic wind t_w and the predicted rate of Type Ia SNe R_{Ia} . Finally, on the last column we specify the adopted IMF.	138

CHAPTER 1

Introduction

WHERE do elements come from and how are they distributed in the Universe? The origin of the cosmic abundances is a critical aspect for understanding the evolution of the Universe, which requires connections between different fields of modern astrophysics, e.g., stellar evolution and nucleosynthesis, stellar spectroscopy and chemical evolution of galaxies. By knowing the composition of individual stars and that of whole galaxies, it is possible to learn about the astrophysical events that produce the different chemical species as well as the history of formation of the galaxies themselves.

The goal of this Thesis is to use constraints coming from chemical abundance observations to develop chemical evolution models able to study the evolution of heavy elements in galaxies of different morphological type, in order to shed light on their stellar sites and timescales of production.

In this Chapter, I outline the framework of this Thesis, by providing a general introduction on the astrophysical background of this work. I first discuss the stellar evolution and nucleosynthesis of the lighter elements and then that of the heavier elements, with emphasis on their main production sites. Then, I introduce the field of the chemical evolution of galaxies, highlighting the model framework adopted in this work. Finally, I present the structure of this Thesis.

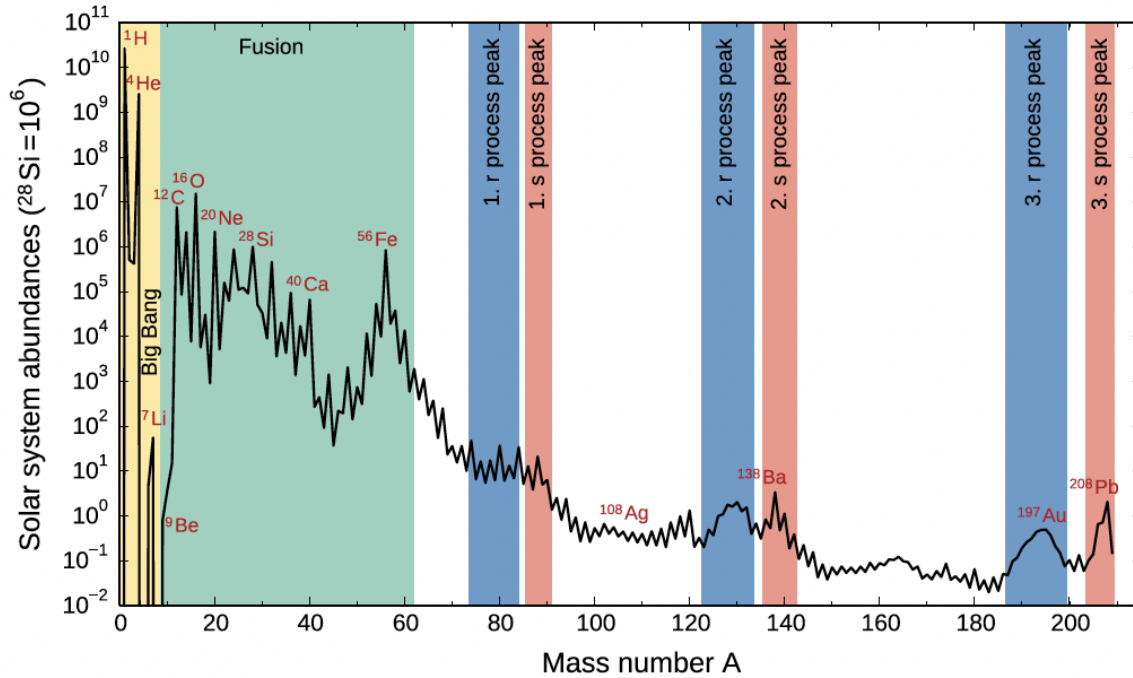


FIGURE 1.1: From Arcones et al. (2023). Solar System abundances as a function of the mass number A ($A = Z + N$, where Z is the number of protons and N the number of neutrons) normalized to $\log(N(\text{Si})) = 6$.

1.1 The origin of elements

Since the pioneering works of Burbidge et al. (1957) and Cameron (1957) it is known that only Hydrogen (H, with its isotopes ^1H , ^2H), Helium (He, with its isotopes ^3He , ^4He) and a very small amount of Lithium (^7Li) and Beryllium (Be) were created during the Big Bang. All the other elements beyond He are made in stars during their lifetime as well as at the moment of their death. The next generation of stars form from gas clouds that include elements from the previous stellar generation. Therefore, from the elemental abundances observed in the present-day stars, we can gain insights on the properties of stars from the past as well as on the star formation history of the host galaxy. Astronomers refer to all the elements formed only through stellar nucleosynthesis (thus excluding those made by spallation processes, as ^6Li , Be and B) as *metals* and their abundance is called *metallicity*, Z . In Figure 1.1, we show the Solar System abundances of elements. We see that H and He dominate the abundance budget, making up roughly 74% and 24% of the total mass of the Sun, respectively. Heavier elements constitute only about 2% of the mass of the Sun. However, despite their low abundances relative to lighter elements, they have a crucial role in most of the astrophysical phenomena.

In the next sections, we will present in some detail the stellar evolution and nucleosynthesis of the different chemical species (for a more comprehensive understanding, you can refer to the recent review by Arcones et al., 2023).

1.1.1 Stellar evolution and nucleosynthesis of elements up to the Iron group

Inside a star, the gravitational pressure is balanced by the gas pressure generated by thermonuclear fusion reactions as well as degeneracy pressure. During its life, a star undergoes different burning stages. First, stars fuse ${}^1\text{H}$ into ${}^4\text{He}$ via the *p-p chains* or the *CNO cycles*, depending on their mass. During the H burning, the star is on the so-called main sequence (MS) of the Hertzsprung-Russel (HR) diagram (Russell, 1914; Hertzsprung, 1976, see Figure 1.2), which relates a star stellar luminosity to its surface temperature (colour). The H burning stage is the longest phase in the life of a star and therefore most stars are found on the MS. The MS phase of stellar evolution ends when H in the core is exhausted.

When the H burning can no longer provide enough energy to balance the gravitational force, the star contracts until the core reaches a critical central temperature to ignite He. During the He burning, ${}^{12}\text{C}$ is formed through the triple-alpha reaction (the fusion of three ${}^4\text{He}$ nuclei into one ${}^{12}\text{C}$ nucleus; see deBoer et al., 2017), followed by ${}^{16}\text{O}$ through a subsequent capture of an alpha particle (and in case by ${}^{20}\text{Ne}$ by another alpha capture on ${}^{16}\text{O}$). When the central He supply is exhausted, the star is left with a C-O core and its subsequent evolution is determined by its mass.

For low- and intermediate-mass stars ($M < 8 M_{\odot}$) the core becomes degenerate before it reaches the temperature for C ignition, therefore the degeneracy pressure can support the core preventing further burning stages. These stars evolve through the asymptotic giant branch (AGB) phase in the HR diagram. In this phase, the star has a C-O core plus two burning shells, an innermost shell where He is burning and an outermost one where H is burning. This configuration is very unstable and in this phase matter is lost from the star, ending with the ejection of the entire mantle (causing what is known as a planetary nebula phase), leaving a stellar remnant known as a C-O White Dwarf (C-O WD).

On the other hand, massive stars ($M \gtrsim 8 M_{\odot}$) can reach temperatures high enough to ignite C into the core. For stars with masses in the range $\sim 7 - 10 M_{\odot}$ (super-AGB stars), the C-O core is partially degenerate and after C burning it turns into a degenerate ONeMg core, where the fusion reactions start explosively as the electron capture begins, making the star explode as an electron-capture supernova.

For larger masses, the core remains non-degenerate and the burnings will start non-catastrophically, until the formation of a Fe core. First C burning, which forms mainly ${}^{20}\text{Ne}$, and subsequently O and Si burning will be ignited. As each nuclear fuel is exhausted in the center, the burning will continue in a shell. The star will consist of a sequence of layers differing in composition all the way up to Fe, in an onion-shell like structure as schematically shown in Figure 1.2. Once the Si in the core of the star has been burned to Fe, thermonuclear reactions cease in the center and the gravitational pressure of the star can no longer be counteracted. In fact, Fe has the maximum binding energy per nucleon. The core then contracts until it reaches densities of the order of nuclear densities ($\sim 3 \times 10^{14} \text{ g cm}^{-3}$). At such high densities, nuclear interactions involve a repulsive force which causes the collapse to stop. The sudden stop produces a bounce

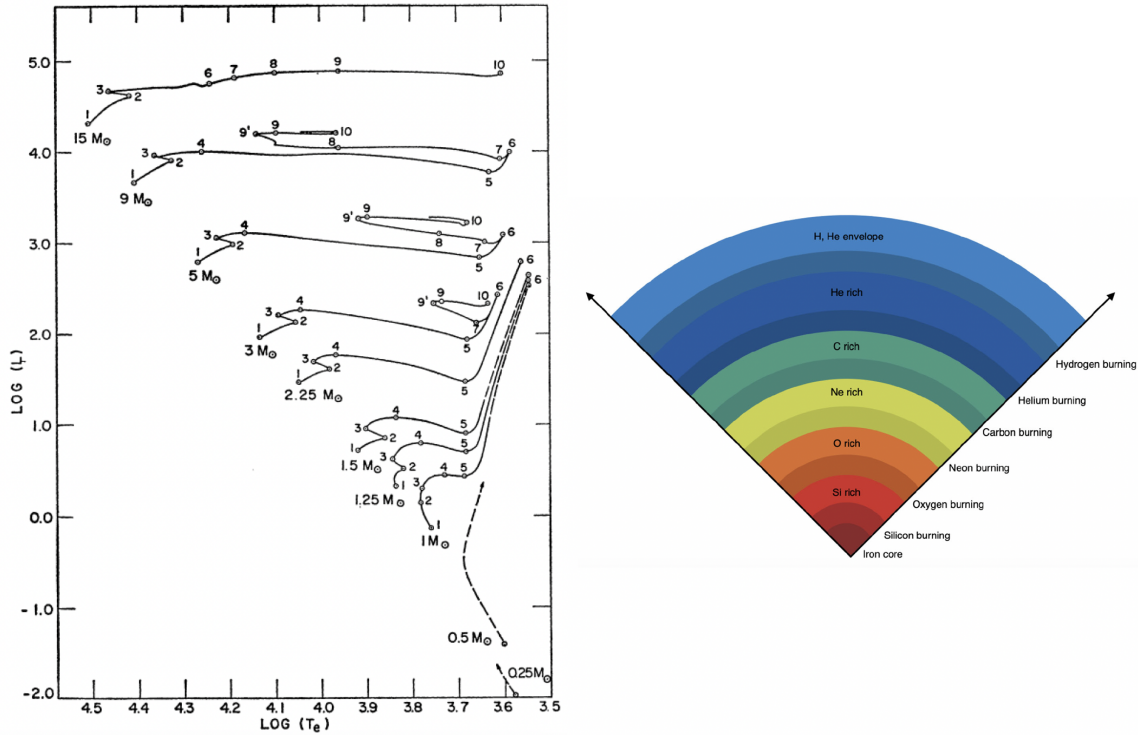


FIGURE 1.2: Left panel: from Iben (1967); paths in the HR diagram for stars of different initial masses. Luminosity is in solar units, $L_{\odot} = 3.86 \times 10^{33}$ erg/s and surface temperature is in K. Right panel: from Arcones et al. (2023), composition and burning stages in a massive star before CC-SN.

and a shock wave is launched outwards in radius. It was at first believed that the shock wave carries enough energy to cause the final explosion (so-called prompt explosion mechanism, e.g., Bruenn, 1989a; Bruenn, 1989b). However, the shock wave loses energy by photodisintegration of heavy nuclei and it stalls at some point. The mechanism to revive it is still subject of investigation and more mechanisms have been proposed (for review of the subject see e.g., Janka et al., 2007; Janka et al., 2016; Müller, 2016; Burrows et al., 2021). A possible explanation is the so-called delayed-neutrino heating scenario (Colgate et al., 1966; Arnett, 1966), in which neutrinos from the freshly formed proto-neutron star (PNS) deposit energy below the shock. The shock revives and moves through the layers, heating them and causing their final ejection. As the shock wave propagates, explosive nucleosynthesis occurs in the different layers. This event is called *core-collapse supernova* (CC-SN). The dominant reactions are α -captures, so that elements up to the Fe group can be synthesized. The remnant of a CC-SNe can be either a neutron star (NS) or a black hole (BH), depending on the mass of the Fe core.

1.1.2 Nucleosynthesis of elements beyond the Iron group

Up to the Fe group (around $A = 56$), light elements can ‘easily’ fuse into heavier ones inside stars, thanks to the right conditions of temperature and density. On the contrary, for heavier nuclei charged particle reactions become unsustainable

in stellar environments because of the increasing Coulomb barriers. While for elements lighter than Fe the fusion of charged nuclei produces energy that can support the star, for heavier elements it becomes energetically expensive. Therefore, elements heavier than Fe cannot be produced by stellar fusion (see Holmbeck et al., 2023 for a review).

The majority of the isotopes beyond Fe are produced by neutron capture processes. Neutron captures can be slow or rapid with respect to the β -decay in the nucleus. When the neutron densities are low, the unstable isotope created by neutron capture decays in a stable nuclide before it has time to capture another neutron. In this case, the neutron capture process is *slow* with respect to the β -decay, and we talk about *s-process*. The nucleosynthetic path proceeds along the valley of stability in the nuclear chart (blue arrow in Figure 1.3). On the other hand, if the neutron density is high, there is time for the unstable isotope to capture many neutrons before the first β -decay occurs. In this case, the neutron capture process is *rapid* with respect to the β -decay, and we talk about *r-process*. The nucleosynthetic path proceeds along the neutron-rich side in the nuclear chart (red arrow in Figure 1.3). The final nucleosynthesis patterns that result from s- and r-process include peaks at the neutron numbers $N=50, 82$ and 126 . In fact, due to higher neutron separation energy in correspondence of these so-called magic numbers, the neutron capture cross-sections are much smaller than for neighbouring neutron numbers. Therefore, once one of these values for N is reached, it becomes less likely for nucleus to capture more neutrons and matter will accumulate. The solar system abundances pattern is indeed characterized by a double peak structure at $A \simeq 80, 130-140$ and $195-208$, corresponding to the magic numbers for N , but related to different proton numbers Z for the two processes.

Because of the different conditions required for the s- and r-process, we expect them to have place in different astrophysical sites. The s-process can be decomposed into three sub-processes: (i) the weak s-process, mainly responsible for the production of the first s-process elements (Y, Sr, and Zr); (ii) the main s-process which produces elements belonging to the second s-process peak (Ba, La, and Ce); and (iii) a strong s-process responsible for the production of the third s-process peak elements (Pb, Au, and Bi). Rotating massive stars ($M > 13 M_{\odot}$) are the main responsible for the production of the weak s-process. Neutrons are released via (α, n) -reactions on ^{22}Ne , through the reaction $^{22}\text{Ne}(\alpha, n)^{25}\text{Mg}$ which takes place mainly during core He- and C-burning phases and can produce elements up to $A \sim 90$ (Pignatari et al., 2010; Frischknecht et al., 2016; Limongi et al., 2018). The main and the strong s-process components occur in LIMS ($M < 8 M_{\odot}$) during thermal pulses in their AGB phase. In AGB stars two major neutron sources are at work: the $^{13}\text{C}(\alpha, n)^{16}\text{O}$ reaction, dominant in low-mass AGB stars, and the $^{22}\text{Ne}(\alpha, n)^{25}\text{Mg}$, more important in more massive AGBs (Busso et al., 1999; Karakas, 2010; Fishlock et al., 2014; Cristallo et al., 2015), producing elements with $90 \leq A \leq 208$. In general, the bulk of the s-process arises from LIMS of $1 - 3 M_{\odot}$.

On the contrary, the major r-process production site, is still under debate and is one of the major challenges in chemical evolution and stellar nucleosynthesis

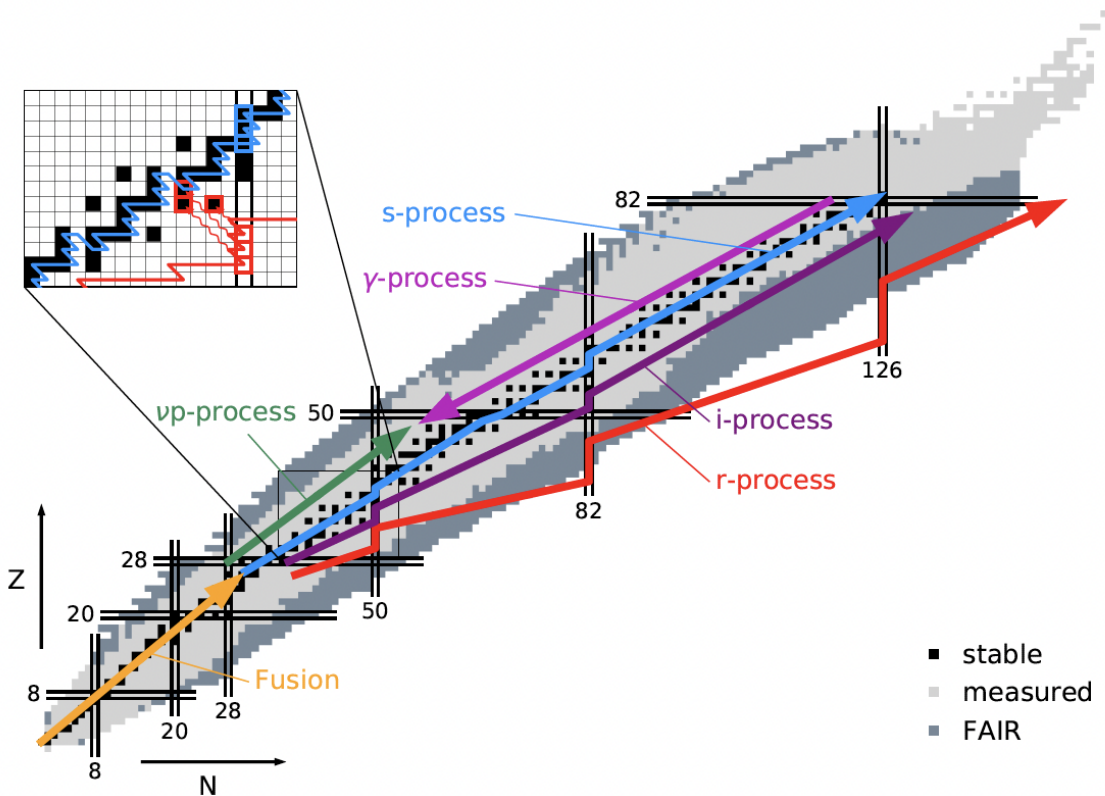


FIGURE 1.3: Courtesy of M. Jacobi; Path of nuclear fusion, s -process, i -process, νp -process, γ -process, and r -process in the nuclear chart.

(for reviews see e.g.: Thielemann et al., 2017; Cowan et al., 2019; Cowan et al., 2021). The first astrophysical site which has been proposed to produce heavy elements via r -process is CC-SNe. However, the prompt explosion mechanism, which was believed to eject extremely neutron-rich matter, has been completely ruled out by earlier hydrodynamical nucleosynthesis calculations. Simulations showed not only difficulties in reproducing the high entropy needed to reproduce the solar r -process abundances (Wanajo, 2006; Arcones et al., 2007), but also that the neutrino winds, which follow the SNe explosion, are only slightly neutron rich or even proton rich (Fröhlich et al., 2006; Fischer et al., 2010; Arcones et al., 2013), providing insufficient conditions for the production of heavy r -process elements. Among massive stars, a rare class of CC-SNe induced by strong magnetic fields and fast rotation of the stellar core (magneto-rotationally driven SNe, MR-SNe) seem to provide a source for the r -process (Winteler et al., 2012; Nishimura et al., 2015; Mösta et al., 2018; Reichert et al., 2021; Reichert et al., 2023).

A more reliable scenario is the merger of compact objects (neutron star-neutron star, neutron star-black hole), which already in 1970s was suggested as a potential candidate for r -process nucleosynthesis. In particular, merging neutron stars (MNS) have been proved to be powerful sources of r -process matter, thanks to the observation of the kilonova AT2017gfo, following the gravitational wave event GW170817 (Abbott et al., 2017), where freshly synthesized Sr was observed (Watson et al., 2019). However, although both the r -process yields and the estimated

rate of this phenomena seem to point towards MNS as the main r- process astronomical source, strong conclusions can be reached only by mean of chemical evolution models. In this Thesis, we will investigate the contribution of both MNS and MR-SNe.

It must be reminded that the s- and r-process alone cannot describe the presence of all the heavy nuclei observed today. Other processes have been proposed, such as the γ -process (see e.g., Pignatari et al., 2016; Roberti et al., 2023), the rp-process (see e.g., Wanajo, 2006) and the intermediate neutron-capture process (i-process) (e.g., Côté et al., 2018; Denissenkov et al., 2019).

Merging neutron stars

MNS are systems consisting of two neutron stars that gradually spiral inward due to gravitational radiation and finally collide (for reviews see e.g., Thielemann et al., 2017; Shibata et al., 2019). In Figure 1.4, we show an illustration from Tauris et al. (2017) of the formation of a double neutron stars (DNS) system. As described by the authors, in order to create a DNS system, the initial binary system must be made of two OB-stars massive enough to end their lives as CC-SNe and live a NS as a remnant. Furthermore, the two progenitors stars must be close enough to ensure mass transfer. The secondary (initially less massive) star accretes mass from the primary (initially more massive) star to reach the threshold limit for core collapse. If the binary system remains bound after the first SN explosion, it may be detectable as a radio pulsar orbiting an OB-star (as in the case of PSRs 1259-63, Johnston et al., 1992, and of J0045-7319, Kaspi et al., 1994), or as a high mass X-ray binary (HMXB). When the secondary star expands, it fills its Roche-lobe and the system becomes dynamically unstable, leading to the formation of a common envelope (CE). The dynamical friction caused by the motion of the NS inside the CE may cause extreme loss of angular momentum and ejection of the H-rich envelope of the giant star. Therefore, if the system survives this phase, it will consist of a NS orbiting an He-star. Then, depending on the orbital separation and on the mass of the He-star, an additional phase of mass transfer may be present (case B RLO). This phase causes extreme stripping of the He-star which will then die as an *ultra-stripped SN*. If the system survives this second explosion, a NS binary system is formed. Then, the system will eventually merge due to gravitational wave (GW) radiation, leaving a BH (or, depending on the equation of state, a NS/metastable NS) as a merged final object. From this picture, it appears clear that the delay between the formation of the progenitors binary system and the merging event will depend on two delay time: the nuclear lifetime of the secondary component of the progenitors binary system and the delay due to the GW radiation. In the next Chapter, we will show how the delay time for MNS is parametrized in our model.

As described in the last section, MNS are considered one of the major astrophysical sites for heavy elements nucleosynthesis through r-process. The radioactive decay of the r-process elements in the merger ejecta powers a strong electromagnetic (EM) emission (also known as *kilonova*), which is the EM counterpart of the GWs. The observation of the spectra of the kilonova is actually used to measure the production of r-process elements by MNS, as for the kilonova AT2017gfo following the neutron stars merger GW170817 (Watson et al., 2019).

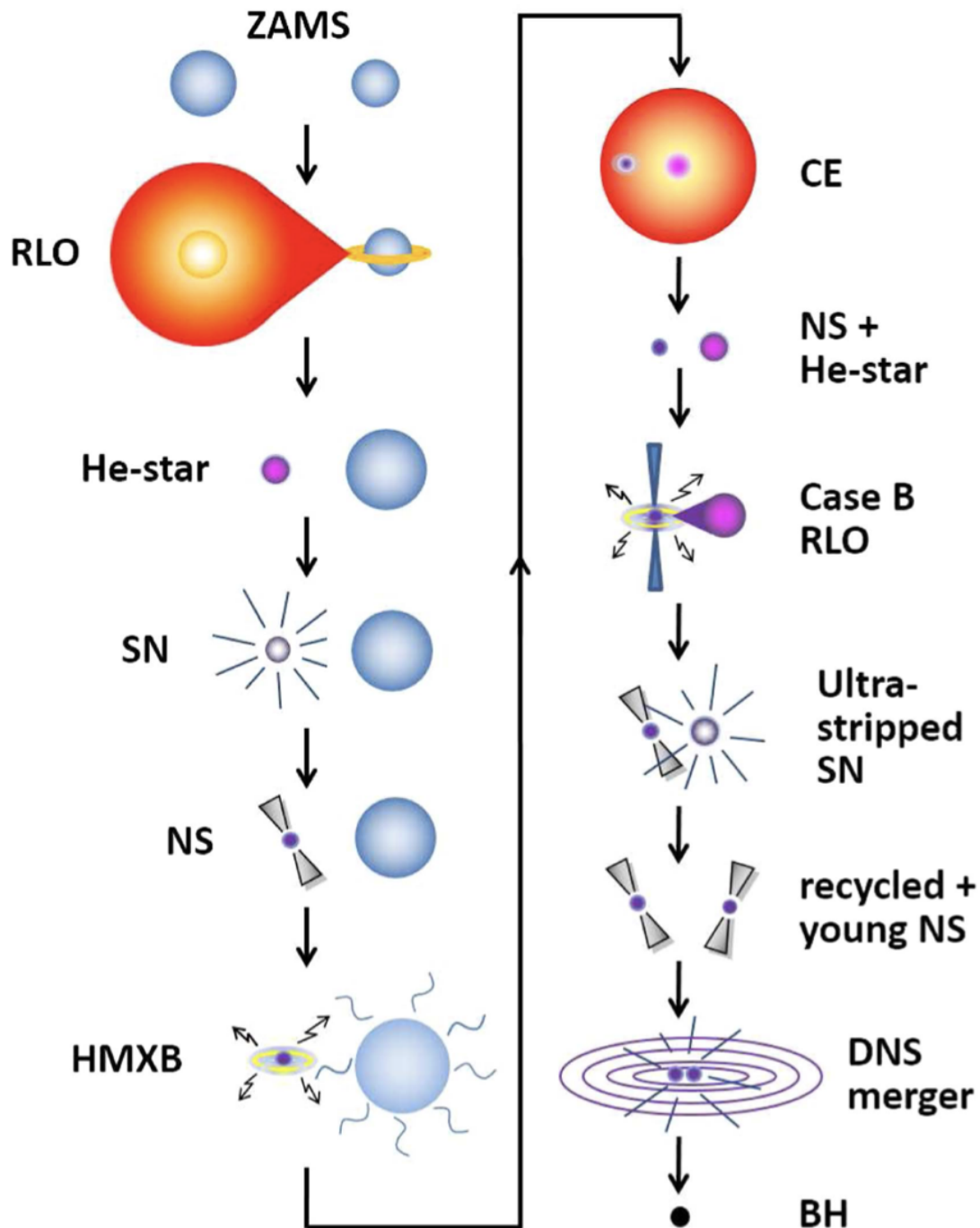


FIGURE 1.4: Adapted from Tauris et al. (2017). Illustration of the formation of a double neutron stars system. Acronyms used in this figure are - ZAMS: zero-age main sequence; RLO: Roche-lobe overflow; He-star: helium star; SN: supernova; NS: neutron star; HMXB: high-mass X-ray binary; CE: common envelope; BH: black hole.

Three components of neutron star merger ejecta contribute to the overall nucleosynthesis: i) dynamical ejecta, ii) neutrinos driven winds and iii) mass outflow from the accretion disk. Dynamical ejecta are matter ejected by tidal forces during the merger of the two neutron stars. This matter is very neutron rich, since it consists of material from the neutron star itself and, since it is located far away from the MNS, it is negligibly affected by neutrinos and therefore it is an ideal host for the r-process, potentially contributing to all r-process elements (see e.g., Korobkin et al., 2012; Thielemann et al., 2020; Perego et al., 2021; Arcones et al., 2023). After the dynamical ejecta, a neutrino wind from the merger remnant (NS or BH surrounded by a massive accretion torus) is emitted which contributes to the r-process nucleosynthesis. The material which is pushed outwards from the accretion disk, is less neutron-rich and therefore it synthesizes mainly lighter elements between the first and second r-process peak (see e.g., Fujibayashi et al., 2017; Fujibayashi et al., 2023). Finally, mass outflows from the black hole accretion disc formed after the merger, powered by angular momentum transport processes and recombination energy, can produce a robust abundance pattern around the second r-process peak and, depending on the disc viscosity, initial mass or entropy of the torus, it can reach also the third r-process peak (see e.g., Wu et al., 2016; Siegel et al., 2017; Fernández et al., 2023).

Magneto-rotational driven supernovae

The MR-SNe are a rare type of CC-SNe which rely on a different explosion mechanism with respect to the neutrino-driven one. In particular, the explosion relies on the extraction of rotational energy from the core via strong magnetic field (see e.g., Obergaulinger et al., 2018). While in typical neutrino-driven CC-SNe matter is processed by neutrinos so that neutrons can react to protons, in MR-SNe the ejected material is dominantly driven by magnetic pressure and therefore it preserves neutron rich conditions, making MR-SNe a promising site for the nucleosynthesis of the heaviest elements, at least theoretically. The first theoretical models of MR-SNe date back to 1970s (e.g., LeBlanc et al., 1970). Early works have been extended and improved until today where simulations include elements such as three dimensions, general relativity, neutrino transport, detailed microphysics (e.g., Obergaulinger et al., 2021; Matsumoto et al., 2022; Varma et al., 2023) as well as the possibility of combining magnetohydrodynamic (MHD) simulations with large nuclear reaction networks to calculate the nucleosynthesis. From the recent simulations by Reichert et al. (2023) (see also Reichert et al., 2021), it emerged that the strongest pre-collapse magnetic fields lead to the strongest r-process ejecta. In particular, if the magnetic field is strong enough, it can impact the proto-neutron star shape which can eventually transit into a toroidal configuration. The change in the neutron star shape may allow ejecta of very neutron rich material from the proto-neutron star itself on very short timescales, leading to production of elements up to the second r-process peak or, for magnetic field high enough, even up to the third r-process peak (see Figure 1.5).

On the contrary, from the observational point of view the situation is more uncertain. There are some observational evidences of very energetic SNe (hypernovae, HNe; Iwamoto et al., 1999, and superluminous SNe, SLSNe; Moriya et al.,

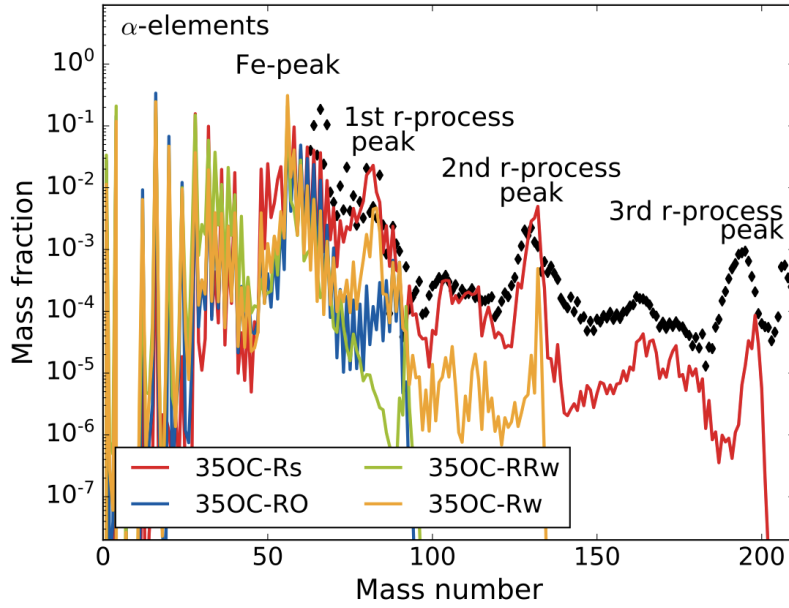


FIGURE 1.5: From Reichert et al. (2021). Integrated nucleosynthetic yields for models with various magnetic fields and rotation: model 35OC-Rs is the one with the strongest magnetic field, model 35OC-RRw is the one with the weakest magnetic field, model 35OC-RO has the same magnetic field of the progenitor (from Woosley et al., 2006b) and model 35OC-Rw has intermediate magnetic field but the fastest rotation.

2018) associated to powerful long gamma-ray bursts (lGRB; Woosley et al., 2006a), whose extreme properties may point towards the presence of some extraordinary conditions of the stellar progenitors and cannot be explained by the neutrino-driven mechanism, however more investigation is still needed.

1.2 Chemical evolution of galaxies

As described in Section 1.1, during the Big Bang only light elements were produced and all the other elements, from C to U and beyond, originated in stars. Stars reprocess material from which they were born in their interior through nuclear reactions. This processed material is then expelled into the ISM in the form of both newly formed and already existing elements, via stellar wind and SNe explosions. As time passes, more and more stellar generations succeed one another with the new ones formed out of gas enriched by the previous stellar generations. This is the process of *chemical evolution* (or *Galactic archaeology*, see e.g., Kobayashi et al., 2020; Matteucci, 2021). When a star forms, it locks a snapshot of the surrounding ISM into its photosphere. Abundances of elements in the photosphere of a star are observable via spectra analysis and yield insights into the chemical composition of the ISM at the time of formation of the star. The abundance of a generic element X in the photosphere of a star can be expressed in absolute values as:

$$A(X) = \log(X/H) + 12, \quad (1.1)$$

where $A(H) = 12$. The most common way to express abundance ratios in stars is relative to the solar chemical composition via the square bracket notation, as:

$$[X/H] = \log(X/H) - \log(X/H)_{\odot}, \quad (1.2)$$

expressed in decimal exponential (dex). In this notation the abundances in the Sun are $[X/H]_{\odot} = 0$.

1.2.1 Chemical evolution models

Chemical evolution models follow the evolution in time and space of the abundances of the different chemical species in the ISM of galaxies of different morphological type. The topic of chemical evolution is highly challenging since it involves many physical processes, such as stellar nucleosynthesis, galactic gas flows, the history of star formation of a galaxy as well as its distribution of stellar mass.

The first seminal papers on chemical evolution date back to 1960s (Schmidt, 1963) and 1970s (Lynden-Bell, 1975; Pagel et al., 1975). However, the chemical evolution is mainly associated to Beatrice Tinsley, who greatly contributed to the field. Her seminal review paper, Tinsley (1980), summarizes all the basic ingredients and equations that still today are at the foundation of modern chemical evolution models.

Numerical chemical evolution models greatly evolved since the very firsts analytical ones, in particular concerning the Milky Way (MW), but also for external galaxies (e.g., Matteucci et al., 1986; Tosi, 1988; Matteucci et al., 1989; Chiappini et al., 1997; Chiappini et al., 1999; Lanfranchi et al., 2006; Cescutti, 2008; Schönrich et al., 2009; Romano et al., 2010; Kobayashi et al., 2011; Matteucci et al., 2014; Haywood et al., 2015; Mollá et al., 2015; Grisoni et al., 2017; Spitoni et al., 2019a; Spitoni et al., 2020). In fact, these models include a more detailed treatment of

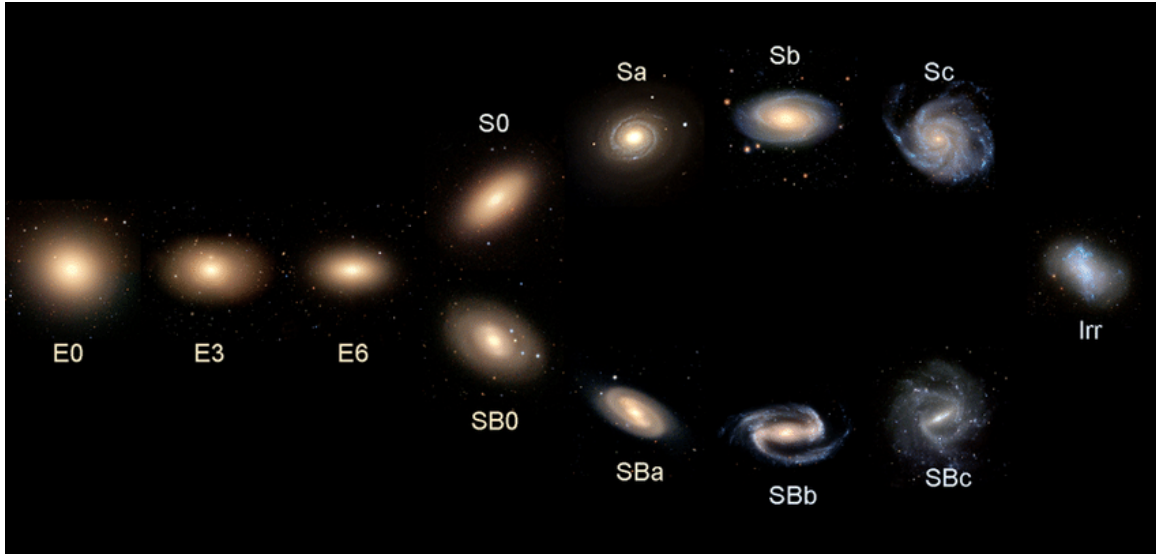


FIGURE 1.6: *The Hubble sequence of galaxies.*

the stellar lifetimes, of the different gas flows and allow a stochastic and/or a 2D approach.

Galaxies of different morphological type and the time-delay model

The Hubble sequence is a classification system for describing the morphological types of galaxies. It was developed by Edwin Hubble in the 1920s (Hubble, 1926) and is one of the most widely used and recognized schemes for categorizing galaxies. The Hubble sequence organizes galaxies into various classes based on their visual appearance and structural characteristics (see Figure 1.6). Early-type galaxies are represented by elliptical galaxies denoted by the letter E followed by an integer n representing their degree of ellipticity. The ellipticity increases from left to right on the Hubble diagram, with near-circular (E0) galaxies situated on the very left of the diagram and more flattened types characterized by higher n index. The two parallel branches on the right of the Hubble sequence are those of spiral galaxies. A spiral galaxy consists of a flattened disk with stars forming a spiral structure and a central concentration of stars known as the bulge. Spiral galaxies are subdivided into normal and barred. Barred spirals have a bar-like structure, with the bar extending from the central bulge; they occupy the lower spiral branch in the diagram and are denoted by the symbol SB, while normal spirals occupy the upper branch and are denoted by the letter S. According to differences in the spiral arms, both type of spirals are further subdivided by adding a letter to the morphological type. The MW is generally classed between SBb and SBc. The third category in the Hubble sequence is that of irregular galaxies, which have no regular structure, with no clear disk and spheroidal components.

The variations in the morphology of different galaxies along the Hubble sequence are due to variations in their physical properties. Irregular galaxies are more gas rich than spirals which however have a much larger gas content than elliptical galaxies. Moreover, elliptical galaxies are characterized by an old stellar population, whereas going from spirals to irregulars there is an increase of

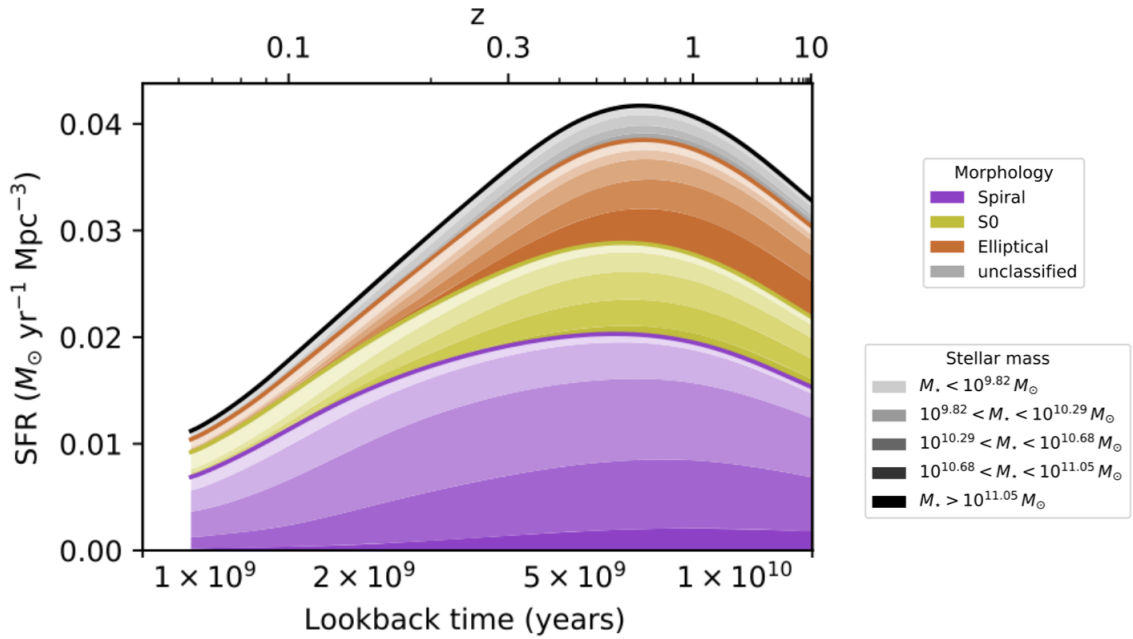


FIGURE 1.7: Adapted from Peterken et al. (2021). The star formation history of the Universe separated into its contributions from galaxies of different morphological type (indicated by colours). Each color is also stratified by present-day stellar mass (darkest to lightest shades for most to least massive galaxies).

young stars and of active star formation. The most common interpretation of the Hubble sequence, in terms of the variations of the physical properties of different galaxies, is that it strongly depends on the different star formation histories. Star formation is very fast and strong in elliptical galaxies and in spheroidal systems, more moderate in spirals and slow in irregular galaxies (see Figure 1.7; see Matteucci, 2012 for a review).

The differences in the star formation histories is reflected also in the different abundance patterns. In particular, the analysis of the abundance ratios, such as $[\alpha/\text{Fe}]$ vs. $[\text{Fe}/\text{H}]$, can allow us to understand the time-scale of formation of different regions. The *time-delay model* explains the observed abundance patterns in terms of different chemical elements produced by different types of stars on different time-scales. α -elements are mostly produced by CC-SNe on short time-scales. In fact, CC-SNe originate from massive stars whose lifetime is typically below 30 Myr. CC-SNe are producing also Fe, however the bulk of it is produced by Type Ia SNe. Type Ia SNe are results of exploding white dwarfs in binary systems and live more than 30 Myr and up to 10 Gyr, and therefore the Fe by Type Ia SNe is produced on longer time-scales. As a consequence, we observe high $[\alpha/\text{Fe}]$ ratios at low $[\text{Fe}/\text{H}]$ values, where the production of both α -elements and Fe is due only to CC-SNe, and lower $[\alpha/\text{Fe}]$ ratios at high $[\text{Fe}/\text{H}]$ because of Type Ia SNe contribution. Moreover, environments where the star formation has been very intense show higher $[\alpha/\text{Fe}]$ ratios which remain almost constant until higher $[\text{Fe}/\text{H}]$ values with respect to environments with a slower star formation. This is shown in Figure 1.8, where predictions for the $[\alpha/\text{Fe}]$ vs. $[\text{Fe}/\text{H}]$ for the Galactic Bulge (taken as representative of a spheroidal system with an intense star formation), for the solar neighborhood (which reflect the evolution of a typical disc

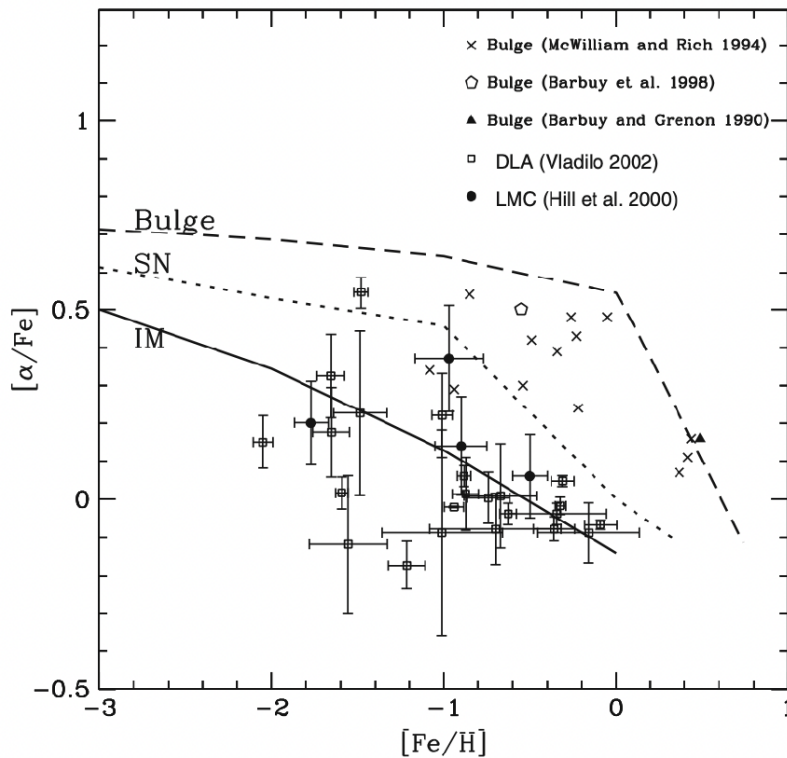


FIGURE 1.8: From Matteucci (2012). Predicted $[\alpha/\text{Fe}]$ vs. $[\text{Fe}/\text{H}]$ abundance patterns for the solar neighborhood (dotted line), for the Galactic Bulge (dashed line) and for the Large Magellanic Cloud (solid line).

region with moderate star formation) and for the Large Magellanic Cloud (a prototype irregular galaxy with slow star formation) are represented. In regions with a very intense star formation, CC-SNe are able to enrich substantially the ISM in Fe and α -elements before Type Ia SNe star exploding. Therefore, the so-called knee in the $[\alpha/\text{Fe}]$ vs. $[\text{Fe}/\text{H}]$ relation is placed at higher metallicities. In spirals and in particular in irregular galaxies the opposite happens: a slow star formation causes the gas to be poorly enriched in metals when Type Ia SNe start ejecting Fe into the ISM.

The first prediction of the *time-delay model* dates back to the 90s (Matteucci et al., 1990). Since then, the $[\alpha/\text{Fe}]$ ratios have been widely used as chemical clock to investigate the evolution of galaxies of different morphological type, from dwarf irregular galaxies to giant ellipticals (e.g., Lanfranchi et al., 2006; Ballero et al., 2007; Vincenzo et al., 2014; De Masi et al., 2018).

1.3 Previous results

The first chemical evolution study that addresses the subject of r-process nucleosynthesis is Argast et al. (2004). The authors analyzed whether if MNS or normal CC-SNe were the dominant source of r-process material in the Galaxy, by means of an inhomogeneous chemical evolution model. Their study ruled out MNS as the dominant r-process source, mainly because of their low rates of occurrence

which led to an underproduction of Eu and of the r-process fraction of Ba at low metallicities.

Indeed, some of the following studies on the nucleosynthesis of neutron capture elements were excluding MNS as production sites (e.g., Travaglio et al., 2004; Cescutti et al., 2006; Lanfranchi et al., 2006; Cescutti et al., 2007; Cescutti, 2008; Lanfranchi et al., 2008) and assumed that r-process nucleosynthesis was happening only in normal CC-SNe.

Matteucci et al. (2014) explored the production of Eu in the MW by adopting MNS and/or normal CC-SNe as main Eu production sites. Their main conclusions were that MNS can be entirely responsible for the production of Eu in the MW, but their coalescence timescale should be no longer than 1 Myr for the bulk of binary systems. If longer timescales are considered, then CC-SNe should also contribute to the Eu production.

Similar prescriptions for the r-process nucleosynthesis have been later applied in the stochastic chemical evolution model of Cescutti et al. (2015). In that work, the s-process contribution from spinstars was also taken into account. Conclusions from Matteucci et al. (2014) were confirmed and, thanks to the inhomogeneous mixing of the model, the low-metallicity scatter observed in the Galactic halo was reproduced as well.

The origin of r-process elements has been analyzed also by Wehmeyer et al. (2015) with an inhomogeneous approach. In that study, the contribution from MR-SNe was also taken into account. Once again, the main conclusions pointed towards a mixed scenario in which both MNS and massive stars produce r-process elements.

The observation of the gravitational wave GW170817 coming from the merger of two NSs represented a breakthrough in the field. As already discussed, from the kilonova following the GW it has been possible to confirm the r-process nucleosynthesis and, moreover, since the event happened in the elliptical galaxy NGC 4993 and a sGRB (GRB 170817A) was observed in the same sky region ~ 1.7 s with respect to the merger time, longer delay times for the coalescence of the DNS systems were considered to be more plausible. As we explained in Section 1.1.2, the delay time is determined by both the stellar nuclear lifetime and the gravitational delay time and, therefore, it can largely vary and it depends on a delay time distribution (DTD). A popular choice in literature is a $\text{DTD} \propto t^{-1}$ (e.g., Côté et al., 2017; Hotokezaka et al., 2018), where t is the total coalescence delay time.

Simonetti et al. (2019) (see also Greggio et al., 2021) derived a new DTD for MNS from theoretical considerations and tested it against the sGRB redshift distribution and the [Eu/Fe] vs. [Fe/H] trend in the MW. The distribution of SGRBs was successfully fitted by using the DTD for MNS, but if such longer delays for merging were assumed a second r-process production site was needed in order to reproduce the [Eu/Fe] vs. [Fe/H] abundance pattern. The DTD of Simonetti et al. (2019) is the one adopted throughout this Thesis and will be described in detail in the next Chapter. DTDs for MNS have been widely adopted in chemical evolution models (e.g., Rizzuti et al., 2019; Kobayashi et al., 2020; Rizzuti et al., 2021; Cavallo et al., 2021). However, as already concluded in the past, if proper

timescales for MNS are considered, then MNS can not be the only source of r-process material in the Galaxy. Whether the second source is represented by MR-SNe or by other mechanisms is still a matter of discussion, that we are going to address in this Thesis.

1.4 Structure of the Thesis

This Thesis is devoted to the development of new chemical evolution models able to follow the evolution and distribution of neutron capture elements in different galactic environments, from external galaxies of different morphological type to Local Group dwarf galaxies, the MW and early-type galaxies.

The Thesis is structured as follows. In Chapter 2, I describe the adopted chemical evolution models with their fundamental ingredients and the complete equations of chemical evolution. In the successive Chapters, I show the original results of my Thesis work. In particular, in Chapter 3, I present the models for external galaxies of different morphological type as well as for the computation of the cosmic rate of MNS in different cosmological scenarios. In Chapter 4, I show the investigation of the Eu and Ba abundances in Local Group dwarf spheroidal and ultra-faint dwarf galaxies. In Chapter 5, I present results for abundance patterns and gradients in the thin disc of the MW for a large sample of neutron capture elements (Y, Zr, La, Ba, Ce, Eu, Mo, Nd and Pr). In Chapter 6, I present the model developed to study the chemical evolution of the Galactic Bulge with different stellar populations and how these prescriptions affect the behavior of the neutron capture element Ce. In Chapter 7, I show a work devoted to the study of the neutron capture elements in early-type galaxies, in which I present a new formulation for the feedback prescriptions. Finally, in Chapter 8 I summarize the main conclusions of this Thesis and discuss the future advancements which are necessary for the development of this field.

CHAPTER 2

Chemical Evolution Models

CHEMICAL evolution models allow us to study the evolution in time and space of the abundances of chemical species in the ISM of different galaxies. Light elements, including hydrogen (H), deuterium (D), helium (He), and a small amount of lithium (${}^7\text{Li}$), were the only ones formed during the Big Bang. All the other chemical elements that make up stars and planets are synthesized in the interiors of stars and then dispersed into the ISM through stellar winds and supernova explosions. Over time, these elements are incorporated into new generations of stars and planets, leading to the gradual enrichment of the ISM and the evolution of the galaxy's chemical composition. The chemical evolution of galaxies is driven by a complex interplay of physical processes, including star formation, stellar nucleosynthesis, gas accretion and gas outflows. The detailed mechanisms and timescales of these processes depend on the galaxy properties such as mass, size, and environment, as well as its history of interactions with other galaxies.

In this Chapter, I present the adopted chemical evolution models for galaxies of different morphological type. I first describe the basic ingredients for the chemical evolution and then I introduce the complete set of equations for the chemical evolution. Finally, I introduce the concept of the delay time distribution for MNS and how it can affect the chemical evolution of neutron capture elements.

The theoretical background for this Chapter is taken from the book *Chemical evolution of galaxies*, by Matteucci (2012).

2.1 Fundamental ingredients

There are four basic ingredients for modeling galactic chemical evolution:

- Initial conditions
- The stellar birthrate function
- The stellar yields
- Gas flows and their chemical composition

Once these ingredients are provided, it is possible to write a set of equations that describe the temporal and spatial variation of the gas content and its chemical composition. In the next Sections, I provide a description of these ingredients.

2.1.1 Initial conditions

The initial conditions for a model of galactic chemical evolution consist in specify:

- The chemical composition of the initial gas
- The boundaries of the studied system

The chemical composition of the initial gas can be primordial or pre-enriched by a pre-galactic stellar generation. The assumption that I adopted during this Thesis is to have an initial primordial chemical composition. Therefore, the chemical composition of the initial gas is made by the elements produced during the Big Bang (see Chapter 1).

The system can be considered a closed or an open box, depending on possible exchange of gas between the galaxy and the surrounding environment via infall and/or outflows of gas. In this Thesis, the studied systems are assumed to be open.

2.1.2 Birthrate function

The stellar birthrate function $B(m, t)$ represents the number of stars formed in the time interval $[t, t + dt]$ with mass in the range $[m, m + dm]$. It is usually expressed as the product of two independent functions, one depending only on the mass m and the other one depending only on the time t :

$$B(m, t) = \psi(t)\phi(m), \quad (2.1)$$

where $\psi(t)$ is the star formation rate (SFR) and $\phi(m)$ is the initial mass function (IMF) in number. In the following, I describe these two quantities in detail.

The star formation rate

The SFR indicates how many solar masses of gas in the ISM are converted into stars per unit of time. It is expressed in units of $M_{\odot} pc^{-2} yr^{-1}$ or $M_{\odot} yr^{-1}$. A common parametrization of the SFR is the Schmidt-Kennicutt law (Kennicutt, 1998; Schmidt, 1959):

$$\psi(t) = \nu \sigma_{gas}^k, \quad (2.2)$$

where σ_{gas}^k is the gas surface density, expressed in $M_{\odot} pc^{-2}$, the index k has usually values between 1 and 2 and ν is the star formation efficiency, which is a free parameter and represents the SFR per unit mass of gas, with the dimensions of the inverse of a time.

For star forming regions with roughly constant scaleheights, the surface density in Eq. 2.2 is equivalent to the volume density one (see Romano et al., 2015). By assuming that the Schmidt-Kennicutt law indicates that the SFR is controlled by the gas self-gravity, one can write:

$$\psi(t) = \frac{\epsilon}{t_{ff}} \rho_{gas}^{k'} = \nu' \rho_{gas}^{k'}, \quad (2.3)$$

where $t_{ff} \propto 1/\sqrt{\rho_{gas}}$, ϵ is a free parameter and $k' = 1$. Integrating over the volume, we can write Eq. 2.3 as:

$$\psi(t) = \nu' M_{gas}^{k'}, \quad (2.4)$$

where M_{gas} is the gas mass withing the galaxy.

In this Thesis, I adopt the surface expression of Eq. 2.2 to model the MW galaxy, and the expression of Eq. 2.4 for external galaxies.

The initial mass function

The IMF is the distribution of stellar masses at birth. It's form has been derived only for the solar vicinity, and it is usually approximated by either a one-slope or a multi-slope power law and is assumed to be constant in space and time. The most common example of a one-slope IMF is the Salpeter (1955):

$$\phi(m) = am^{-(1+x)}, \quad (2.5)$$

with $x = 1.35$ and with a being the normalization constant derived by imposing that:

$$1 = \int_{0.1}^{100} \varphi(m) dm = \int_{0.1}^{100} m\phi(m) dm, \quad (2.6)$$

where $\varphi(m)$ is the IMF in mass.

Since the work of Salpeter (1955), many other multi-slope IMF have been derived. In this Thesis, I made use of the ones by Scalo (1986) (the approximate expression by Chiappini et al., 2000):

$$\phi(m) \propto \begin{cases} m^{-(1+1.35)} & \text{if } m < 6M_{\odot} \\ m^{-(1+1.7)} & \text{if } m \geq 6M_{\odot}, \end{cases} \quad (2.7)$$

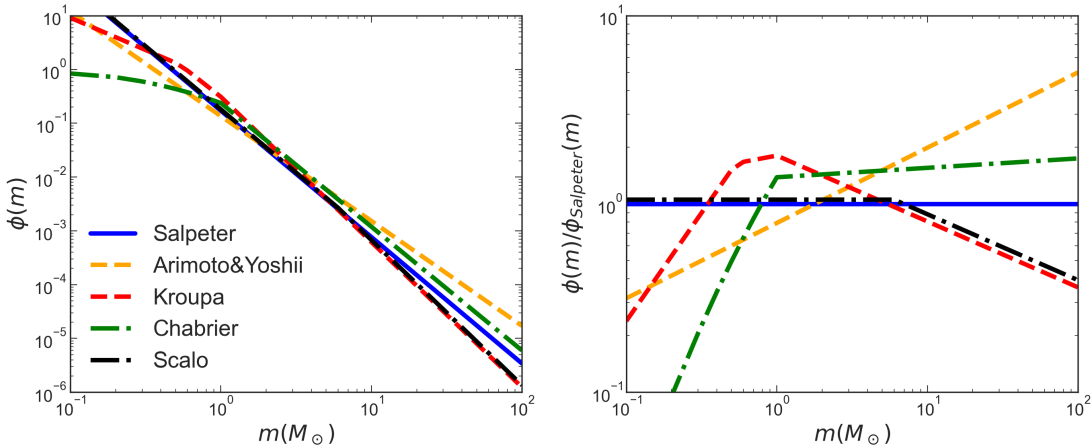


FIGURE 2.1: *Left panel: Salpeter (1955), Scalo (1986), Yoshii et al. (1987), Kroupa et al. (1993) and Chabrier (2003) IMFs. Right panel: same as left panel but with each IMFs divided by the Salpeter one to allow a better comparison of the different mass distributions.*

by Kroupa et al. (1993):

$$\phi(m) \propto \begin{cases} m^{-(1+0.3)} & \text{if } m \leq 0.5M_{\odot} \\ m^{-(1+1.2)} & \text{if } 0.5 < m/M_{\odot} < 1.0 \\ m^{-(1+1.7)} & \text{if } m > 1.0M_{\odot}, \end{cases} \quad (2.8)$$

and by Chabrier (2003), who proposed a log-normal form for the low-mass part of the IMF:

$$\phi(m) \propto \begin{cases} e^{-(\log m - \log m_c)^2 / 2\sigma^2} & \text{if } m \leq 1.0M_{\odot} \\ m^{-(1+1.3)} & \text{if } m > 1.0M_{\odot}, \end{cases} \quad (2.9)$$

with $m_c = 0.079 M_{\odot}$ and $\sigma_c = 0.69$.

The Kroupa et al. (1993) IMF is usually preferred to model the chemical evolution of the solar neighborhood (Romano et al., 2005), while the Chabrier (2003) is preferred for the evolution of spheroids. In this Thesis, I adopt the Kroupa et al. (1993) IMF for the evolution of the MW disc, the Chabrier (2003) IMF for modelling the MW bulge and the Salpeter (1955) IMF for dSph and UFD galaxies. For elliptical galaxies I followed the work of De Masi et al. (2018) who assumed that the IMF goes from being bottom heavy in less massive galaxies to top heavy in more massive ones, producing a downsizing in SE, favouring massive stars in larger galaxies. Therefore, I used the Scalo (1986) IMF for low-mass elliptical galaxies, the Salpeter (1955) for intermediate mass galaxies and the Yoshii et al. (1987) IMF for high-mass galaxies, which is a one-slope IMF with $x = 0.95$.

The IMFs are shown in Figure 2.1, where it is possible to appreciate the differences between a one-slope and multi-slope IMFs.

2.1.3 Stellar yields

The stellar yields describe the amount of both newly formed and pre-existing elements ejected into the ISM by stars. They represent a fundamental ingredient for

modelling chemical evolution and are computed by means of stellar evolution and nucleosynthesis models.

Stars of different masses produce different chemical elements:

- Stars with mass $< 0.8 M_{\odot}$: these stars have a lifetime longer than the age of the Universe. They never ignite H, therefore they do not contribute to the chemical enrichment of the ISM, but they affect the chemical evolution by subtracting gas to the star formation process;
- LIMS in the mass range $0.8 M_{\odot} - 8 M_{\odot}$, which are divided into single stars and binary systems which can give rise to Type Ia SNe:
 - Single stars, which contribute to the chemical enrichment of the ISM through post-MS mass loss and the final ejection of a planetary nebula. These stars produce mainly ${}^4\text{He}$, ${}^{12}\text{C}$ and ${}^{14}\text{N}$ plus some CNO isotopes and heavy ($A > 90$) s-process elements.
 - Type Ia SNe, which originate from the explosion of a C-O white dwarf triggered by accretion of material from a companion, which can either be a red giant or another white dwarf. They produce mostly iron ($\simeq 0.626 M_{\odot}$ per event), and enrich the medium with traces of elements from C to Si. They also contribute to other elements, such as C, Ne, Ca and Mg, but in negligible amounts with respect to Type II SNe.
- Massive stars with masses $> 8 M_{\odot}$:
 - Stars in the mass range $7 - 10 M_{\odot}$ explode as e-capture SNe. Electron capture triggers instability in the stars and at the same time O ignites explosively in the ONeMg degenerate core.
 - Stars in the mass range $10 M_{\odot} - M_{WR}$, end their life as Type II SNe and explode by core collapse. The explosion can lead to the formation of either a neutron star or a black hole, depending on the amount of the ejected material which falls back on the contracting core during the explosion. The upper limit of the mass range, M_{WR} , is the minimum mass for the formation of a Wolf-Rayet star, it is rather uncertain since it depends on the stellar mass loss, which in turn depends on the initial stellar mass and metallicity (e.g. for a solar chemical composition $M_{WR} \simeq 25 M_{\odot}$).
 - Stars with masses above M_{WR} , because of the large mass loss, end up as Type Ib/c SNe and explode also by core collapse. They are linked to the long Gamma Ray Bursts (LGRBs) and some of them can be particularly energetic (with an initial blast wave energy of $\sim 10^{52} - 10^{53} \text{ erg}$) so to be known as HNe (see Chapter 1).

Massive stars are responsible for the production of most of α -elements, some Fe-peak elements, light ($A < 90$) s-process elements (especially if stellar rotation is included) and, as discussed in Chapter 1, may contribute also to r-process nucleosynthesis (if strong magnetic field and fast rotation are included).

- Merging of compact object and in particular neutron stars binary systems discussed in Chapter 1 are also a powerful source of r-process material.

The most important factor governing the nucleosynthesis production is the initial stellar mass. However, also the initial metallicity, rotation and magnetic fields play an important role. In this Thesis, I adopt different sets of yields for massive stars and for LIMS, including stellar rotation and magnetic fields, to explore the impact on the production of neutron capture elements. In the next Chapters, I will provide details of the datasets included in the chemical evolution models.

2.1.4 Gas flows

Gas flows are of fundamental importance for studying the chemical evolution of galaxies, since they are required to explain several features, such as the abundance gradients along galactic disks and the heavy element abundances in the intracluster medium.

Gas flows can be divided in infall and outflow. In chemical evolution models, the infall rate is commonly parameterised as an exponentially decaying law:

$$\dot{\Sigma}_{in,f}(t) \propto e^{-t/\tau_{in,f}}, \quad (2.10)$$

where $\tau_{in,f}$ is the infall timescale defined as the time at which half of the total mass of the galaxy has assembled. The chemical composition of the infalling material can be assumed to be primordial or pre-enriched.

Gas outflows are defined as galactic winds if they leave the galaxy potential well, or as galactic fountains if they fall back into the galaxy. In both cases, the chemical composition of the gas is that of the system. In the case of galactic winds, they develop when the thermal energy of the gas, heated by SNe explosions, stellar winds and eventually AGN feedback (see Chapter 7), exceeds its binding energy. Except for the specific MW models which will be presented in Chapters 5 and 6 that do not include winds, in this Thesis I adopt two different wind parametrizations:

- a wind rate proportional to the SFR:

$$\dot{\Sigma}_{out}(t) = -\omega\psi(t) \quad (2.11)$$

where ω is a free parameter measuring the efficiency of the wind and which can vary according to the morphological type of the galaxy. In that way, galactic winds can be treated as continuous processes depending just on the SFR. This parametrization is adopted in the study of external irregular and spiral galaxies (Chapter 3) as well as for dSph and UFD galaxies (Chapter 4).

- a sudden wind occurring when the thermal energy of the gas in the ISM exceeds its binding energy and all the gas is lost. Afterwards, the galaxy is assumed to evolve passively. This formulation is adopted in the study of elliptical galaxies (Chapter 7).

2.2 Chemical evolution equations

Once the fundamental ingredients have been specified, we can write a complete set of equations describing the evolution, in time and space, of the gas and its chemical composition.

Let us define $G(t)$ as the surface mass density at the time t in the ISM ($\Sigma_{ISM}(t)$) normalized to the total surface mass density accreted to the galaxy at the present time t_f ($\Sigma_{inf}(t_f)$):

$$G(t) = \frac{\Sigma_{ISM}(t)}{\Sigma_{inf}(t_f)}, \quad (2.12)$$

and $G_i(t)$ as the normalized surface mass density of the element i at the time t , as:

$$G_i(t) = G(t)X_i(t), \quad (2.13)$$

where $X_i(t)$ indicates the abundance by mass of the element i (with $\sum_i X_i = 1$). Therefore, the complete equation for the evolution of the generic chemical element i can be written as:

$$\dot{G}_i(r, t) = -\psi(r, t)X_i(r, t) + R_i(r, t) + \dot{G}_{i,inf}(r, t) - \dot{G}_{i,out}(r, t), \quad (2.14)$$

where $\psi(t)X_i(t)$ is the rate at which the element i is subtracted by the ISM to be included in stars, $\dot{G}_{i,inf}(t)$ is the rate at which the element i is accreted through infall of gas and $\dot{G}_{i,out}(t)$ represents the rate at which the element i is lost through galactic wind. The term $R_i(t)$ is the rate of restitution of matter from the stars with different masses into the ISM in the form of the element i , and it corresponds to:

$$\begin{aligned} R_i(r, t) = & \int_{M_L}^{M_{Bm}} \psi(t - \tau_m) Q_{mi}(t - \tau_m) \phi(m) dm + \\ & + A \int_{M_{Bm}}^{M_{BM}} \phi(m) \left[\int_{\mu_{min}}^{0.5} f(\mu) \psi(t - \tau_{m2}) Q_{mi}(t - \tau_{m2}) d\mu \right] dm + \\ & + (1 - A) \int_{B_m}^{M_{BM}} \psi(t - \tau_m) Q_{mi}(t - \tau_m) \phi(m) dm + \\ & + \int_{M_{BM}}^{M_U} \psi(t - \tau_m) Q_{mi}(t - \tau_m) \phi(m) dm. \end{aligned} \quad (2.15)$$

The term $Q_{mi}(t - \tau_m)$ corresponds to $\sum_j Q_{ij}(m) X_j(t - \tau_m)$, where $Q_{ij}(m)$ is the production matrix (Talbot et al., 1973), which takes into account the newly formed element i originating from the element j and the already present in the star of mass m . $X_j(t - \tau_m)$ is the abundance of the element j (which is later transformed into the element i and ejected) present into the star at the time of its birth ($t - \tau_m$). The function τ_m describes the stellar lifetimes as a function of mass (see Romano et al., 2005). In this Thesis, I adopt the relation of Schaller et al. (1992) with the polynomial fit of Gibson (1997).

The first integral of Eq. 2.15 takes into account the contribution from stars with masses in the range $[M_L - M_{Bm}]$, where M_L represents the minimum mass dying at the time t (equal to $M_L \simeq 0.9 M_\odot$ for $t \simeq 14 \text{ Gyr}$).

The second integral refers to the total mass of a binary system which can give rise to a Type Ia SN event. In this case, the rate is calculated assuming a binary system made of a C-O WD and a red giant companion (single-degenerate scenario). In Matteucci et al. (2009) it has been shown that this scenario is equivalent to the double degenerate one of Greggio (2005), from the point of view of Galactic chemical evolution. M_{Bm} and M_{BM} are the minimum and maximum mass of the whole binary system, in particular $M_{Bm} = 3 M_{\odot}$ to make sure that both the WDs would reach the Chandrasekhar mass after accretion from the companion, while $M_{BM} = 16M_{\odot}$ to make sure that the mass of both component of the binary system do not exceed the maximum mass which can give rise to a C-O WD, which is $M_{up} = 8M_{\odot}$. The function $f(\mu)$ is the distribution of the mass ratio of the secondary star of the binary system, being $\mu = m_2/m_B$, namely the ratio between the mass of the secondary component (m_2) and the total mass of the binary system (m_B). μ_{min} is the minimum mass fraction producing a Type Ia SN at the time t and $f(\mu)$ has the following form:

$$f(\mu) = 2^{1+\gamma}(1 + \gamma)\mu^{\gamma}, \quad (2.16)$$

with $\gamma = 2$ to favour values of μ towards 0.5 (see Matteucci et al., 2001). The constant A is a free parameter representing the fractions of binary systems with the right properties to give rise to a Type Ia SN and it is fixed in order to reproduce the present time Type Ia SNe rate in the studied galaxy. The quantity τ_{m2} is the lifetime of the secondary star of the binary system and therefore it represents the clock of the system in the SD scenario. This second integral, without the matrix Q_{mi} , represents the rate of Type Ia SNe.

The third integral represent the contribution from stars with masses in the range $[M_{Bm} - M_{BM}]$ which can end their lives either as C-O WDs or as Type II SNe.

Finally, the fourth integral refers to the material restored into the ISM by stars ending their lives as CC-SNe, where M_U is the upper mass limit for stars contributing to the chemical evolution.

2.3 The rate of merging neutron stars

As described in Chapter 1, the two main sites that have been identified for the production of neutron capture process elements are massive stars and MNS. The challenge is to better understand the r-process and its nucleosynthetic site(s) using observable constraints such as the current rate of events linked to those sites and the measurements of stellar chemical abundances.

In the context of chemical evolution of galaxies, the timescales for the production of each elements are of great importance. In the case of massive stars, the timescale is given by the nuclear lifetime of the massive stars. On the other hand, for what concerns MNS, the timescale is given by the sum of the progenitors lifetime and the delay due to gravitational radiation, which mainly depends on the initial separation of the binary system and on the masses of the two components.

In this Thesis, the rate of MNS in galaxies of different morphological type has been computed using two different approaches. The first one, consisted in assuming a constant delay time between the formation of the neutron stars binary

system and the merging event, while the second one consisted in assuming a probability distribution of delay times.

The DTD for MNS represents the distribution of the coalescence times of MNS formed in an instantaneous burst of star formation, namely, a single stellar population. It gives the probability of the merging event to occur at a given time t from the formation of the neutron stars binary system progenitors. Then, the MNS rate is simply obtained as the convolution of a given DTD with a given SFR:

$$R_{MNS}(t) = k_\alpha \int_{\tau_i}^{\min(t, \tau_x)} \alpha_{MNS}(\tau) \Psi(t - \tau) f_{MNS}(\tau) d\tau, \quad (2.17)$$

where Ψ is the SFR and f_{MNS} is the DTD. α_{MNS} is the fraction of neutron stars binary systems which can give rise to a merging event, and in principle it can vary with time. τ is the total delay time defined in the range (τ_i, τ_x) , so that:

$$\int_{\tau_i}^{\tau_x} f_{MNS}(\tau) d\tau = 1, \quad (2.18)$$

where τ_i is the minimum delay time of occurrence for MNS (here fixed at 10 Myr) and τ_x is the maximum delay time which can be larger than a Hubble time. Finally, k_α is the number of stars per unit mass in a stellar generation and it depends on the IMF, in particular:

$$k_\alpha = \int_{m_m}^{m_M} \varphi(m) dm, \quad (2.19)$$

where m_m and m_M are the progenitor minimum and maximum mass to produce a neutron star, respectively.

In this Thesis, we used the DTD derived by Simonetti et al. (2019) (see also Greggio et al., 2021). Here we will review the main steps of its derivation.

2.3.1 The delay time distribution for MNS

Simonetti et al. (2019) derived a new DTD for MNS, following the formalism of the DTD for Type Ia SNe found by Greggio (2005) (see next Section).

For MNS the delay time is given by the sum of the nuclear lifetime and the delay due to the emission of gravitational waves, namely the gravitational time delay. This last term can be expressed by the Landau et al. (1966) relation:

$$\tau_{gw} = 0.15 \frac{A^4}{m_1 m_2 (m_1 + m_2)} Gyr, \quad (2.20)$$

as a function of the system initial separation A and of the masses m_1 and m_2 of the primary and secondary star of the system, respectively. Simonetti et al. (2019) simplified this relation, demonstrating that the gravitational time delay can be expressed as a function of the total mass of the system, instead that of the masses of the two components, with a negligible error. In particular, they found that:

$$\tau_{gw} = 0.6 \frac{A^4}{M^3} Gyr, \quad (2.21)$$

with $M = m_1 + m_2$ being the total mass of the system. According to this last equation, the distribution of the gravitational time delays now depends on the initial separation A and on the total mass M . Since these two variables are independent, it is possible to factorize the number of systems with gravitational delay time between τ_{gw} and $\tau_{gw} + d\tau_{gw}$ as the product of two different functions, one depending only on A and the other only on M :

$$df(\tau_{gw}) = df(A, M) = g(A)h(M)dAdM. \quad (2.22)$$

The function $g(A)$ describes the initial separations, while $h(M)$ is the distribution of the total masses of the systems that will merge. Both of these functions can be expressed as a power law, however in order to simplify the calculation, in the case of $h(M)$ it is assumed a flat distribution, so that:

$$\begin{cases} g(A) \propto A^\beta \\ h(M) \propto \text{const}, \end{cases} \quad (2.23)$$

where the parameter β parametrizes the shape of the distribution of initial separations.

The number of systems which merge with a gravitational time delay τ_{gw} is:

$$n(\tau_{gw}) = f(\tau_{gw})d\tau_{gw} = d\tau_{gw} \int_{A_m}^{A_M} g(A)h(M) \left| \frac{\partial M}{\partial \tau_{gw}} \right| dA, \quad (2.24)$$

where A_m and A_M are the minimum and maximum separations for systems, respectively:

$$A_m = \left(\frac{M_m^3 \tau_{gw}}{0.6} \right)^{1/4}, \quad (2.25)$$

$$A_M = \left(\frac{M_M^3 \tau_{gw}}{0.6} \right)^{1/4}, \quad (2.26)$$

and M can vary between $M_m = 2 M_\odot$ and $M_M = 4 M_\odot$. From these two last expressions, it is possible to derive M as:

$$M = \left(\frac{0.6A^4}{\tau_{gw}} \right)^{1/3}, \quad (2.27)$$

so that, after deriving it with respect to τ_{gw} and substituting it in Eq. 2.24, the number of systems which merge with a gravitational time delay τ_{gw} , becomes:

$$f(\tau_{gw}) \propto \int_{A_m}^{A_M} A^\beta \left(\frac{A}{\tau_{gw}} \right)^{4/3} dA = \frac{1}{\tau_{gw}^{4/3}(\beta + 7/3)} [A^{\beta+7/3}]_{A_m}^{A_M}. \quad (2.28)$$

Using the relations 2.25 and 2.26, one obtains:

$$f(\tau_{gw}) \propto \tau_{gw}^{(1/4)\beta - 3/4} (M_m^{3/4(\beta+7/3)} - M_M^{3/4(\beta+7/3)}). \quad (2.29)$$

Following the result of Greggio (2005) to develop a DTD for binary white dwarfs, the following distribution of the total (nuclear plus gravitational) delay time for

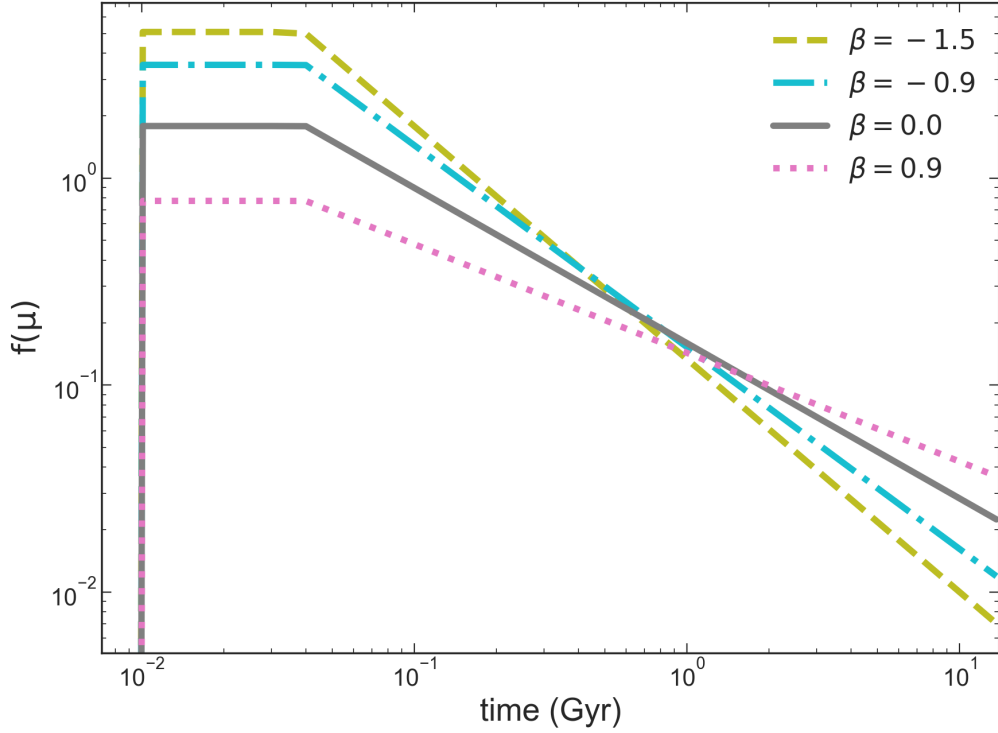


FIGURE 2.2: Delay time distributions for MNS computed for the three different values of β . A normalization factor of 1 has been assumed.

MNS can be constructed:

$$f(\tau) \propto \begin{cases} 0 & \text{if } \tau < 10 \text{ Myr} \\ p_1 & \text{if } 10 < \tau < 40 \text{ Myr} \\ p_2 \tau^{0.25\beta - 0.75} (M_m^{0.75(\beta+2.33)} - M_M^{0.75(\beta+2.33)}) & \text{if } 40 \text{ Myr} < \tau < 13.7 \text{ Gyr} \end{cases} \quad (2.30)$$

where p_1 and p_2 must be chosen in order to obtain a continuous and normalized function. In Figure 2.2, we show the DTDs obtained for four different values of β . As one can see, the first portion of the distribution ends with the formation of the first double neutron star system, with 10 Myr being the nuclear lifetime of a typical massive star. The second portion refers to systems which merge soon after the formation of the double neutron star systems. This portion of the distribution is described by a flat plateau, up to the lifetime of the minimum mass progenitor of a neutron star. The third part of the distribution is the distribution of the gravitational delay times and attains to those systems for which the time delay is dominated by gravitational radiation.

2.4 Delay time distribution for Type Ia SNe

As described in Section 2.2, the rate of Type Ia SNe can be computed by assuming a SD scenario or a double-degenerate (DD) one, with very few differences from the chemical evolution point of view. Throughout this Thesis we mainly adopt the SD scenario, except that for the evolution of external galaxies (Chapter 3) for which the DD one has been tested. In this case, by adopting the same formulation used for the rate of MNS, the rate in number of Type Ia SNe can be computed as:

$$R_{Ia}(t) = k_{\alpha, Ia} \int_{\tau_i}^{\min(t, \tau_x)} \alpha_{Ia}(\tau) \Psi(t - \tau) f_{Ia}(\tau) d\tau, \quad (2.31)$$

where α_{Ia} is the fraction of binary systems giving rise to Type Ia SNe. This quantity can vary with time, but here we assume it to be constant. f_{Ia} is the DTD of Type Ia SNe which, in analogy with the DTD for MNS, represents the distribution of the explosion times from an instantaneous burst of star formation of unitary mass. It must be normalized to 1 in the allowed range for the delay time τ :

$$\int_{\tau_i}^{\tau_x} f_{Ia}(\tau) d\tau = 1, \quad (2.32)$$

where τ_i is the minimum total delay time of occurrence of Type Ia SNe, here fixed at 40 Myr (corresponding to the lifetime of a $8 M_{\odot}$ star) and τ_x is the maximum total delay time which can be larger than a Hubble time, according to the chosen progenitor model. We adopted for Type Ia SNe the DTD suggested by Greggio, 2005 for the wide DD scenario:

$$f_{Ia} \propto \int_{\tau_{n,i}}^{\min(\tau_{n,x}, \tau)} n(\tau_n) S(\tau, \tau_n) d\tau_n, \quad (2.33)$$

where $\tau_{n,i}$ and $\tau_{n,x}$ are the nuclear lifetimes of the most and least massive secondary in the progenitor binary systems, respectively. $n(\tau_n)$ is the distribution function of the nuclear delays of the Type Ia SN progenitors and

$$S(\tau, \tau_n) = \begin{cases} (M_m^{0.75\beta_{Ia}+1.75} - M_M^{0.75\beta_{Ia}+1.75})(\tau - \tau_n)^{-0.75+0.25\beta_{Ia}} & \text{if } \tau_n \leq \tau - \tau_{gw,i} \\ 0 & \text{if } \tau_n \geq \tau - \tau_{gw,i} \end{cases} \quad (2.34)$$

where $\tau_{gw,i}$ is the minimum gravitational time delay. We adopted a distribution characterized by an initial separation function with exponent equal to $\beta_{Ia} = -0.9$ (as also suggested by Matteucci et al., 2009) and a maximum nuclear delay time $\tau_{n,x} = 0.4$ Gyr. Finally, $k_{\alpha, Ia}$ is the number of stars per unit mass in a stellar generation, in particular:

$$k_{\alpha, Ia} = \int_{m_L}^{m_U} \varphi(m) dm, \quad (2.35)$$

where $m_L = 0.1M_{\odot}$ and $m_U = 100M_{\odot}$. For a Salpeter (1955), we have $k_{\alpha, Ia} = 2.83$.

CHAPTER 3

External Galaxies and the Cosmic Merging Neutron Stars Rate

IN this Chapter, I present our computed rates of MNS in external galaxies of different morphological type (ellipticals, spirals and irregulars), as well as the cosmic MNS rate for different cosmological scenarios, with the aim of providing predictions of kilonova rates for future observations, both at low and high redshift.

The Chapter is organized as follows. In Section 3.1, I give a brief introduction to the context to which this Chapter belongs. In Section 3.2, I describe the chemical evolution model adopted. In Section 3.3, I show our results for the MNS rate in external galaxies as well as our predictions for the [Eu/Fe] vs. [Fe/H] abundance patterns. In Section 3.4, I present results for the cosmic MNS rate. Finally, Section 3.5 summarizes the results and conclusions.

The results presented in this Chapter are described in the published paper Molero et al. (2021b).

3.1 Introduction

As introduced in Chapter 1, the merging of two neutron stars due to gravitational wave radiation produces a strong GW signal together with its optical counterpart, the kilonova (powered by the decay of heavy r-process elements synthesized during the merging event) and possibly a short gamma-ray burst (sGRB). The strong connection between all these different physical phenomena with neutron stars merging has been proved thanks to the detection of the event GW170817, by the Laser Interferometer Gravitational-Wave Observatory (LIGO) (Abbott et al., 2017), the first detection of a GW due to a MNS. Moreover, the observation of the kilonova AT2017gfo following the event, allowed us to detect the presence of heavy nuclei (Watson et al., 2019; Pian et al., 2017; Smartt et al., 2017), as well as to localize the neutron star binary system in the galaxy NGC 4993, an early-type galaxy with an old stellar population (Coulter et al., 2017). However, it is not to rule out the probability that the galaxy NGC 4993 underwent a recent galactic merger (Ebrova et al., 2020), thus the neutron stars binary system which gave rise to GW170817 may have come from the second accreted galaxy, which can potentially be a smaller late-type galaxy.

In this Chapter, we are investigating on the production of Eu in different galaxies which, as already discussed, can be produced in massive stars and/or MNS. In the context of galactic chemical evolution, it is possible to investigate the sites of production of chemical elements by using observational constraints such as the present day rate and the stellar chemical abundances. In several chemical evolution models, the MNS have been included as r-process element producers. In some of these models (Cescutti et al., 2015; Matteucci et al., 2014) a constant gravitational time delay has been adopted for all the systems, whereas in others a more realistic delay time distribution function for such timescales has been tested (Hotokezaka et al., 2018; Cote et al., 2019; Simonetti et al., 2019, from now on S19). Long time delays for merging are also requested by the fact that the event GW170817 occurred in an early-type galaxy where star formation has stopped several Gyrs ago, and by the cosmic rate of sGRBs.

The preferred model for the sGRBs is the merger of two compact objects (neutron stars and/or black holes), as a result of gravitational inspiral Narayan et al. (1992). Previous results (S19) have showed that the distribution of sGRBs is better reproduced with $DTD \propto t^{-1}$, while too short timescales are not able to produce a good agreement with observations. Another problem with short timescales arises also from the fact that $\simeq 30\%$ of the 26 sGRBs with classified host galaxies are found in early-type galaxies Berger (2014) and D’Avanzo (2015) and a similar fraction has been derived by Fong et al. (2017) with the 36 sGRBs detected between 2004 and 2017. This fact appears to be strongly in favour of long coalescence timescales for MNS. S19 also concluded that if one wants to reconcile the observed occurrence of MNS with the cosmic sGRB rate and the [Eu/Fe] vs. [Fe/H] in the MW by assuming that only MNS produce Eu, then the DTD should contain long delay times but the fraction of binary systems giving rise to MNS should vary in time, an hypothesis that still needs to be proven.

Here we aim at computing, for the first time, the rate of MNS in galaxies of

different morphological type (ellipticals, spirals and irregulars), and making predictions for future observations (e.g. LSST, VST, THESEUS). Moreover, we study the effect of MNS on the evolution of the [Eu/Fe] vs. [Fe/H]. In order to do that, we use both a DTD containing long delays and a constant delay time for MNS. We compare our results of the MNS rate for a typical spiral galaxy with the MW observations, such as the local rate of MNS ($\sim 80_{-60}^{+200} \text{Myr}^{-1}$) derived by Kalogera et al. (2004) and the [Eu/Fe] vs. [Fe/H] pattern, and derive constraints on the main Eu producers. In particular, we compare the Eu enrichment of MNS to that of massive stars. Finally, we compute the cosmic MNS rate (CMNSR) in three different cosmological scenarios of galaxy formation and compare the theoretical CMNSR with that observed by LIGO/Virgo ($1540_{-1220}^{+3200} \text{Gpc}^{-3} \text{yr}^{-1}$, Abbott et al., 2017). and also with the sGRBs redshift distribution reconstructed by Ghirlanda et al. (2016). From these comparisons we derive constraints on the origin of r-process elements as well as on the formation and evolution of galaxies of different morphological type.

3.2 The model

In this work, the evolution of external galaxies of different morphological type (ellipticals, spirals and irregulars) has been studied. It is assumed that galaxies form by infall of primordial gas in a pre-existing diffuse dark matter halo. The stellar lifetimes are taken into account, thus relaxing the instantaneous recycling approximation (IRA). The model is able to follow in detail the chemical evolution of 22 elements, from H to Eu during 14 Gyr, with timesteps of 2 Myr.

The set of equations which describes the evolution of the surface mass density of the gas in the form of the generic element i is described by equation 2.14. Here, we adopt a Schmidt-Kennicutt law (Schmidt, 1959; Kennicutt, 1998) with $k = 1$ for the SF (see equation 2.2), an exponentially decaying law for the infall rate (see equation 2.10) and a wind rate proportional to the SFR (see equation 2.11).

The input parameters adopted for the different galaxies are reported in Table 3.1, where we specified in the first column the type of galaxy, in the second column the infall mass, in the third column the star formation efficiency, in the fourth column the infall timescale, in the fifth column the effective radius and in the sixth column the wind parameter. The parameters for spiral and irregular galaxies have been fine tuned in order to reproduce the measured present day SFR for the MW disc ($1.9 \pm 0.4 \text{M}_{\odot} \text{yr}^{-1}$; Chomiuk et al., 2011) and in the Small Magellanic Cloud ($0.053_{-0.02}^{+0.03} \text{M}_{\odot} \text{yr}^{-1}$; Rubele et al., 2015), respectively (see Figure 3.1). For elliptical galaxies, instead, the parameters adopted trace the typical behaviour of an elliptical galaxy with a quenching of the star formation, determined by the action of the galactic winds, after an initial and very intense burst (see Pipino et al., 2004). The SFR of ellipticals is higher than the one of irregulars and spirals, according to the downsizing scenario for which larger galaxies have higher star formation efficiency (Matteucci, 1994). On the other hand, the simulated spiral galaxy is characterized by a continuous SFR which is higher than the one of irregulars.

TABLE 3.1: Parameters used for the chemical evolution models of spiral, irregular and elliptical galaxies. In the first column it is reported the morphological type of the galaxy, in the second, third, fourth and fifth column the infall mass M_{infall} , the star formation efficiency ν , the infall timescale τ_{infall} , the effective radius R_{eff} , and the wind parameter ω_i , respectively.

Type	$M_{\text{infall}} (M_{\odot})$	$\nu (\text{Gyr}^{-1})$	$\tau_{\text{infall}} (\text{Gyr})$	$R_{\text{eff}} (\text{pc})$	ω_i
Spiral	5.0×10^{10}	1	7	3.5×10^3	0.2
Irregular	5.5×10^8	0.1	7	1×10^3	0.5
Elliptical	5.0×10^{11}	17	0.2	7×10^3	10

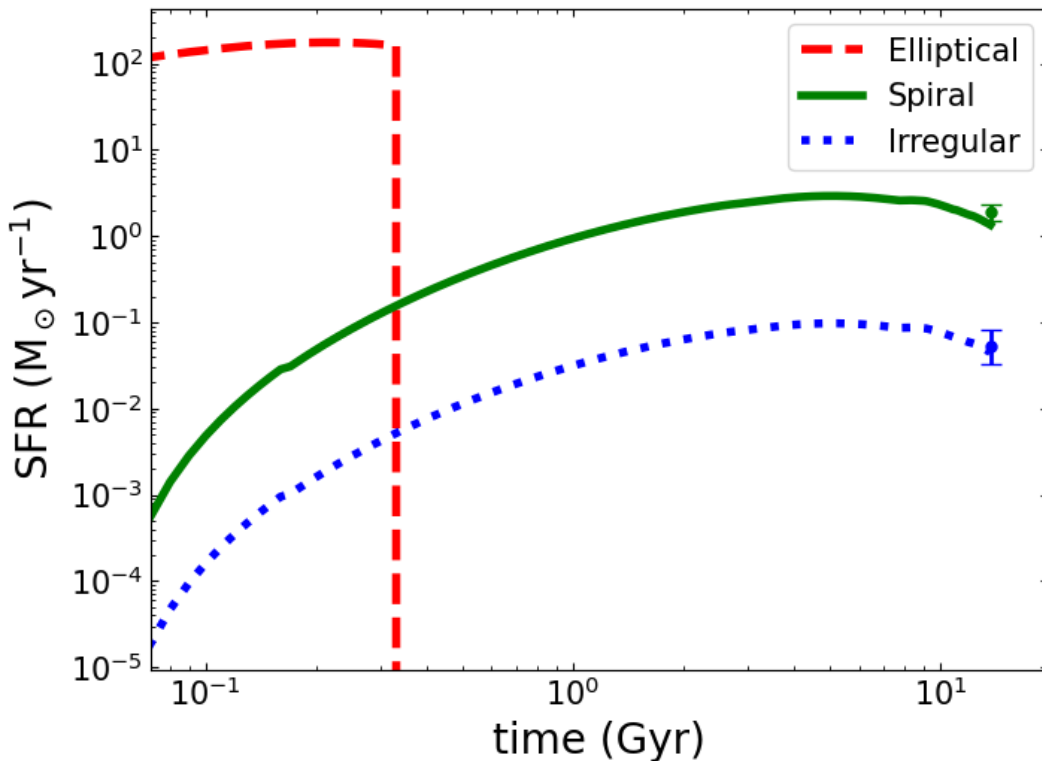


FIGURE 3.1: Predicted SFRs for galaxies of different morphological type as a function of time. Red dashed, green solid and blue dotted lines represent elliptical, spiral and irregular galaxies, respectively. Present time data are taken from Chomiuk et al. (2011) (green circle) and Rubele et al. (2015) (blue circle) for the Galaxy and for the Small Magellanic Cloud, respectively.

For all the stars sufficiently massive to die in a Hubble time, the following stellar yields have been adopted:

- For LIMS with mass lower than $6M_{\odot}$ we used the yields by Karakas (2010);
- For super-AGB stars and e-capture SNe with masses between $6M_{\odot}$ and $10M_{\odot}$ we used the yields by Doherty et al. (2014);
- For massive stars that explode as CC-SNe we used the yields by Nomoto et al. (2013);
- For Type Ia SNe we used the yields by Iwamoto et al. (1999). Their rate has been computed by convolving the adopted SFR with the Greggio (2005) DTD for wide double degenerate Type Ia SNe (see previous Chapter).

For what concerns the yields of Eu from massive stars, they are the same adopted by Simon (2019), which are a modified version of those found in Argast et al. (2004) (their model SN2050) and also used by Matteucci et al. (2014), in particular:

- For stars in the $20 - 23 M_{\odot}$ mass range, a constant yield of $3.8 \times 10^{-8} M_{\odot}$ of Eu has been used;
- A decreasing yield from $3.8 \times 10^{-8} M_{\odot}$ of Eu for a $23 M_{\odot}$ star to $1.7 \times 10^{-9} M_{\odot}$ of Eu for a $50 M_{\odot}$ star has been used.

It should be noted that we assume that Eu is produced only by a fraction of massive stars, in particular from those in the range $20-50 M_{\odot}$. Therefore, the rate of massive stars producing Eu is only a fraction (a factor of ~ 5 less) of the total CC-SN rate, which is related to the entire range of massive stars from 8 to $100 M_{\odot}$.

The yield of Eu from MNS, instead, is described following the theoretical calculations of Korobkin et al. (2012), who estimate the production of Eu from each event to be in the range of $10^{-7} - 10^{-5} M_{\odot}$.

It is worth noting that there is a degeneracy between the Eu yields and the rates of its progenitors (MNS and CC-SNe). In fact, Matteucci et al. (2014) first showed that it is possible to reproduce the $[\text{Eu}/\text{Fe}]$ vs $[\text{Fe}/\text{H}]$ pattern in the Galaxy only with MNS by adopting a specific yield from a merging event. However, if one allows CC-SNe to produce Eu as well, then the yield of Eu from MNS should be lower.

The rate of MNS in the different galaxies has been computed using two different approaches. The first one consisted in assuming a constant delay time between the formation of the neutron stars binary system and the merging event, while the second one consisted in assuming a DTD, as described by equations 2.31 and 2.30 (see Chapter 2, Section 2.3 for a complete discussion). Here, we test the DTDs corresponding to the four different values β shown in Figure 2.2.

3.3 Simulations for galaxies of different morphological type

In order to predict the rate of MNS and the [Eu/Fe] vs. [Fe/H] pattern in galaxies of different morphological type (Ellipticals, Spirals and Irregulars) we run several chemical evolution models where we need to specify the following parameters:

1. The DTD of MNS;
2. The fraction of neutron stars in binaries which produce a MNS, α_{MNS} ;
3. The production of Eu by CC-SNe;
4. The Eu produced per merging event.

In particular:

- We tested four different DTDs derived by S19 corresponding to four different values of β parameter ($-1.5, -0.9, 0.0, 0.9$), as well as a constant total delay time (which includes both the nuclear lifetime and the time necessary to merge) for all the neutron stars binary systems, equal to 10 Myr;
- The parameter α_{MNS} has been fixed in order to reproduce, for spiral galaxies, the MNS rate in the MW as suggested by Kalogera et al. (2004), $\sim 80_{-60}^{+200} \text{ Myr}^{-1}$;
- For half of the models we considered the Eu to be co-produced by CC-SNe and MNS, while for the other half we assumed that MNS were the only Eu producers in the simulated galaxy;
- The yield of Eu per merging event has been fixed in order to reproduce, for spiral galaxies, the solar absolute abundance of Eu as derived by Lodders et al. (2009). In particular, we compared the ISM Eu abundance at 9 Gyr since the beginning of the star formation, with the solar abundance.

On the other hand, the parameters left constant are:

1. The progenitor mass range for MNS, between 9 and $50 M_{\odot}$;
2. The mass range of the CC-SNe producing Eu, between 20 and $50 M_{\odot}$, with prescriptions for the yield of Eu, as described in Section 3.2;
3. Prescriptions about IMF, SFR and yield of elements other than Eu, which are also specified in Section 3.2;
4. The DTD for Type Ia SNe, as described in Section 2.4.

The different models that we run are reported in Table 3.2 and in Table 3.3, together with their predictions. For both Tables, in the first column it is specified the name of the model; in the second column is reported the type of simulated galaxy; in the third column it is specified if CC-SNe contributed to the Eu production; in the fourth and fifth columns are reported the adopted DTD for Type Ia and

the occurrence probability α_{Ia} , respectively; in the sixth and seventh columns are shown the DTD for MNS and their occurrence probability α_{MNS} , respectively; in the eighth column it is reported the yield of Eu per merging event and in the last column the predicted MNS rate.

3.3.1 Predicted MNS rate

First, we show the results of our simulations for spiral galaxies. The predicted rate of MNS as a function of time can be seen in Figure 3.2, where we show the rate of MNS both in the case of a DTD and in the case of a constant total delay time of 10 Myr for all neutron star binary systems. As it is clear from the Figure, the constant and short time delay predicts a higher MNS rate at early times, relative to the cases adopting DTDs including also long delay times. On the other hand, no much difference is predicted for the present time MNS rate by all the studied cases. This is due to the fact that a typical spiral suffers continuous star formation until the present time. A large difference in the present time value of the MNS rate is instead predicted for ellipticals (see later). As it is possible to see from Tables 3.2 and 3.3, all of our simulations for spiral galaxies give us results consistent with the observed MNS rate for the MW. More precisely, the rate is best represented by DTDs with lower values of β , so by bottom heavy distributions, in particular the one corresponding to $\beta = -0.9$. We also remind that lower values of β imply systems with small initial separations. Also the case of a constant total delay time of 10 Myr appears to be a good candidate to represent the MNS rate. In those two cases, the occurrence probability of MNS (α_{MNS}) is found to be 5.42% and 6.15%, respectively.

In Figure 3.3, we show the predicted rates of MNS for elliptical, spiral and irregular galaxies. In particular, in panel (a) we report the results of the simulations in the case of a DTD for MNS with $\beta = -0.9$ and in panel (b) we report the results of the simulations in the case of a constant total delay time of 10 Myr. In the case of elliptical galaxies, our results show clearly which is the main effect of using a DTD instead of a constant delay time. In fact, in the case of a constant and short total delay time, the rate of MNS follows the evolution of the SFR of the simulated galaxy. Therefore, we would not expect to observe any merging event in galaxies with no SF at the present time, such as ellipticals (see Tables 3.2 and 3.3). On the other hand, when we hypothesize a probability distribution of delay times including long ones, the dependence of the MNS rate on the given SFR is not as strong as in the case of a constant delay time (as it is clearly expressed by equation 2.31). As a consequence, in this case the rate of MNS differs from zero in elliptical galaxies. This is a result which must be taken into account, given the fact that the host galaxy of the GW170817 event has a predominantly old population and probably no recent star formation (Abbott et al., 2017). Therefore, we conclude that a DTD including long delay times should be preferred for computing the MNS rate. In particular, among the DTDs tested here we consider as the best the one with $\beta = -0.9$, since it reproduces very well the present time observed MNS rate of Kalogera et al. (2004) for the MW.

Concerning the observed present time rate in ellipticals, there are indications (Berger, 2014; D’Avanzo, 2015; Fong et al., 2017) that it should be lower ($\sim 30\%$

TABLE 3.2: All the models for galaxies of different morphological type with Eu production from CC-SNe. In the 1st column the name of the model, in the 2nd column the galaxy type, in the 3rd column the production of Eu from CC-SNe, in the 4th column the DTD used for SNeIa, in the 5th column the occurrence probability of SNeIa (α_{Ia}), which has been tuned to obtain the estimated current rate of SNeIa, in the 6th column the DTD used for MNS, in the 7th column the occurrence probabilities of MNS (α_{MNS}) which has been tuned in order to obtain for spiral galaxies the estimated rate of MNS in the MW, in the 8th column the yield of Eu from MNS and in the 9th column the predicted rates of MNS.

Model	Galaxy Type	Eu from CC-SNe	Type Ia SNe DTD	α_{Ia} ($\times 10^{-3}$)	MNS DTD	α_{MNS} ($\times 10^{-2}$)	MNS Eu yield ($\times 10^{-6} M_{\odot}$)	MNS rate (Myr^{-1})
1Sa	Spiral	yes	$\beta_a = -0.9$	3.29	$\beta = -1.5$	5.58	0.5	72
2Sa	Spiral	yes	$\beta_a = -0.9$	3.29	$\beta = -0.9$	5.42	0.5	80
3Sa	Spiral	yes	$\beta_a = -0.9$	3.29	$\beta = 0.0$	5.21	0.5	92
4Sa	Spiral	yes	$\beta_a = -0.9$	3.29	$\beta = 0.9$	5.06	0.5	105
5Sa	Spiral	yes	$\beta_a = -0.9$	3.29	Constant 10 Myr	6.15	0.5	77
1Ia	Irregular	yes	$\beta_a = -0.9$	4.29	$\beta = -0.9$	5.58	0.5	12
2Ia	Irregular	yes	$\beta_a = -0.9$	4.29	Constant 10 Myr	6.15	0.5	13
1Ea	Elliptical	yes	$\beta_a = -0.9$	5.05	$\beta = -0.9$	5.58	0.5	15
2Ea	Elliptical	yes	$\beta_a = -0.9$	5.05	Constant 10 Myr	6.15	0.5	0

TABLE 3.3: All the models for galaxies of different morphological type with no Eu production from CC-SNe. In the 1st column the name of the model, in the 2nd column the galaxy type, in the 3rd column the production of Eu from CC-SNe, in the 4th column the DTD used for Type Ia SNe, in the 5th column the occurrence probability of Type Ia SNe (α_{Ia}), which has been tuned to obtain the estimated current rate of Type Ia SNe, in the 6th column the DTD used for MNS, in the 7th column the occurrence probabilities of MNS (α_{MNS}) which has been tuned in order to obtain for spiral galaxies the estimated rate of MNS in the MW, in the 8th column the yield of Eu from MNS and in the 9th column the predicted rates of MNS.

Model	Galaxy Type	Eu from CC-SNe	Type Ia SNe DTD	α_{Ia} ($\times 10^{-3}$)	MNS DTD	α_{MNS} ($\times 10^{-2}$)	MNS Eu yield ($\times 10^{-6} M_{\odot}$)	MNS rate (Myr^{-1})
1Sb	Spiral	no	$\beta_a = -0.9$	3.29	$\beta = -1.5$	5.58	2.0	72
2Sb	Spiral	no	$\beta_a = -0.9$	3.29	$\beta = -0.9$	5.42	2.0	80
3Sb	Spiral	no	$\beta_a = -0.9$	3.29	$\beta = 0.0$	5.21	2.0	92
4Sb	Spiral	no	$\beta_a = -0.9$	3.29	$\beta = 0.9$	5.06	2.0	105
5Sb	Spiral	no	$\beta_a = -0.9$	3.29	Constant 10 Myr	6.15	2.0	77
1Ib	Irregular	no	$\beta_a = -0.9$	4.29	$\beta = -0.9$	5.58	2.0	12
2Ib	Irregular	no	$\beta_a = -0.9$	4.29	Constant 10 Myr	6.15	2.0	13
1Eb	Elliptical	no	$\beta_a = -0.9$	5.05	$\beta = -0.9$	5.58	2.0	15
2Eb	Elliptical	no	$\beta_a = -0.9$	5.05	Constant 10 Myr	6.15	2.0	0

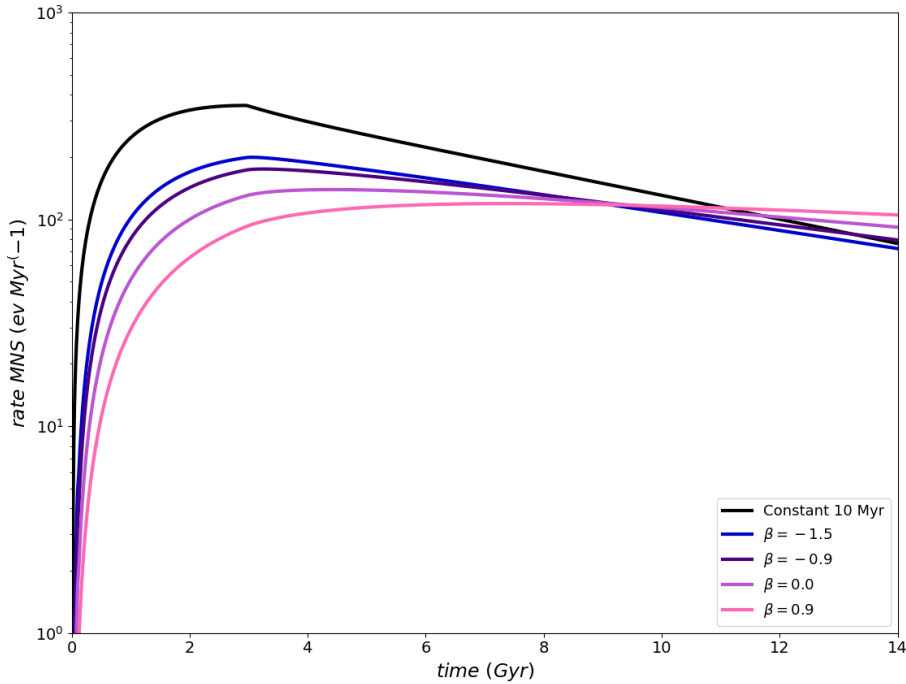


FIGURE 3.2: Predicted rate of MNS in spiral galaxies as a function of time for the four different DTDs derived by S19 corresponding to four different values of β (-1.5 , -0.9 , 0.0 , 0.9) and for a constant total delay time equal to 10 Myr.

of the total) but comparable with the one in spirals. Our predicted present time MNS rate in ellipticals, when assuming a DTD with long time delays, is a factor of 10 lower than the one predicted for spirals. However, our predictions cannot be really compared to those data, since they refer to a single typical galaxy for each morphological type, while the observations refer to group of galaxies with different masses and rates.

3.3.2 Predicted [Eu/Fe] vs [Fe/H] pattern in spiral galaxies

For what concerns our predictions for the [Eu/Fe] vs. [Fe/H] patterns, for spiral galaxies we tested the ability of our models to reproduce the evolution of the abundance of Eu in the MW. In both panels of Figure 3.4, we report the observed [Eu/Fe] vs. [Fe/H] relation for the Galaxy as well as the results of our simulations. For what concerns the observational data, it is possible to see that there is a large spread in the [Eu/Fe] ratio at low [Fe/H], which decreases with increasing metallicity, becoming nearly negligible for $[\text{Fe}/\text{H}] \geq -2.0$ dex. This spread in the data has been analysed by several authors (e.g. Cescutti et al., 2015; Wehmeyer et al., 2015), which interpreted it as due to an initial inhomogeneous mixing. We remind that our goal here is to reproduce the main trend in the data and not the spread. The main [Eu/Fe] pattern in the MW is similar to that of a typical α -element, with a plateau in the halo phase and a decrease of the [Eu/Fe] ratio for $[\text{Fe}/\text{H}] \geq -1.0$ dex, due to the fact that for $[\text{Fe}/\text{H}] \geq -1.0$ dex, Type Ia SNe start contributing in a substantial way to the Fe enrichment. Therefore, we have first verified the ability

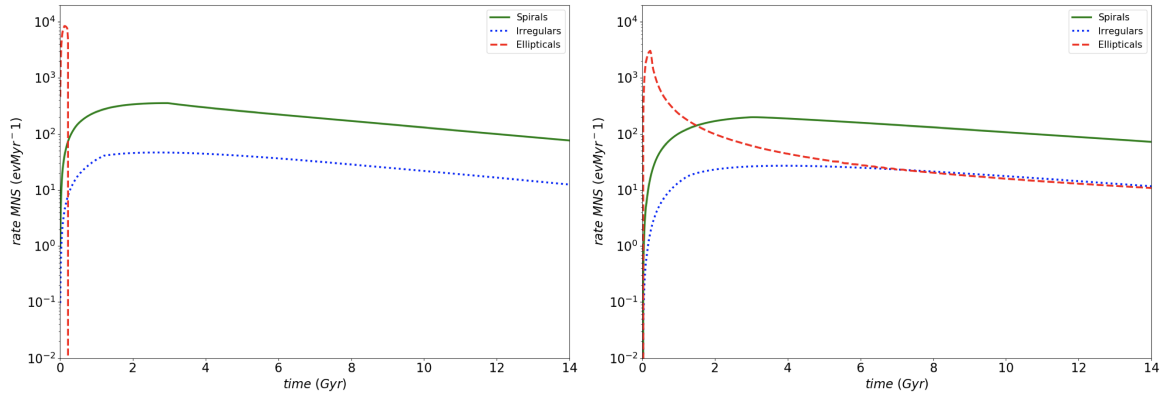


FIGURE 3.3: Predicted MNS rates for galaxies of different morphological type as a function of time. Left panel: case of a total delay time for all neutron stars binary systems equal to 10 Myr; right panel: case of a DTD for MNS with $\beta = -0.9$.

of our model to reproduce the expected behaviours of four α -elements (O, Mg, S, Ca). Those are reported in Figure 3.5, where it is possible to see a quite good agreement with the observational data. We also remind that, since the decreasing trend at higher metallicities originates from the extra production of Fe by Type Ia SNe (Matteucci et al., 2009), the production of Eu should occur on timescales shorter than Type Ia SNe.

In the left panel of Figure 3.4, we show the results of the models (1 – 5)Sa in which we consider the Eu production from CC-SNe, while in the right panel we show the results of the models (1 – 5)Sb where MNS are the only producers of Eu (as reported in Tables 3.2 and 3.3).

In the case in which CC-SNe are not allowed to produce Eu, the DTDs derived by S19 are not able to reproduce neither the decreasing trend in the $[\text{Eu}/\text{Fe}]$ for $[\text{Fe}/\text{H}] \geq -1.0$ dex, nor the plateau at lower metallicities, under-producing the $[\text{Eu}/\text{Fe}]$ over the entire range of $[\text{Fe}/\text{H}]$. However, if we drop the assumption of Eu produced only by MNS and we include CC-SNe as Eu producers, we can see from the upper panel of Figure 3.4 that the agreement with the data is improved, making us able to reproduce both the plateau in the halo phase and the decreasing trend for $[\text{Fe}/\text{H}] \geq -1.0$ dex. However, in this case the models (1 – 4)A, which differ between themselves only for the assumed DTD for MNS, do not show much differences in their results. This is due to the fact that we have tuned the parameter α_{MNS} and the yield of Eu from MNS, in order to reproduce the rate of MNS and the solar abundance of Eu at the same time. With those prescriptions, CC-SNe appear to be the major producers of Eu in the simulated galaxy. For what concerns the knee at $[\text{Fe}/\text{H}] \simeq -3.5$ dex, the interpretation is that only for $[\text{Fe}/\text{H}] > -3.5$ dex stars with $M \leq 23 M_{\odot}$ start to die and for such stars we assumed higher yields of Eu.

In the same Figure 3.4 models 5Sa and 5Sb are also shown, where all binary neutron stars systems are supposed to merge on a fixed timescale of 10 Myr. With this assumption, we are able to reproduce the expected pattern of $[\text{Eu}/\text{Fe}]$ either in the case of Eu produced only by MNS or in the case in which Eu is produced by both MNS and CC-SNe. In particular, the model 5Sb (with no Eu from CC-SNe)

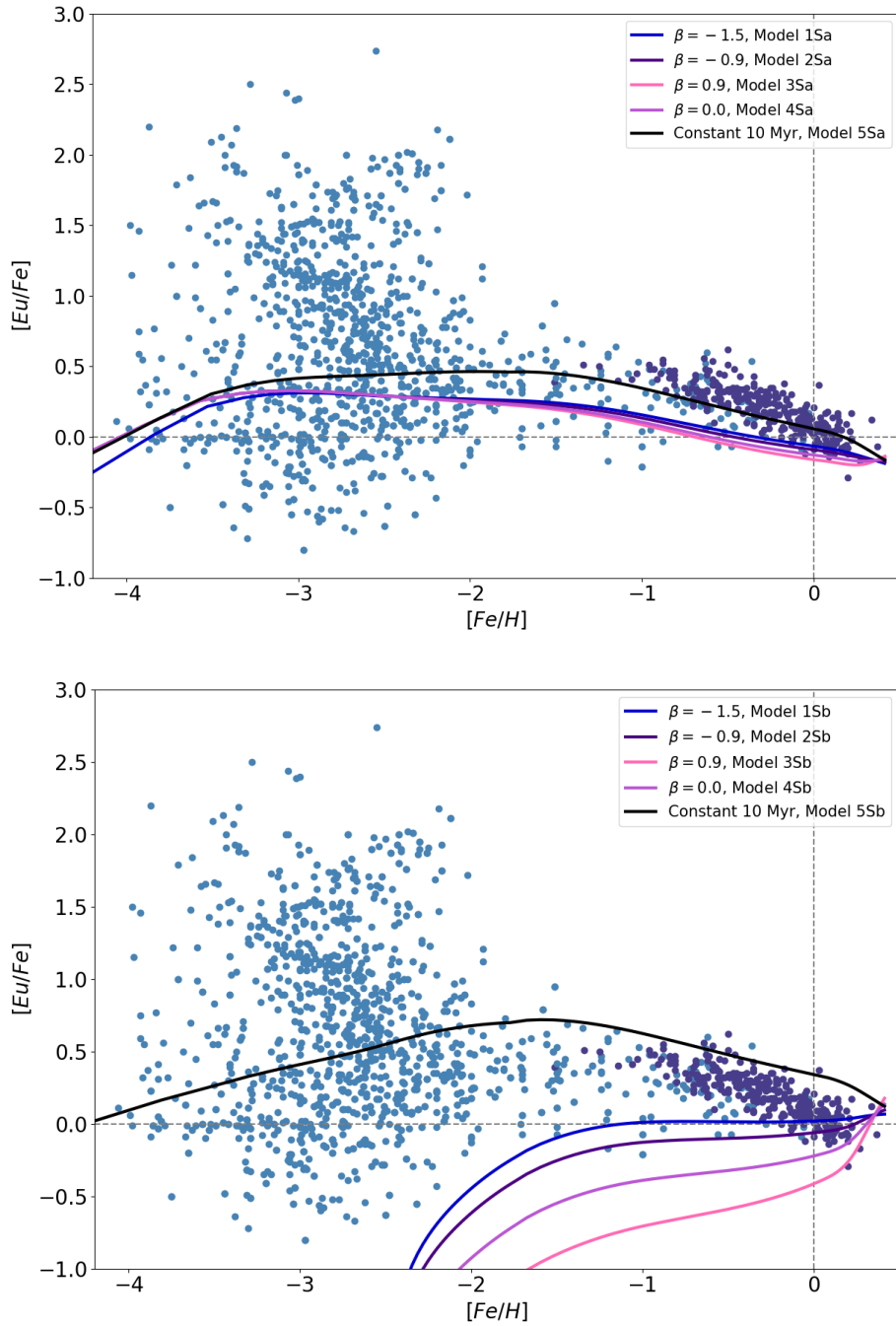


FIGURE 3.4: Upper panel: results of models (1-5)A with Eu production from both CC-SNe and MNS; bottom panel: results of models (1-5)B with no Eu production from CC-SNe. Observational data used: 428 MW halo stars from JINABase and 374 MW thin disk stars from Battistini et al. (2016).

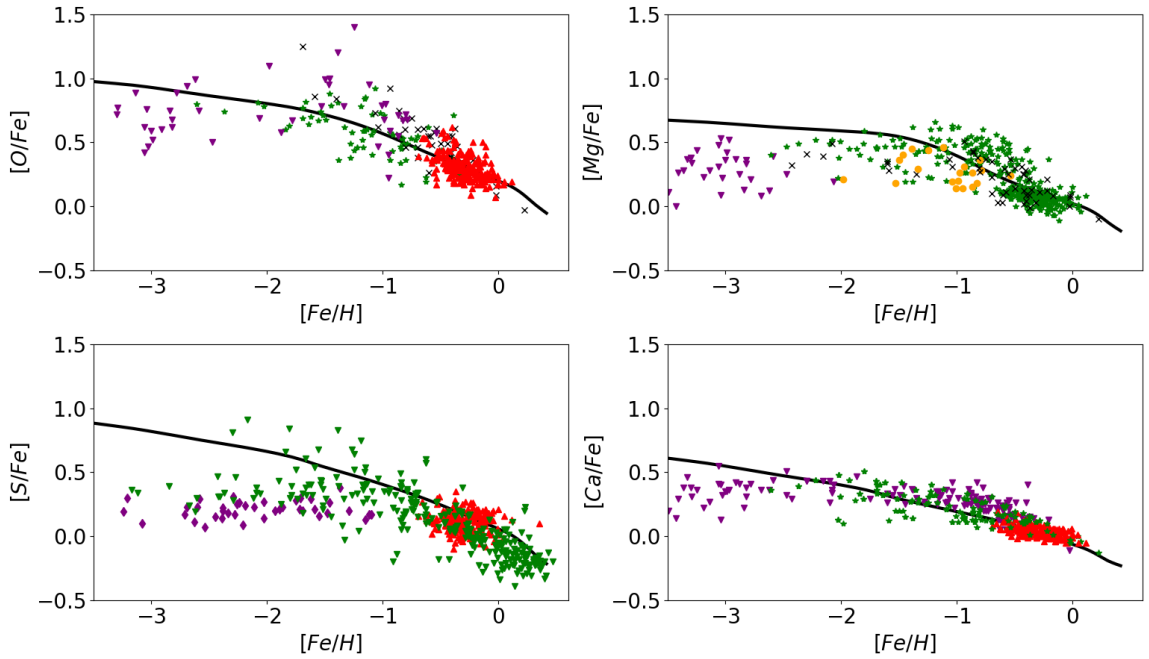


FIGURE 3.5: $[\alpha/\text{Fe}]$ vs $[\text{Fe}/\text{H}]$ predicted patterns in spiral galaxies for O, Mg, S and Ca. The observational data used are those of the MW and are from Cayrel et al. (2004) (purple upside-down triangles), Reddy et al. (2003) (red triangles), Gratton et al. (2003) (green stars), Reddy et al. (2006) (orange points), Ramya et al. (2012) (black crosses), Caffau et al. (2005) (purple diamonds) and (n.d.[b]) (green upside-down triangles).

produces a higher track with respect to that produced by the model 5Sa (with Eu from CC-SNe). This is again due to the fact that when CC-SNe do not produce Eu, we are forced to assume a higher yield of Eu from MNS (keeping fixed α_{MNS}), in order to reproduce the observed solar abundance. It can also be observed that the model 5B does not reproduce the flat trend of the $[\text{Eu}/\text{Fe}]$ for $[\text{Fe}/\text{H}] < -1.0$ dex, producing instead an increasing relation. This is probably due to the fact that, while for MNS we are assuming a constant total delay time of 10 Myr, for SNeIa (the major Fe producers) we are assuming a DTD. Moreover, the nuclear lifetimes for the progenitors of MNS are assumed to be much shorter than those of the progenitors of SNeIa, which range from 40 Myr to a Hubble time.

The fact that Fe is mainly produced by Type Ia SNe can complicate the interpretation of the abundance ratio of $[\text{Eu}/\text{Fe}]$ vs. $[\text{Fe}/\text{H}]$. As suggested by Skúladóttir et al. (2019), it could be useful to study also the $[\text{Eu}/\text{Mg}]$ vs. $[\text{Fe}/\text{H}]$, since Mg is a good tracer of CC-SNe. In Figure 3.6, are reported the observed abundances of $[\text{Eu}/\text{Mg}]$ vs. $[\text{Fe}/\text{H}]$ in the MW, together with results of models (1–5)Sa. It is possible to see a flat trend of $[\text{Eu}/\text{Mg}]$ with $[\text{Fe}/\text{H}]$ data, with an average $[\text{Eu}/\text{Mg}] \simeq 0$ at all $[\text{Fe}/\text{H}]$ and with an increasing scatter toward the lowest metallicities. If there was a significant delay in the production of Eu with respect to that of Mg, we would expect an increasing trend of the $[\text{Eu}/\text{Mg}]$ vs. $[\text{Fe}/\text{H}]$. The absence of such a trend in the observational data of the Galaxy, suggests that the timescales of Eu and Mg production are quite similar. As we can see from the same Figure, models (1–5)Sa are able to reproduce the flat trend. Even in this case

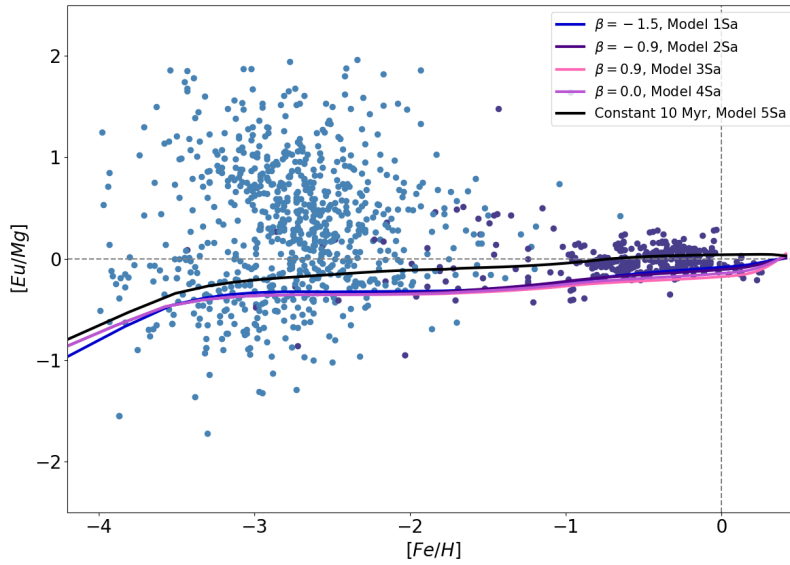


FIGURE 3.6: $[Eu/Mg]$ vs $[Fe/H]$ as reproduced by models (1-5)A. Observational data are a collection of 412 MW halo stars from JINABase and 216 thin disk stars from a Venn et al., (2004).

the model which best fits the data is the model 5Sa. However, this should be not surprising, since for this model we are assuming a fixed short merging timescale for all neutron stars systems, therefore it should not be expected a delay in the enrichment of Eu with respect to Mg. On the other hand, models (1 – 4)Sa for which a delay in the coalescence time is assumed, also show a flat trend for all $[Fe/H]$, but with a slight increase toward high metallicities, as expected.

In conclusion, it is possible to state that when MNS are the only producers of Eu, the model which best reproduces the $[Eu/Fe]$ vs. $[Fe/H]$ pattern in the Galaxy is the one with a constant and short total delay time of 10 Myr, equal for all neutron star binary systems. In this case, the yield of Eu should be equal to $2.0 \times 10^{-6} M_{\odot}$ per merging event. On the other hand, if a DTD including longer timescales is assumed, the $[Eu/Fe]$ pattern can be reproduced only if CC-SNe are included as Eu producers. In this case the yield of Eu per merging event is reduced to $0.5 \times 10^{-6} M_{\odot}$. Our values for the yields of Eu are slightly lower than those estimated from the kilonova AT2017gfo (which are in the range of $(3 - 15) \times 10^{-6} M_{\odot}$), but they are well inside the theoretical range of $(10^{-7} - 10^{-5}) M_{\odot}$ predicted by Korobkin et al. (2012). The best DTD in the case with MNS and CC-SNe as Eu producers is again that with $\beta = -0.9$, therefore we will adopt only this DTD since now on.

3.3.3 Predicted $[Eu/Fe]$ vs $[Fe/H]$ patterns for ellipticals and irregulars

In Section 3.3.1, we showed that we are not able to observe any merging event in elliptical galaxies if a constant delay time of 10 Myr is assumed. Since the event GW170817 has been observed to come from an early-type galaxy, here we

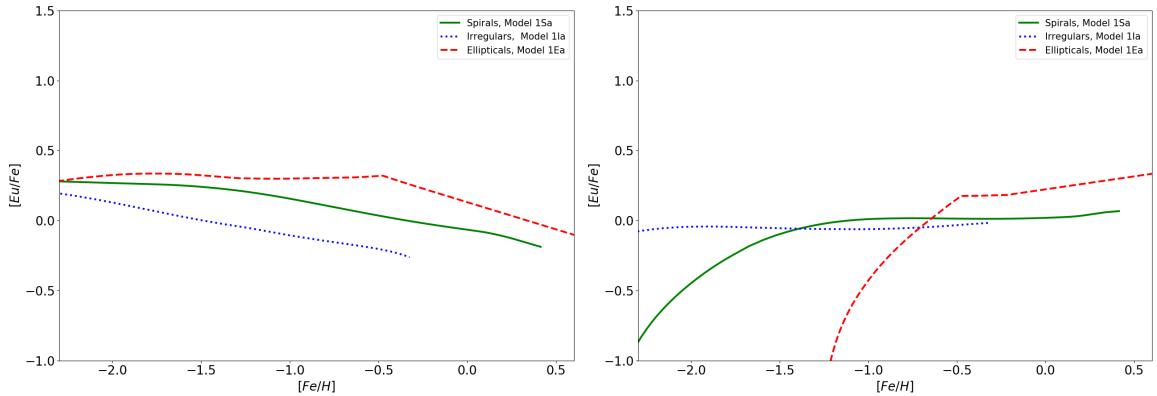


FIGURE 3.7: Predicted $[Eu/Fe]$ vs. $[Fe/H]$ by models 1S(a-b), 1I(a-b) and 1E(a-b) in which a DTD with $\beta = -0.9$ has been assumed. Panel (a): results of models with Eu from CC-SNe; panel (b): results of models with no Eu from CC-SNe.

will show our predictions of the $[Eu/Fe]$ vs. $[Fe/H]$ patterns in galaxies of different morphological type excluding the case of a constant delay of 10 Myr.

In particular, in Figure 3.7 we show the results of models 1S(a-b), 1I(a-b) and 1E(a-b), for which a DTD with $\beta = -0.9$ has been adopted. In panel (a) are shown the results of the models with Eu production from CC-SNe and in panel (b) are shown the results of the models for which MNS are assumed to be the only producers of Eu.

As one can see, our predictions are those expected on the basis of the time-delay model, according to which we would expect to find a larger plateau of the $[Eu/Fe]$ ratio at low metallicities for ellipticals than for spirals and irregulars (see Matteucci, 2012). The same behaviour holds for the α -elements, as shown in Figure 3.8 where the predicted $[\alpha/Fe]$ vs. $[Fe/H]$ patterns are reported. In fact, for galaxies with an intense SF (ellipticals), the Fe abundance grows more rapidly because of Type II SNe (they also produce part of Fe). Therefore, when Type Ia SNe (the main Fe producers) appear and the ratio $[\alpha/Fe]$ begins to decrease, the Fe abundance is higher than in galaxies with a lower SF (spirals). As a consequence, the $[\alpha/Fe]$ plateau extends for a larger range of metallicity (as described in Chapter 1). On the other hand, when the SF proceeds slowly, the Fe abundance grows less rapidly and it will be lower with respect to spirals. Therefore, for spirals and irregulars galaxies (which have an even lower SF), the $[\alpha/Fe]$ plateau extends for a smaller range of $[Fe/H]$. Our predicted trend for the $[Eu/Fe]$ vs. $[Fe/H]$ seems also to be in agreement with those obtained by Grisoni et al. (2020) for the three main Galactic components (thick disc, thin disc and bulge) for which they adopt different timescales of formation and star formation efficiencies, similarly to what we assume for our simulated elliptical, spiral and irregular galaxies.

3.4 Cosmic rates

In this Section, we present our analysis of the evolution of the cosmic rate of MNS (CMNSR). We define a cosmic rate as the rate in a comoving unitary volume of

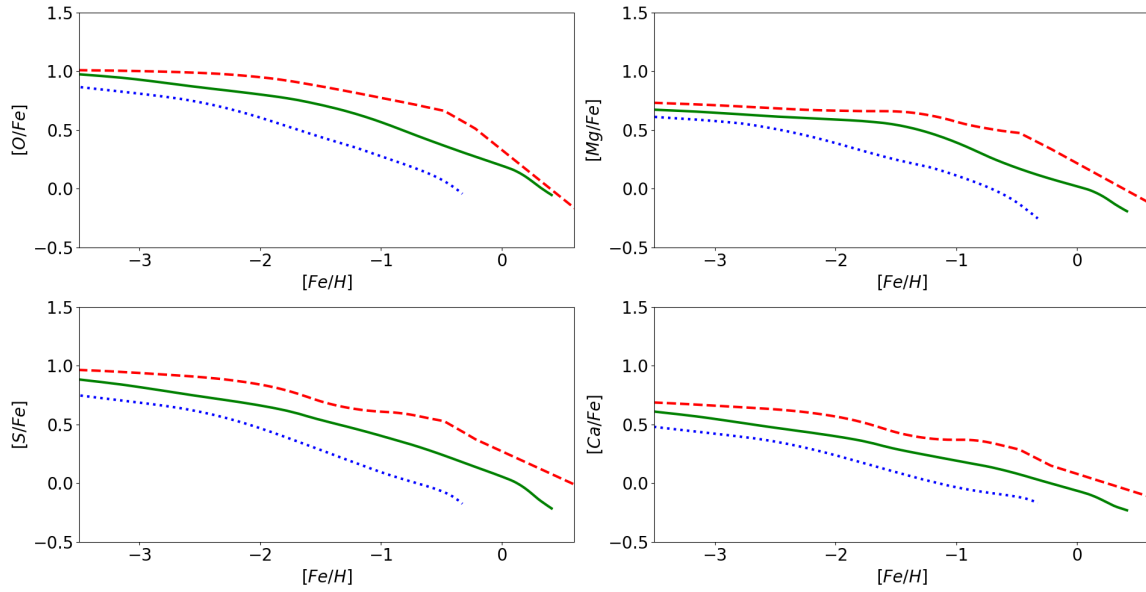


FIGURE 3.8: Predicted $[\alpha/Fe]$ vs. $[Fe/H]$ patterns in galaxies with different SF histories for O, Mg, S and Ca for the same models of Figure ??.

the Universe and we compute it as the result of the contribution of galaxies of different morphological type which are weighted according to their number densities. As already done in previous studies concerning the cosmic star formation rate (CSFR) (Gioannini et al., 2017; Calura et al., 2003; Vincoletto et al., 2012) and the cosmic SN rates Grieco et al. (2012b), here we will assume the galaxy number density to be a function of redshift. In particular, if n_k is the number density of galaxies of the k -th morphological type, its evolution with the redshift z can be written in the following way:

$$n_k = n_{k,0}(1+z)^{\gamma_k}, \quad (3.1)$$

where $n_{k,0}$ is the number density at $z = 0$ and γ_k is the parameter which determines the evolution of the number density.

We consider the following cosmological scenarios:

1. A pure luminosity evolution scenario (PLE), which consists of the case of $\gamma_k = 0$, therefore the number density of galaxies is constant and does not evolve with redshift. In other words, all galaxies started forming at the same redshift and the number density of each morphological type has been constant since then;
2. A number density evolution scenario (DE), which consists of the case of $\gamma_k \neq 0$, therefore the number density will evolve with redshift according to equation 3.1, with the parameter shown in Table 3.4, the same suggested by Vincoletto et al. (2012). This scenario is a typical hierarchical clustering scheme for galaxy formation, where spirals form first and then ellipticals form by subsequent mergers of spirals. In the first column we specify the morphological type of the galaxy, in the second column the number density

TABLE 3.4: Parameters used for the evolution of the number density for galaxies of different morphological type. In the 1st column it is reported the type of galaxy, in the 2nd column the adopted number density at redshift $z = 0$ and in the 3rd column the parameter γ_k . These parameters are the same as those adopted in Gioannini et al. (2017)

Type	$n_0 (\times 10^{-3}) \text{ Mpc}^{-3}$	γ_k
Spirals	8.4	0.9
Irregular	0.6	0.0
Ellipticals	2.24	-2.5

at $z = 0$ and in the third column the parameter γ_k . These parameters were chosen in order to reproduce the present time number densities of galaxies, as in Marzke et al. (1998);

3. An alternative observationally based scenario, as suggested by Pozzi et al. (2015) and adopted by Gioannini et al. (2017), where the number density of spiral galaxies increases from $z = 0$ to $z = 2.3$ according to equation 3.1, and decreases exponentially for higher redshifts as

$$n_S = n_{0,S}(1+z)e^{-(1+z)/2}. \quad (3.2)$$

In this context, ellipticals are assumed to start forming at $z = 5$ and half of them form in the range $1 \leq z \leq 2$.

3.4.1 Cosmic stellar mass density

In order to compute the CMNSR, we first verify the ability of our model to reproduce the cosmic stellar mass density (CSMD). We define the CSMD as

$$CSMD = \sum_k \rho_{*,k}(t)n_k, \quad (3.3)$$

where n_k is the galaxy number density for the k -th morphological type of galaxy defined in the previous section. The quantity $\rho_*(t)$ is the stellar mass density, namely the total mass density of long-lived stars (see also Madau et al., 2014).

We have computed this quantity in details by means of our galaxy models: our results for the three different cosmological scenarios of galaxy formation are shown in Figure 3.9, together with data from Madau et al. (2014).

In both the DE and the alternative scenario the CSMD increases regularly over all the range of redshift, with the only difference that is steeper in the case of the alternative scenario.

On the other hand, in the PLE scenario the CSMD is characterized by a rapid increase from redshift $z = 10$ to redshift $z \simeq 7.5$ caused by elliptical galaxies, followed by an almost constant growth until $z \simeq 2$ and a second slight increase until present time. Similar patterns have also been found for the cosmic dust mass density evolution, as shown in Gioannini et al. (2017).

All the three different scenarios are in good agreement with data at low redshift ($0 \leq z \leq 1$). However, the DE and in particular the PLE scenarios both predict an

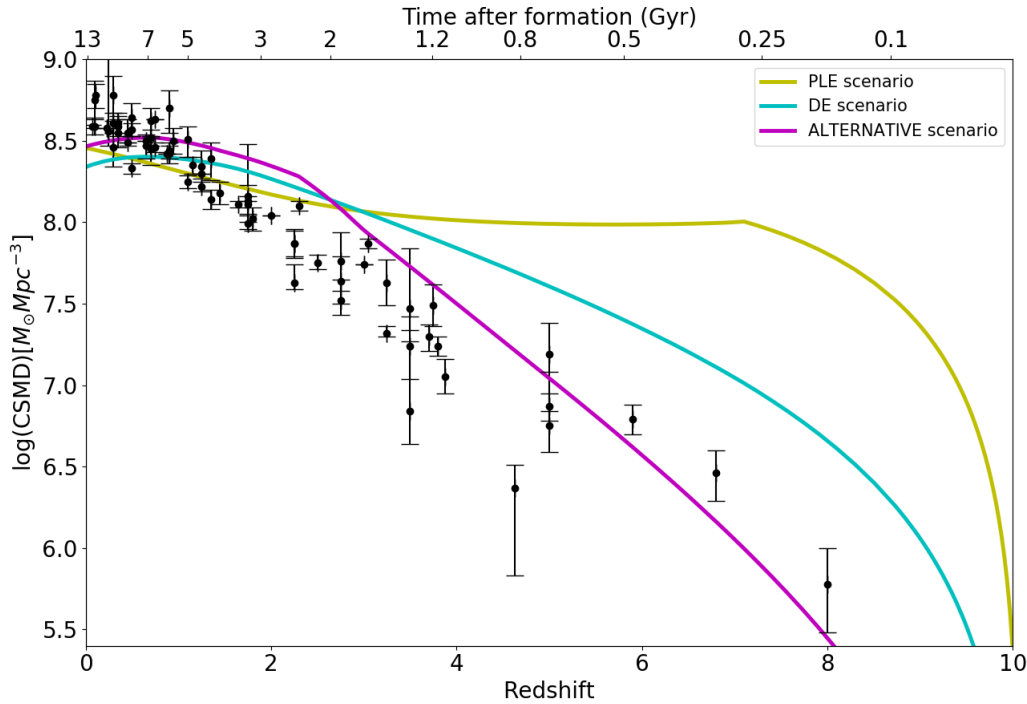


FIGURE 3.9: Cosmic stellar mass density as a function of redshift for the three different cosmological scenarios of galaxy formation. Observational data are a collection from Madau et al. (2014).

evolution which is too high for $z \geq 2$. On the other hand, the trend in the data seems to be quite well reproduced by the alternative scenario.

By the way a comparison with the CSFR shows also that the alternative scenario is the best, as shown in Gioannini et al. (2017).

3.4.2 Cosmic merging neutron stars rate

We define the CMNSR as:

$$CMNSR = \sum_k R_{MNS,k}(t)n_k, \quad (3.4)$$

where $R_{MNS,k}$ is the rate of MNS at the time t as defined by equation 2.31 for the k -th morphological type of galaxy. We compute the CMNSR in the three different cosmological scenarios, both in the case of a DTD with $\beta = -0.9$ and in the case of a constant total delay time of 10 Myr.

In the upper panels of Figure 3.10, it is reported the behaviour of the CMNSR for the PLE scenario for galaxies of different morphological type, both in the case of a total delay time of 10 Myr (left panel) and in the one of a DTD with $\beta = -0.9$ (right panel). In the case of a constant total delay time, since the rate of MNS is essentially given by the integral of the SFR, we expect no contribution to the CMNSR from elliptical galaxies from redshift $z \simeq 7.5$ to the present day. On the other hand,

when we adopt the DTD, the elliptical galaxies contribute to the CMNSR for the whole redshift range.

In the middle and lower panels of the same Figure, are shown the evolution of the CMNSR for the DE and for the alternative scenario, respectively, for galaxies of different morphological type, either in the case of a total delay time of 10 Myr (left panels) and in the one of a DTD with $\beta = -0.9$ (right panels). Also in these scenarios, it appears evident the effect of adopting a DTD rather than a constant time delay. However, it must be noted that in both these two scenarios the contribution to the CMNSR from elliptical galaxies has a lower impact than that of spirals. Therefore, the effect of using a DTD or a constant time delay will have almost no consequences on the total CMNSR behaviour.

Our results for the total CMNSR rate for the three different cosmological scenarios are shown in Figure 3.11, where in the top panel are reported the results of our simulations in the case of a constant total delay time and in the lower panel are reported the results in the case of the assumed DTD for MNS.

For what concerns the PLE scenario, in the case of a constant total delay time of 10 Myr, the CMNSR shows two peaks: the first peak is at $z \simeq 8$ and a second one is at redshift $z \simeq 2$. In analogy with the CSFR (see Gioannini et al., 2017), the first peak is due to elliptical galaxies, which dominate the PLE scenario at highest redshift. When the star formation of elliptical galaxies stops, the CMNSR abruptly decreases and from that moment on its evolution will be due to spiral galaxies.

In the case of a DTD with $\beta = -0.9$, the CMNSR decrease after the first peak, is smoother. As we explained this is the main effect of using a DTD.

In the DE scenario, both in the case of a constant total delay time and of a DTD, the CMNSR does not show the high redshift peak, because of the lower impact of elliptical galaxies.

For what concerns the alternative scenario, the CMNSR is dominated by spirals for all the range of redshifts, with a peak around $z = 3$.

Finally, in Table 3.5 both the total CMNSR and the single contributions to the CMNSR from galaxies of different morphological type, in the three different scenarios, are reported. In particular, in the first column we specify the DTD for MNS, in the second column the total CMNSR for the PLE, DE and alternative scenario, in the third column it is reported the contribution to the total CMNSR from spiral galaxies, in the fourth the contribution from ellipticals galaxies and in the last column that from irregular galaxies. By the end of the Table there are also reported the observed MNS rate. Our predictions for the total CMNSR in all the three different cosmological scenarios, both in the case of a constant total delay time and in the case of a DTD with $\beta = -0.9$, are consistent, within the error bars, with the rate of MNS predicted by LIGO/Virgo and equal to $1540_{-1220}^{+3200} \text{ Gpc}^{-3}\text{yr}^{-1}$. Moreover, the rate of MNS in the Galaxy estimated by Kalogera et al. (2004) and equal to $\sim 80_{-60}^{+200} \text{ Myr}^{-1}$ can be converted to a cosmic rate of MNS equal to $800_{-600}^{+2000} \text{ Gpc}^{-3}\text{yr}^{-1}$ for a Galaxy number density of $\sim 10^{-2} \text{ Mpc}^{-3}$ Della Valle et al. (2018). Our predictions for the total CMNSR seem to be in a very good agreement with this last estimate.

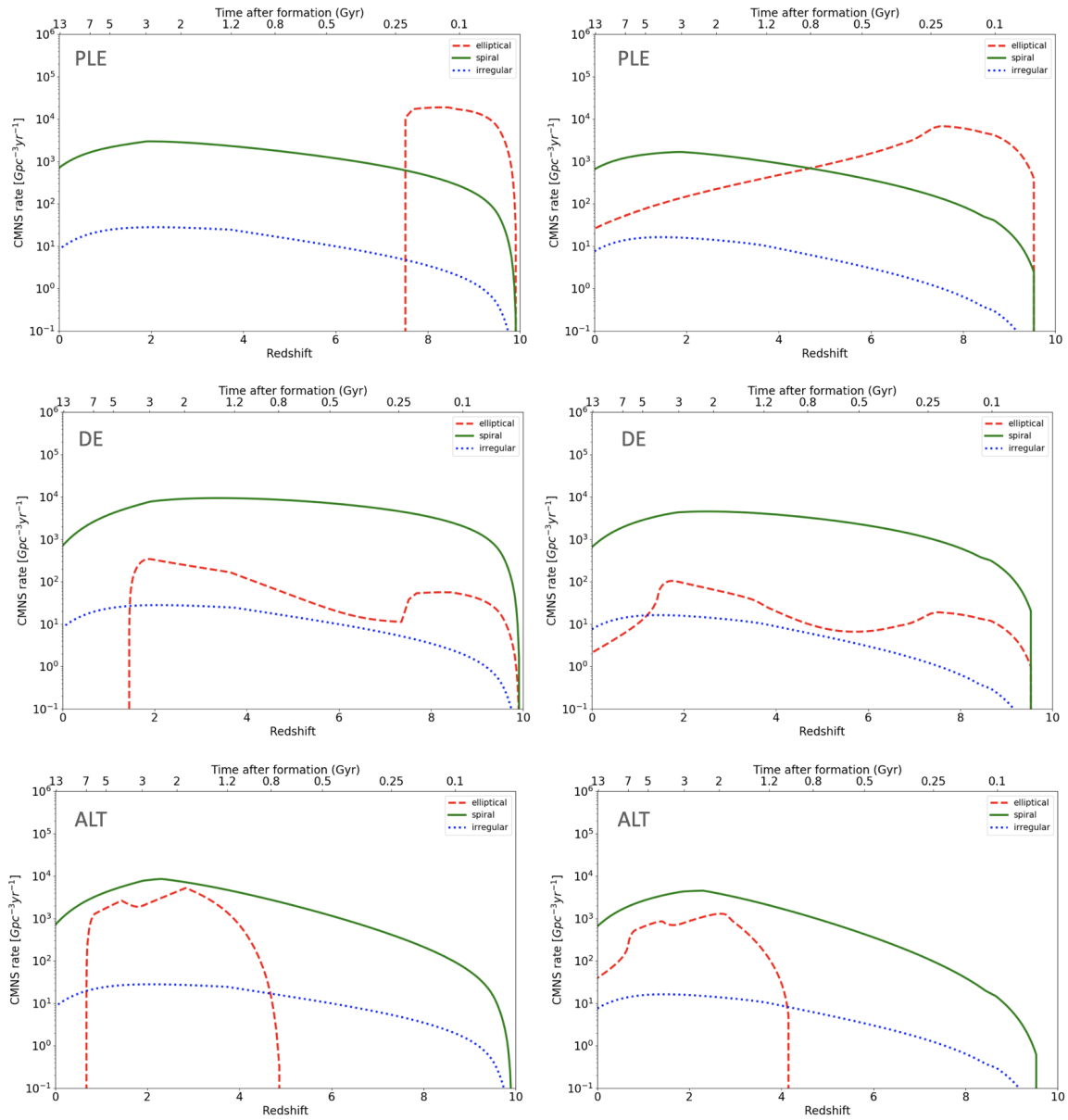


FIGURE 3.10: Contributions to the CMNSR from galaxies of different morphological type for the PLE, DE and alternative scenarios, in the case of a total delay time of 10 Myr (left panels) and in the case of a DTD with $\beta = -0.9$ (right panels).

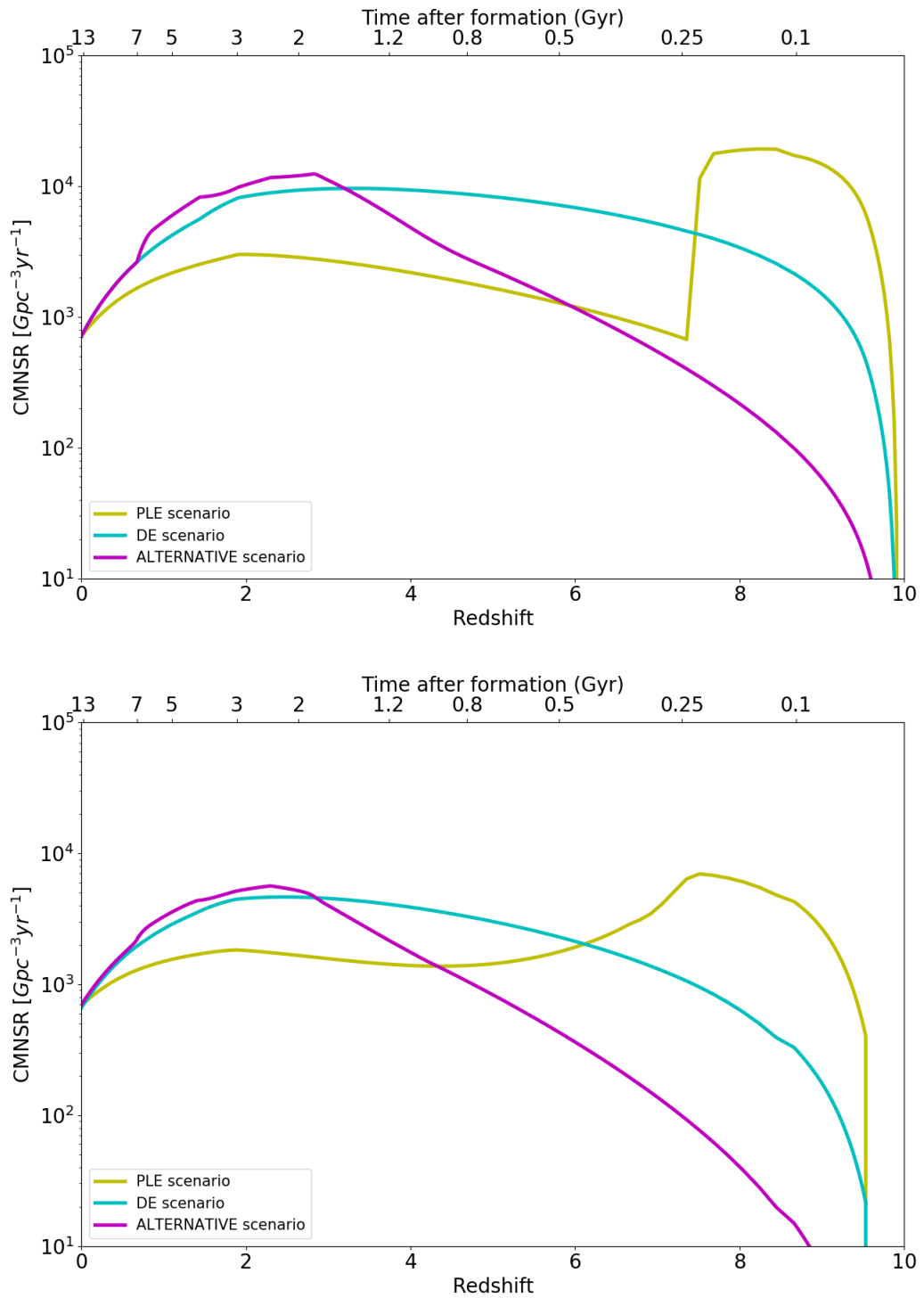


FIGURE 3.11: CMNSR as a function of the redshift for the three different scenarios (PLE, DE and alternative) in the case of a total delay time of 10 Myr (upper panel) and in the case of a DTD with $\beta = -0.9$ (lower panel).

TABLE 3.5: CMNSR for galaxies of different morphological type and in the three different cosmological scenarios (PIE, DE and alternative). In the 1st column it is reported the DTD for MNS used, in the 2nd column it is reported the total CMNSR, in the 3rd, 4rd and 5th columns are reported the contribution to the total CMNSR from spirals, ellipticals and irregulars galaxies, respectively. By the end of the Table we also report the observed rates of MNS as predicted by Abbott et al. (2017) and by Kalogera et al. (2004).

PIE scenario				
MNS	TOT CMNSR	Spirals CMNSR	Ellipticals CMNSR	Irregulars CMNSR
DTD	($\text{yr}^{-1}\text{Gpc}^{-3}$)	($\text{yr}^{-1}\text{Gpc}^{-3}$)	($\text{yr}^{-1}\text{Gpc}^{-3}$)	($\text{yr}^{-1}\text{Gpc}^{-3}$)
Constant 10 Myr	651	643	0	8
$\beta = -0.9$	647	607	33	7
DE scenario				
MNS	TOT CMNSR	Spirals CMNSR	Ellipticals CMNSR	Irregulars CMNSR
DTD	($\text{yr}^{-1}\text{Gpc}^{-3}$)	($\text{yr}^{-1}\text{Gpc}^{-3}$)	($\text{yr}^{-1}\text{Gpc}^{-3}$)	($\text{yr}^{-1}\text{Gpc}^{-3}$)
Constant 10 Myr	751	706	0	8
$\beta = -0.9$	662	651	3	7
ALTERNATIVE scenario				
MNS	TOT CMNSR	Spirals CMNSR	Ellipticals CMNSR	Irregulars CMNSR
DTD	($\text{yr}^{-1}\text{Gpc}^{-3}$)	($\text{yr}^{-1}\text{Gpc}^{-3}$)	($\text{yr}^{-1}\text{Gpc}^{-3}$)	($\text{yr}^{-1}\text{Gpc}^{-3}$)
Constant 10 Myr	715	706	0	8
$\beta = -0.9$	711	651	52	7
MNS observed rates ($\text{yr}^{-1}\text{Gpc}^{-3}$)				
Central Value	Confidence Interval	Reference		
800	200 – 2800	Kalogera et al. (2004)		
1540	320 – 4740	Abbott et al. (2017)		

3.4.3 Comparison with the SGRB redshift distribution

Our predicted redshift distributions of the total CMNSR is directly comparable with the redshift distributions of SGRBs derived by Ghirlanda et al. (2016). To make the comparison possible, the SGRBs redshift distribution has been multiplied by a suitable factor in order to reproduce the cosmic rate of MNS. The comparison can be seen in Figure 3.12, for the three cosmological scenarios and both in the case of a total delay time of 10Myr (top panel) and in the case of DTD for MNS with $\beta = -0.9$ (bottom panel). We remind that our cosmic rate has been obtained by weighting the rate of MNS in galaxies of different morphological type. We do not compare our predicted rate of MNS in a single galaxy with the observed SGRBs rate. In fact, we model only one typical galaxy per morphological type, while observations refers to galaxy of the same type but different masses.

We will consider the alternative scenario as the best one, since it also best reproduces both the CSMD (3.4.1) and the cosmic star formation rate (CSFR), as shown in previous studies (Grieco et al., 2012b; Gioannini et al., 2017). The PLE scenario, in fact, is probably unrealistic at high redshift (due to the fact that in this scenario we are neglecting the evolution of the number density) and it also underestimates data at low redshift. The DE scenario, on the other hand, has a smoother evolution, but it is shown to overestimate data at low redshift.

With that in mind, our results seem to be in good agreement with those previously found by S19. In other words, the rate of SGRBs as proposed by Ghirlanda et al. (2016) is best represented by a bottom heavy distribution, which here is given by a DTD for MNS with $\beta = -0.9$. This value of β gives rise to a distribution of time delays which scales basically as $\propto t^{-1}$. On the other hand, in the case of a total delay time of 10Myr we are not able to obtain a good agreement with Ghirlanda et al. (2016) SGRBs distributions, since we are producing a maximum which seems to overestimate those predicted by Ghirlanda et al. (2016) by a significant factor.

Ghirlanda et al. (2016) find an isotropic rate of SGRBs equal to $0.2 \text{ yr}^{-1} \text{Gpc}^{-3}$ (their model (a)). After comparison *a posteriori* their derived rate with the rate of MNS derived from population synthesis models and from the statistics of Galactic binaries, they infer an average opening angle θ of $3^\circ - 6^\circ$. From this value, we can derive a beaming correction factor¹ of (183–730), so that the true rate will be (36–146) $\text{yr}^{-1} \text{Gpc}^{-3}$. We can compare this value with the one obtained by Wanderman et al. (2015), which find an isotropic rate of SGRBs of $4.1 \text{ yr}^{-1} \text{Gpc}^{-3}$ and suggest that a typical beaming correction factor would be 30 (as also suggested by Fong et al. (2012)). By correcting their observed rate by this factor, we find a true rate of $123 \text{ yr}^{-1} \text{Gpc}^{-3}$, comparable with that derived by Ghirlanda et al. (2016).

3.4.4 Predicted number of Kilonovae detections for future surveys

On the basis of our results for the contributions to the CMNSR from galaxies of different morphological type (Figure 3.10), we can predict the number of Kilonovae detections for future LSST and VST surveys. The sky areas and the corresponding volumes patrolled by LSST and VST for Kilonovae detections have been

¹ $f_b^{-1} \equiv (1 - \cos\theta)^{-1}$, where θ is the jet opening angle.

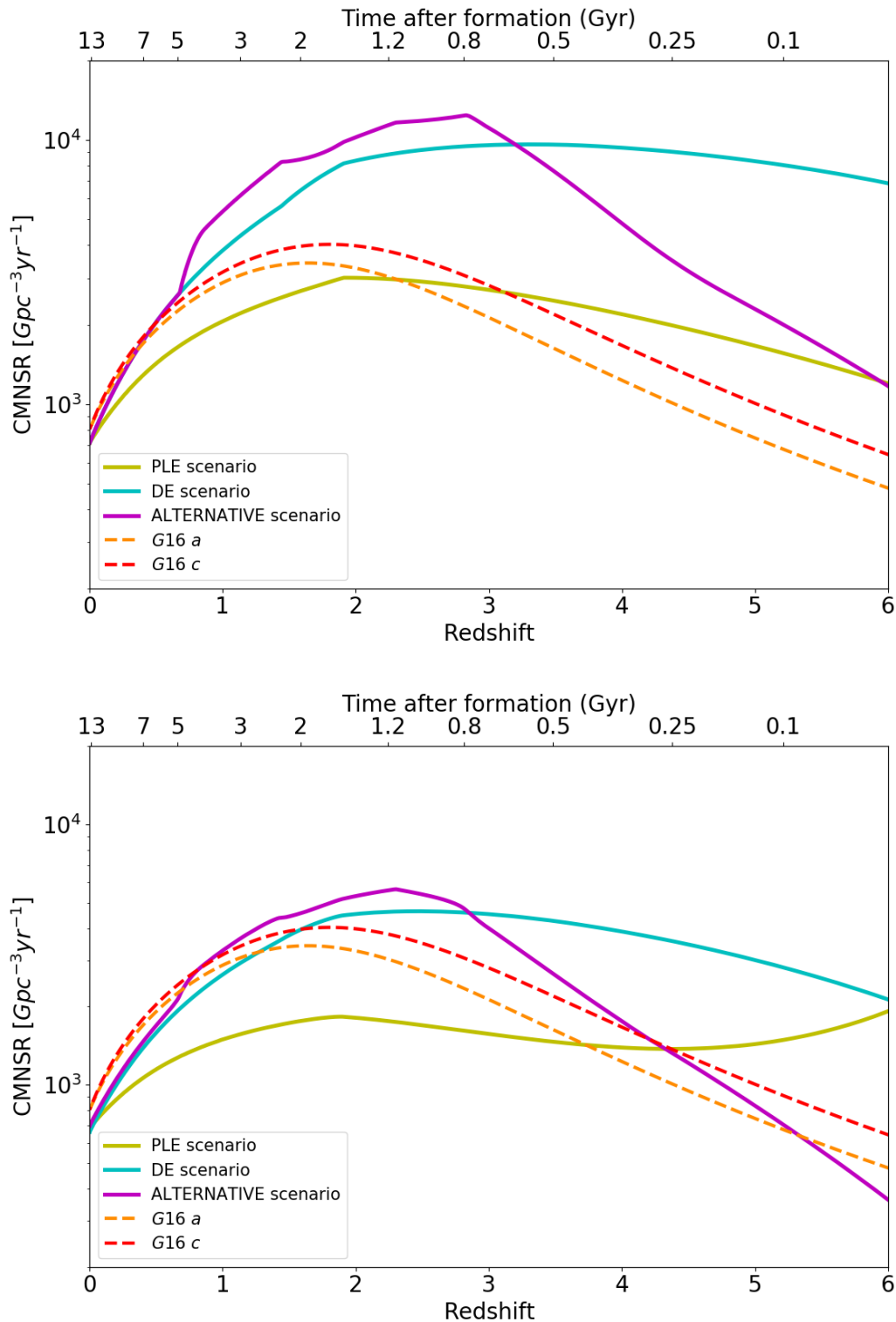


FIGURE 3.12: Redshift distributions of SGRB as found by Ghirlanda et al. (2016) (their case 'a', orange dashed line; their case 'c', red dashed line) against our predicted redshift distribution of MNS rate in the three different cosmological scenarios (PLE, DE and alternative), in the case of assuming a total delay time of 10 Myr (upper panel) and in the case of a DTD for MNS with $\beta = -0.9$ (lower panel).

TABLE 3.6: *Predicted Kilonovae rates ($\text{yr}^{-1}\text{Gpc}^{-3}$) for LSST and VST surveys in the case of a DTD with $\beta = -0.9$. In the 1st it is specified the type of galaxy, in the 2nd column the cosmological scenario, in the 4th and 5th columns the predicted Kilonovae detections for LSST and VST surveys, respectively.*

Type	Scenario	LSST	VST
Spiral	PLE	1850	91
Irregular	PLE	21	1
Elliptical	PLE	74	4
Elliptical	DE	17	0
Elliptical	alternative	130	6

TABLE 3.7: *Predicted Kilonovae rates ($\text{yr}^{-1}\text{Gpc}^{-3}$) for LSST and VST surveys in the case of a constant total delay time of 10 Myr. In the 1st it is specified the type of galaxy, in the 2nd column the cosmological scenario, in the 4th and 5th columns the predicted Kilonovae detections for LSST and VST surveys, respectively.*

Type	Scenario	LSST	VST
Spiral	PLE	2215	100
Irregular	PLE	28	1
Elliptical	PLE	0	0
Elliptical	DE	0	0
Elliptical	alternative	0	0

taken from Della Valle et al. (2018) and are equal to $\simeq 2.1 \text{ Gpc}^3$ and $\simeq 0.13 \text{ Gpc}^3$, respectively. The predicted number of Kilonovae detections in different morphological type of galaxies and for the three cosmological scenarios are reported in Tables 3.6 and 3.7. In particular, in Table 3.6 we report the predicted rates obtained hypothesizing a DTD with $\beta = -0.9$ and in Table 3.7 are reported those computed adopting a constant delay of 10 Myr. In both Tables we report in the first column the morphological type of galaxies, in the second column the cosmological scenario and in the third and fourth columns the predicted rate for LSST and VST, respectively. For spiral and irregular galaxies we report only the predicted detections in the PLE scenario, since there are no significant differences in the CMNSR among different cosmological scenarios.

These predictions should be corrected by a factor η that accounts for the "efficiency" of a given survey. η depends on several parameters, such as the control time (i.e. a quantity that depends on the survey cadence and on the photometric time scale evolution of the transient, see e.g. Cappellaro et al., 1999b), sky conditions, technical downtime and scheduling constraints. Typical values are of the order of $\eta \simeq 50\%$, but they can be as low as 5% Grado et al. (2020).

The Transient High-Energy Sky and Early Surveyor (THESEUS) space mission Amati et al. (2018), currently under study by the European Space Agency (ESA) for a possible launch in 2032, would be able to reveal electromagnetic counterparts of MNS and SGRBs up to $z \sim 1$ Stratta et al. (2018). THESEUS should detect a few dozens of SGRBs on-axis per year.

3.5 Conclusions

In this Chapter, we have computed for the first time the rate of MNS in galaxies of different morphological type (ellipticals, spirals and irregulars) and we have studied the effect of these events on the chemical evolution of a typical r-process element, namely the Eu, in the MW, taken as a typical spiral galaxy. The models for galaxies of different type differ mainly by the history of star formation, with the ellipticals suffering a strong and short burst of star formation, while the spirals and even more the irregulars suffer a continuous and more moderate star formation. The adopted galaxy models can reproduce the main features of typical galaxies of each type, as shown by Gioannini et al. (2017). The evolution of the Eu in the MW has been investigated by assuming either that MNS are the only producers of this element or that both CC-SNe and MNS contribute to the Eu enrichment. For the MW we also tested four different delay time distributions, the same derived by S19 and corresponding to four different values of the β parameter ($-1.5, -0.9, 0.0, 0.9$), as well as a constant total delay time of 10 Myr equal for all neutron star binary systems. In particular, we have tuned the parameters of our simulations in order to reproduce the following observational constraints of the MW: the present time rate of MNS, the solar Eu and Fe abundances and the [Eu/Fe] vs. [Fe/H] relation.

Our main results for spiral galaxies can be then summarized as follows:

- The present time rate of MNS in the Galaxy is well reproduced either by assuming a DTD with parameter $\beta = -0.9$ ($\text{DTD} \propto t^{-1}$) or a constant total delay time of 10 Myr. In the first case, the occurrence probability of MNS is 5.42% while in the second case it is found to be 6.15%;
- The [Eu/Fe] vs. [Fe/H] in the MW can be reproduced by assuming only MNS as Eu producers only if a constant total delay time (stellar lifetime plus gravitational time delay) of 10 Myr is adopted, a result already suggested by previous works (e.g., Matteucci et al., 2014; Cescutti et al., 2015). In this case, the yield of Eu for merging event should be $2.0 \times 10^{-6} M_{\odot}$, which is slightly lower than those estimated from the kilonova AT2017gfo, but well inside the theoretical range of $(10^{-7} - 10^{-5}) M_{\odot}$ predicted by Korobkin et al. (2012) ;
- If a DTD including long time delays for MNS is assumed, the [Eu/Fe] vs. [Fe/H] in the MW is reproduced only if CC-SNe are also included as Eu producers. The best DTD has $\beta = -0.9$. In this case, the yield of Eu for merging event should be $0.5 \times 10^{-6} M_{\odot}$, while the yield of Eu from CC-SNe is the modified version of the model SN20150 from Argast et al. (2004). In this case, CC-SNe become the main production site of Eu, in agreement with S19 results for the MW.

For what concerns the chemical evolution of ellipticals and irregulars, our main results can be summarized as follows:

- We are not able to see any merging event at the present time in ellipticals galaxies if a constant total delay time of 10 Myr is assumed, since in this

case the rate of MNS will follow the evolution of the SFR, which has stopped $1 \sim 10$ Gyr ago in elliptical galaxies;

- If we instead assume a DTD ($\beta = -0.9$), namely a distribution of gravitational time delays, the present time rate of MNS is different from zero. This fact is in agreement with the probability that the galaxy NGC 4993, host of the event GW170817, is an early-type galaxy with an old dominant stellar population Abbott et al. (2017);
- The predicted [Eu/Fe] vs. [Fe/H] patterns in galaxies of different morphological type follow the expectations of the time-delay model, either in the case of MNS being the only Eu producers or if CC-SNe also participate to the Eu production. This means a longer plateau for [Eu/Fe] in the case of ellipticals with higher SFR, and a shorter plateau for irregulars with a weak SFR. (see Matteucci, 2012).

We have also studied the cosmic evolution of the stellar mass density and MNS rate in three cosmological scenarios: (i) a PLE (pure luminosity evolution) scenario, in which the number density of the different morphological types of galaxies does not evolve with redshift; (ii) a DE (density evolution) scenario, in which the number density is assumed to evolve with redshift in order to reproduce a typical hierarchical galaxy formation; (iii) an alternative scenario, where both spirals and ellipticals are assumed to evolve on the basis of observational constraints (see Pozzi et al., 2015), which is very similar to the DE scenario. The CMNSR has been computed both in the case of a DTD with $\beta = -0.9$ and of a constant total delay time of 10 Myr. Our results have been then compared with the redshift distributions of SGRBs, as derived by Ghirlanda et al. (2016).

Our conclusion are the following:

- The CSMD is best reproduced in the case of an alternative scenario of galaxy formation. By the way, this same scenario is also the best to reproduce the CSFR, as shown already by Gioannini et al. (2017). On the other hand, in both the PLE and the DE scenarios our results overestimate the data for redshift $z \geq 2$;
- The CMNSR in the PLE scenario, with a constant delay time for MNS, shows a first peak at redshift $z \sim 8$, due to the high redshift formation of ellipticals. When the star formation in ellipticals stops, the CMNSR abruptly decreases and its evolution is then due to spiral galaxies, leading to a second peak at redshift $z \sim 2$;
- If a DTD for MNS is assumed, the decrease of the CMNSR after the high redshift peak in the PLE scenario is smoother, since it does not stop with the quench of star formation. Therefore, in this case the elliptical galaxies will contribute to the CMNSR during the whole range of redshift. In particular, the contribution from ellipticals appears to be dominant at high redshift, whereas that from spirals is dominant at lower redshift;
- Both in the DE and alternative scenario, the contribution to the CMNSR from elliptical galaxies has a lower impact with respect to that of spirals.

Therefore, the effect of using a DTD or a constant and short time delay has almost no consequences on the total CMNSR behaviour;

- Our predictions of the present time CMNSR in all the three different cosmological scenarios, both in the cases of a constant total delay time and DTD, are consistent with the rate of MNS observed by LIGO/Virgo and the one estimated by Della Valle et al. (2018);
- Assuming the alternative scenario as the best one (see also Gioannini et al., 2017), the SGRBs redshift distribution proposed by G16 is best represented by our CMNSR with an assumed DTD $\propto t^{-1}$. On the other hand, in the case of a constant delay time too many events at higher redshift with respect to G16 are produced. Therefore, we conclude that in order to reproduce the SGRB rate, the assumption of a constant total delay time should be rejected. However, S19 found a way to reconcile a short time delay, good for reproducing the [Eu/Fe] ratio in the Galaxy, with the SGRBs rate; that is by assuming that the percentage of systems giving rise to a MNS event (α_{MNS}) is variable in time. The adoption of a variable α_{MNS} will be the subject of future work.

Finally, for what it concerns our predictions of the number of Kilonovae detections for the LSST and VST surveys, we can conclude that:

- On the basis of the results shown in Tables 3.6 and 3.7, it is possible to state that, at least in principle, the observations of the number of MNS can be used to discriminate the different scenarios at play. However, Kilonovae are intrinsically weak objects detectable only up to $z \sim 0.25$ and $z \sim 0.05$ with LSST and VST, respectively. A comparison with Figure 3.10 indicates that the number of MNS detections occurring in spirals and irregulars at low z cannot be used to disentangle among different scenarios, since they provide similar results. Differences in results emerge only at very high values of redshift, which, unfortunately are not observable with current/future structures. On the other hand, each scenario is capable of predicting significantly different Kilonovae rates in ellipticals even at very low z . Therefore, observations of MNS in early-type galaxies are of the utmost importance because they can effectively help to discriminate models characterized by a constant total delay (10 Myr) or by delay time distribution functions.

CHAPTER 4

Dwarf Spheroidal and Ultra Faint Dwarf Galaxies

IN this Chapter, I present our work on the evolution of Eu and Ba abundances in Local Group dwarf spheroidal and ultrafaint dwarf galaxies. We investigate on the production of r-process material by MNS and MR-SNe with different yields and time-scales prescriptions, and compare our results with a new sets of homogeneous abundances.

The Chapter is organized as follows. In Section 4.1, I outline the context of this Chapter. In Section 4.2, I present the observational data which have been considered to make a comparison with the predictions of the chemical evolution model. In Sections 4.3 and 4.4, I describe the chemical evolution model and the adopted stellar yields, respectively. In Section 4.5, I present our results for Sculptor, Fornax and Reticulum II. Finally, in Section 4.6 I summarize our conclusions.

The results presented in this Chapter are described in the published paper Molero et al. (2021a).

4.1 Introduction

Among the MW satellites it is possible to distinguish between classical and ultra-faint dwarf spheroidal galaxies. Classical dwarf spheroidal galaxies (dSphs) are among the least luminous and most dark-matter-dominated galaxies observed. They can be classified as early-type galaxies, since they are characterized by low present time gas mass and iron-poor stars (Koch, 2009; Tolstoy et al., 2009; McConnachie, 2012). Ultrafaint dwarf (UFD) spheroidals have very similar physical properties to dSph galaxies, but are characterized by even smaller average surface brightness and effective radii (see Simon, 2019 for a recent review). Dwarf galaxies show metal-poor and old or intermediate-aged stellar populations, with only some of them hosting younger stars (indication of a recent SF activity). They are thought to be the surviving building blocks of the halos of more massive galaxies, formed in part through accretion (e.g., De Lucia et al., 2008; Starkenburg et al., 2013; Mackereth et al., 2019) and, in particular, to have contributed to the outer halo of the MW, being important sources of very metal-poor stars (e.g., Salvadori et al., 2009). Moreover, Local Group dwarf galaxies are close enough for spectroscopic analyses of individual stars and for derivation of their ‘true’ SF histories through colour-magnitude diagrams (CMDs), which allow chemical evolution models to perform a more detailed analysis of these objects (Romano et al., 2006; Lanfranchi et al., 2010; Romano et al., 2013). In general, dwarf galaxies offer a good opportunity to investigate fundamental properties of galaxy formation and chemical evolution across different environments and they can play a key role in the development of more sophisticated galaxy formation models.

As described in Chapter 1, the majority of heavy elements beyond the Fe peak originate via neutron capture processes, which can be rapid (r-process) or slow (s-process) depending on the timescales with respect to the β -decay in nuclei. The s-process takes place in LIMS during the AGB phase via the reaction $^{13}\text{C}(\alpha, n)^{16}\text{O}$ and in massive stars as a weak s-process (Langer et al., 1989; Prantzos et al., 1990). The efficiency of the weak s-process depends on the metallicity and, if rotation is not considered, nucleosynthesis calculations show that for metallicity lower than $\sim 10^{-4}$ the s-process becomes negligible (e.g., Limongi et al., 2003). However, rotation increases the efficiency of the s-process in massive stars, in particular at low metallicities where stars are expected to be more compact and to rotate faster (Chiappini et al., 2011; Frischknecht et al., 2016; Limongi et al., 2018). On the contrary, the r-process sites are still under debate, with possible candidates being MNS and peculiar CC-SNe, as the MR-SNe described in Chapter 1. However, the required rotation rates and magnetic energies for the MR-SNe restrict the mechanism to a minority of progenitor stars: only 1% of all stars with initial mass larger than $10 M_{\odot}$ may have the necessary conditions to host strong enough magnetic fields, according to Woosley et al. (2006b). Nevertheless, the rarity of progenitors with this required initial conditions can provide an explanation for the observed scatter in the abundance of r-process elements for low-metallicity stars. On the other hand, according to their observed yields and rate, MNS are potentially a powerful source of r-process nucleosynthesis. However, as shown in Chapter 3, because of their time-delayed nature of formation, they predict an [Eu/Fe] vs. [Fe/H] abundance pattern completely different from what is observed

in the Galaxy (see e.g., Matteucci et al., 2014; Simonetti et al., 2019; Molero et al., 2021b; Fraser et al., 2022). The issue can be solved by including a second source for r-process nucleosynthesis which should be active especially at low metallicities, pointing towards a scenario in which both a quick and a delayed source produce r-process material. While this scenario can solve the [Eu/Fe] vs. [Fe/H] ‘puzzle’, we are wondering which are its predictions for other neutron-capture elements. With the goal of better understanding both the r- and the s-process production sites at low metallicity, here we study the chemical evolution of Eu and Ba abundances in six dSph and two UFD galaxies for which homogeneous abundances have been recently published by Reichert et al. (2020).

4.2 Observational Data

We have modelled the chemical evolution of 6 dSph and 2 UFD galaxies, which are: Böotes I (Boo I), Carina (Car), Fornax (For), Leo I (Leo), Reticulum II (Reticulum II), Sculptor (Scl), Sagittarius (Sgr) and Ursa Minor I (Umi I). Here, we will focus on the results for Sculptor, Fornax and Reticulum II. Our results for the other galaxies are provided as Supplementary Material (online only) of the paper Molero et al. (2021a). We chose Sculptor and Fornax since their results are representative of those obtained for all the other dSphs, and Reticulum II because of its peculiar heavy elements abundances.

We have chosen abundances data of Reichert et al. (2020) for all galaxies, while for the metallicity distribution functions (MDF) we adopted collections of data from the SAGA database (Suda et al., 2008) for all galaxies, except for Sculptor, for which the observational MDF is taken from Romano et al. (2013). All abundances are scaled to the solar photosphere abundances of Asplund et al. (2009), which is the one adopted in our chemical evolution code. For comparison, we adopt the star formation histories (SFH) as derived by color-magnitude diagrams (CMD) fitting analysis of several authors (Hernandez et al., 2000; Dolphin, 2002; de Boer et al., 2012b; de Boer et al., 2012a; Brown et al., 2014; de Boer et al., 2015). In particular, we assumed the same number and duration of the SF episodes of the CMDs.

4.3 The Model

We use an updated version of the model presented by Lanfranchi et al. (2004) to describe the chemical evolution of both UFDs and dSphs. Galaxies form by infall of primordial gas in a pre-existing diffuse dark matter (DM) halo. The model is a one zone with instantaneous and complete mixing of gas. The stellar lifetimes are taken into account, thus relaxing the instantaneous recycling approximation (IRA). The model is able to follow the evolution of 31 elements, from H to Eu, during 14 Gyr.

The basic equations that follow the evolution of G_i , namely the mass fraction of the element i in the gas, are described by Eq. 2.14. Here, the dependence on the radius is relaxed, since the adopted model is a one-zone. We include both infall

and outflow of gas, with the infall law given by the following relation:

$$(\dot{M}_{gas,i})_{infall} = aX_{i,infall}e^{t/\tau_{infall}}, \quad (4.1)$$

where a is a normalization constant constrained to reproduce the present time total infall mass, $X_{i,infall}$ describes the chemical abundance of the element i of the infalling gas (here assumed to be primordial) and τ_{infall} is the infall time-scale. As explained in Chapter 2, the wind rate is assumed to be proportional to the SFR (see Eq. 2.11) which in this work it is described by a Schmidt-Kennicutt law:

$$\psi(t) = \nu M_{gas}^k, \quad (4.2)$$

with $k = 1$. For all the galaxies simulated in this work, we assume a Salpeter (1955) IMF.

4.4 Nucleosynthesis prescriptions

For all the stars sufficiently massive to die in a Hubble time, the following stellar yields have been adopted:

- For LIMS we included the metallicity-dependent stellar yields of Karakas (2010);
- For massive stars we assumed yields of Kobayashi et al. (2006);
- For Type Ia SNe we included yields of Iwamoto et al. (1999). We adopted the SD scenario for Type Ia SNe, in which SNe arise from the explosion via C-deflagration of a C-O white dwarf in a close binary system as it has reached the Chandrasekhar mass due to accretion from its red giant companion.

The same stellar yields have been adopted in Vincenzo et al. (2015). Also, a complete and detailed description of those yields can be found in Romano et al. (2010).

4.4.1 Eu and Ba yields

For both Eu and the r-process fraction of Ba we considered two different production sites: MNS and MR-SNe. We assume r-process elements to be produced by (i) only MNS, (ii) only MR-SNe, (iii) both MNS and MR-SNe.

In our simulations, MNS are systems of two $1.4 M_{\odot}$ neutron stars with progenitors in the $9-50 M_{\odot}$ mass range. In order to include the production of r-process elements from MNS in our chemical evolution code, we need to specify the following parameters (see Matteucci et al., 2014):

- the mass of each elements which is produced per merging event, Y_{Eu}^{MNS} and Y_{Ba}^{MNS} ;
- the time delay between the formation of the double neutron star system and the merging event, τ ;

TABLE 4.1: *Yields of Sr, Eu and Ba from MNS adopted in this work. Yields of Sr are those measured by Watson et al. (2019) while those of Eu and Ba have been obtained as described in the text.*

$Y_{\text{Sr}}^{\text{MNS}} (M_{\odot})$	$Y_{\text{Eu}}^{\text{MNS}} (M_{\odot})$	$Y_{\text{Ba}}^{\text{MNS}} (M_{\odot})$
$(1 - 5) \times 10^{-5}$	$3.0 \times 10^{-7} - 1.5 \times 10^{-6}$	$3.2 \times 10^{-6} - 1.58 \times 10^{-5}$
$(1 - 5) \times 10^{-4}$	$3.0 \times 10^{-6} - 1.5 \times 10^{-5}$	$3.2 \times 10^{-5} - 1.58 \times 10^{-4}$
$(1 - 5) \times 10^{-3}$	$3.0 \times 10^{-5} - 1.5 \times 10^{-4}$	$3.2 \times 10^{-4} - 1.58 \times 10^{-3}$

- the fraction of neutron stars in binaries that produce a MNS, α_{MNS} .

For what it concerns the yields of r-process elements from MNS, they have been obtained by assuming that there is a scaling relation between them and those of Sr. The adopted scaling factors are equal to 0.03 for Eu and to 3.16 for Ba, and have been found from the solar system r-process contribution, as determined by Simmerer et al. (2004). For the yields of Sr, we adopted the value found by Watson et al. (2019) in the reanalysis of the spectra of the kilonova AT2017gfo which followed the neutron-star merger GW170817, equal to $(1 - 5) \times 10^{-5} M_{\odot}$. Those yields have also been multiplied by two different factors (1×10^1 , 1×10^2) in order to take into account the uncertainties that could affect them, because of their model assumptions as well as the scatter of Sr compared to Eu in old stars. The yields of Sr with the scaled yields of Eu and Ba are reported in Table 4.1.

For the time delay, τ , we adopt two different approaches. The first one consists in assuming a constant delay time between the formation of the neutron stars binary system and the merging event (as first done by Argast et al., 2004 and later by Matteucci et al., 2014), while the second one consists in adopting a DTD. In the first case we adopt a delay time $\tau = 1 \text{ Myr}$. This is equivalent to assume that all neutron stars binary systems would merge on the same time-scale, which is short and constant. In the second case, we adopt the DTD of Simonetti et al. (2019) with $\beta = -0.9$, as explained in Chapter 2. The parameter α_{MNS} , namely the probability of the MNS event has been found to be $\alpha_{\text{MNS}} = 5.42 \times 10^{-2}$ for a DTD with $\beta = -0.9$ for external spiral galaxies by Molero et al. (2021b) (see previous Chapter), in order to reproduce the observed present time MNS rate in the MW as the one predicted by Kalogera et al., 2004, equal to $\sim 80_{-60}^{+200} \text{ Myr}^{-1}$. For dwarf galaxies, we adopt a lower probability of MNS in order to take into account the less efficient r-process material enrichment which characterizes these systems. In particular, we set $\alpha_{\text{MNS}} = 2.15 \times 10^{-2}$ and based our consideration on the work of Bonetti et al. (2019), according to which in low mass galaxies neutron stars binary systems tend to merge with a large off-set from the host galaxy, because of the kicks imparted by the two SN explosions. As stated by the authors, the immediate consequence of a merger location detached from the disc plane, is a dilution of the amount of r-process material retained by the galaxy.

For the production of r-process elements from MR-SNe, we select a set of yields from different nucleosynthetic studies as reported in Table 4.2. Another possibility could have been that of adopting as Ba yields those obtained by scaling the Eu yields of the studies reported in the Table by taking into account the solar system r-process contribution, as done for MNS. We checked that this choice did

TABLE 4.2: Yields of *r*-process elements from MR-SNe adopted in this work.

$Y_{\text{Eu}}^{\text{MRD}} (M_{\odot})$	$Y_{\text{Ba}}^{\text{MRD}} (M_{\odot})$	Model	Reference
1.11×10^{-5}	2.10×10^{-4}	–	Winteler et al. (2012) ¹
1.56×10^{-6}	2.72×10^{-6}	B12 β 0.25	Nishimura et al. (2015)
6.85×10^{-6}	2.58×10^{-4}	L0.10	Nishimura et al. (2017)
2.81×10^{-6}	1.23×10^{-4}	L0.60	"
4.69×10^{-7}	7.66×10^{-6}	L0.75	"
5.19×10^{-6}	2.07×10^{-5}	35OC-Rs	Reichert et al. (2021)

TABLE 4.3: Yields of Eu and *r*-process Ba of Cescutti et al. (2006) for massive stars in the mass range 12 – 30 M_{\odot} .

$M_{\text{star}} (M_{\odot})$	$Y_{\text{Ba}} (M_{\odot})$	$Y_{\text{Eu}} (M_{\odot})$
12	9.0×10^{-7}	4.5×10^{-8}
15	3.0×10^{-8}	3.0×10^{-9}
30	1.0×10^{-9}	5.0×10^{-10}

not significantly affect our results. Moreover, we run also models in which we assume that Eu and *r*-process Ba are produced by massive stars in the mass range (12 – 30) M_{\odot} with the yields of Cescutti et al. (2006) (their model 1). Details of those yields are reported in Table 4.3.

MR-SNe may be indeed important contributors to the enrichment of heavy elements. However, the required rotation rates and magnetic energies restrict the mechanism to a minority of progenitor stars (Nishimura et al., 2017; Mösta et al., 2018; Reichert et al., 2021). Woosley et al. (2006b) speculated that approximately 1% of all stars with initial mass $\geq 10 M_{\odot}$ have the necessary conditions to host strong enough magnetic fields. Therefore, here, we assume that only 1 – 2% of all stars with initial mass in the mass range (10 – 80) M_{\odot} would explode as a MR-SNe. Furthermore, it has been suggested that these events occur more frequently at low metallicities, because of the lower opacity that result in higher rotation rates and, as a consequence, stronger magnetic fields (see e.g., Brott et al., 2011, Thielemann et al., 2017). Therefore, we also test models in which the production of *r*-process elements from MR-SNe is active only at metallicity $Z \leq 10^{-3}$, as suggested also in Winteler et al. (2012) (see also Cescutti et al., 2015).

Finally, for the Ba *s*-process component, which is the predominant one, we have adopted yields of Busso et al. (2001) for LIMS of (1.5 – 3.0) M_{\odot} . Those yields have a strong dependence on the initial metallicity of the stars. For stars of (1.0 – 1.5) M_{\odot} we have adopted yields of Cescutti et al. (2015), which are obtained simply by scaling the yields of Busso et al. (2001) to stars of 1.5 M_{\odot} .

Details of the different models that we run are reported in Tables 4.4 and 4.5.

4.5 Results

For each galaxy we set the input parameters of the chemical evolution model in order to reproduce the star formation, the observed MDF and the [Mg/Fe]

¹The values are based on a recent recalculation that was presented in Côté et al. (2020).

TABLE 4.4: Summary table of the nucleosynthesis prescriptions adopted by different models. In the 1st column in is reported the name of the model, in the 2nd column it is specified if there is production from MNS, in the 3rd it is specified if we adopted a DTD for MNS, in the 4th column it is reported the adopted yield of Eu from MNS, in the 5th column the yield of Ba from MNS, in the 6th it is specified if there is production from MR-SNe, in the 7th column it is reported the yield of both Eu and Ba from MR-SNe, in the 8th column the percentage of stars in the $(10 - 80)M_{\odot}$ mass range which explode as MR-SNe and in the last column the range of metallicities in which the MR-SNe channel is active for the Eu and/or Ba production.

Model	MNS	DTD	$Y_{\text{Eu}}^{\text{MNS}} (M_{\odot})$	$Y_{\text{Ba}}^{\text{MNS}} (M_{\odot})$	MR-SNe	$Y_{\text{Eu,Ba}}^{\text{MR-SNe}}$	%	Z
C54	yes	no	3.00×10^{-5}	1.50×10^{-4}	3.20×10^{-4}	1.58×10^{-3}	no	—
C65	yes	no	3.00×10^{-6}	1.50×10^{-5}	3.20×10^{-5}	1.58×10^{-4}	no	—
C76	yes	no	3.00×10^{-7}	1.50×10^{-6}	3.20×10^{-6}	1.58×10^{-5}	no	—
D54	yes	yes	3.00×10^{-5}	1.50×10^{-4}	3.20×10^{-4}	1.58×10^{-3}	no	—
D65	yes	yes	3.00×10^{-6}	1.50×10^{-5}	3.20×10^{-5}	1.58×10^{-4}	no	—
D76	yes	yes	3.00×10^{-7}	1.50×10^{-6}	3.20×10^{-6}	1.58×10^{-5}	no	—
W12	no	—	—	—	—	—	yes	Winteler et al., 2012
N15	no	—	—	—	—	—	yes	Nishimura et al., 2015
N17a	no	—	—	—	—	—	yes	Nishimura et al., 2017 L0.10
N17b	no	—	—	—	—	—	yes	Nishimura et al., 2017 L0.60
N17c	no	—	—	—	—	—	yes	Nishimura et al., 2017 L0.75
R21	no	—	—	—	—	—	yes	Reichert et al., 2021
N15Z	no	—	—	—	—	—	yes	Nishimura et al., 2015
N17cZ	no	—	—	—	—	—	yes	Nishimura et al., 2017 L0.75
R21Z	no	—	—	—	—	—	yes	Reichert et al., 2021

TABLE 4.5: Table 4.4 continue.

Model	MINS	DTD	$Y_{\text{Et}}^{\text{MINS}} (M_{\odot})$	$Y_{\text{Ba}}^{\text{MINS}} (M_{\odot})$	MIR-SNe	$Y_{\text{Et, Ba}}^{\text{MIR-SNe}}$	%	Z
NI5Z	no	-	-	-	yes	Nishimura et al., 2015	1-2	$< 10^{-3}$
NI7cZ	no	-	-	-	yes	Nishimura et al., 2017 L0.75	1-2	$< 10^{-3}$
R21Z	no	-	-	-	yes	Reichert et al., 2021	1-2	$< 10^{-3}$
CN54	yes	no	$3.00 \times 10^{-5} - 1.50 \times 10^{-4}$	$3.20 \times 10^{-4} - 1.58 \times 10^{-3}$	yes	Nishimura et al., 2017 L0.75	1	all
CN65	yes	no	$3.00 \times 10^{-6} - 1.50 \times 10^{-5}$	$3.20 \times 10^{-5} - 1.58 \times 10^{-4}$	yes	Nishimura et al., 2017 L0.75	1	all
CN76	yes	no	$3.00 \times 10^{-7} - 1.50 \times 10^{-6}$	$3.20 \times 10^{-6} - 1.58 \times 10^{-5}$	yes	Nishimura et al., 2017 L0.75	1	all
CR54	yes	no	$3.00 \times 10^{-5} - 1.50 \times 10^{-4}$	$3.20 \times 10^{-4} - 1.58 \times 10^{-3}$	yes	Reichert et al., 2021	1	all
CR65	yes	no	$3.00 \times 10^{-6} - 1.50 \times 10^{-5}$	$3.20 \times 10^{-5} - 1.58 \times 10^{-4}$	yes	Reichert et al., 2021	1	all
CR76	yes	no	$3.00 \times 10^{-7} - 1.50 \times 10^{-6}$	$3.20 \times 10^{-6} - 1.58 \times 10^{-5}$	yes	Reichert et al., 2021	1	all
DN65	yes	yes	$3.00 \times 10^{-6} - 1.50 \times 10^{-5}$	$3.20 \times 10^{-5} - 1.58 \times 10^{-4}$	yes	Nishimura et al., 2017 L0.75	1	all
DN65Z	yes	yes	$3.00 \times 10^{-6} - 1.50 \times 10^{-5}$	$3.20 \times 10^{-5} - 1.58 \times 10^{-4}$	yes	Nishimura et al., 2017 L0.75	1	$< 10^{-3}$
DR54	yes	yes	$3.00 \times 10^{-5} - 1.50 \times 10^{-4}$	$3.20 \times 10^{-4} - 1.58 \times 10^{-3}$	yes	Reichert et al., 2021	1	all

vs [Fe/H] pattern. Except that for Fornax and Reticulum II, in general we follow previous literature results which provide an estimate of the parameters of the model able to reproduce the relevant data for each galaxy. The input parameters of chemical evolution models adopted in this work are reported in Table 4.6.

After tuning our models with the observed data, we analysed the production of neutron capture elements by comparing the results of our models for the evolution of [Eu/Fe], [Ba/Fe] and [Ba/Eu] vs. [Fe/H] with observed patterns. In this way, it is possible to investigate on the nucleosynthesis of those elements.

4.5.1 Sculptor and Fornax

For Sculptor dSph galaxy, we have adopted similar theoretical prescriptions to Lanfranchi et al. (2004) (who first modelled the chemical evolution of Sculptor) and to Vincenzo et al. (2014). We assumed a dark matter halo of mass $M_{\text{DM}} = 3.4 \times 10^8 M_{\odot}$ (Battaglia et al., 2008) and a core radius $R_{\text{DM}=1 \text{ kpc}}$. The effective radius of the luminous component of the galaxy has been set to $R_{\text{L}} = 260 \text{ pc}$ (Walker et al., 2009). The SF of Sculptor has been derived from the CMD fitting analysis by de Boer et al. (2012b) and it consists of one episode of star formation which lasts 7 Gyr. Our predicted SFR as a function of time is shown in panel (a) of Figure 4.1. It is characterized by an initial fast increase, due to the short time-scale of the infall, followed by a decline caused by the onset of the galactic wind. Our model predicts a final stellar mass of $M_{\star, \text{f}} = 2.6 \times 10^6 M_{\odot}$, similar to the observed one $M_{\star, \text{f}} = 1.2 \times 10^6 M_{\odot}$ derived by de Boer et al. (2012b) by integrating the SFR up to the present time.

In panel (b) of the same Figure, we show the [Mg/Fe] vs. [Fe/H] evolution together with the prediction of our model. The pattern is characterized by a flat plateau at low metallicities² followed by a decrease for $[\text{Fe}/\text{H}] \geq -1.5 \text{ dex}$ due to the fact that, for $[\text{Fe}/\text{H}] \geq -1.5 \text{ dex}$, SNeIa start contributing in a substantial way to the Fe enrichment (Matteucci et al., 2001). In fact, we remind that while α -elements are mainly produced in Type II SNe on short time-scales, the majority of Fe and Fe-peak elements are produced by Type Ia SNe on longer time-scales (see Palla, 2021 for a detailed discussion). Also, as the galactic wind is activated, the SF starts to decline until it stops at 7 Gyr. Consequently, the production of α -elements by Type II SNe will decrease too. On the other hand, Fe-peak elements are continuously ejected into the ISM even when there is no SF activity, because of the long lifetimes of the progenitors of Type Ia SNe. Because of these two facts, the [Mg/Fe] vs. [Fe/H] trend will be strongly influenced by the efficiency of the SF (ν) and by the wind parameter (ω): the higher ν is, the longer the [Mg/Fe] plateau will be, while the higher ω is, more pronounced the [Mg/Fe] decrease will be. As seen, our model with $\nu = 0.2 \text{ Gyr}^{-1}$ and with $\omega = 9$ is able to perfectly fit the observed [Mg/Fe] vs [Fe/H] abundances.

In panel (c) of Figure 4.1 we report the rates of different phenomena predicted by our simulations. It is possible to see how Type II SNe follow the SF history of the

²The flat plateau is due to the assumption that stars more massive than $20 M_{\odot}$ explode as hypernovae. If all stars explode as CC-SNe, a [Mg/Fe] trend increasing with decreasing [Fe/H] is obtained instead (see Romano et al., 2010, their Figure 12). We note that a flat trend fits the data much better.

TABLE 4.6: *Input parameters of the chemical evolution model for specific dSphs and UFDs. In the 1st column it is reported the name of the galaxy, in the 2nd column the infall mass, in the 3rd column the efficiency of star formation, in the 4th column the infall timescale, in the 5th column the wind parameter and in the last three columns the number, time and duration of the bursts of star formation, respectively. The first three galaxies are discussed at length in the main text, while results for the others are presented as Supplementary Material of Molero et al. (2021a) in the online version of the journal.*

Galaxy	$M_{\text{inf}} (M_{\odot})$	$\nu (\text{Gyr}^{-1})$	$\tau_{\text{inf}} (\text{Gyr})$	ω	n	$t (\text{Gyr})$	$d (\text{Gyr})$
Fornax (For)	5.0×10^8	0.1	3	1	1	0	14
Sculptor (Scl)	1.0×10^8	0.2	0.5	9	1	0	7
Reticulum II (RetII)	1.0×10^5	0.01	0.05	6	1	0	1
Bootes I (BootI)	1.1×10^7	0.005	0.05	12	1	0	1
Carina (Car)	5.0×10^8	0.15	0.5	5	4	1 – 3 – 8 – 10	2 – 2 – 2 – 2
Sagittarius (Sgr)	2.1×10^9	1	0.5	9	2	0 – 4.5	4 – 2.5
Sextan (Sex)	5.0×10^8	0.005	0.5	11	1	0	8
Ursa Minor (UMI)	5.0×10^8	0.05	0.5	11	1	0	3

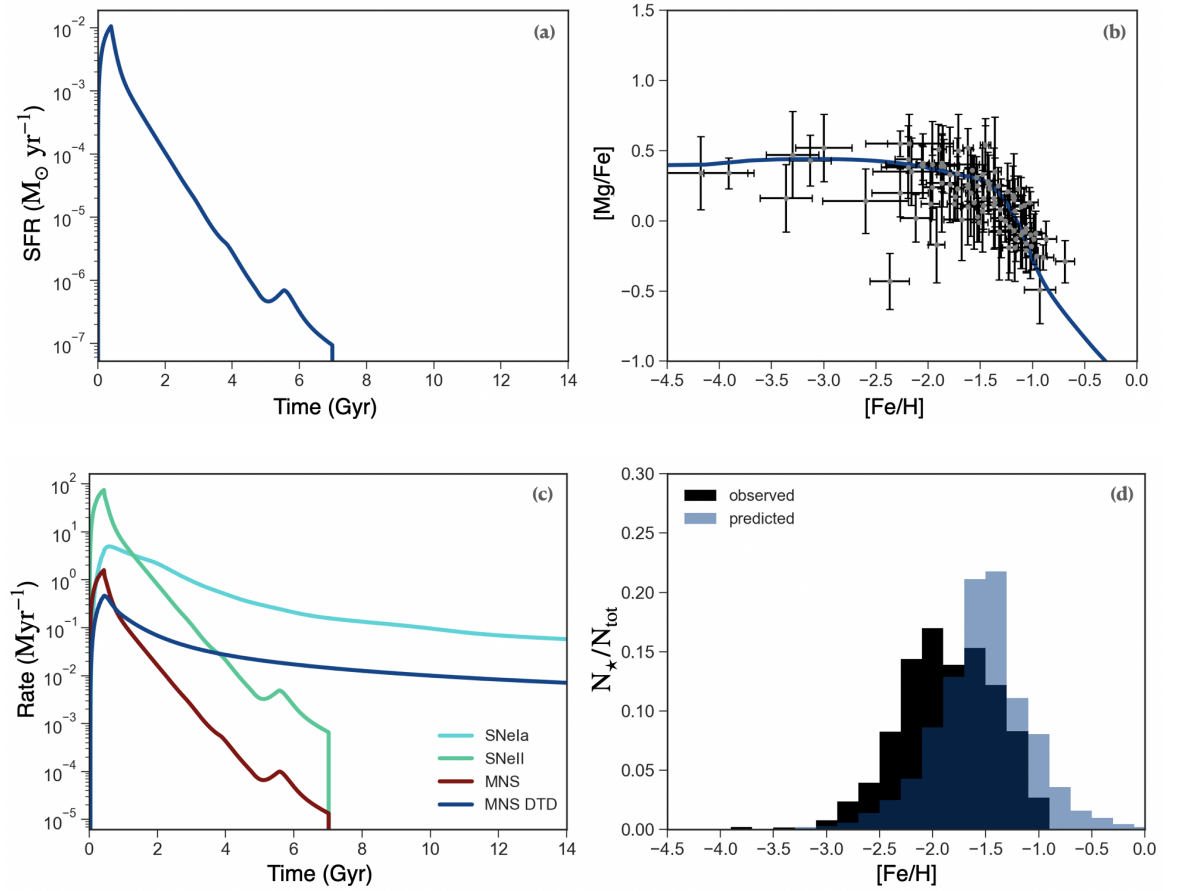


FIGURE 4.1: Results for Sculptor dSph. Panel (a): predicted SF history as a function of time; panel (b) predicted $[Mg/Fe]$ vs. $[Fe/H]$ pattern together with observational data; panel (c) predicted rates of Type Ia SNe (turquoise), Type II SNe (green), MNS with a constant delay time for merging (red) and MNS with a DTD (light blue); panel (d) comparison between predicted and observed MDF

simulated galaxy, while Type Ia SNe continue to explode even after the quenching of the SF. Rates of MNS are also reported in the panel, showing both constant delay time and DTD. In the case of a constant total delay time, the rate of MNS follows the evolution of the SFR of Sculptor, so that no MNS event is predicted at the present time. On the other hand, when we assume a DTD, the dependence of the MNS rate on the SFR is not so important (see Simonetti et al., 2019; Côté et al., 2019; Greggio et al., 2021 for an extensive discussion about the delay times of MNS in the Galaxy). In this case, the evolution of the MNS rate will be similar to that of Type Ia SNe and its present time value will differ from zero, being equal to $R_{\text{MNS}} \simeq 7$ events/Gyr.

In panel (d) of the same Figure, the observed MDF together with the prediction from our model is reported. There is a quite good agreement between model and the data, even if our results appear to be shifted towards higher metallicities. In order to predict a MDF peaked at lower metallicities one could lower the star formation efficiency. However, we point out that this may also lead to a higher

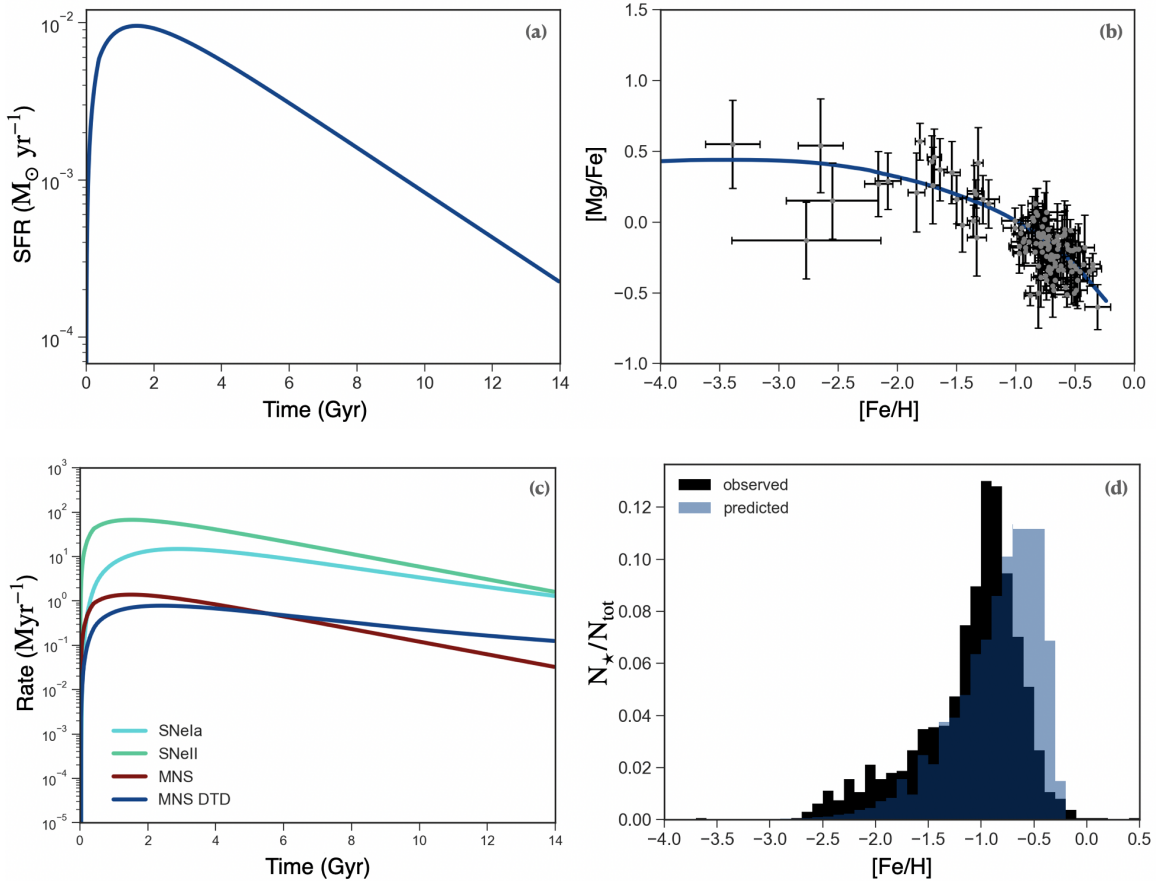


FIGURE 4.2: Same as Figure 4.1 but for Fornax.

MDF peak, as well as a shorter plateau in the $[\text{Mg}/\text{Fe}]$ abundances ratio. Therefore, in order not to lose the really good agreement for the $[\text{Mg}/\text{Fe}]$ evolution, we do not change our choice of the parameters.

Concerning the chemical evolution of Fornax, we assumed a dark matter halo of mass $M_{\text{DM}} = 5 \times 10^9 M_{\odot}$ and a core radius $R_{\text{DM}} = 15.5$ kpc. The effective radius of the luminous component has been set to $R_{\text{L}} = 1.55$ kpc. For the SF history, we take into consideration that of de Boer et al. (2012a), which is derived from the CMD fitting analysis, according to which Fornax formed stars at all ages, from as old as 14 Gyr to as young as 0.25 Gyr. In particular, they conclude that, even if stars are formed continuously during the evolution of the galaxy, most of the star formation takes place at intermediate ages (see also Coleman et al., 2008). We model a continuous SF, characterized by one long episode lasting 14 Gyr, with a constant efficiency equal to $\nu = 0.1 \text{ Gyr}^{-1}$. Our predicted star formation as a function of time is reported in panel (a) of Figure 4.2. It is seen that in our model a high number of stars formed in the first Gyr, and then the gas gets depleted due to the star formation itself and to the action of galactic winds causing a gas loss until the present time. Our model predicts a final stellar mass of $M_{\star, \text{f}} = 2.9 \times 10^7 M_{\odot}$, similar to the one estimated by de Boer et al., 2012a equal to $M_{\star, \text{f}} = 4.3 \times 10^7 M_{\odot}$.

Panels (b) and (d) of Figure 4.2 show that the results of our model are in agreement with both the observed $[\text{Mg}/\text{Fe}]$ vs. $[\text{Fe}/\text{H}]$ and the MDF. A better agreement

could have been obtained for the MDF by lowering the star formation efficiency in order to shift our MDF peak towards lower metallicities. However, as we already pointed out for Sculptor, that would also bring to a higher MDF peak and to a shorter plateau for the $[\text{Mg}/\text{Fe}]$ vs. $[\text{Fe}/\text{H}]$.

Finally, in panel (c) of the same Figure we report the evolution of the rates of different phenomena. The present time value of the rate of MNS will be different from zero both in the case in which we adopt a constant total delay time for merging and in the case in which we adopt a DTD, because of the long and continuous episode of SF. The rate of MNS in the two cases will be $R_{\text{MNS}} \simeq 33 \text{ events/Gyr}$ and $R_{\text{MNS}}^{\text{DTD}} \simeq 125 \text{ events/Gyr}$, respectively.

Results for Eu in Sculptor and Fornax

In Figures 4.3 and 4.4, we report the observed $[\text{Eu}/\text{Fe}]$ vs. $[\text{Fe}/\text{H}]$ abundance pattern together with predictions of our models for Sculptor and Fornax dSphs, respectively. We remind that details about different nucleosynthesis prescriptions implemented in the models are reported in Tables 4.4 and 4.5 of Section 4.4.1.

From the observational point of view, the evolution of the $[\text{Eu}/\text{Fe}]$ vs. $[\text{Fe}/\text{H}]$ shows the typical trend of Eu in the Galaxy, similar to that of an α -element. Especially in the case of Sculptor, we can easily distinguish the plateau at low to intermediate metallicities (from ~ -2.25 to ~ -1.25 dex) and the decrease at higher $[\text{Fe}/\text{H}]$. In the case of Fornax it is more difficult to distinguish such a trend. The data appear to be more concentrated in the high metallicity range of the $[\text{Eu}/\text{Fe}]$ - $[\text{Fe}/\text{H}]$ diagram, so that the results of our models in this range must be considered just a prediction. We decided not to add more data from other authors, in order not to lose the homogeneity of our sample. We do however note that additional high-resolution data containing Ba and Eu are limited. Moreover, from a theoretical point of view, a plateau at low metallicities in Fornax is expected to be present because of the time-delay model (Matteucci, 2012) which applies to any galaxy. As already discussed, in the early phases of galaxy evolution we expect a plateau in the $[\alpha/\text{Fe}]$ vs. $[\text{Fe}/\text{H}]$ due to the sole contribution of CC-SNe, independently of the SF history. The $[\text{Eu}/\text{Fe}]$ vs $[\text{Fe}/\text{H}]$ usually shows a pattern similar to those of the α -elements, so that a plateau at low metallicities also in the $[\text{Eu}/\text{Fe}]$ of Fornax is expected.

In panels (a) of both Figures 4.3 and 4.4, we report results of models C54, C65 and C76, in which we consider Eu production only by MNS with a constant delay time for merging. The model which best reproduces the expected trend is model C65. In this case, the yield of Eu from MNS is in the range $(3.0 \times 10^{-6} - 1.5 \times 10^{-5}) M_{\odot}$, with a lower limit which is in agreement with the one predicted by Matteucci et al. (2014) for the chemical evolution of the MW. On the other hand, models C54 and C76 seem to overestimate and underestimate the expected trend, respectively.

In panels (b) of the same Figures, we present results of models D54, D65 and D76 for which Eu is produced by only MNS with a DTD. Those models differ from the previous ones just by the adoption of the DTD. Because of the longer delay times assumed, there is an increasing trend rather than a plateau at low metallicities, as expected. Also, as discussed in the previous section, the adoption of a DTD causes NS continuing to merge until present time, so that the production of

Eu from MNS will not stop, even when there is no SF activity (see panel (c) of Figure 4.1). This results in producing a plateau or even an increasing trend at high metallicities for Sculptor and Fornax, respectively, rather than a decrease. Because of that, models D54, D65 and D76 are not able to reproduce the observed pattern, as seen from the Figures, in agreement with the findings of previous studies for the MW (e.g.: Simonetti et al., 2019; Côté et al., 2019). Moreover, models D54 and D76 overestimate and underestimate the general trend for all the range of metallicities, respectively.

In panels (c), we report the results from models with Eu produced only by MR-SNe. As already discussed, we try different yields of Eu proposed in literature. Among those, model N17c with yields from Nishimura et al. (2017) appears to be the best one for Sculptor, while model N15 with yields from Nishimura et al. (2015) better reproduce the [Eu/Fe] of Fornax. We remind that in both cases we assume that (1-2)% of all stars with mass in the range $(10 - 80) M_{\odot}$ would explode as MR-SNe. Furthermore, we stress that theoretical calculations of the r-process involve large uncertainties in the modelling (see e.g., Cowan et al., 2019; Horowitz et al., 2019 for recent reviews).

In panels (d) of the Figure, we show the effect of activating the MR-SNe channel only at metallicities lower than 10^{-3} , without changing the Eu yield with respect to models N17c and N15 for Sculptor and Fornax, respectively. Model N17cZ reproduces the plateau at low metallicities in the Sculptor dSph as well as the decrease at higher [Fe/H]. The decrease is actually faster than that produced by model N17c, but the data are also well reproduced. On the other hand, activating MR-SNe only at low metallicities in Fornax results in losing the agreement with observations, as expected. Actually, because of the concentration of data at high [Fe/H], it seems that only a highly implausible scenario in which MR-SNe are acting only at high metallicities can reproduce the expected trend, as represented by the light green curve of Figure 4.4. Therefore, if MR-SNe are the only producers of Eu in the Fornax dSph, they must be active at all metallicities.

In panels (e) of Figures 4.3 and 4.4, we show results of models CN54, CN65 and CN76, in which we assume Eu produced by both MNS with a constant total delay time for merging together with MR-SNe. Yields of Eu from MR-SNe are those of Nishimura et al. (2017), and the three models differ because of the different yields for MNS. Obviously, when more than one channel contribute to the Eu production, the Eu yields from each channel should be lower than in the case of only one active source, in order to maintain the fit.

Finally, in panels (f), we show results of models DN65 and DN65Z in which both MNS with a DTD and MR-SNe can produce Eu. For both models the yield of Eu from MNS is in the $(3.0 \times 10^{-6} - 1.5 \times 10^{-5}) M_{\odot}$ range, while that of MR-SNe is equal the one of Nishimura et al. (2017). The two models differ only for the range of metallicities in which MR-SNe are active: in model DN65 they act for the whole range, while in model DN65Z they act only at low metallicities. Both models seems to be able to reproduce the main trend. In particular, the lack of Eu from MNS at low metallicities, due to longer delay times for merging, is compensated by the production of Eu from MR-SNe which, in both models, are active at low metallicities. In the same way, when in model DN65Z MR-SNe stop to produce Eu from metallicities higher than 10^{-3} , MNS can compensate. For model DN65

we get Eu from both MNS and MR-SNe also at high metallicities, resulting in a slightly higher trend with respect to model DN65Z which, in the case of Fornax, is more in agreement with the data.

Results for Ba in Sculptor and Fornax

In Figures 4.5 and 4.6, we report predictions for the [Ba/Fe] and [Ba/Eu] vs. [Fe/H] patterns together with the observational data.

The observed [Ba/Fe] vs. [Fe/H], is characterized by a low abundance of Ba at low metallicities ($[\text{Fe}/\text{H}] \leq -2.25$ dex) and by almost solar values from intermediate to high metallicities, suggesting different mechanisms for the production of the s- and r- process fractions of Ba. In fact, at low metallicities Ba is mostly created by r-process, but as more LIMS go through the AGB phase, the s-process becomes more important and the [Ba/Fe] ratio increases with increasing [Fe/H] until a plateau is reached (see also Skúladóttir et al., 2020b). For the [Ba/Eu] vs. [Fe/H], the data are characterized by a plateau at lower metallicities, followed by an increase of the [Ba/Eu] at higher [Fe/H]. The plateau is indicative of the fact that the Ba and Eu elements are growing at the same rate at low metallicities as a function of Fe. This does not necessarily mean that the two elements are produced by the same events, but they must be produced at least with the same time delay (Reichert et al., 2020). On the other hand, the increasing trend of the [Ba/Eu] at higher metallicities sets in when the production of s-process Ba from LIMS starts to be non negligible. We remind that for all of our simulations, we fixed the yields of Ba from the s-process and varied only the contribution from the r-process.

In panels (a) and (b) of Figures 4.5 and 4.6, we show results of models C65 and D65 in which we adopt MNS as the only producers of r-process Ba with and without a DTD, respectively. In both cases yields of r-process Ba are in the $(3.20 \times 10^{-5} - 1.58 \times 10^{-4}) M_{\odot}$ range while those of Eu are in the $(3.0 \times 10^{-6} - 1.5 \times 10^{-5}) M_{\odot}$ range. For the [Ba/Fe] (panels (a)), in the case of a constant delay time for merging models are able to fit the data from intermediate to high metallicities, but fails at lower ones. On the other hand, if we adopt a DTD for MNS the agreement at low metallicities is improved, but the data are underestimated at intermediate ones ($-2.6 \leq [\text{Fe}/\text{H}] \leq -1.5$), suggesting that a second source should be active. For the [Ba/Eu], both our models are able to reproduce the plateau in the data, thanks to the same delay assumed for the production of Eu and r-process Ba, as well as the increase when the production of s-process Ba from LIMS sets in.

In panels (c) and (d) of the same Figures, we report results of model N17c in which we assume r-process Ba and Eu produced only by MR-SNe with yields from Nishimura et al. (2017). Also models in which we adopt yields of Cescutti et al. (2006) for the r-process production by massive stars are shown. For the [Ba/Fe], both models fit the data at high metallicities, but fail at lower ones overproducing the data. In particular, model N17c produces almost a plateau rather than an increasing trend at low [Fe/H], because of the production of r-process Ba from stars with initial masses in a too wide range ($10 - 80 M_{\odot}$). If a more narrow range and, in particular, decreasing amount of r-process material with increasing stellar mass, are assumed, as in the case of models with the yields of Cescutti et al. (2006), we can predict a more intense increase, even though it sets in too early

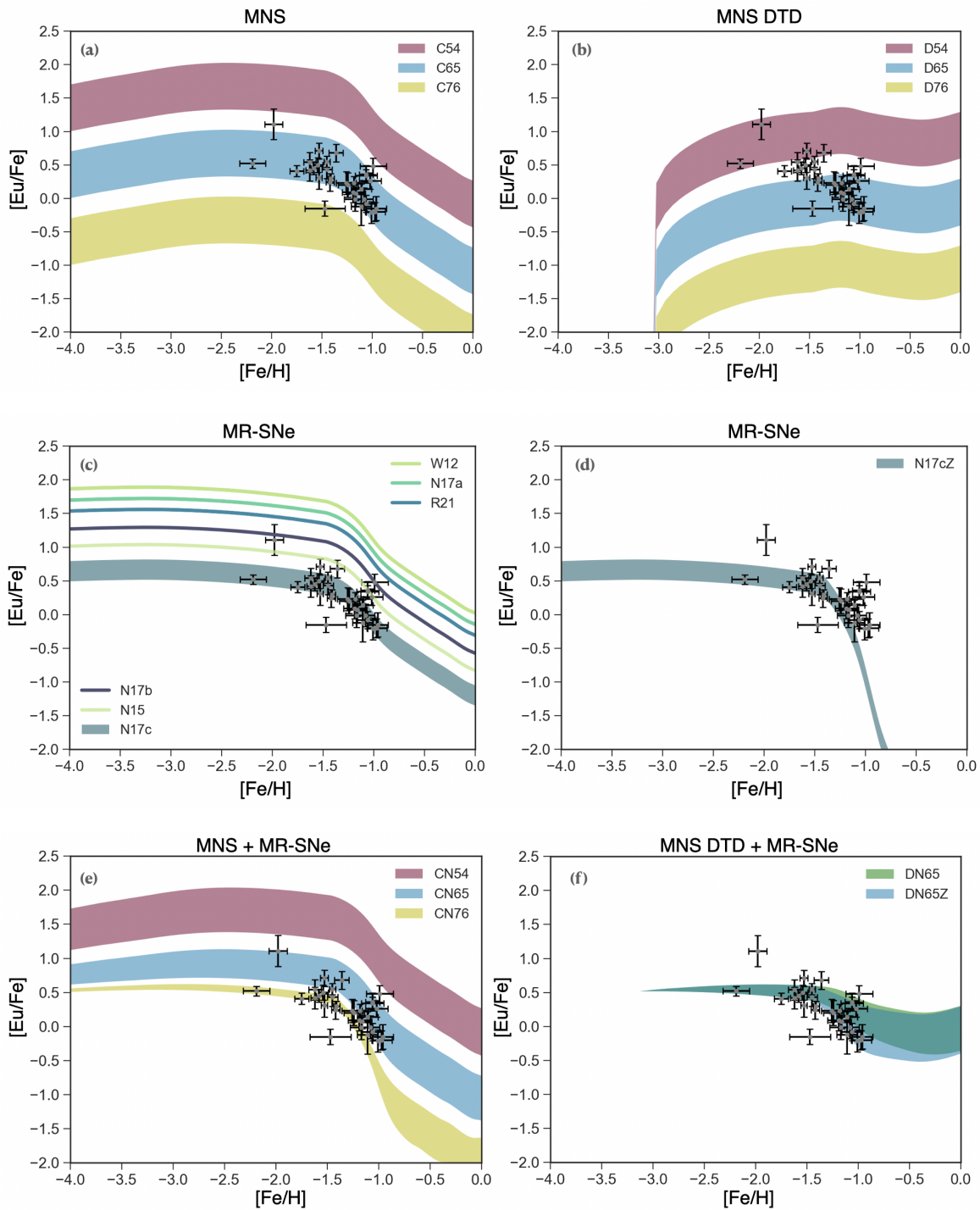


FIGURE 4.3: Results of models with different nucleosynthesis prescriptions for the $[Eu/Fe]$ vs. $[Fe/H]$ pattern for Sculptor dSph. Details of models are in Tables 4.4 and 4.5.

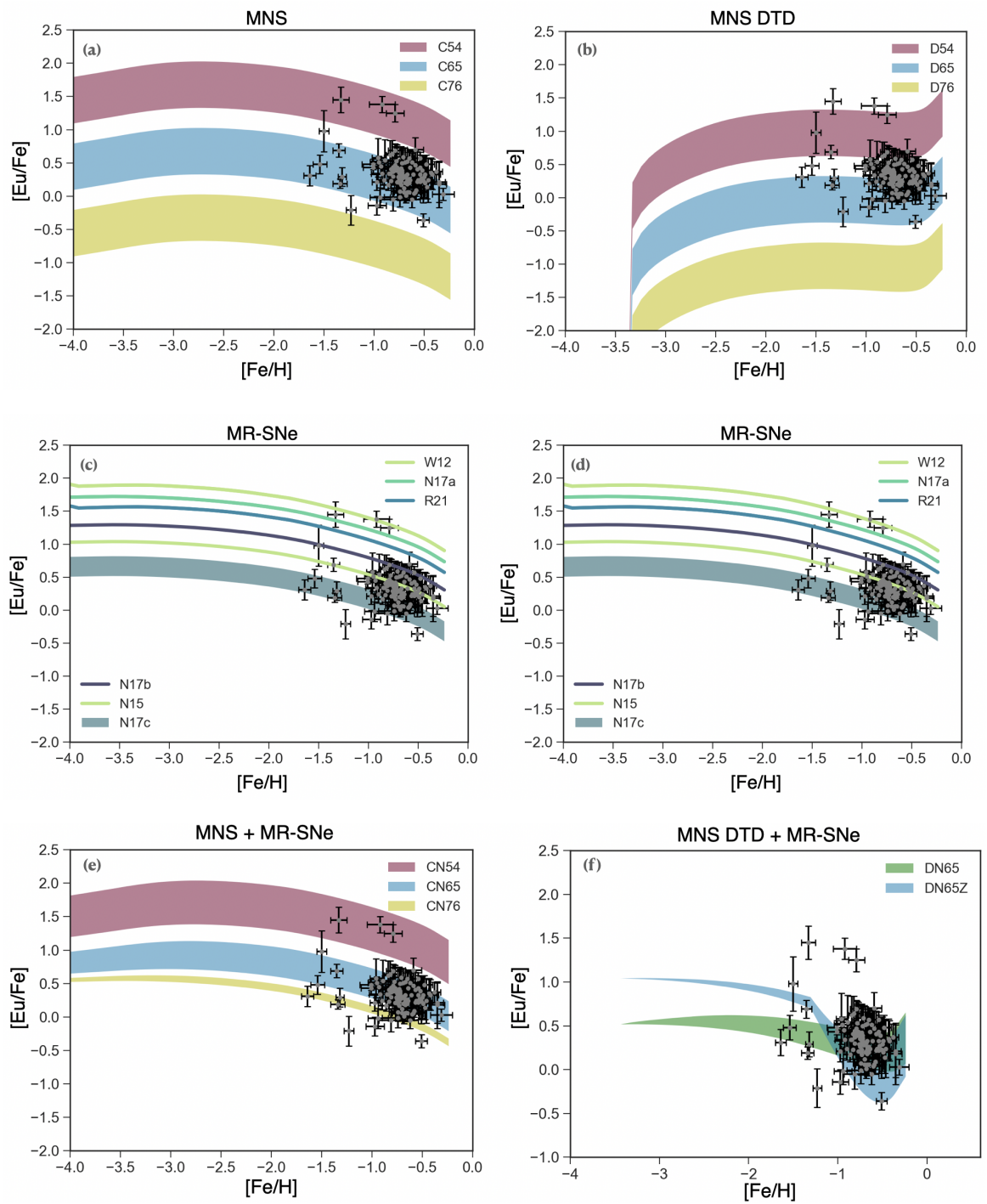


FIGURE 4.4: Same as Figure 4.3 but for Fornax. Note that in panel (d) the light green curve refers to the case in which the MR-SNe are producing r-process material only for metallicities higher than 10^{-3} . See text for details.

with respect to the data. In the case of the [Ba/Eu], models N17c can reproduce the expected trend for all the range of metallicities for Sculptor, but underestimate the data in the case of Fornax. On the other hand, if the yields of Cescutti et al. (2006) are adopted, the models overestimate the expected abundance trends in both galaxies. However, the general pattern is reproduced in all cases, since Eu and r-process Ba are produced by the same event and therefore with the same delay.

Finally, in panels (e) and (f), we show results of models CN65 and DN65 in which r-process Ba and Eu are produced by both MR-SNe and MNS. In model CN65 we assume a short and constant delay time for MNS, while in model DN65 a DTD is adopted. As expected, both models are not able to reproduce the low data of [Ba/Fe] at low metallicities. For both models, in fact, the production of r-process Ba sets in too early and a too high trend is produced at low [Fe/H]. The models are able to reproduce only the [Ba/Eu], producing the expected plateau at low metallicities and the increase at larger [Fe/H] thanks to the production of s-process Ba by LIMS. The plateau is reproduced not only because of the same delay assumed for the production of the two elements in the case of model CN65, but also because of the similar r-process Ba/Eu yields between MR-SNe and MNS.

4.5.2 Reticulum II

For the chemical evolution of Reticulum II UFD, we assume a dark matter halo of mass $M_{\text{DM}} = 3.0 \times 10^6 \text{ } \mathit{M}_{\odot}$ and a core radius $R_{\text{DM}} = 170 \text{ pc}$. The effective radius of the luminous component of the galaxy has been set at $R_{\text{L}} = 50 \text{ pc}$. We predict a present time stellar mass of $M_{\star, \text{f}} = 0.6 \times 10^3 \text{ } \mathit{M}_{\odot}$, similar to the one observed by Bechtol et al. (2015) equal to $M_{\star, \text{f}} = 2.6 \times 10^3 \text{ } \mathit{M}_{\odot}$.

In panel (a) of Figure 4.7, we show our assumed SFR as a function of time. It consists of one short episode of SF which lasts 1 Gyr.

In panel (b) of the same Figure, we report the [Mg/Fe] vs. [Fe/H] together with the prediction of our model. Because of the poor dataset, it is not possible to derive strong conclusions on the observed trend. Therefore, we model the [Mg/Fe] in order to reproduce the typical evolution of an α -element, characterized by a plateau at low metallicities and by a decrease which set in when Type Ia SNe start contributing in a substantial way to the Fe enrichment.

In panel (c) of Figure 4.7, we report the rates of different phenomena. Also in this case, it is seen that the rate of MNS follows the evolution of the star formation only in the case of a constant delay time for merging, leading to a predicted present time rate of MNS equal to zero. In the case of DTD, instead, the present time rate of MNS will be equal to $R_{\text{MNS}} \simeq 5 \times 10^{-4} \text{ events/Gyr}$.

Finally, in panel (d) we report the observed MDF together with the prediction from our model. Because of the low number of stars observed in Reticulum II, it is very difficult to assess the quality of the fit. The observational sample is likely incomplete. Therefore, our theoretical MDF has to be regarded as a prediction, to be confirmed (or disproved) by future observations, rather than a fit to the existing data.

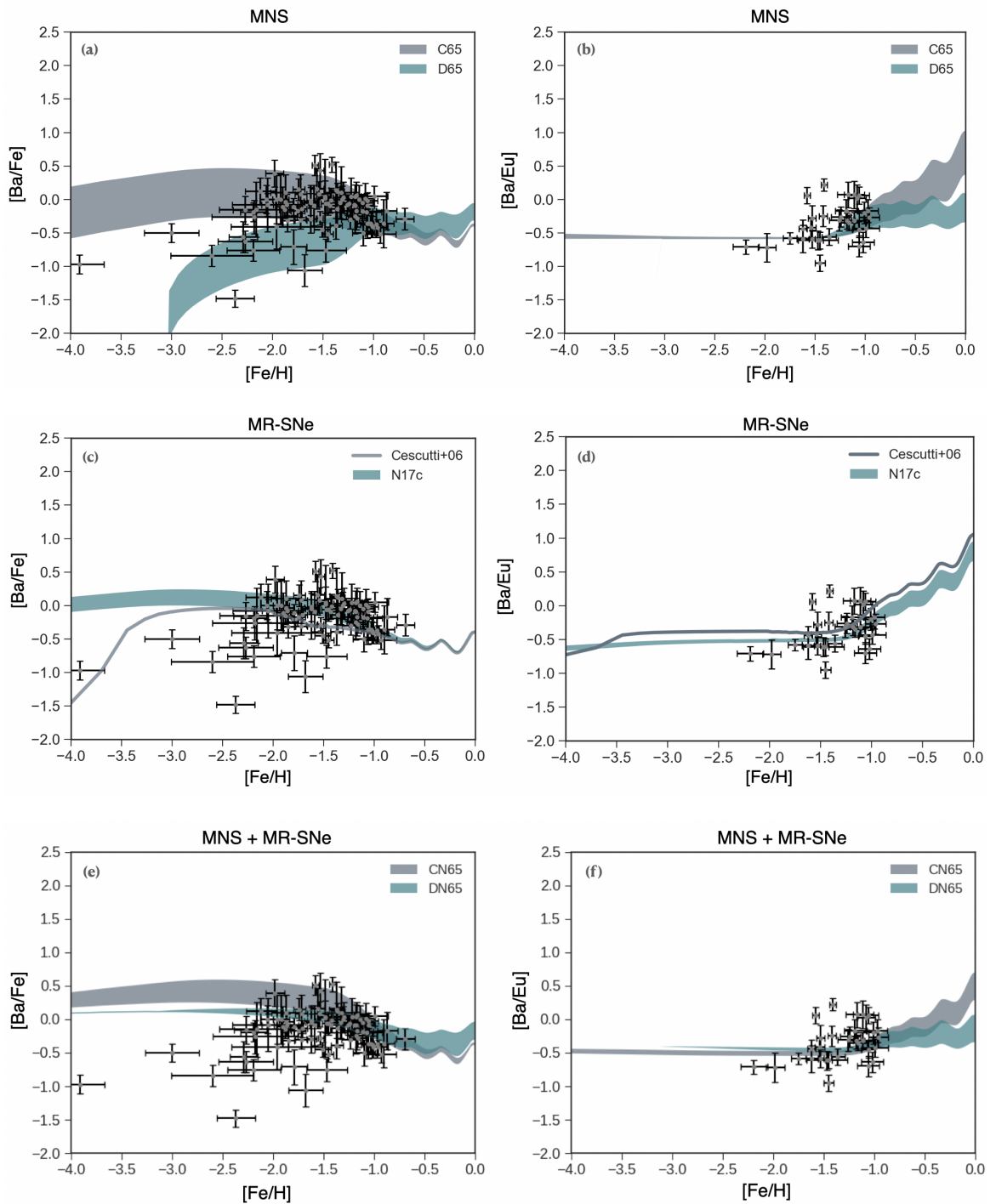


FIGURE 4.5: Results of models for the evolution of $[Ba/Fe]$ and $[Ba/Eu]$ vs. $[Fe/H]$ for Sculptor dSph. For all models s-process Ba production comes from LIMS. Details of models are in Tables 4.4 and 4.5.

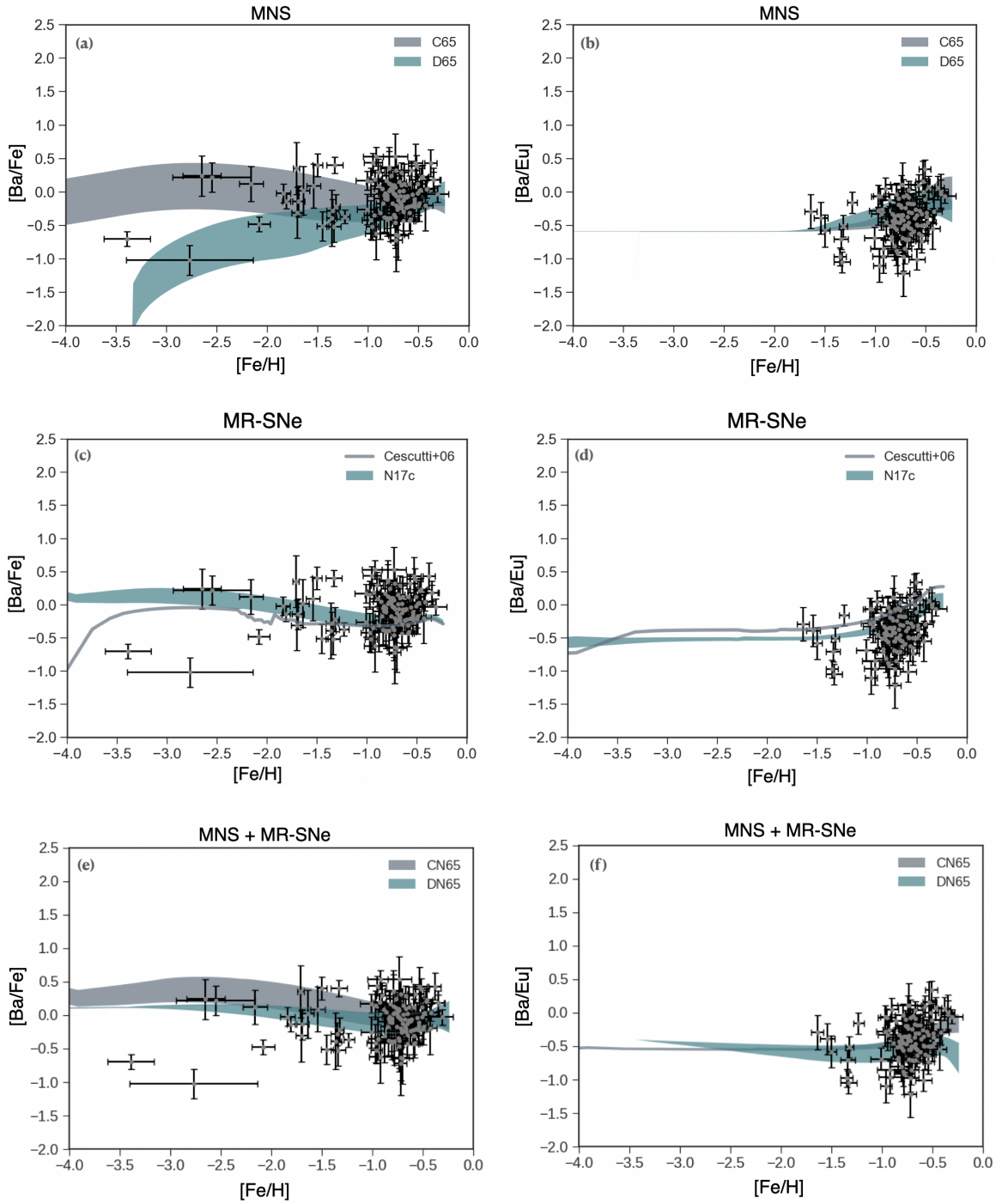


FIGURE 4.6: Same as Figure 4.5 but for Fornax.

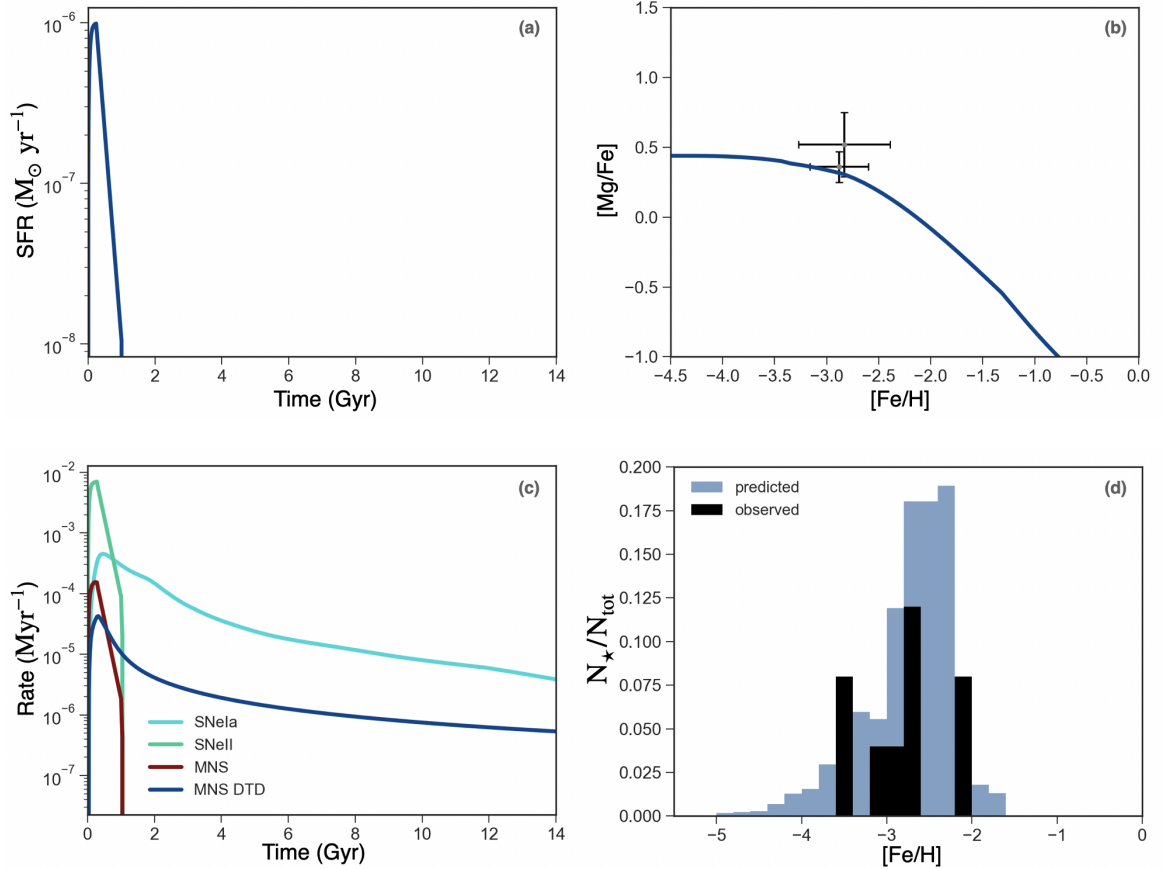


FIGURE 4.7: Same as Figures 4.1 and 4.2 but for Reticulum II.

Results for Eu in Reticulum II

In Figure 4.8 we report our results together with the observational data for the [Eu/Fe] vs. [Fe/H] in the Reticulum II UFD.

Concerning the observational data, Reticulum II stands out among all the other galaxies because of its peculiar Eu and Ba abundances. The data are concentrated at low metallicities and also show strong enhancements, which is about 2 orders of magnitude higher than what is observed in the other dwarf galaxies.

In panel (a), we report results of models in which MNS are the only Eu producers and their delay time for merging is assumed to be short and constant. In this case model C54, in which the yield of Eu from MNS is in the $(3.0 \times 10^{-5} - 1.5 \times 10^{-4}) M_{\odot}$ range, well reproduce the high [Eu/Fe] abundance ratio. On the other hand, when we hypothesize a DTD for MNS (panel (b) of the same Figure), we are no more able to reproduce the observational constraints because of the longer delay assumed for merging.

In the case in which we assume that Eu is produced only by MR-SNe, models R21 and W12 are able to reproduce the observed [Eu/Fe] both in the case in which MR-SNe are active at all metallicities (panel (c)) and in the case in which they are active only at the low end (panel (d)). Actually, because of the really short SF assumed for Reticulum II, there are small differences between these two cases. For these two models the yield of Eu from MR-SNe has been set equal to that

predicted by Reichert et al. (2021) for model R21 and by Winteler et al. (2012) for model W12. In panel (c) we report also model N17c for which the yield of Eu is equal to that of Nishimura et al. (2017), showing how high the yield of Eu is required to be to fit the data in Reticulum II with respect to the other galaxies.

In panel (e) of the same Figure, we report results of models in which Eu is produced by both MNS (with no DTD) and MR-SNe. The yield of Eu from MR-SNe has been set equal to that of model R21. As expected model CR54, is the one which best reproduce the data. However, models CR65 and CR76 are only slightly below the observations, showing once again that if a second channel other than MNS is activated then the yield of Eu from MNS can be lower in order to fit the data.

In panel (f) of Figure 4.8, we report results of models in which both MNS (with a DTD) and MR-SNe are producing Eu. In particular, we assumed that MR-SNe are acting for all metallicities, but we note that we would have obtained basically the same results even if MR-SNe would have been activated only at low metallicities. The yield of Eu from MNS is equal to $(3.0 \times 10^{-5} - 1.5 \times 10^{-4}) M_{\odot}$ and that from MR-SNe is that of model R21, equal to $5.19 \times 10^{-6} M_{\odot}$ for each event. Because of the contribution from MR-SNe we are now able to fit the data at low metallicities despite the longer delay assumed for MNS. An even better agreement would have been obtained if we adopted even higher yield of Eu from MR-SNe (for example those of model W12). However one should note that, because of the lack of data at high metallicities, it is impossible to distinguish which is the best model between CR54 and DR54, since they differ only in the absence/presence of a DTD for MNS.

Results for Ba in Reticulum II

In Figure 4.9, we report predictions for the $[Ba/Fe]$ and $[Ba/Eu]$ vs. $[Fe/H]$ together with the observational data. We remind that for all models the production of the s-process fraction of Ba comes from LIMS and the adopted yields are those of Busso et al. (2001), as for the other dwarfs.

In panels (a) and (b), we show results of models C54 and D54 in which we adopt MNS as the only producers of the r-process Ba and Eu with and without a DTD, respectively. For both models, we chose higher yields of r-process Ba from MNS with respect to those adopted for the other galaxies, fixing them in the $(3.20 \times 10^{-4} - 1.58 \times 10^{-3}) M_{\odot}$ range. Yields of Eu from MNS are in the $(3.0 \times 10^{-5} - 1.5 \times 10^{-4}) M_{\odot}$ range. As seen from the $[Ba/Fe]$, model C54 is able to fit the data at low metallicities. Then it predicts a constantly decreasing trend, as expected. On the other hand, model D54 is not able to fit the data, because of the delay in the production of r-process Ba. For the $[Ba/Eu]$ vs. $[Fe/H]$, since we are assuming that both Eu and r-process Ba are produced by the same event (and therefore on the same timescale), the two models are both producing the expected plateau at low metallicities and are able to fit the observed data. Then, model C54 predicts an increasing pattern towards high metallicities, because of the s-process Ba production from LIMS. On the other hand, model D54 in which we have a DTD for MNS, predicts a constant plateau for all the range of metallicities. This is due to the fact that, because of the high yields of r-process Ba and of the delay in its production by MNS, the contribution to Ba from LIMS at high

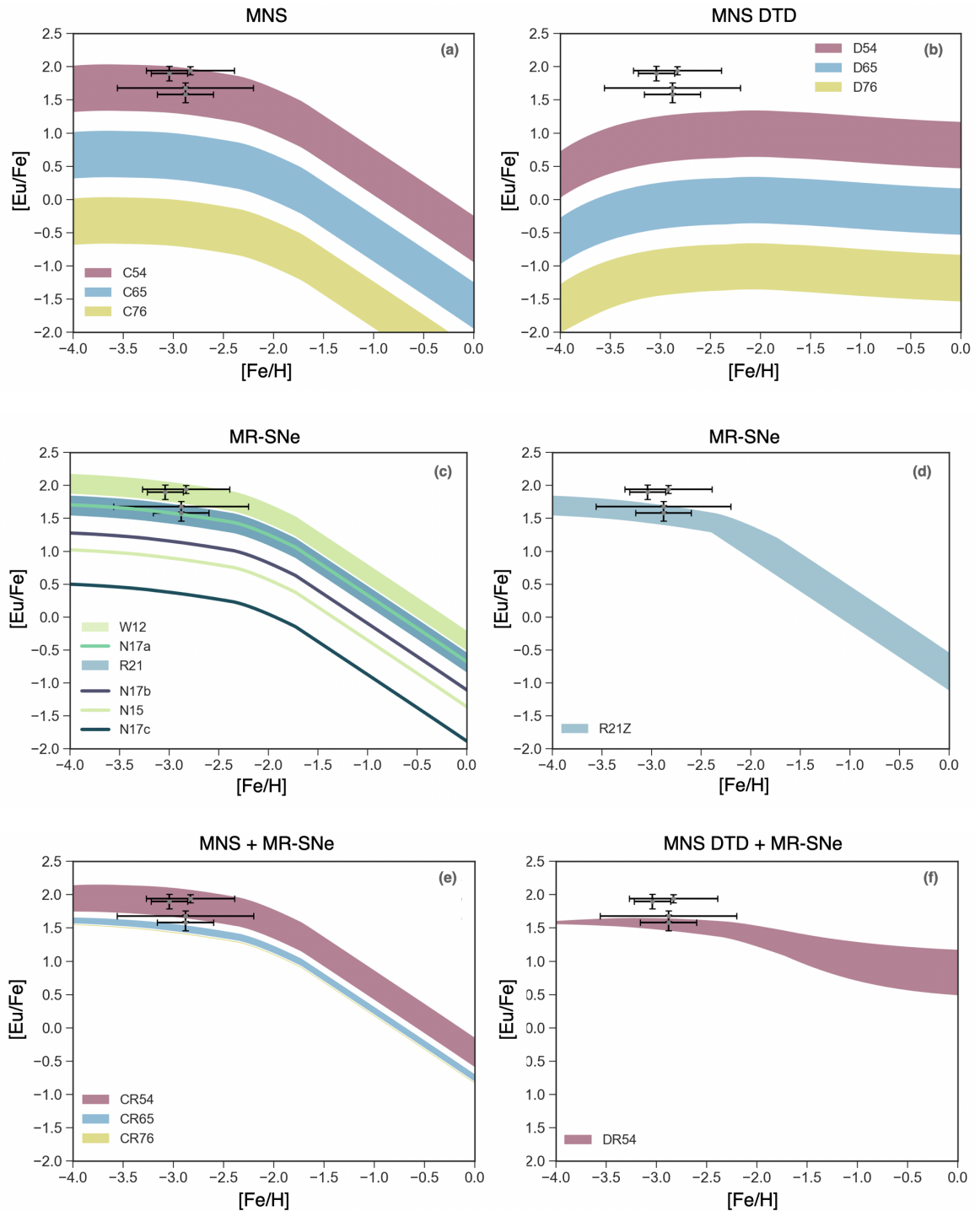


FIGURE 4.8: Same as Figures 4.3 and 4.4, but for Reticulum II.

metallicity appears to be negligible. This happens only when we adopt a DTD, because in this case the contribution to the Ba production from MNS is stronger at high metallicities (see also panel (a) of the same Figure) with respect to the case in which we adopt a constant delay time for merging. This is the case, even though we adopt the same r-process yields for Ba and Eu in both models. We note that we cannot comment on the nature of Ba and Eu in Reticulum II at higher metallicities owing to the lacking observational data.

In panels (c) and (d) of the same Figure, we report results of model N17c in which we assume r-process Ba and Eu produced only by MR-SNe with yields from Nishimura et al. (2017). Also the case in which we adopt yields of Cescutti et al. (2006) for the production of both elements is shown. It clearly appears that, both models are not able to fit the high abundances of the [Ba/Fe], underproducing Ba by more than one order of magnitude. We tested also models W12, N12a and R21 for the [Ba/Fe], since they matched the [Eu/Fe] described in the previous sections. However, all of them overproduce the observed Ba abundances. In the case of the [Ba/Eu] vs [Fe/H], the two models produce a similar trend, but none of them is able to fit the observed data, underproducing or overproducing the expected abundances, respectively.

In panels (e) and (f), we show results of models DN54 and CN54 in which r-process elements are produced by both MR-SNe and MNS (with and without a DTD, respectively). Yields for MR-SNe are those of Nishimura et al. (2017) and yields for MNS are in the $(3.20 \times 10^{-4} - 1.58 \times 10^{-3}) M_{\odot}$ range. For the [Ba/Fe], model CN54 in which two fast sources are producing r-process elements are able to fit the high observed abundances, while model DN54 in which also a delayed source is active underproduces the data. For [Ba/Eu], model CN54 can produce the expected plateau at low metallicities and the increasing pattern at higher [Fe/H], because the production of Eu and r-process Ba happens on the same timescales. On the other hand, model DN54 produces almost a constant plateau both at low metallicities, because of the similar r-process Ba/Eu yields between MR-SNe and MNS, and at higher ones because of the same reasons explained for model D54 (panel (b) of the same Figure).

A single r-process event

The generally accepted explanation for the high r-process abundances observed in Reticulum II is that a single nucleosynthetic event produced a large quantity of r-process material ($\sim 10^{-4.5} M_{\odot}$ of Eu according to Ji et al., 2016). As we showed in the previous sections, the amount of r-process material produced in our model by MNS should be in the $(10^{-5} - 10^{-4}) M_{\odot}$ range for Eu, in agreement with Ji et al. (2016) estimation, and in the $(10^{-4} - 10^{-3}) M_{\odot}$ range for Ba.

However, these yields are 1-2 order of magnitude higher than those estimated for the other galaxies. The reason why we need high r-process yields in our model is that we are actually working with a fraction of one enrichment event. During the first Gyr of SE, in fact, we have a total of 2.39×10^{-2} events of MNS when a DTD is adopted and of 5.65×10^{-2} events in the case of a constant delay.

Therefore, we performed a test in which we increased the value of the α_{MNS} parameter to 1 in order to artificially obtain a total of 1 event of MNS in the first Gyr. A probability of 100% of having a MNS event is a strong condition, but it

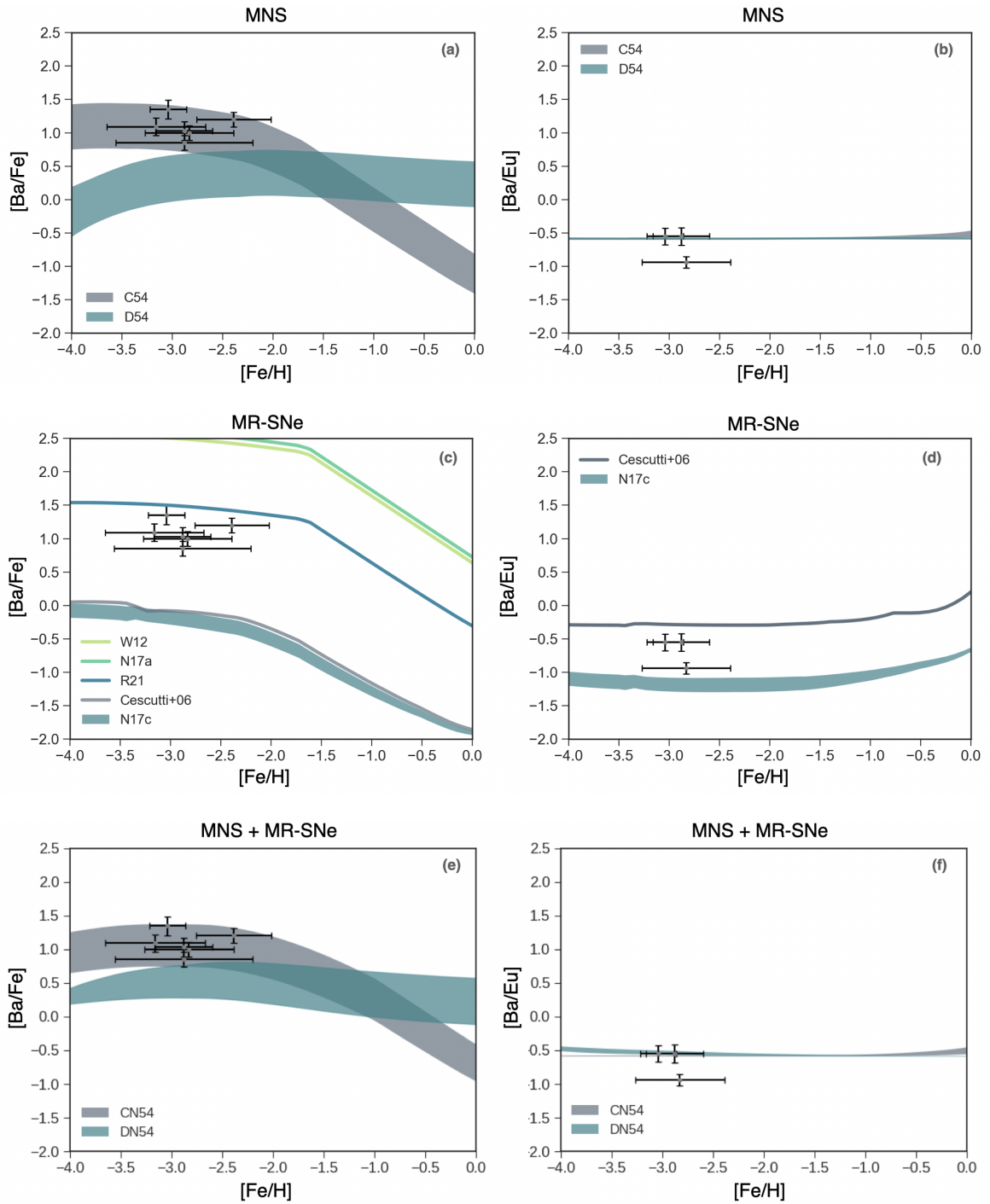


FIGURE 4.9: Same as Figures 4.5 and 4.6 but for Reticulum II.

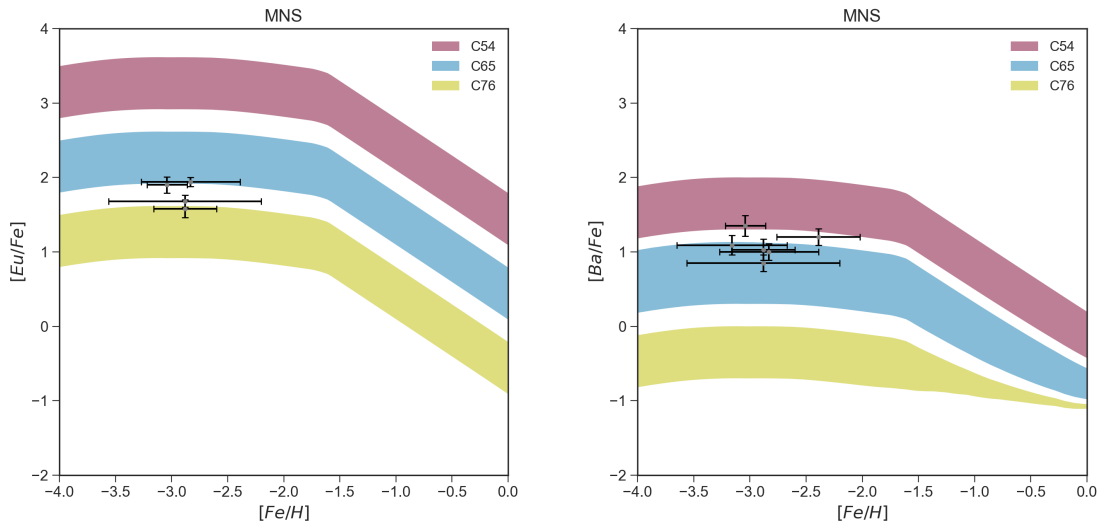


FIGURE 4.10: Results of models C54, C65 and C76 for Reticulum II for $[Eu/Fe]$ and $[Ba/Fe]$ vs $[Fe/H]$ in the case of 1 event of MNS in the first Gyr.

is justified by the low stellar mass content of Reticulum II. We then computed the $[Eu/Fe]$ and the $[Ba/Fe]$ vs. $[Fe/H]$ abundances for the three sets of yields reported in Table 4.1. The results are shown in Figure 4.10. As one can see, the observational data can now be reproduced by models which assume more reasonable r-process yields, similar to those of the other dwarfs. The yields can be in the $(1.50 - 3.00) \times 10^{-6} M_{\odot}$ range for Eu and around $1.50 \times 10^{-5} M_{\odot}$ for Ba, at least one order of magnitude lower than those estimated by Ji et al. (2016).

4.6 Conclusions

We modelled the chemical evolution of seven dSph and two UFD galaxies in order to study the evolution of their Eu and Ba abundances. In the main text of the present work, we focused on the results obtained for Sculptor and Fornax, which can be taken as representative of those obtained for the others dSphs. Reticulum II UFD was shown for its peculiar elemental abundances. The results for the other galaxies are provided as Supplementary Material and available online only. We adopted new nucleosynthesis prescriptions for the production of Eu and the r-process Ba produced in MNS, scaled to the yields of Sr measured in the spectra of the kilonova AT2017gfo (Watson et al., 2019). We also tested different nucleosynthesis prescriptions for MR-SNe r-process elements. Here, we summarize our main results and conclusions:

-For both Sculptor and Fornax we can conclude that:

- Models in which r-process elements are produced only by a unique quick

source, such as MNS with a constant and short delay for merging or MR-SNe, are able to reproduce the [Eu/Fe] vs. [Fe/H] abundance pattern. However, those models fail in reproducing the low-metallicity data for [Ba/Fe] vs. [Fe/H] trend;

- On the contrary, models in which r-process elements are produced only with longer delays, namely by MNS with a DTD, have difficulties in reproducing the [Eu/Fe] vs. [Fe/H], but succeed in reproducing the low-metallicity data for [Ba/Fe] vs. [Fe/H];
- If both a quick source and a delayed one are adopted for the production of r-process elements, the [Eu/Fe] vs. [Fe/H] is successfully reproduced. In particular, the quick source can be represented by MR-SNe and the delayed one by MNS with a DTD. However, those models still fail in reproducing the low-metallicity data for [Ba/Fe] vs. [Fe/H].

It is reasonable to presume that a possible scenario is one in which NS merge with a DTD and produce Eu together with MR-SNe. In this case, MR-SNe can produce Eu at all metallicities or only at low ones, without making any significant difference in the final results. This allows us to reproduce the [Eu/Fe] vs. [Fe/H] abundances, in agreement with what has been proposed by several authors (e.g.: Simonetti et al., 2019; Côté et al., 2019; Skúladóttir et al., 2020a; Molero et al., 2021b). In particular, the amount of Eu produced by each MNS event would be in the $(3.0 \times 10^{-6} - 1.5 \times 10^{-5}) M_{\odot}$ range, while that produced by MR-SNe would be in the range of the theoretical calculations of Nishimura et al. (2017) and equal to $4.69 \times 10^{-7} M_{\odot}$. Here we assume that only 1-2% of all stars with initial mass in the range $(10 - 80) M_{\odot}$ would explode as MR-SNe (according also to Woosley et al., 2006b). However, within this scenario the low metallicity data of [Ba/Fe] vs. [Fe/H] cannot be reproduced. The only way to reproduce them is if only MNS (with DTD) are producing the r-process fraction of Ba, with yields in the $(3.20 \times 10^{-5} - 1.58 \times 10^{-4}) M_{\odot}$ range. If also MR-SNe participate to this process, the agreement with the data is lost. Nevertheless, excluding MR-SNe from the production of Ba cannot be physical motivated. Moreover, models in which r-process Ba is produced only by MNS with a DTD, still underestimate the [Ba/Fe] at intermediate metallicities, suggesting that a source for the production of the "weak" s-process fraction must be included. In particular, this second source for the production of s-process elements could be rotating massive stars, which have already been included in several studies to successfully explain the evolution of neutron capture elements. In particular, Cescutti et al. (2013), Cescutti et al. (2014a), and Cescutti et al. (2015) and more recently Rizzuti et al. (2021), showed that including the s-process from rotating massive stars in chemical evolution models is fundamental in order to explain the heavy element enrichment, in particular of Sr and Ba.

-For Reticulum II we conclude that:

- A quick source for the r-process production of both Eu and r-process Ba is needed in order to reproduce both the [Eu/Fe] and [Ba/Fe] vs. [Fe/H] trend.

This quick source can be represented either by NS with a constant and short delay time for merging or by MR-SNe. However, the yields must be 1-2 order of magnitude higher than those estimated for the other galaxies.

- If only one quick event of MNS is assumed to happen, a more realistic r-process yield can be adopted in order to reproduce both the [Eu/Fe] and [Ba/Fe] vs. [Fe/H]. However, in this case the probability of having a MNS event must be 100%.

Therefore, our conclusions for Reticulum II are different from those for the other galaxies, because of the peculiar r-/s-process elements pattern which characterizes this galaxy.

Actually, a way to reproduce the high abundances observed is to adopt higher yields of Eu and r-process Ba. Moreover, for this galaxy we are inclined to discard models which adopt a DTD for MNS because of their inability to fit the [Ba/Fe] at low metallicities. Therefore, a scenario which well reproduces the Eu and Ba evolution in Reticulum II is the one in which a quick source pollutes the ISM really fast and with large amount of r-process elements. This source can be represented either by MR-SNe or by NS which merge in a very short time, contrary to what happens in other galaxies. In particular, the quantity of r-process material produced should be in the $(10^{-5} - 10^{-4}) M_{\odot}$ range for Eu (in agreement with previous estimate of $\sim 10^{-4.5} M_{\odot}$ by Ji et al., 2016).

However, the assumption that the same nucleosynthesis events produce different total amounts of r-process material in different environments needs further discussion. As also analysed by Simon (2019), the only way the same mechanism which enriched Reticulum II could account for lower r-process abundances in other dwarfs is if the gas masses of those systems were much larger than in Reticulum II or if the retention fraction of r-process ejecta were much lower. However, analytical calculations (e.g., Safarzadeh et al., 2017; Beniamini et al., 2018; Safarzadeh et al., 2019; Tarumi et al., 2020) excluded these possibilities. At the moment, the most common accepted theory is that a single nucleosynthetic event polluted the galaxy at early times with copious amount of r-process material. We therefore computed a test in which the rate of MNS was forced to be equal to 1 in the first Gyr of SF. This allowed us to adopt realistic r-process yields, similar to those obtained for other dwarfs/UFDs. In order to obtain such a rate of MNS we had to set $\alpha_{\text{MNS}} = 1$, namely we had to assume a probability of 100% of having a MNS event. This is a strong assumption, which can be justified by the low stellar mass content of Reticulum II. However, in our opinion, the peculiar trend in Reticulum II needs to be further investigated. In particular, it could also be explained by a poor mixing of metals into the galaxy gas (see Emerick et al., 2020; Tarumi et al., 2020) and/or by a low Fe content due to the small number of SN. If this is the case, it would be difficult to prove it in the framework of a homogeneous model so that stochastic chemical evolution simulations, which take inhomogeneous mixing into account, would be required (e.g., Cescutti et al., 2015).

CHAPTER 5

Milky Way - The Disc

IN this Chapter, I present our study on the origin of neutron capture elements in the Galactic disc in which we analyze both their abundance patterns and radial gradients. We adopt a delayed two-infall chemical evolution model for the MW and tested the most up to date nucleosynthesis and timescales prescriptions for the production of neutron capture elements, extending our investigation to 9 different chemical species. Our predictions are compared with data of both open clusters and field stars from the sixth data release of the *Gaia*-ESO survey.

The Chapter is organized as follows. In Section 5.1, I introduce the context of this Chapter. In Section 5.2, I describe the *Gaia*-ESO sample. In Sections 5.3 and 5.4, I present the details of the chemical evolution models. In Section 5.5, I show our results first for the $[E/Fe]$ vs. $[Fe/H]$ abundance patterns and then for the radial gradients of both $[Fe/H]$ and the neutron capture elements. Finally, in Section 5.6, I draw our summary and conclusions.

The results presented in this Chapter are described in the published paper Molero et al. (2023b).

5.1 Introduction

As described throughout this Thesis, the majority of elements beyond the Fe peak are produced by r- and s-processes. Understanding which are the astrophysical sites of these two processes has become one of the major challenges in stellar physics and chemical evolution. While it is now recognised that the s-process comes from rotating massive stars and AGB stars, the r-process sites are still under debate. A large number of works (e.g., Wehmeyer et al., 2015; Cescutti et al., 2015; Côté et al., 2019; Simonetti et al., 2019; Kobayashi et al., 2020; Cavallo et al., 2021; Molero et al., 2021b) point towards a scenario in which both a quick source and a delayed one produce r-process material. The delayed source is represented by MNS with a DTD while the quick source is usually represented by massive stars (e.g. MR-SNe). In such a way, the lack of Eu from MNS at low $[\text{Fe}/\text{H}]$, due to their long delay times for merging, is compensated by the production from MR-SNe. However, as observed in the last Chapter (see Molero et al., 2021a), if these sources are active also for the production of the r-process component of Ba, then the above models struggle to reproduce the observed $[\text{Ba}/\text{Fe}]$ vs. $[\text{Fe}/\text{H}]$ trend at low metallicities in Local Group dwarf spheroidal galaxies, suggesting that more investigation is still needed. The purpose of this work is that of extending our investigation to all the neutron capture elements for which observational data are available in order to study their distribution and evolution with the most up to date prescriptions of both the nucleosynthesis and the timescales of production from different sites. In order to do that, we need to consider a better observationally constrained environment, namely the MW.

We take advantage of the sixth data release (DR) of the *Gaia*-ESO survey from which our sample has been collected. The sample consists of 62 open clusters (OCs) located between ~ 5 and 20 kpc in Galactocentric distances, with ages from 0.1 to 7 Gyr and covering a metallicity range of $-0.5 < [\text{Fe}/\text{H}] < 0.4$ dex, together with ~ 1300 MW disc field stars in the metallicity range of $-1.5 < [\text{Fe}/\text{H}] < 0.5$ dex (see also Van der Swaelmen et al., 2023; Magrini et al., 2023, hereafter M23). In fact, OCs are considered excellent tracers of the chemical properties of the thin disc stellar population and, either by their own or appropriately combined with other stellar and nebular Galactic tracers, have broadened our understanding of the thin disc formation and evolution (see e.g., Friel et al., 2002; Chen et al., 2003; Magrini et al., 2009; Cunha et al., 2016; Méndez-Delgado et al., 2022).

In that sense, a fundamental constraint is represented by abundance gradients along the Galactic thin disc. Gradients can indeed provide important informations about both the nucleosynthesis and the timescales of enrichment of chemical elements. Moreover, they can help us to constrain the SF, the gas flows and stellar migration phenomena. The metallicity gradient is generally characterized by a decrease outwards from the Galactic Centre. Models of chemical evolution are able to reproduce such a decrease, by assuming that the disc is formed by in-fall of gas in an *inside-out* fashion, namely with a time-scale which increases with Galactocentric distances (Matteucci et al., 1989; Chiappini et al., 2001; Cescutti et al., 2007; Schönrich et al., 2017; Grisoni et al., 2018), as well as with a variable star formation efficiency (Colavitti et al., 2009; Palla et al., 2020) and/or radial gas

flows (Spitoni et al., 2011; Bilitewski et al., 2012; Cavichia et al., 2014). Here, in order to study both the metallicity and the neutron-capture elements gradients, we adopt a delayed two-infall chemical evolution model with an inside-out scenario of formation and with a variable SF efficiency, i.e. higher in the inner regions than in the outer ones. The delayed two infall model (see Noguchi, 2018; Spitoni et al., 2019b; Spitoni et al., 2020; Palla et al., 2020) is a variation of the classical two infall model of Chiappini et al. (1997) and Chiappini et al. (2001) developed in order to fit the dichotomy in α -element abundances observed both in the solar vicinity (e.g., Hayden et al., 2014; Recio-Blanco et al., 2014; Mikolaitis et al., 2017) and at various radii (e.g., Hayden et al., 2015). With respect to classical two infall model, the delayed one simply assumes a delayed formation of the thin disc of at least ~ 3 Gyr. We emphasize that the two-infall model adopted here is constrained to reproduce the *chemically* thick and thin discs, namely the *high- α* and *low- α* sequences, without aiming at distinguish the thick and thin discs populations geometrically or kinematically (see Kawata et al., 2016 for a discussion).

5.2 Observational Data

The *Gaia*-ESO survey is a large public spectroscopic survey that observed for 340 nights at the VLT from the end of 2011 to 2018 using the FLAMES spectrograph (Randich et al., 2022; Gilmore et al., 2022). During the survey, FLAMES was used at intermediate spectral resolution with GIRAFFE, and at high resolution with UVES. In this work, we select the spectra of FGK stars obtained with UVES at $R=47000$, covering the spectral range 480.0–680.0 nm. The spectra were analysed by the *Gaia*-ESO Working Group (WG 11) dedicated to the analysis of FGK stars. We refer the reader to Randich et al. (2022) and Gilmore et al. (2022) for a general description of the structure of *Gaia*-ESO and of the analysis procedure. The final catalogue containing among others atmospheric parameters, elemental abundances, radial and projected rotational velocities is publicly available in the ESO archive¹. The high spectral resolution of UVES and the large collecting area of VLT make it possible to obtain precise abundances of many neutron capture elements: the slow-process elements Y, Zr, Ba, La, and Ce, and the mixed/r-process elements Mo, Pr, Nd, and Eu. Throughout the paper, we use these abundances, normalizing them to the Solar scale as in Viscasillas Vázquez et al. (2022a) and Magrini et al. (2023).

Other surveys as the Apache Point Observatory Galactic Evolution Experiment (APOGEE-1 and APOGEE-2; Majewski et al., 2017a) and the Galactic Archaeology with HERMES (GALAH; De Silva et al., 2015) are providing abundances of some neutron-capture elements as well. For example, APOGEE provides for a limited percentage of stars abundances of Ge, Rb, Ce, Nd, and Yb, but only Ce has been used in scientific works (Cunha et al., 2017; Donor et al., 2020). Recently, Hayes et al. (2022) explored weak and blended species in the APOGEE database, providing also new and improved abundances of Ce and Nd. The GALAH survey provided in its third data release (Buder et al., 2021) abundances of several neutron capture elements, namely Y, Ba, La, Rb, Mo, Ru, Nd, Sm, and of Eu. However, their

¹<https://www.eso.org/qi/catalogQuery/index/393>

accuracy is often limited because of the lower spectral resolution. The quality of the neutron-capture abundances in the UVES spectra of *Gaia*-ESO remains, thus, unrivalled.

5.2.1 The data samples

In this work, we used two different samples of stars: a first sample composed by stars that are members of open clusters, and a second sample of field stars. For the former, we benefit of the large sample of stars members of open star clusters, located at various Galactocentric distances and covering a wide age range, from a few million years to about 7 Gyr. Star clusters, containing groups of coeval and chemically homogeneous stars, allow, indeed, a more accurate determination of age and chemical properties with respect to field stars. The latter is, instead, composed of stars of the main sequence turn off (MSTO), (see Stonkutė et al., 2016, for the description of the selection function).

The sample of open clusters

In the present paper, we consider among the sample of open clusters observed by *Gaia*-ESO, the 62 clusters older than 100 Myr, as done in Magrini et al. (2023). The motivation is twofold: younger stars might be affected by problems in the spectral analysis, as shown by (Baratella et al., 2020; Baratella et al., 2021; Spina et al., 2021); young clusters represent only the last moments of global galactic chemical evolution, with negligible variations of the abundance with respect to the overall time scale. The distribution in age and distances of our sample open clusters is given in Viscasillas Vázquez et al. (2022a, see their Figure 1). For each cluster, we considered the average abundances of its member stars. The membership analysis is performed as in Viscasillas Vázquez et al. (2022a), based on three-dimensional kinematics, complementing the radial velocities from *Gaia*-ESO with proper motions and parallaxes from *Gaia* DR3 (Gaia Collaboration et al., 2021). Ages and Galactocentric distances are homogeneously derived with *Gaia* DR2 data in Cantat-Gaudin et al. (2020). In the paper, we use the open cluster sample to trace the abundance radial gradients, and thanks to the wide age range, also their evolution over time.

The sample of field stars

The sample of field stars is composed, as in Viscasillas Vázquez et al. (2022a), by stars selected through the GES_FLD keywords related to the field stars (GES_MW for general MW fields, GES_MW_BL for fields in the direction of the Galactic bulge, GES_K2 for stars observed in Kepler2 (K2) fields, GES_CR for stars observed in CoRoT fields, and benchmark stars GES_SD), and stars which are non-members of open clusters. We combined the two samples, applying a further selection on the signal-to-noise ratio (SNR) and on the uncertainties on the stellar parameters: $\text{SNR} > 20$; $\sigma T_{\text{eff}} < 150$ K, $\sigma \log g < 0.25$, $\sigma[\text{Fe}/\text{H}] < 0.20$ and $\sigma \xi < 0.20$ km s⁻¹. A final selection was introduced considering only stars with at least one measurement of the abundances of one of the considered neutron capture elements, and with an uncertainty $eA(El) < 0.1$. These selections produce a sample of approximately

1300 stars. Due to the selection function of the *Gaia*-ESO survey (see Stonkutė et al., 2016), this sample is dominated by stars at the MSTO, with some giant stars which are non members of open clusters. Due to the wide metallicity range covered by the field stars, we use them to study the evolution in the [El/Fe] vs. [Fe/H] planes.

5.3 The Model

The adopted chemical evolution model is the one of Spitoni et al. (2019b), which derives from the two-infall model originally developed by Chiappini et al. (1997). Here we use the revised version of Palla et al. (2020) focusing our study on the disc only, without taking into account the evolution of the Galactic halo. In Spitoni et al. (2019b), the classical two-infall chemical evolution model is revised in order to reproduce the data from the APOKASC (APOGEE + *Kepler* Asteroseismology Science Consortium) catalogue by Silva Aguirre et al. (2018). The data sample suggested the existence of a clear distinction between two sequences of disc stars in the [α /Fe] vs. [Fe/H] diagram, known as the high- α and low- α sequences (dichotomy observed also in the APOGEE data, Nidever et al., 2014; Hayden et al., 2015, and also confirmed by the *Gaia*-ESO survey, Recio-Blanco et al., 2014; Rojas-Arriagada et al., 2016, and the AMBRE project, Mikolaitis et al., 2017).

The two-infall model assumes that the MW disc forms as a result of two distinct accretion episodes of gas. The first one forms the high- α sequence while the second one, delayed with respect to the first, is responsible for the creation of the low- α sequence.

The disc is approximated by independent rings 2 kpc wide and in each ring the basic equations which describe the evolution of the fraction of gas mass in the form of a generic element i , G_i , are those described in Eq. 2.14, where, in the case of the two-infall model, the gas accretion rate is computed in the following way:

$$\dot{G}_{i,\text{inf}}(R, t) = A(R)X_{i,\text{inf}}e^{-t/\tau_1} + \theta(t - t_{\text{max}})B(R)X_{i,\text{inf}}e^{-(t-t_{\text{max}})/\tau_2}, \quad (5.1)$$

where $G_{i,\text{inf}}(R, t)$ is the infalling material in the form of the elements i and $X_{i,\text{inf}}$ is the composition of the infalling gas, here assumed to be primordial. τ_1 and $\tau_2(R)$ are the infall time-scales for the first and the second accretion episodes onto the disc, respectively. We fix $\tau_1 = 1$ Gyr and let τ_2 vary with the radius according to the inside-out scenario (e.g.: Matteucci et al., 1989; Romano et al., 2000; Chiappini et al., 2001) as:

$$\tau_2(R) = \left(1.033 \frac{R}{\text{kpc}} - 1.267\right) \text{Gyr}. \quad (5.2)$$

t_{max} is the time for the maximum infall on the second accretion episode and indicates the delay of the beginning of the second infall. The typical value assumed for t_{max} in previous models (e.g.: Chiappini et al., 2001; Spitoni et al., 2009; Romano et al., 2010; Grisoni et al., 2018) is ~ 1 Gyr. However, more recent works found out that the gap between the formation of the two discs should be higher in order to reproduce both stellar abundance constraints and ages. Here, we follow the prescriptions adopted in Palla et al. (2020), who found a best value of

$t_{\max} \simeq 3.25$ Gyr (in agreement with Spitoni et al., 2019b; Spitoni et al., 2020). The parameters $A(R)$ and $B(R)$ are fixed in order to reproduce the present time total surface mass densities of the high- α and low- α sequence stars, as a function of the radius. Here we assume that the surface mass densities of the disc both follow exponential laws. In particular we adopt the following profiles:

$$\Sigma_1(R) = \Sigma_{0,1} e^{-R/2.3}. \quad (5.3)$$

$$\Sigma_2(R) = \Sigma_{0,2} e^{-R/3.5}, \quad (5.4)$$

where $\Sigma_{0,2} = 531 M_{\odot} \text{pc}^{-2}$ is the central surface mass density, and $\Sigma_{0,1}$ is fixed in order to obtain $\Sigma_1(8 \text{ kpc}) = 12 M_{\odot} \text{pc}^{-2}$. As explained in Palla et al. (2020), these choices for the disc surface mass densities allow us to obtain $\Sigma_2(8 \text{ kpc}) \sim 54 M_{\odot} \text{pc}^{-2}$ (in agreement with Bovy et al., 2013 and Read, 2014) and a ratio $\Sigma_2(8 \text{ kpc})/\Sigma_1(8 \text{ kpc}) \sim 4$ (in agreement with Spitoni et al., 2020).

In this model for the MW, we do not include galactic winds. In fact, it is found that in galactic discs galactic fountains are more likely to occur which do not alter significantly the chemical evolution of the disc as a whole (see Spitoni et al., 2009; Melioli et al., 2009).

For what concerns the SFR and the IMF functions, for the former we adopt a Schmidt-Kennicutt law (see Eq. 2.2) with $k = 1.5$ and with a star formation efficiency ν variable as a function of the Galactocentric distance, while for the latter a Kroupa et al. (1993) is adopted.

5.4 Nucleosynthesis Prescriptions

For all stars sufficiently massive to die in a Hubble time, the following stellar yields have been adopted:

- For LIMS ($1 \leq M/M_{\odot} \leq 8$) we adopted the non-rotational set of yields available on the web pages of the FRUITY data base² (Cristallo et al., 2009; Cristallo et al., 2011; Cristallo et al., 2015).
- For massive stars we implemented Limongi et al. (2018)'s recommended yield set R where mass loss and rotation are taken into account.
- For Type Ia SNe we assumed the SD scenario (see Matteucci et al., 2001; Palla, 2021 for details) for the progenitors. The adopted stellar yields are from Iwamoto et al. (1999) (model W7).
- We consider also chemical enrichment from novae. They do not affect the heavy elements treated here, but they can be important for the production of ${}^7\text{Li}$ and CNO isotopes (see José et al., 2007).

5.4.1 Heavy elements production

All the neutron capture elements studied in this work (apart from Eu) are assumed to be partially produced by the r- and s-processes.

²<http://fruity.oa-teramo.inaf.it>

The s-process nucleosynthesis takes place in LIMS during the (AGB) phase and in rotating massive stars, with yields specified in the previous paragraph. Neutrons are produced via the reactions $^{13}\text{C}(\alpha, n)^{16}\text{O}$ and $^{22}\text{Ne}(\alpha, n)^{25}\text{Mg}$, with the former reaction being the dominant contribution in low-mass stars and the latter in more massive AGBs (see Cristallo et al., 2011; Cristallo et al., 2015 for details) and massive stars (Longland et al., 2012).

For the r-process nucleosynthesis we considered two channels: MNS and MR-SNe. MNS are computed as systems of two neutron stars of $1.4 M_{\odot}$ with progenitors in the $9 - 50 M_{\odot}$ mass range. Their rate is computed as the convolution between a DTD and the SFR, as explained in Chapter 2. Here, we adopt the DTD of Simonetti et al. (2019) with $\beta = -0.9$. In this work, the α_{MNS} parameter, namely the fraction of stars in the correct mass range which can give rise to a double neutron star merging event, is fine tuned in order to reproduce the latest estimation of the MNS rate of Abbott et al. (2021).

The yields from MNS of the various elements considered in this study have been obtained as in Molero et al. (2021a) by assuming a scaling relation between them and those of Sr. The adopted yield of Sr is equal to $Y_{\text{Sr}}^{\text{MNS}} = 1 \times 10^{-4} M_{\odot}$, which corresponds to that measured by Watson et al. (2019) in the reanalysis of the spectra of the kilonova AT2017gfo multiplied by a factor of 10 (see Chapter 3 for details).

For what concerns MR-SNe, although they are theorized to be among the most important contributors to the enrichment of r-process material, Woosley et al. (2006b) speculated that only 1% of stars with initial mass $\geq 10 M_{\odot}$ can have the necessary conditions to die as a MR-SNe. A common assumption in chemical evolution models is that only 10% of all stars with initial mass in the $10 - 80 M_{\odot}$ range end their lives as MR-SNe (e.g. Cescutti et al., 2014b; Cescutti et al., 2015; Rizzuti et al., 2019; Rizzuti et al., 2021; Molero et al., 2021a, see also Chapter 3). Both the percentage of stars, their mass range and the yields of r-process material are free parameters in chemical evolution simulations and they are usually fine tuned in order to reproduce the observations of abundances. In order to avoid degeneracy issues, in this work we fixed the mass range and yields, while keeping the percentage of stars as a free parameter. The mass range is reduced to $10 - 25 M_{\odot}$ in order to be consistent with the set of yields adopted for massive stars. In fact, in Limongi et al. (2018)'s set R, stars more massive than $25 M_{\odot}$ are assumed to fully collapse to a black hole and their chemical enrichment is due to the stellar winds. Therefore, in these conditions it would be impossible for the star to develop magnetic fields strong enough to generate a MR-SNe. It must be noted that this variation in the mass range will not produce a too significant difference in the results, because of the adopted IMF (here a Kroupa et al., 1993), which is known to be top-light, i.e. which disfavours the presence of very massive stars due to its steep high mass end slope (see Figure 2.1 of Chapter 2). The set of yields adopted for the MR-SNe is the one of Nishimura et al. (2017), their model L0.75, chosen in order to be consistent with the best model of our previous work (Molero et al., 2021a). For some of the studied elements for which those yields predicted a much higher/lower production (Y, Zr, Mo, Nd and Pr) they have been scaled to the one of Eu according to the solar abundances. Finally, the percentage of stars able to explode as MR-SNe has been fine tuned in order to fit the observed

TABLE 5.1: *Nucleosynthesis prescriptions. In the 1st column we report the name of the model, in the 2nd the initial rotational velocities for massive stars. In the 3rd, 4th and 5th columns we list whether LIMS, MR-SNe and MNS channels are active or not, respectively. We point out that in the case of model 'R-150 MNS' MNS are assumed to merge with a short and constant time delay of 10 Myr instead that with a DTD.*

Model	v_{MS} (km/s)	LIMS	MR-SNe	MNS
R-0	0	✓	✓	✓
R-150	150	✓	✓	✓
R-300	300	✓	✓	✓
R-150 MNS	150	✓	X	✓
R-150 MRD	150	✓	✓	X
noR-0	0	✓	X	X
noR-150	150	✓	X	X
noR-300	300	✓	X	X

[Eu/Fe] vs. [Fe/H] relation (see next sections), and set to 20%.

In Table 5.1, we summarize the adopted nucleosynthesis prescriptions.

5.5 Results

Before discussing the comparison between our model predictions and the relevant observations for neutron capture elements, we show the evolution of some important quantities as functions of time.

In the left panel of Figure 5.1, we report the time evolution of the SFR as predicted by our model at different Galactocentric radii. In contrast with Grisoni et al. (2018), the SFR during the first infall phase is not the same for every Galactocentric distance up to 18 kpc, since we do not assume a constant disc mass density, but rather an exponentially decaying surface density profile, as described in Palla et al. (2020). As in the previously mentioned works, even without assuming a threshold for the SF, we are still able to obtain a quenching in the SF between the the two infall phases. The observed SFR in the solar neighborhood (see Guesten et al., 1982; Prantzos et al., 2018) is well reproduced by our model, as shown in the zoomed plot.

In the right panel of Figure 5.1, we report our predictions for the rates of Type Ia SNe, Type II SNe and MNS, averaged over the whole disc. The observational data are taken from Cappellaro et al. (1999a) for Type Ia and Type II SNe. For MNS we consider the latest cosmic rate observed by Abbott et al. (2021), i.e., $320^{+490}_{-240} \text{ Gpc}^{-3} \text{ yr}^{-1}$. We then applied the same conversion procedure developed by Simonetti et al. (2019) in order to convert the cosmic rate into a Galactic one. The rate so obtained is $R_{\text{MNS}} = 32^{+49}_{-24} \text{ Myr}^{-1}$, in agreement within the error bars with the rate of Kalogera et al. (2004), derived from binary pulsars (see Chapter 3).

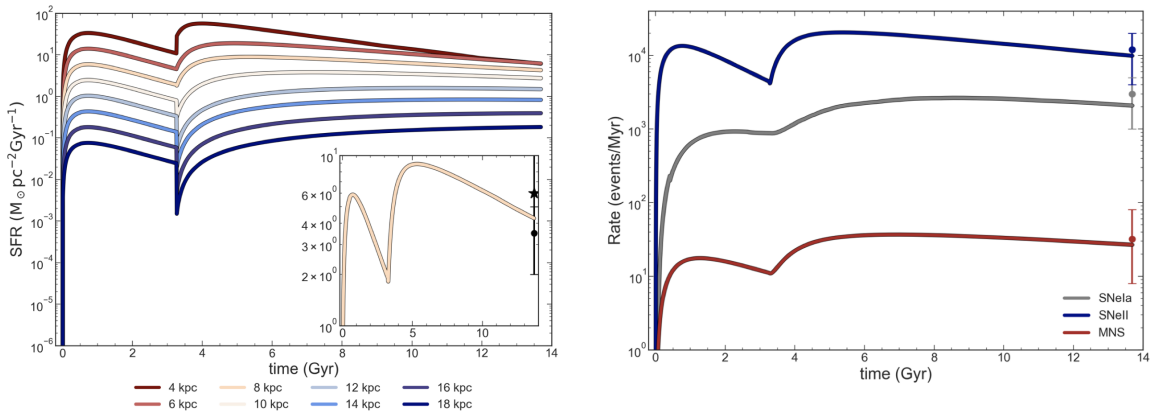


FIGURE 5.1: *Upper panel: time evolution of the SFR as predicted by our models at various Galactocentric distances. Right corner plot: predicted SFR in the solar neighborhood compared to present day estimates (Guesten et al., 1982; Prantzos et al., 2018); lower panel: predicted Type Ia SNe, Type II SNe and MNS rates compared to present day observations from Cappellaro et al. (1999a) (for SNe) and estimate from Abbott et al. (2021) (for MNS).*

5.5.1 Abundance ratios vs. metallicity trends

In the next sections we will show results for the evolution of the $[\text{El}/\text{Fe}]$ vs. $[\text{Fe}/\text{H}]$ abundance patterns of the neutron capture elements studied in this work. First, we will discuss results for Eu, a pure r-process element, and then for the other s-process and mixed/r- process elements.

Europium

In Figure 5.2, we report the $[\text{Eu}/\text{Fe}]$ vs. $[\text{Fe}/\text{H}]$ abundance pattern traced by the observational data (field stars and OCs) and compare it to the predictions of our models. As reported by Van der Swaelmen et al. (2023), who investigated the same Eu data, only for metallicity lower than ~ -0.8 dex it is possible to distinguish the famous Eu plateau at $[\text{Eu}/\text{Fe}] \sim 0.4$ dex for the field stars sample. Moreover, the plateau is visible more clearly only for stars belonging to the inner disc ($R_{\text{GC}} < 7$ kpc). For inner disc stars, a scatter of ~ 1 dex is present below $[\text{Fe}/\text{H}] \sim -1.8$. However, this is due most probably to measurement errors rather than the stochastic enrichment of Eu characteristic of the halo (see Cescutti et al., 2014b; Cescutti et al., 2015; Wanajo et al., 2021). On the other hand, the field stars sample does not extend below $[\text{Fe}/\text{H}] = -1.2$ (-0.5) dex for $7 < R_{\text{GC}}/\text{kpc} < 9$ ($R_{\text{GC}} > 9$ kpc). The OC sample well overlaps with the field one for all R_{GC} and it is affected by a lower scatter, especially in the inner disc region.

Figure 5.2 shows results of model R-150 computed at $R_{\text{GC}} = 12$ kpc, $R_{\text{GC}} = 8$ kpc and $R_{\text{GC}} = 6$ kpc compared with outer-disc, local and inner-disc data, respectively. No difference is expected if the rotational velocity of massive stars is changed, since in our model rotation does not affect Eu production. The curves are color coded by the age of the stars created by the chemical evolution code. At $\text{Age} \simeq 10.44$ Gyr, we notice the characteristic loop feature of the model due to the second infall phase. The accretion of pristine gas has the effect of decreasing the metallicity while having little impact on the $[\text{Eu}/\text{Fe}]$ ratio. When the SF resumes,

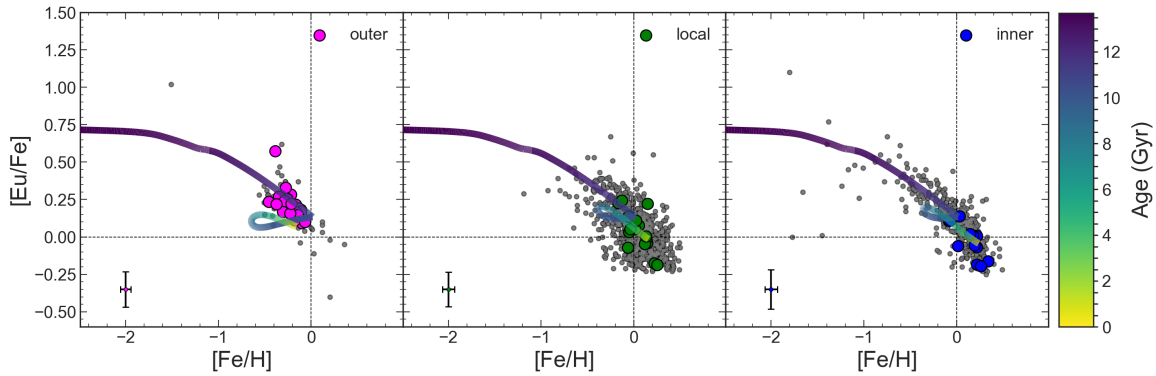


FIGURE 5.2: Predicted $[Eu/Fe]$ vs $[Fe/H]$ abundance patterns for the outer ($R_{GC} = 12$ kpc), local ($R_{GC} = 8$ kpc) and inner disc ($R_{GC} = 6$ kpc). The curves refer to the predictions of model R-150 (see Table 5.1) and are color coded by the age of the stars created by the chemical evolution code. The grey small dots refer to the sample of field stars.

a rise in the $[Eu/Fe]$ ratio is produced, then the ratio decreases while $[Fe/H]$ increases because of the enrichment from Type Ia SNe (see also Figures 3 and 4 of Spitoni et al., 2019b). The model tends to overestimate the age of the clusters in the outer zone, since the OCs have $Age \lesssim 7$ Gyr. However, the observed $[Eu/Fe]$ vs. $[Fe/H]$ trend is overall well reproduced for all the three different regions. We fixed the percentage of MR-SNe in order to fit the main trend, rather than the solar value. In order to reproduce the solar abundance of Eu, a smaller percentage of MR-SNe progenitors should be assumed, of the order of 15%. The local and the inner-disc curves slightly underestimate the metallicity reached by the observational data. This may be due to a too low SF efficiency and/or fraction of Type Ia SN systems. However, the model seems to reproduce rather well the SF and Type Ia rates at the present time in the solar neighborhood (see Figure 5.1). We also remind that in our model we do not include stellar migration effects which in principle can help reproducing the stars with larger $[Fe/H]$ values (see e.g. Spitoni et al., 2015; Palla et al., 2022). We confirm once again that the best scenario is the one in which both a quick source and a delayed one are responsible for the production of Eu. Here, the quick source is represented by MR-SNe and the delayed one by MNS with a DTD. This is not a novelty in chemical evolution simulations (e.g.: Matteucci et al., 2014; Cescutti et al., 2015; Simonetti et al., 2019; Côté et al., 2019; Molero et al., 2021b). However, it must be noted that the quick source completely dominates the production of Eu. In fact, without the contribution from MNS, we would still be able to reproduce the observed abundance pattern. On the other hand, the $[Eu/Fe]$ vs. $[Fe/H]$ pattern cannot be reproduced if MNS were the only producers of Eu, if a DTD is adopted. Only by assuming a constant and short time delay (~ 1 Myr) it is possible to explain the Eu enrichment as due to MNS alone (see Matteucci et al., 2014). Our model and prescriptions are slightly different from those adopted in Van der Swaelmen et al. (2023), but we confirm their same conclusion: Eu is produced mainly by a quick source and there is no need for an additional source at late times, at least in order to reproduce the observed Eu abundance pattern in the thin disc. However, it must be pointed out that MNS are the only source of heavy elements observed up to date, and because

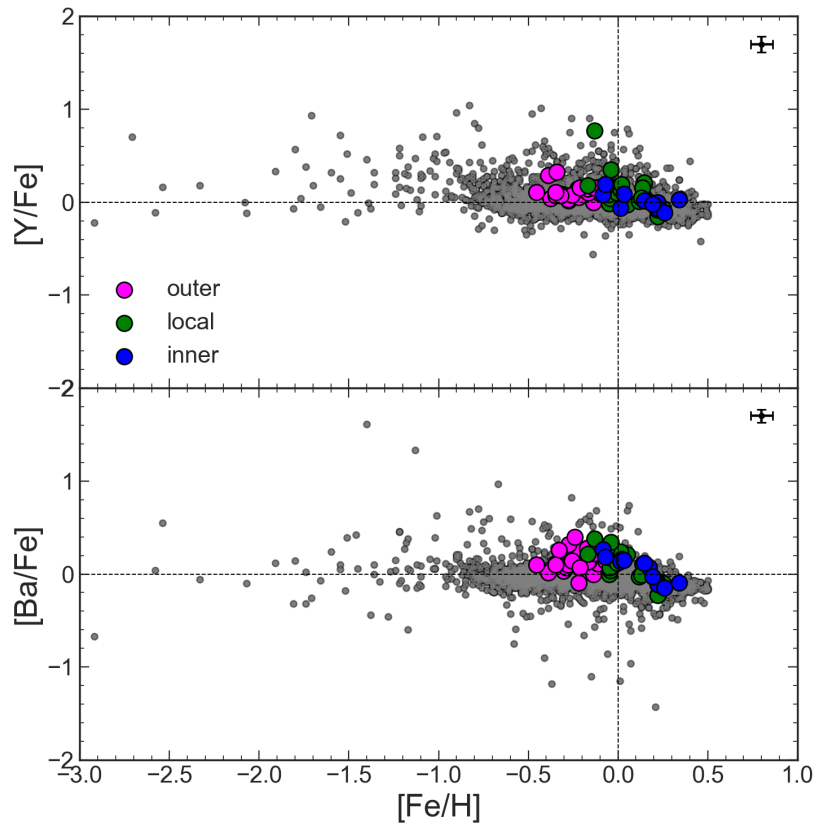


FIGURE 5.3: $[Y/Fe]$ and $[Ba/Fe]$ vs. $[Fe/H]$ for our sample of field stars (in grey) and OCs (magenta, green and blue dots) at all Galactocentric distances.

of that they cannot be excluded from chemical evolution simulations.

s-process elements

The s-process elements studied in this work are: Ba, La, Zr, Y and Ce. In Figure 5.3 we report the observational data for both the field stars and the OC sets at each galactocentric radius for $[Y/Fe]$ and $[Ba/Fe]$ vs. $[Fe/H]$, taken as representative of the abundance pattern of s-process elements belonging to the first and second peak, respectively. A characteristic s-process elements ‘banana’ shape is clearly seen at high metallicity, more pronounced in the $[Ba/Fe]$ than in the $[Y/Fe]$. This shape is assumed to reflect the pollution from LIMS during the AGB phase, which enrich the ISM with s-process material at later times creating the peak at $[Fe/H] \sim -0.04$ dex. The decrease for higher metallicity values is then due to Fe production from Type Ia SNe. This pattern is visible both in the field and in OCs. In particular, the OCs belonging to the outer disc have lower $[Fe/H]$ and are characterized by an increasing pattern, the ones belonging to the solar region have nearly solar metallicity and display the peak followed by a slight decrease and finally the inner disc OCs, which have the highest $[Fe/H]$, are characterized by a decreasing pattern, even if some of them overlaps with the trend defined by the solar-vicinity ones.

According to Prantzos et al. (2020) the fraction of the s-process elements studied in this work which is produced by the s-process is 78%, 82%, 89%, 80% and

85% for Y, Zr, Ba, La and Ce, respectively, with the remaining fractions due mainly to the r-process (and in negligible or null amount to the p-process). Although the r-process fractions of those elements is not the predominant one, we will show that from a chemical evolution point of view it is necessary to include it as well, in order to reproduce the observed abundance trends. Therefore, as a first step, we focus on the results of our model obtained when no r-process nucleosynthesis is taken into account by showing what happens when only rotating massive stars and LIMS contribute to the s-process elements production. Results of our model together with the observed abundance patterns for the s-process elements Y and Ba are reported in Figure 5.4. Outer, local and inner data are compared with our predicted evolution for $R_{GC} = 12$ kpc, $R_{GC} = 8$ kpc and $R_{GC} = 6$ kpc, respectively. The three different curves refer to the three different initial rotational velocities for massive stars: 0, 150 and 300 km/s (see Table 5.1). The effect of rotation is clearly that of increasing the production of the s-process elements, especially for the elements belonging to the first s-process peak (Y in the Figure), as expected. For the elements which belong to the second s-process peak (Ba in the Figure), rotation must be increased to 300 km/s in order to see a significant enhancement in the stellar production. The second s-process production channel is represented by LIMS. With respect to previous chemical evolution studies, which adopted only yields from LIMS in the range $1.5 - 3.0 M_{\odot}$, here we extend the mass range to $1.5 - 8.0 M_{\odot}$. We adopt yields from Cristallo et al. (2009), Cristallo et al. (2011), and Cristallo et al. (2015) up to $6.0 M_{\odot}$ and yields obtained by extrapolation in the range $6.0 - 8.0 M_{\odot}$. Moreover, since those yields tend to overproduce the solar abundances of the s-process elements, we reduced them by a factor of 2, as suggested by Rizzuti et al. (2019) (see also Rizzuti et al., 2021).

In Figure 5.5, we report the results of model R-150 for the evolution of all the s-process elements studied in this work with both the s- and the r-process astrophysical sites activated. We are showing only the model with massive stars with initial rotational velocities of 150 km/s since, once the contribution from MR-SNe is considered, the differences in the predicted abundance patterns between model assuming $v_{rot} = 0$ and 150 km/s are negligible and, as previously shown, models with $v_{rot}=300$ km/s overestimate the observed abundance trends. The predicted curves are color coded by the ages of the synthetic stars. We notice that the model is able to reproduce the main observed trends in the data, especially in the OC sample. The rise in the outer disc data as well as the peak followed by the decrease in the local and inner-disc data are reproduced by our model at $R_{GC} = 12, 8$ and 6 kpc. The only exceptions are represented by the $[Y/Fe]$ and the $[Zr/Fe]$ vs. $[Fe/H]$ trends in the outer region for which the model does not produce the expected increase, but rather a decrease. This is probably due to the combination of too high MR-SNe yields and too low LIMS ones for those two elements. Because of the MR-SNe yields, the model predicts high $[Y/Fe]$ and $[Zr/Fe]$ value at relatively low metallicities and it is not able to produce an increasing trend at higher ones because LIMS are not producing enough Zr and Y abundances. However, it must be reminded that LIMS are not supposed to be among the main producers of Y and Zr, since those two elements belong to the first s-process peak. $[La/Fe]$ vs. $[Fe/H]$ is slightly overproduced by the model in the local and inner disc regions. The $[Ce/Fe]$ vs. $[Fe/H]$ has recently been already studied

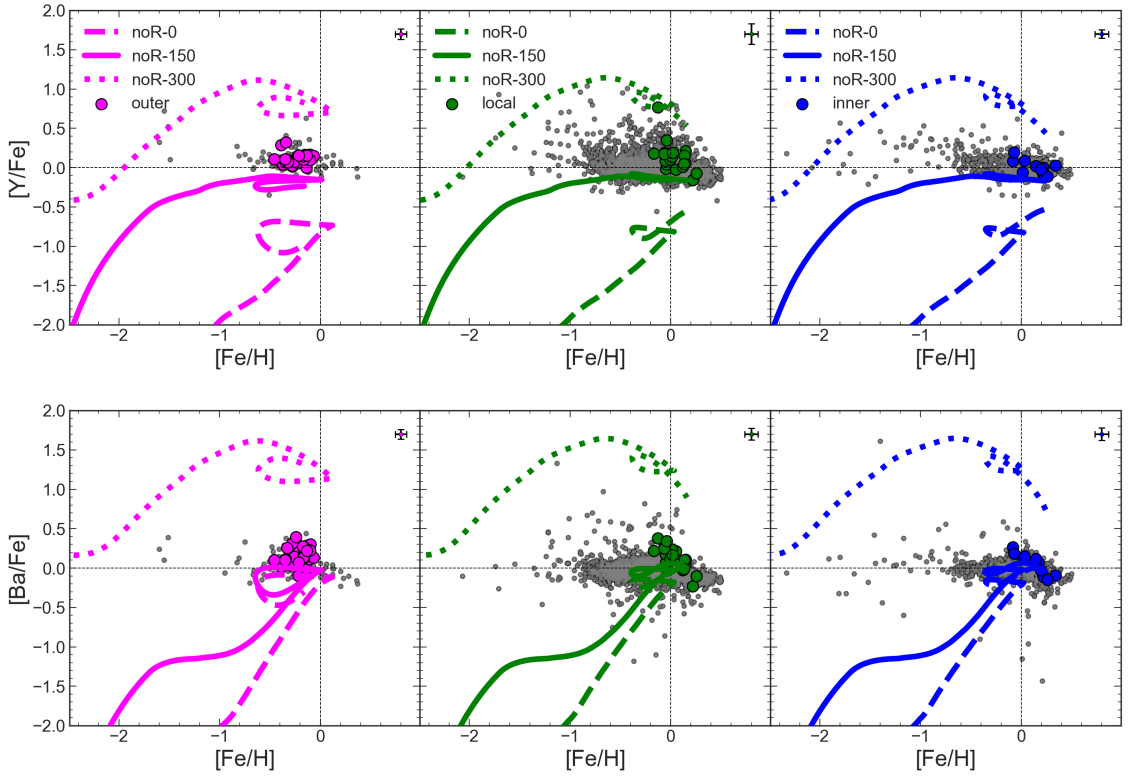


FIGURE 5.4: Predicted abundance patterns for $[Y/Fe]$ and $[Ba/Fe]$ vs. $[Fe/H]$ for outer ($R_{GC} = 12$ kpc), local ($R_{GC} = 8$ kpc) and inner ($R_{GC} = 6$ kpc) disc regions. We assume that only massive stars and LIMS are Y and Ba producers. The three lines in each plot corresponds to different initial rotational velocities of massive stars (see legend and Table 5.1).

by Contursi et al. (2023) in the MW halo and disc component through a high quality samples of GSP-Spec Ce abundances. They find a rather flat trend at a mean level of $[Ce/Fe] \sim 0.2$ dex for $-0.7 < [M/H] < 0.3$ dex which are able to reproduce by means of the three-infall chemical evolution model by Spitoni et al. (2023). On the other hand, our OC sample clearly show the characteristic *banana* shape of s-process elements, rather than a flat trend, which is well reproduced by our two-infall model. The three curves reach metallicities of $[Fe/H] \sim -0.16, 0.16$ and 0.33 dex in the outer, local and inner-disc, respectively, which slightly underestimate the ones observed in the OC samples for the outer and local disc, similarly to what happen for Eu (see previous Section).

Mixed-process elements

In Figure 5.6, we report the observed abundance patterns for both field stars and OCs in our *Gaia*-ESO DR6 samples together with the predictions from our model for Mo, Nd and Pr. We refer to those elements as mixed process elements. In fact, even if for all the elements studied in this work both the contributions from the s- and the r-process have been considered, Mo, Nd and Pr are found to owe a large fraction of their Galactic abundances to the r-process. As also discussed

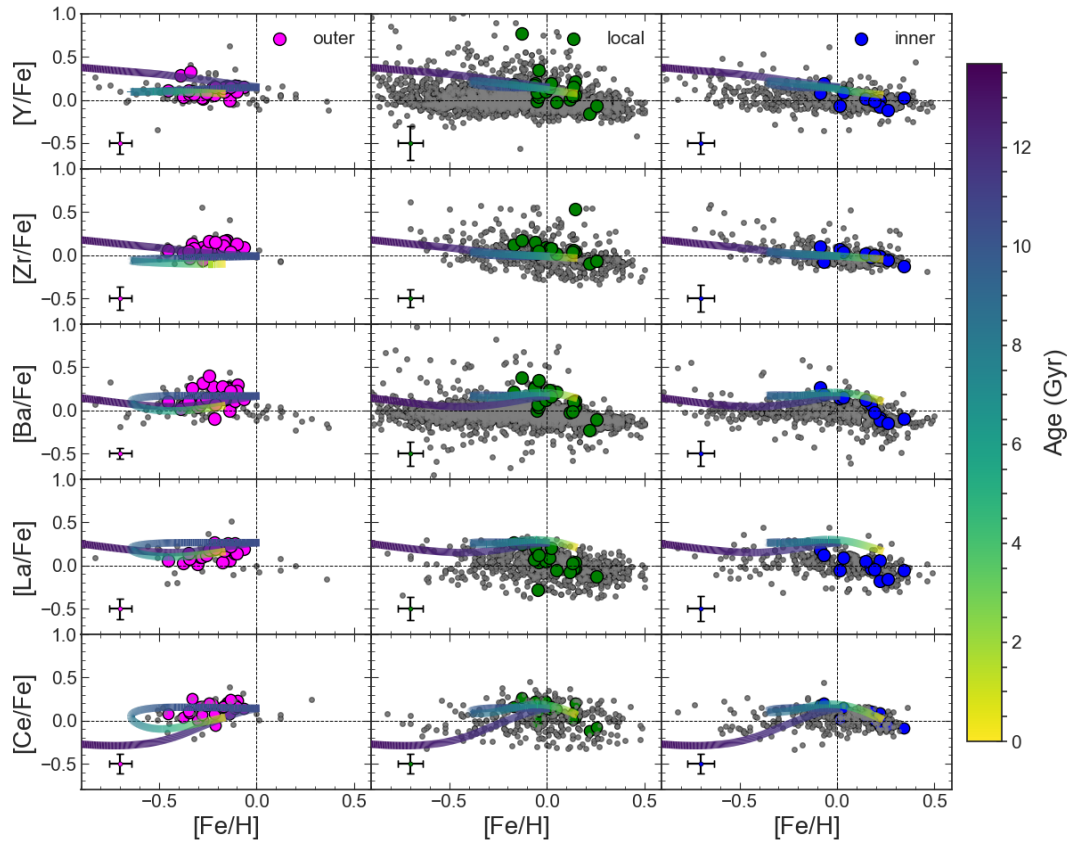


FIGURE 5.5: Predictions from model R-150 for the *s*-process element abundance patterns vs. $[Fe/H]$ for outer ($R_{GC} = 12$ kpc), local ($R_{GC} = 8$ kpc) and inner ($R_{GC} = 6$ kpc) disc regions. The channels considered for the production of the *s*-process components are: massive stars with initial rotational velocities of 150 km/s and LIMS. The channels for the *r*-process components are: MR-SNe and MNS with a DTD. The curves are color coded by the age of the stars created by the chemical evolution code.

by Van der Swaelmen et al. (2023), different studies (e.g. Sneden et al., 2008; Bisterzo et al., 2014; Prantzos et al., 2020) agree in assigning $\sim 40\%$ of the r-process component to Nd and $\sim 50\%$ to Pr. On the other hand, the contributions of the different processes to the abundance of Mo in the Sun differ from one author to another. According to Hansen et al. (2014), who presented a study of both Mo and Ru abundances in the MW covering both dwarfs and giants from $[\text{Fe}/\text{H}] \sim -0.7$ down to ~ -3.2 dex, Mo can be considered as a highly mixed element, with contributions from the main and weak s-processes as well as from the p-process and, in a smaller fraction, from the main r-process. In agreement with that study, more recently Prantzos et al. (2020) proposed for Mo a contribution of 50% from s-process, 27% from r-process and 23% from p-process. Van der Swaelmen et al. (2023), which adopted our same data set, examined also the origin of these elements from an observational point of view, comparing their abundance with that of Eu. From their study, it appears that Nd should be characterized by a significant s-process contribution, whereas for Pr they expect a lower contribution from the s-process. Results of our model are not in agreement with these hypotheses for Nd and Pr. In fact, as shown in Figure 5.6, our model predicts a too low $[\text{Nd}/\text{Fe}]$ vs. $[\text{Fe}/\text{H}]$ abundance pattern with respect to the observed one. This discrepancy between predictions and observations may be attributed to LIMS which produce a too low amount of Nd with respect to what is expected in Van der Swaelmen et al. (2023). On the other hand, our model fits properly the $[\text{Pr}/\text{Fe}]$ vs. $[\text{Fe}/\text{H}]$ trend, only slightly overproducing the observed pattern in the local and inner parts. This may be due both to a too strong production of Pr by massive stars and by LIMS, contrary to what happens for Nd. It is worth noting that the observed abundance pattern of $[\text{Pr}/\text{Fe}]$ vs. $[\text{Fe}/\text{H}]$ resembles more that of an s-process elements than the one of the $[\text{Nd}/\text{Fe}]$ vs. $[\text{Fe}/\text{H}]$, at least when considering the *Gaia*-ESO OC data. In fact, in the case of Pr we distinguish a rise in the abundances in the outer region, followed by a peak and then a decrease in the local and inner regions. On the other hand, this typical 'banana' shape is not recognisable in the observed abundance pattern of Nd.

The behaviour of Mo is much more uncertain. As discussed in Van der Swaelmen et al. (2023), the elusive nature of this chemical element together with the difficulty in measuring its abundance caused chemical evolution studies to reach discordant conclusions about its cosmic origin. In Mishenina et al. (2019), the $[\text{Mo}/\text{Fe}]$ vs. $[\text{Fe}/\text{H}]$ abundance pattern has been studied in a wider range of metallicities with respect to our samples and with chemical evolution models from Travaglio et al. (2004), Prantzos et al. (2018) and with the open-source galactic chemical evolution code OMEGA+ (Côté et al., 2018). Their main conclusion is that canonical stellar sources of heavy elements are not producing a sufficient amount of Mo to reproduce observations. They showed that, despite the fact that the r-process contributes to a small fraction of the solar Mo, it is of significant importance especially at low metallicities, where the s-process contribution from AGB stars is negligible. In fact, in Mishenina et al. (2019) the model that better agrees with the data is the one in which the r-process component of Mo is produced on quick timescales (the r-process production site considered is associated with MNS with a short and constant delay time for merging). Our results for the $[\text{Mo}/\text{Fe}]$ vs. $[\text{Fe}/\text{H}]$ abundance pattern are in agreement with Mishenina

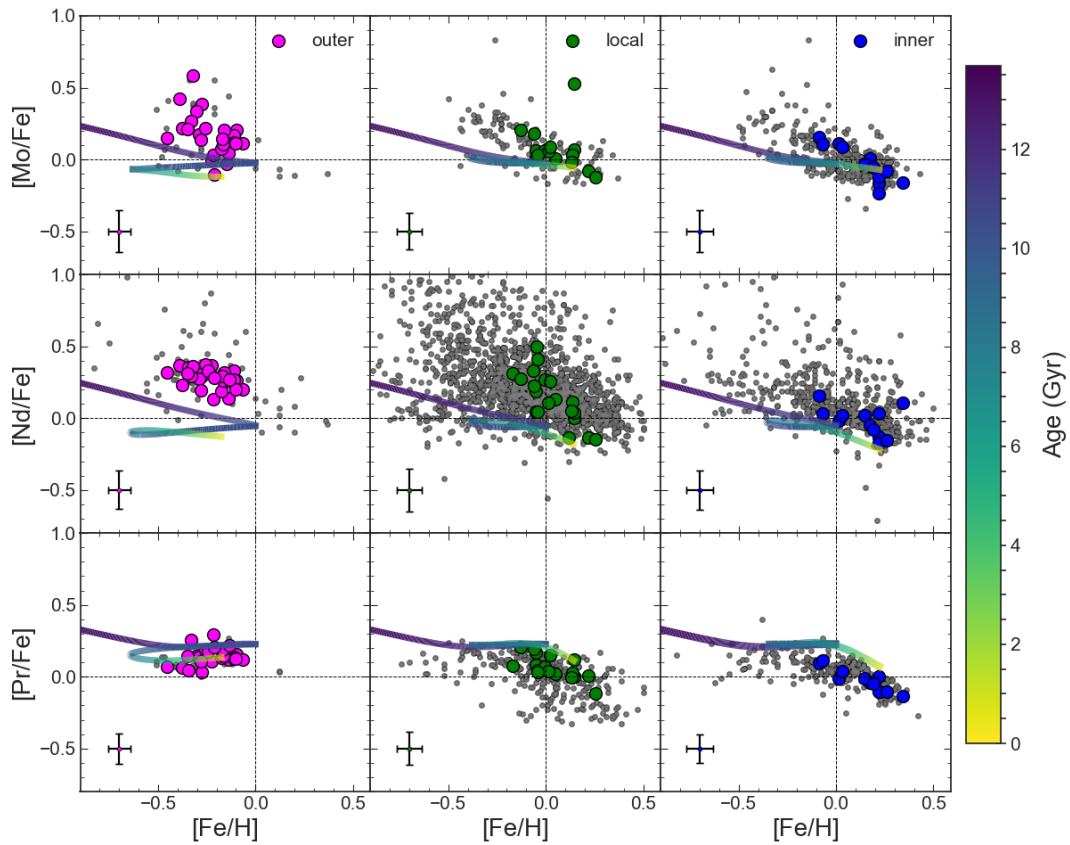


FIGURE 5.6: Predictions from model R-150 for the mixed-process elements abundance patterns vs. $[Fe/H]$ for outer ($R_{GC} = 12$ kpc), local ($R_{GC} = 8$ kpc) and inner ($R_{GC} = 6$ kpc) disc regions. The curves are color coded by the age of stars created by the chemical evolution code.

et al. (2019) conclusions. In fact, even with a quick r-process source activated (in our case represented by MR-SNe) the predicted trends appear to slightly underestimate the observed ones at each Galactocentric radius. However, this is most probably due to the lack in our model of an additional contribution from neutrino-driven SNe which may be important producers of Mo at all metallicities (see e.g., Bliss et al., 2018; Bliss et al., 2020).

Comparison with previous studies

Similar prescription to those adopted in this work have been already included in chemical evolution studies by Prantzos et al. (2018) (from now on P18) and Rizuti et al. (2019) (from now on R19) in order to study the contribution from rotating massive stars to the enrichment of different chemical species in the MW. The main differences between the work of R19 and this one are: i) the set of Limongi et al. (2018) for rotating massive stars used by R19 is the Set F whereas we adopt Limongi et al. (2018)'s recommended Set R (see also Romano et al., 2019); ii) in R19 LIMS in the $1.3 - 3.0 M_{\odot}$ mass range are assumed to produce s-process elements, whereas we extend the mass range to $1.3 - 8.0 M_{\odot}$; iii) for the r-process nucleosynthesis we use both MR-SNe and MNS, with these latter characterized by having a DTD, while R19 used either one source or the other (with the coalescence time-scale for MNS constant and equal to 1 Myr); iv) the iron yields from CC-SNe adopted in R19 are those from Kobayashi et al. (2006), while for consistency here we adopt the ones from Limongi et al. (2018). On the other hand, the main differences between the work of P18 and our are: i) in P18 r-process elements are assumed to be produced in CC-SNe and their yields are scaled to the yield of oxygen according to the solar system r-process contribution as determined by Sneden et al. (2008). The yields so obtained, are functions of the mass and of the metallicity of the star; ii) the yields of rotating massive stars are weighted with a metallicity dependent function empirically determined.

The main difference between our results and those of R19 is that in their model it appears that the contribution from MR-SNe is not the dominant one at really low metallicities. In fact, it is still possible to appreciate differences between their model in which massive stars have an initial rotational velocity of 150 km/s and the one in which massive stars do not rotate at all, even when the MR-SNe channel is active (their models LC000+MRD and LC150+MRD). These differences are visible only at really low metallicities (< -4 dex). For higher [Fe/H] the two models are very similar, exactly as it happens in our case. So that, for the metallicities we are interested in this work, we do not expect significant differences. The dissimilarities in the prescriptions adopted for MR-SNe nucleosynthesis between our work and that of R19 may be responsible for the slightly different results between the two studies.

The discrepancies between our predictions and those of P18 are not so strong, even if their prescriptions for the production of heavy elements from massive stars is substantially different from ours. In fact, they assume that all CC-SNe can produce heavy elements and scale their yields to the one of oxygen, whereas in our case only a small fraction of massive stars can produce r-/s- process material with the nucleosynthesis of Nishimura et al. (2017). The major issue which results from our approach is that the adopted yields are not a function of the mass of the

progenitor. That means that all the assumed 20% of stars with progenitor mass of $10 - 25 M_{\odot}$ are producing the same amount of r- process material independently, which is of course an oversimplification. P18 assumed that the yield of each heavy element considered scales with another element produced exclusively by massive stars which reproduce the solar abundance, with this latter being already a function of mass (and metallicity, which may be an issue for r-process nucleosynthesis). This method still has some uncertainties but it can be reliable for the purpose of P18, which is the study of the effect of rotating massive stars yields. In our case, the primary goal is that of studying the origin of neutron capture elements by adopting the state-of-the-art in the nucleosynthesis prescriptions and, as a result, to reveal the main uncertainties in both the chemical evolution models and the nucleosynthesis itself.

5.5.2 Gradients

Here, we present the abundance gradients of the studied elements. We first show our predictions for the present time abundance gradients along the disc and then discuss their time evolution.

Present day radial abundance gradients

In Figure 5.7, we compare the theoretical present-day gradients of [Fe/H] and [Eu/H] to the observational data. In order to compare present day results of our model with the observations, we restricted our OC sample to clusters with $Age \leq 3$ Gyr. As discussed in Magrini et al. (2023) (from now on M23; see also references therein) there is a general agreement about the existence of a steeper [Fe/H] gradient in the inner disc and an extended plateau in the outer region, with a cutoff point at $R_{GC} \sim 11.2$ kpc. This change of slope is evident in the OC sample used in this work and it is still visible when we restrict our sample to OCs younger than 3 Gyr. Considering the entire OC sample and a weighted single slope fit, M23 find a slope of the [Fe/H] gradient of -0.054 ± 0.004 dex kpc $^{-1}$. Considering the two radial region they obtain a steeper inner gradient (-0.081 ± 0.008 dex kpc $^{-1}$) and a much flatter outer plateau (-0.044 ± 0.014 dex kpc $^{-1}$). The slopes of the restricted OC sample are in good agreement with the ones of the whole sample, as reported in Table 5.2. The slope of the [Fe/H] gradient predicted by our model is equal to -0.067 ± 0.003 dex kpc $^{-1}$. As shown in Figure 5.7, this is slightly steeper both with respect to the gradients of the restricted OC sample (upper panel) and to the one of the Cepheid sample including the data of Luck et al. (2011) and Genovali et al. (2015) (lower panel). However, our result is in good agreement with other recent literature slopes of the [Fe/H] gradient from OC samples, (Carrera et al., 2019; Donor et al., 2020; Zhang et al., 2021; Spina et al., 2021; Spina et al., 2022, see Table 1 in M23). If instead of adopting R_{GC} to compute the gradient of the OCs sample, one adopts the guiding radius, R_{mean} (defined as the average between the minimum and maximum radius of the orbits calculated with the GALPY code and with the axisymmetric potential MWPotential 2014 from Bovy, 2015, see M23 for details), then the obtained gradient is equal to -0.060 ± 0.005 dex kpc $^{-1}$, much more in agreement with the one predicted by our simulation.

TABLE 5.2: Slopes of the $[Fe/H]$ and $[Eu/H]$ gradients of the reduced ($\text{Age} \leq 3 \text{ Gyr}$) OC sample and as predicted by our model for the all, inner ($R_{GC} < 11.2 \text{ kpc}$) and outer ($R_{GC} > 11.2 \text{ kpc}$) radial region. For comparison we show also the one obtained from the Cepheid sample of Luck et al. (2011) and Genovali et al. (2015). In the case of Eu we show predictions also of models in which Eu is produced either by MR-SNe or by MNS with a constant and short delay time for merging.

	[Fe/H]			[Eu/H]		
	m_{tot} (dex kpc $^{-1}$)	m_{inner} (dex kpc $^{-1}$)	m_{outer} (dex kpc $^{-1}$)	m_{tot} (dex kpc $^{-1}$)	m_{inner} (dex kpc $^{-1}$)	m_{outer} (dex kpc $^{-1}$)
OCs	-0.049 ± 0.005	-0.081 ± 0.013	-0.045 ± 0.017	-0.017 ± 0.003	-0.024 ± 0.009	-0.015 ± 0.014
Cepheids	-0.046 ± 0.003	-	-	-0.031 ± 0.004	-	-
Model R-150 var ν	-0.067 ± 0.002	-0.064 ± 0.008	-0.063 ± 0.007	-0.051 ± 0.003	-0.038 ± 0.004	-0.057 ± 0.007
Model R-150 con ν	-0.021 ± 0.004	-0.044 ± 0.008	-0.007 ± 0.001	-0.014 ± 0.003	-0.029 ± 0.006	-0.004 ± 0.001
Model R-150 MRD	-	-	-	-0.049 ± 0.003	-0.034 ± 0.003	-0.057 ± 0.007
Model R-150 MNS	-	-	-	-0.049 ± 0.003	-0.034 ± 0.003	-0.057 ± 0.007

In the right panels of Figure 5.7 we compare the slopes predicted by our model under different assumptions (see Table 5.1) for the $[Eu/H]$ gradient with those observed in the restricted OC sample and in the Cepheid one from Luck et al. (2011). The OC restricted sample shows a flat $[Eu/H]$ gradient, with a global slope equal to $-0.017 \pm 0.004 \text{ dex kpc}^{-1}$ and an inner slope slightly steeper than the outer one (see Table 5.2). In general, elements which are produced on longer timescales are characterized by steeper gradients than elements produced on fast timescales. For example, α -elements have flatter slopes than Fe-peak elements (even if there may be differences also between elements of the same group). Therefore, the shape of the $[Eu/H]$ gradient points towards a short timescale of production. We remind that in model R-150 (variable ν) the r-process material comes from both a quick source (MR-SNe) and a delayed one (MNS with a DTD). In Figure 5.7 this model is represented by the olive line. It predicts a global slope equal to $-0.051 \pm 0.003 \text{ dex kpc}^{-1}$, which is too steep with respect to the one observed from the OC sample. The agreement with the data does not improve even if we assume that Eu is produced on short timescales only (purple and teal lines in the Figure, corresponding to Eu production from solely MR-SNe and MNS with a constant and short (10 Myr) delay time for merging, respectively). Moreover, these two models predict the same slope of the $[Eu/H]$ gradient, equal to $-0.049 \pm 0.003 \text{ dex kpc}^{-1}$. Our results do not improve noticeably even if the contribution from the delayed source is suppressed, since MNS with DTD are not the main source of r-process material in model R-150. In fact, even if their Eu yield is higher with respect to that of MR-SNe, their rate is low (see Figure 5.1). We stress once again that MNS are the only source of r-process material confirmed by observations and therefore they must be included in the computation. However, when compared with the MR-SNe, they are not the dominant source. On the other hand, by including them the agreement between our predicted $[Eu/H]$ inner slope and the observed one improves, especially for models with no delayed source (see Table 5.2). Contrary to Fe, in the case of Eu, computing the gradient of the OCs sample with R_{mean} instead that with R_{GC} does not improve the agreement with our models.

To reproduce flatter present-day abundances gradients we tested also a model with constant SF efficiency ($\nu = 1 \text{ Gyr}^{-1}$). Results for the $[Fe/H]$ and for the $[Eu/H]$

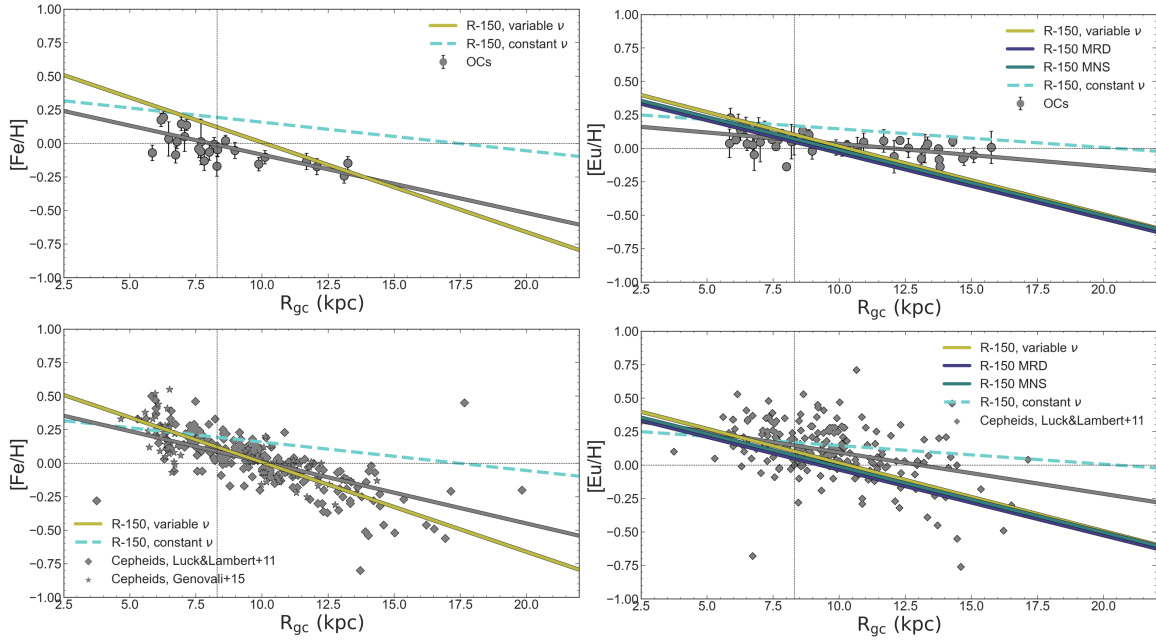


FIGURE 5.7: Prediction of the present day slope of the $[Fe/H]$ and $[Eu/H]$ gradients from our models with variable (olive line) and constant (dashed turquoise line) SF efficiency compared to the the one of the restricted (Age ≤ 3 Gyr) OC sample (upper panel) and the Cepheid sample (lower panel) with data from Luck et al. (2011) (grey diamonds) and Genovali et al. (2015) (grey stars). For the $[Eu/H]$ we show also models with Eu produced only by MR-SNe (purple line) and Eu produced only by MNS with a constant and short delay time for merging (teal line). The grey lines represent the linear fit of the observational data.

are reported in Figure 5.7 as well as in Table 5.2. By assuming a constant SF efficiency we obtain a satisfactory agreement with the OCs $[Eu/H]$ gradient. On the other hand, we lose the agreement with the observed $[Fe/H]$ gradient, in particular in the outer regions where the predicted SF turns out to be too intense. As already pointed out by Grisoni et al. (2018), the inside-out scenario, although is a key ingredient for the formation of the Galactic discs, is not enough to explain the abundance pattern at different Galactocentric distances and the abundance gradients by itself. Models with only an inside-out scenario usually predicts too flat present day gradients, as is the case of our model with constant SF efficiency. In order to steepen the gradients further assumptions are needed. In particular, one need to consider either a variable SF efficiency, or radial gas flows or a combination of both (Palla et al., 2020). Models with decreasing SF efficiency with increasing Galactic radius produce a steeper gradient, since they boost the chemical enrichment in the inner regions relative to the outer ones. Radial migration of stars, which is not taken into account in any of our models, on the contrary, should have the effect of flattening the gradient on long enough timescales (Minchev et al., 2018; Quillen et al., 2018). Whether clusters are affected by migration as much as field stars is not completely understood yet. If also clusters with Age < 3 Gyr are affected by migration, the discrepancy between our models and the data (especially in the outer region) may be partially due to the moving outward of "old" clusters formed in the inner disc (see M23 and references therein). In favor of

this hypothesis, the slopes of the [Eu/H] gradient predicted by our models with variable SF efficiency are in better agreement with the one computed from the younger Cepheid sample of Luck et al. (2011), shown in the lower panels of Figure 5.7 (see Table 5.2).

Time evolution of the radial abundance gradients

In the upper left panel of Figure 5.8, we report the time evolution of the radial [Fe/H] gradients of the completed OC sample divided in three age bins together with results of our model at 0.5, 2 and 5 Gyr. In the upper right panel of the same Figure we report the predictions about [Fe/H] evolution as a function of Age for different radii. The drop at $Age \sim 10.44$ Gyr, in correspondence of the vertical grey dotted line, is the effect of the dilution event which happens when the second infall takes place. Since the OCs in our sample are younger than ~ 7 Gyr, we are interested only in the evolution from $Age \sim 10.44$ Gyr until the present day.

As observed by M23, the youngest clusters of the sample ($Age < 1$ Gyr) have lower metallicity than the older ones in the inner disc ($R_{GC} < 10$ kpc). As expected, the trend in the youngest clusters is not in agreement with our chemical evolution simulations which predict that the oldest population should be less enriched than the youngest one (on the other hand, an additional recent third infall episode produces a chemical impoverishment of the young population; see Spitoni et al., 2023). The young clusters also show a flatter [Fe/H] gradient with a slope of -0.038 ± 0.004 dex kpc $^{-1}$ (for $Age < 1$ Gyr), -0.063 ± 0.006 dex kpc $^{-1}$ (for $1 \leq Age \leq 3$ Gyr) and -0.084 ± 0.019 dex kpc $^{-1}$ (for $Age > 3$ Gyr) (see Table A.10 of M23). The slopes predicted by our model at 5, 2 and 0.5 Gyr reproduce this trend, but the difference between the three slopes is not that significant (see Table 5.3). Larger variations with time of the gradient slopes would be obtained by comparing our model results at older times. On the other hand, really small changes are expected in the latest Gyrs, as it appears clear from the upper right panel of Figure 5.8. According to M23, the observed trend in the youngest clusters is most likely due to a bias introduced by the standard spectroscopic analysis of low gravity giant stars. If the gradient of the youngest population is recomputed by removing giant stars with $\log g < 2.5$ the final gradient is very close to that of OCs with $1 < Age < 3$ Gyr which suggests a limited time evolution of the gradient, in agreement with our models.

The lower panels of Figure 5.8 are the same as the upper panels, but for Eu. Here, we show results of our model R-150. Unlike [Fe/H], in the case of Eu the OC sample gradient does not show different shapes with time. The youngest population shows abundances consistent with that of the intermediate and older clusters. Our model is in agreement with this trend, in fact it predicts very similar slopes for the three different lines corresponding to ages of 0.5, 2 and 5 Gyr (see Table 5.3). As already discussed previously, we predict a steeper present day slope with respect to the observed one. This is true also for the different ages shown in Figure 5.8. However, as for the present day gradients, also at different ages we obtain a much better agreement with the data of the inner ($R_{GC} < 11.5$ kpc) disc rather than with those of the outer parts, where our model struggles to reproduce the observed plateau. This could be due to the too low SF efficiencies assumed for the outer part of the disc. However, it must be pointed out that we

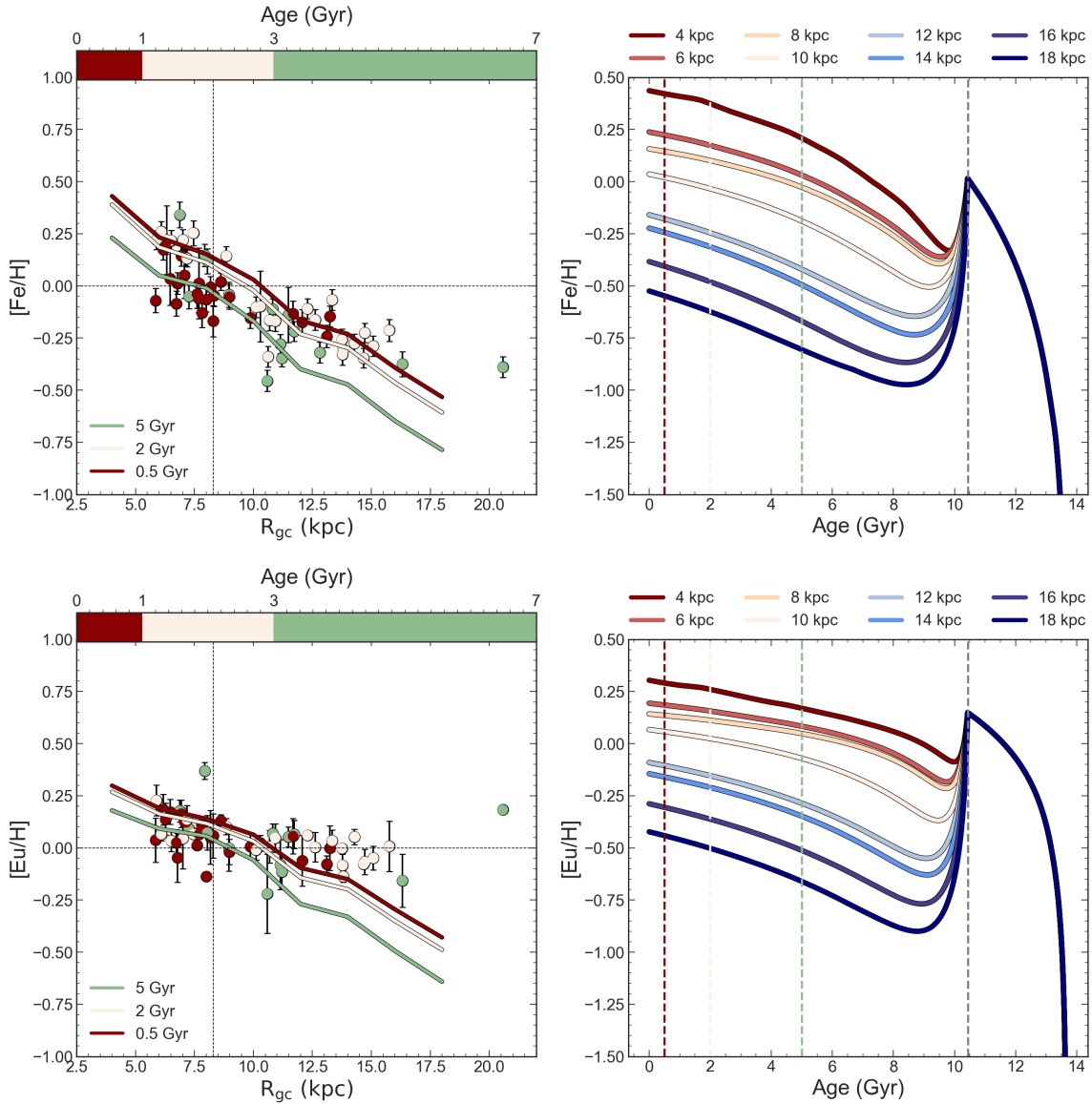


FIGURE 5.8: Left panels: Time evolution of the radial $[Fe/H]$ and $[Eu/H]$ gradients as predicted by model R-150. The OC sample is divided in three age bins: young (Age < 1 Gyr), intermediate (1 < Age < 3 Gyr) and old (Age > 3 Gyr). Solid lines are the results for the $[Fe/H]$ gradient as predicted by our model at 0.5 Gyr, 2 Gyr and 5 Gyr. Right panels: time evolution of the $[Fe/H]$ and $[Eu/H]$ as predicted by model R-150 for different Galactocentric distances. Vertical dotted lines indicate the ages considered to compute the gradients.

TABLE 5.3: Slopes of the $[El/H]$ gradients predicted by our model at Age = 0.5, 2 and 5 Gyr.

	Age = 0.5 Gyr	Age = 2 Gyr	Age = 5 Gyr
[Fe/H]	-0.067 ± 0.002	-0.069 ± 0.002	-0.073 ± 0.003
[Eu/H]	-0.051 ± 0.003	-0.053 ± 0.004	-0.059 ± 0.004
[Y/H]	-0.067 ± 0.004	-0.070 ± 0.004	-0.077 ± 0.005
[Zr/H]	-0.075 ± 0.004	-0.078 ± 0.004	-0.083 ± 0.004
[Ba/H]	-0.078 ± 0.008	-0.084 ± 0.007	-0.095 ± 0.006
[La/H]	-0.073 ± 0.008	-0.080 ± 0.007	-0.092 ± 0.006
[Ce/H]	-0.077 ± 0.011	-0.087 ± 0.011	-0.105 ± 0.008
[Mo/H]	-0.071 ± 0.003	-0.073 ± 0.003	-0.077 ± 0.004
[Pr/H]	-0.078 ± 0.012	-0.089 ± 0.012	-0.109 ± 0.009
[Nd/H]	-0.058 ± 0.004	-0.062 ± 0.004	-0.070 ± 0.005

do not expect much higher SF in the outer disc and the SF efficiency has been fine tuned to reproduce the abundance patterns of the OCs with $R_{GC} > 9$ kpc, as shown in the previous sections. Higher values of the SF efficiency would produce a too high metallicity and the agreement with both the abundance patterns and the $[Fe/H]$ gradients would be lost.

In Figures 5.9 and 5.10, we display the time evolution of the first and second peak s-process elements, respectively. In this case, the OC sample shows much more scatter. According to M23, the OC sample is characterized by an inverse main trend with respect to $[Fe/H]$, with the youngest clusters being characterized by lower (or almost equal) abundances of Y, Zr, Ba, La and Ce than their older counterparts. Predictions of our model are in agreement with these trends. For Y and Zr the lines corresponding to ages of 0.5 and 2 Gyr show a very similar pattern and are characterized by both the same slope and almost the same abundances at all Galactocentric distances. Similarly, in the case of Ba, La and Ce, our model predicts an almost identical flat or slightly decreasing pattern at all ages in the inner zones ($R_{GC} < 10$ kpc), while the predictions diverge for higher R_{GC} values. The plateau observed for the s-process elements belonging to the second peak at low Galactocentric distances, is due to the effect of LIMS, which contribution reaches a maximum value faster in the inner regions than in the outer ones (see also Casali et al., 2023). The slopes predicted by our model for the first peak s-process elements are globally flatter with respect to those expected for the second peak elements. This is because Y and Zr are mainly produced by rotating massive stars (Limongi et al., 2018) and therefore on quicker timescales with respect to Ba, La and Ce which, on the other hand, have a production dominated by LIMS (Cristallo et al., 2009; Cristallo et al., 2011; Cristallo et al., 2015).

The time evolution of the gradients of the other r/mixed-process elements is reported in Figure 5.11. The OC sample shows a slope similar to that of Eu (~ -0.002 dex kpc^{-1} , see M23), but, as in the case of the s-process elements, also the mixed/r-process elements are characterized by a larger scatter, in particular Mo and Nd. Unlike the $[Fe/H]$ gradient, in the case of those elements the youngest population does not appear to be more abundant than the oldest one. As already discussed in Section 5.5.1, because of the specific nucleosynthesis prescriptions adopted in this study our model underestimates the observed Mo and

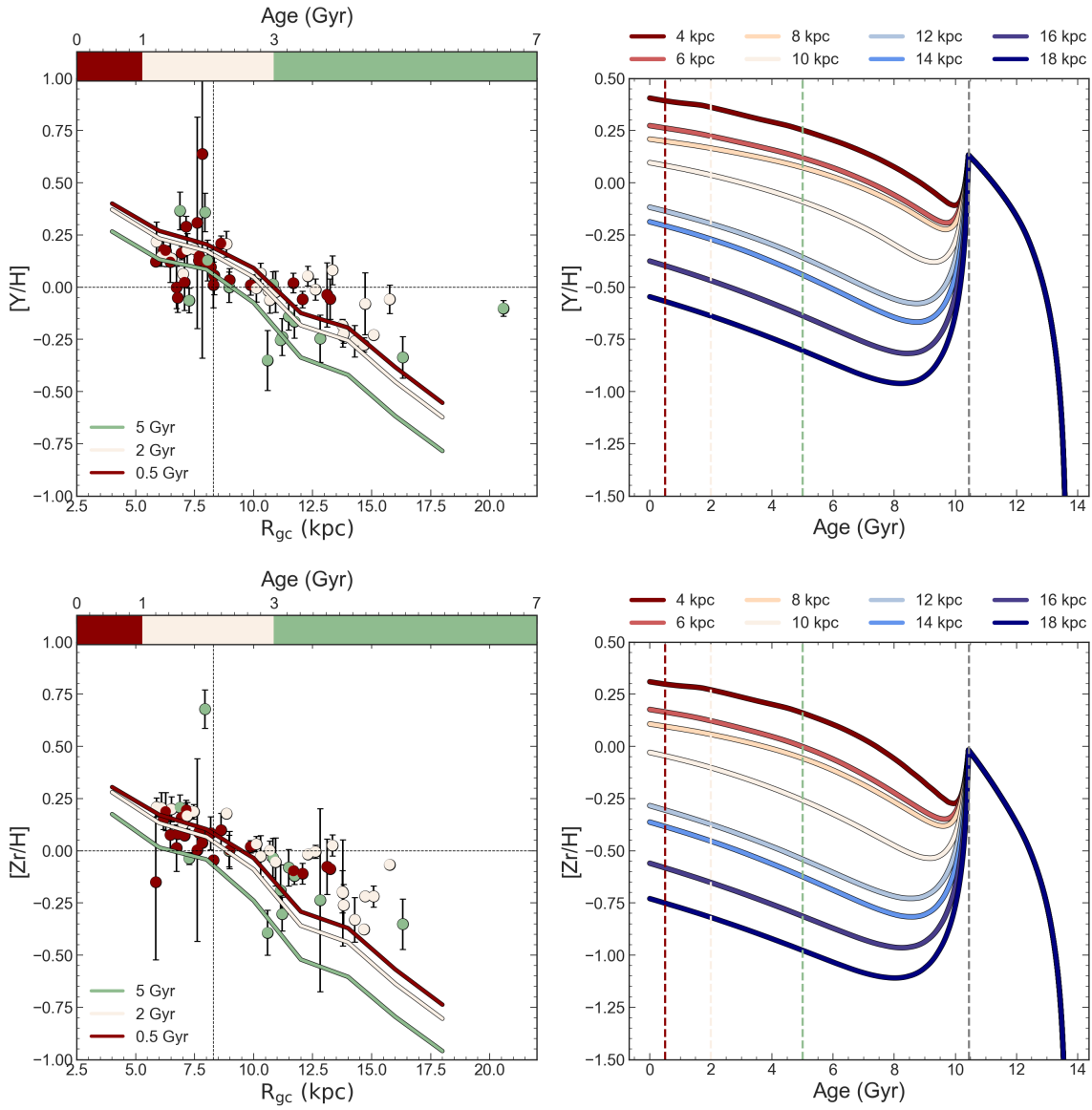


FIGURE 5.9: Same as Figure 5.8 but for 1st peak s-process elements.

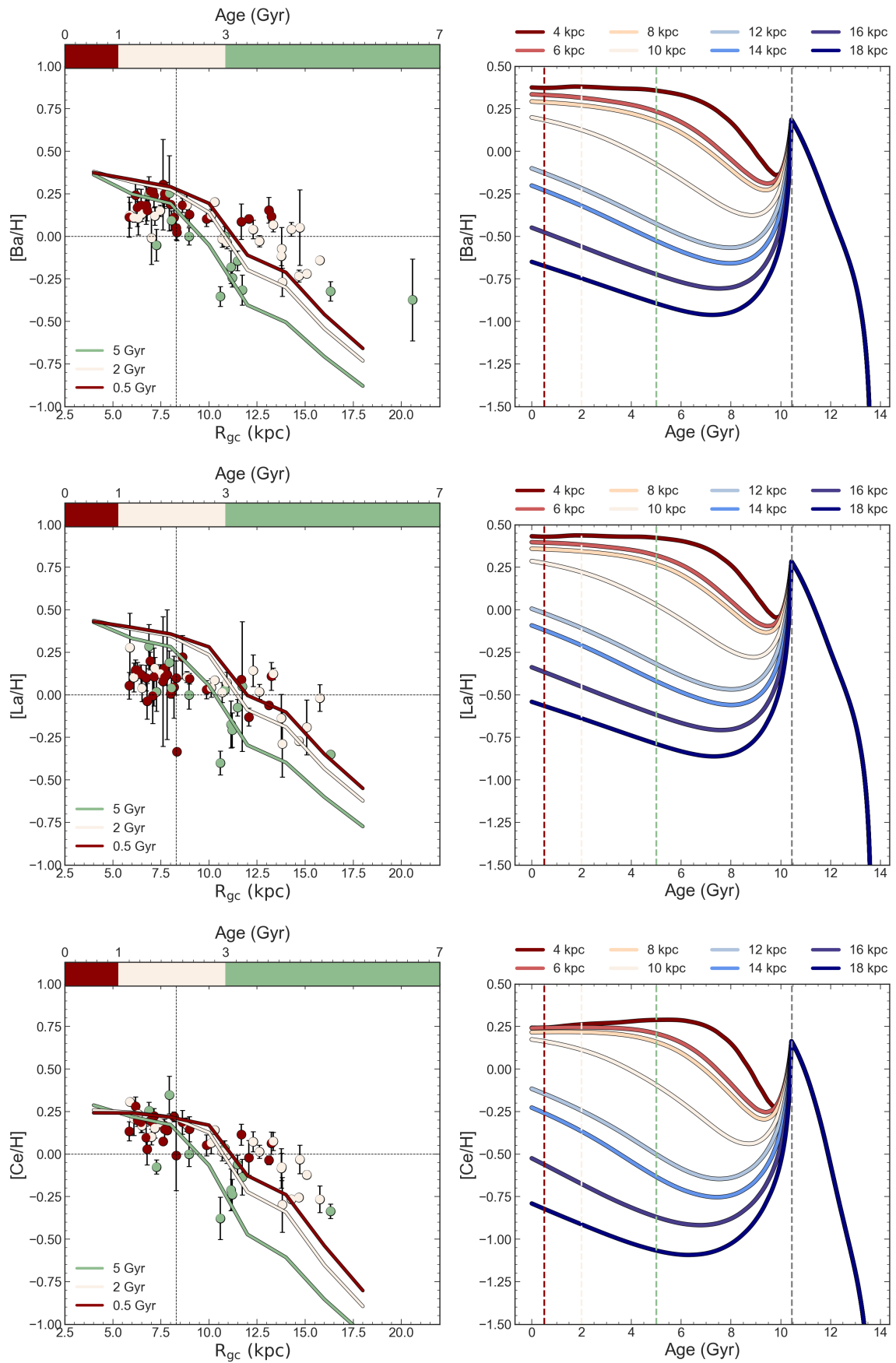


FIGURE 5.10: Same as Figure 5.8 but for 2nd peak s-process elements.

Nd abundances. It is possible to note that a similar plateau in the inner region predicted by our model for the s-process elements belonging to the second peak appears also for Nd and Pr. Once again, this may be due to the contribution from LIMS which reaches its maximum value faster in the inner regions.

5.6 Conclusions

In this Chapter, we studied the origin of neutron capture elements in the MW by taking advantage of the large sample of OCs from the *Gaia*-ESO DR6. To this aim we adopted the revised two-infall model (Palla et al., 2020; see also Spitoni et al., 2019b). We investigated the abundance patterns and the radial gradients of 5 s-process (Y, Zr, Ba, La and Ce) and 4 mixed/r-process elements (Eu, Mo, Nd and Pr). In order to do that, we adopted the following nucleosynthesis prescriptions: s-process material is produced by i) rotating massive stars ($M > 13 M_{\odot}$) with yields from Limongi et al. (2018) with three different initial rotational velocities (0, 150, and 300 km/s) and by ii) LIMS ($1 \leq M/M_{\odot} \leq 8$) with yields from the FRUITY data base (Cristallo et al., 2009; Cristallo et al., 2011; Cristallo et al., 2015) in the $1 - 6 M_{\odot}$ range, arbitrarily extrapolated up to $8 M_{\odot}$. R-process material is produced by both a prompt and a delayed source, namely i) MR-SNe which are supposed to be 20% of all massive stars with initial mass between $10 - 25 M_{\odot}$ with yields from Nishimura et al. (2017) (model L0.75) and ii) MNS with a DTD from Simonetti et al. (2019) with $\beta = -0.9$ with yields prescriptions from Molero et al. (2021a) best model. Our conclusions for the abundances patterns of $[Eu/Fe]$ vs. $[Fe/H]$ can be summarized as follows:

- The $[Eu/Fe]$ vs. $[Fe/H]$ abundance pattern is well reproduced if both a quick source and a delayed one act as r-process producers. This is a well known result in chemical evolution. However, here we stress how with the assumed prescriptions the quick source completely dominates the production of Eu, in agreement with the recent work of Van der Swaelmen et al. (2023) according to which there is no need for an additional delayed source at least to reproduce the abundance pattern in the thin disc. However, since MNS are the only observed source of neutron capture elements up to now, they cannot be excluded from chemical evolution models computations.
- The s-process elements abundances patterns is not reproduced if one considers only production from typical s-process astrophysical sources as rotating massive stars and LIMS. Rotation increases the production of s-process material, especially at low metallicities and for elements belonging to the first s-process peak, but the r-process component must also be taken into account.
- When the contribution from MNS and MR-SNe to the production of the r-process component of the s-process elements is added, MR-SNe dominate at low metallicities and it is no longer possible to appreciate differences between different rotational velocities for massive stars (up to ~ 150 km/s). The s-process abundance pattern of the OC sample is well reproduced. The rise in the outer disc data as well as the peak followed by the decrease in the

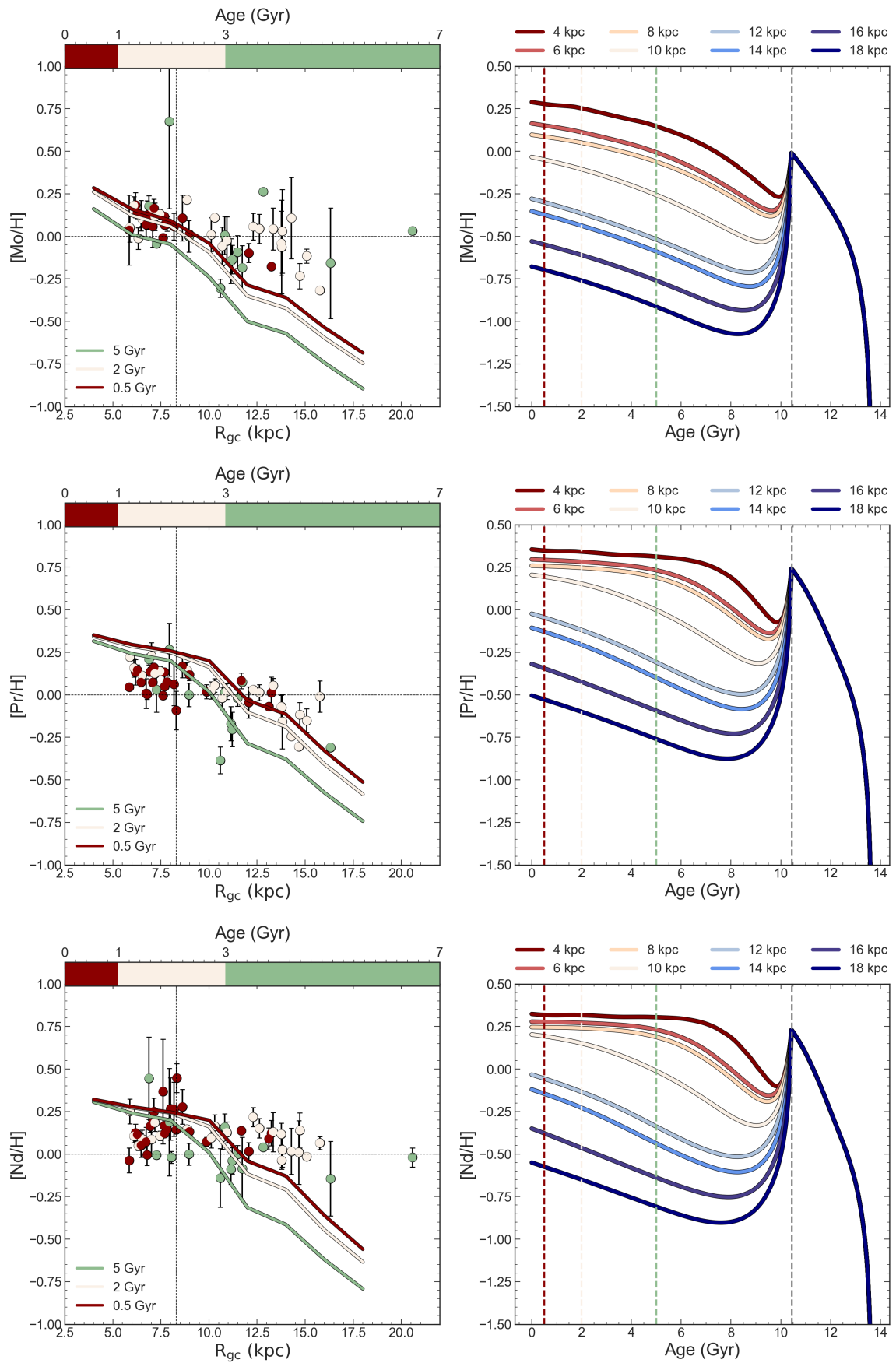


FIGURE 5.11: Same as Figure 5.8 but for mixed-process elements.

local and inner-disc are reproduced by our model at $R_{GC} = 12, 8$ and 6 kpc. Only for $[Y/Fe]$ and $[Zr/Fe]$ vs. $[Fe/H]$ in the outer region our model predicts a decrease rather than the observed increase, due to too low yields of these elements from LIMS and too high ones from MR-SNe.

- The picture for the mixed/r-process elements is more complex. A good agreement with the relevant data is obtained for Mo, even if the model still slightly underestimates the observations, most probably because of the lack of an additional contribution from neutrino-driven SNe. For Nd and Pr, we disagree with Van der Swaelmen et al. (2023), who claim that Nd is characterized by a significant s-process contribution, whereas Pr by a lower one. On the contrary, our model shows a higher production from LIMS of Pr than of Nd. Also in this case the model underproduces the $[Nd/Fe]$ vs. $[Fe/H]$ abundance pattern, while nicely reproduces the $[Pr/Fe]$ vs. $[Fe/H]$ one.

As for the abundance gradients, we first compared predictions of our model for the present day radial gradients of $[Fe/H]$ and $[Eu/H]$ with those traced by GES DR6 OCs with $Age < 3$ Gyr and Cepheids from Luck et al. (2011) and Genoali et al. (2015). Then we discussed the evolution with time of the abundance gradients of all the neutron capture elements studied in this work in comparison with the full OC sample. Our conclusions can be summarized as follows:

- The present day slope of the $[Fe/H]$ gradient predicted by our model is -0.067 ± 0.003 dex kpc^{-1} , slightly steeper both with respect to that of the restricted OC sample and to the one of the Cepheid sample, yet it agrees with other recent slopes of the $[Fe/H]$ gradient from OC samples (Carrera et al., 2019; Donor et al., 2020; Zhang et al., 2021; Spina et al., 2021; Spina et al., 2022) and in particular with the gradient computed with R_{mean} .
- The flat slope observed in the OC sample for $[Eu/H]$ is not reproduced by the model in which Eu is produced by a quick and a delayed source (MR-SNe + MNS with a DTD). Models with no delayed source (only with MR-SNe or only with MNS with a constant and short delay time for merging) do not improve the fit to the data. We discussed the possibility of flattening the predicted $[Eu/H]$ gradient by adopting a constant SF efficiency. However, we are not inclined to relax the assumption of a variable SF efficiency, since it has already been proved by many authors (e.g. Colavitti et al., 2009; Spitoni et al., 2015; Grisoni et al., 2018; Palla et al., 2020) that the inside-out scenario by itself is not able to explain the abundance patterns at different Galactocentric distances and the abundance gradients for several elements, as well as the gradient of the SFR and gas density along the thin disc (see Palla et al., 2020). A reasonable explanation for the discrepancy between model results and observations could thus be that clusters with intermediate age ($1 \leq Age \leq 3$ Gyr) are affected by radial migration. In favor of this hypothesis, predictions of our model are much more in agreement with the slopes observed in the inner-disc rather than with the outer ones and a better agreement is also obtained with the radial gradients of the Cepheid sample.

- Regarding the time evolution of the [Fe/H] gradient, results of our model for $Age = 0.5, 2$ and 5 Gyr are in agreement with the observed trend if the gradient of the youngest population is computed by removing all giant stars with $\log g < 2.5$ (see M23 for details). In particular, a really limited time evolution of the [Fe/H] gradient between the considered ages should be expected.
- Also for the [Eu/H] gradients a limited evolution with time is predicted by our model, in agreement with the observations. However, as already seen in the case of the present day gradient also at different ages we obtain slopes which are too steep with respect to the observations.
- Predictions of our model for the radial [Y/H] and [Zr/H] gradients show a very similar pattern for $Age = 0.5$ and 2 Gyr , in agreement with the OC sample. Also in the case of Ba, La and Ce the model predicts an almost identical flat or slightly decreasing pattern for all ages in the inner zone, as observed in the OC sample.
- As for the abundance patterns, also for the radial gradients much more uncertainty is present in reproducing the trend of the other mixed/r-process elements. Due to the adopted nucleosynthesis prescriptions, we underestimate the trends for Mo and Nd, and always produce steeper gradients with respect to the observed ones.
- For all the elements belonging to the second s-process peak as well as for Nd and Pr, our model produces a plateau for low Galactocentric distances at all the considered ages. This is most probably due to the effect of LIMS, whose production of those elements reaches an equilibrium value before that in the outer regions, as a consequence of a faster SF.

CHAPTER 6

Milky Way - The Bulge

IN this Chapter, I present our study of the chemical evolution of both α -elements and the neutron capture element Ce in the bulge of the MW. We assume that the bulge is formed by different stellar populations which are formed both *in situ*, following a fast and violent star formation episode, and that are accreted from the inner disc as a consequence of a growing bar.

The Chapter is organized as follows. In Section 6.1, I introduce the context of this Chapter. In Section 6.2, I describe the APOGEE sample adopted for comparison with our model. In Section 6.3, I present the chemical evolution model and the nucleosynthesis prescriptions. In Section 6.5, I show results for the bulge MDF and for the abundance patterns obtained without the inclusion of disc stars. In Section 6.4, I present results for the MDF with the inclusion of disc stars. Finally, In Section 6.6, I draw our preliminary conclusions.

6.1 Introduction

The formation and evolution of the MW bulge has been subject of intense study during the last decade. According to the original picture, the Galactic bulge can be considered a *classical bulge*, namely a spheroidal remnant of mergers of primordial structures in a Lambda cold dark matter (Λ CDM) context (Ortolani et al., 1995; Baugh et al., 1996; Abadi et al., 2003a; Abadi et al., 2003b). However, both observations of our own bulge (e.g., Binney et al., 1991; Bissantz et al., 2002; López-Corredoira et al., 2005) and observations at higher redshift (e.g., Tacchella et al., 2015; Nelson et al., 2016; Shen et al., 2023) point towards a much more complex picture. Contrary of classical bulges, *pseudo-bulges* should have formed from disc stars through vertical instability of a stellar bar (Combes et al., 1990). This scenario should lead to the formation of a triaxial boxy bar structure, the so-called boxy/peanut (B/P) shape of the Galactic bulge (Weiland et al., 1994; Wegg et al., 2013; Ness et al., 2016), which also in N -body simulations had been seen to form from barred stellar disc galaxies (Raha et al., 1991; O’Neill et al., 2003; Athanassoula, 2005; Ciambur et al., 2021; Ghosh et al., 2023). Moreover, fully formed bulges or high central SF are observed in galaxies at redshift $z \sim 2$ which suggests that those bulges assembled before the formation of the bar which, in case of MW type galaxies, should happen at $z \sim 1$ (corresponding to ~ 8 Gyr). Therefore, the mechanism responsible for the creation of those structures should rather be a fast and strong primordial collapse of gas responsible for, at least one, rapid SF episode.

The Galactic bulge region can be very hard to observe, because of the heavy extinction and crowding. Nevertheless, several spectroscopic (e.g., *Gaia*-ESO, Gilmore et al., 2012, APOGEE, Majewski et al., 2017b, Argos, Freeman et al., 2013, GIBS, Zoccali et al., 2014) and photometric (e.g., the VVVX survey, Minniti et al., 2010) surveys have been developed in order to shed light on the history of the bulge (see Barbuy et al., 2018 for a review of the different surveys). The picture which emerge from observations appears however to be quite complex. The metallicity distribution function (MDF) of stars observed in the bulge region revealed a bimodal shape (observed for the first time by Hill et al., 2011 and later confirmed by a large number of studies, e.g., Bensby et al., 2011; Uttenthaler et al., 2012; Gonzalez et al., 2015; Rojas-Arriagada et al., 2017; Zoccali et al., 2017; Rojas-Arriagada et al., 2019; Rojas-Arriagada et al., 2020; Queiroz et al., 2020; Queiroz et al., 2021; Johnson et al., 2022), which can be an indication of two (or more) stellar populations: a metal-rich (MR) population centered at $[\text{Fe}/\text{H}] \sim 0.25$ and a metal poor (MP) population centered at $[\text{Fe}/\text{H}] \sim -0.3$. The two stellar populations may also have different kinematics, with the MR one being rapidly rotating and dynamically cold and the MP one being dynamically hotter and more slowly rotating. Babusiaux et al. (2010), who further inspected the kinematics of the large sample of over 500 RGB stars presented in Zoccali et al. (2008), concluded that the MR population shows a vertex deviation compatible with the MW bar, while the MP population is compatible with a spheroid (and/or a thick disc). Moreover, results of the chemodynamical model presented by Portail et al. (2017), show that MR stars (with $[\text{Fe}/\text{H}] \geq -0.5$) are strongly barred with dynamical properties consistent with a common disc origin, while MP stars (with $[\text{Fe}/\text{H}] < -0.5$)

show more kinematic variations with the metallicity, which is interpreted as due to the contributions from different stellar populations.

As already pointed out by Baba et al. (2020), if the Galactic bar significantly impacts the dynamic of the stars in the bulge (and therefore also in the inner disc, e.g., Minchev et al., 2016), identifying its formation epoch should be one of the key questions to understand the history of the MW. As discussed above, the age of formation of the Galactic bar is very uncertain. From the distribution of infrared carbon stars, Cole et al. (2002) estimated an age of ~ 2 Gyr. From observations of luminous face-on spiral galaxies, Sheth et al. (2008) analyzed the variation with redshift of the fraction of galactic bars and estimated that the bar in spirals with similar mass of the MW should form at $z \simeq 1$ (~ 8 Gyr ago) (result which is confirmed also by zoom-in cosmological simulations from Kraljic et al., 2012). More recently, the bar formation and building epoch have been estimated to happen 8 – 9 Gyr ago also from the study of the Gaia Data Release 2 set of long-period variables of Grady et al. (2020). However, it should be pointed out that the age of the stars in the bar does not necessarily correspond to the age of the bar itself, since the bar can capture stars which may be formed before its formation (even if absence of SF in the bar can not be excluded *a priori*, see e.g., Anderson et al., 2020). This process is described by Chiba et al. (2021a) (see also Chiba et al., 2021b; Chiba et al., 2022). According to the authors, the bar experiences angular momentum loss due to dynamical friction by the dark matter halo which slows its pattern speed Ω_p (see also Hernquist et al., 1992; Debattista et al., 2000; Martinez-Valpuesta et al., 2006a). When the bar slows down, resonance sweeps radially outwards in radius throughout the disc, sequentially capturing and dragging new stars. A fraction of stars which are trapped into the corotation radius can than be captured by the bar itself. So, from a chemical point of view, stars in the bar should reflect the composition of the location where they were trapped (assuming it is the same where they were born).

The first chemical evolution model for the Galactic bulge which released the instantaneous recycling approximation has been developed by Matteucci et al. (1990) in order to explain the results of Rich (1988). The authors suggested that the Bulge should have formed on short timescales (~ 0.5 Gyr), with a more top-heavy IMF than the one of the solar neighbourhood (as Scalo, 1986 or Chabrier, 2003). The prediction of this model was a plateau in the $[\alpha/\text{Fe}]$ ratios in bulge stars longer than in the solar vicinity (see Chapter 1), which was later confirmed by McWilliam et al. (1994) and is now an observationally established fact. The prescriptions of the model were then confirmed by updated versions (e.g., Ballero et al., 2007; Cescutti et al., 2011a). Later on, more chemical evolution models started to try modelling the bimodal MDF of the bulge (e.g., Grieco et al., 2012a; Tsujimoto et al., 2012; Grieco et al., 2015), trying to explain it as due to a second infall/accretion episode. More recently Matteucci et al. (2019), successfully reproduced the MR peak of the bulge MDF by assuming a stop of ~ 250 Myr in the SF of the bulge and proposed a scenario in which the MR population is made of stars formed in the inner disc and brought into the bulge by early secular evolution of the bar. The main goal of this work is to confirm (or disprove) this hypothesis, by adopting a chemical evolution model which includes both multiple SF episodes as well as the accretion of stars from the MW disc.

6.2 Observational data

The observational data adopted in this work as a comparison to our model predictions are from Rojas-Arriagada et al. (2020), who use data of ~ 13000 stars from the SDSS/APOGEE survey to study the shape of the bulge MDF in the region constrained to $R_{GC} \leq 3.5$ kpc. According to Rojas-Arriagada et al. (2020), the shape of their MDF can be represented as the contribution of three overlapping components which, once measurement errors are taken into account, is in agreement with the bimodal MDF found in previous studies (Rojas-Arriagada et al., 2019). We compared our model with both the MDF and the abundances ratios of the α -elements Mg, O, Al and Si as well as with the neutron capture element Ce. A detailed description of the observational sample can be found in Rojas-Arriagada et al. (2020). Here we report a brief summary.

APOGEE is a high-resolution, NIR spectroscopic survey designed to perform far-reaching chemical observations of the MW stellar populations, with main targets being giant stars. Thanks to the NIR observations, APOGEE is able to observe in region of the Galaxy (such as the Galactic bulge) which are affected by extinction due to the large amount of dust of the Galactic plane. Spectra of the observed stars are extracted using the pipeline described in Nidever et al. (2015) and abundances of the different elements are computed using the APOGEE Stellar Parameters and Chemical Abundances Pipeline (ASPCAP; García Pérez et al., 2016). Spectro-photometric distances for the whole sample are calculated by following the method described in Rojas-Arriagada et al. (2017) and Rojas-Arriagada et al. (2019) and are validated against other established pipelines (e.g., STARHORSE; Queiroz et al., 2018; Queiroz et al., 2020, and ASTRONN; Leung et al., 2019). The orbital parameters are estimated by integrating orbits with the GALPY code (Bovy, 2015) under the MWPotential2014 model for the MW gravitational potential. Uncertainties for the computed orbital parameters are estimated by generating 600 random Gaussian realizations of the set of observed parameters from their individual uncertainties, from which 1σ errors are estimated which are used to set the R_{GC} limit for the stars bulge sample.

6.3 The model

The chemical evolution model adopted for the Galactic bulge is similar to the one developed by Grieco et al. (2012b) and later used by Matteucci et al. (2019) (see also Ballero et al., 2007; Cescutti et al., 2011b). We assumed that the bulge forms by fast infall of gas (see equation 2.10) with a timescale $\tau = 0.1$ Gyr. The gas is efficiently converted into stars with a SF parametrized by a Schmidt-Kennicutt law (Schmidt, 1959; Kennicutt, 1998) with $k = 1.4$ and with an efficiency of SF $\nu = 25$ Gyr $^{-1}$. The chemical evolution set of equations is the one described by equation 2.14. The adopted IMF is a Chabrier (2003), even if we investigated also the possibility of using a Salpeter (1955) IMF, as done in the previous chemical evolution works.

After the first main SF episode, mainly responsible for the formation of the MP population observed in the MDF, a second SF burst is present with a delay with

respect to the first of the order or 10^2 Myr. The second burst is partially responsible for the creation of the MR population but, as we show in the next sections, it is not enough to completely populate the MR peak observed of the MDF. Here, we assume that also a fraction of stars originally belonging to the innermost part of the MW disc are populating the Galactic bulge and are partially responsible for the formation of the MR peak. The disc is modelled as described in Chapter 5.

For both the Galactic bulge and the inner disc the same nucleosynthesis prescriptions are adopted, which are those used in Molero et al. (2023b). In particular, for massive stars, besides testing the three sets of yields of Limongi et al. (2018) corresponding to three velocities (0, 150 and 300 km/s), three more sets have been considered, corresponding to three different theoretical distributions for the initial rotational velocities. These new sets of yields have been obtained by assuming that the probability that a star rotates at a certain speed is a function of the metallicity, Z , with faster initial rotational velocities being most likely at lower Z . In this way, we obtained the first two distributions (DIS 1 and DIS 2) reported in Figure 6.1. In DIS 2, velocities of 0 km/s and of 150 km/s are slightly more likely than in DIS 1 at intermediate and high metallicities. The third distribution shown in the Figure, DIS 3, is the one adopted by Romano et al. (2019) for studying the CNO isotopes, according to which rotation becomes negligible beyond a metallicity threshold equal to $Z = 3.236 \times 10^{-3}$ (corresponding to $[\text{Fe}/\text{H}] = -1$ dex). All the three distributions are supported by the fact that massive stars are expected to rotate faster at lower metallicities, where they are more compact. This view is supported both theoretically (Frischknecht et al., 2016) and by the observations of an increase ratio of Be/B-type star with increasing metallicity (Martayan et al., 2007a; Martayan et al., 2007b), as well as by the presence of faster rotating massive stars in the Small Magellanic Cloud than in the MW (Hunter et al., 2008) and by observations of stars in the globular cluster NGC6522 with high abundances of s-process elements (Chiappini et al., 2011). We assume a flat distribution of the initial rotational velocities with the stellar mass. Although this is a simplification, it still finds agreement in theoretical computations (e.g., Frischknecht et al., 2016) which show that for the same metallicity and initial ratio of surface velocity to critical velocity ($v_{\text{ini}}/v_{\text{crit}}$), the changes in the surface velocity during the MS phase as a function of mass are relatively small and in any case less than the variations as a function of metallicity.

As mentioned in the Introduction, the MW bar does not exhibit static rotation. Indeed, simulations of the Galactic bar in the presence of dark matter indicate that the bar experiences angular momentum loss, leading to a decrease in its rotational frequency and an expansion of the bar (Hernquist et al., 1992; Martinez-Valpuesta et al., 2006b; Bhattarai et al., 2022). As described by Chiba et al. (2021a), as the bar decelerates, the resonance regions sweep through the stellar phase-space, capturing and dragging a number of stars. Chiba et al. (2021b) estimated an increase in corotation radius, R_{cr} , since the formation of the bar (here assumed to happen 8 Gyr ago) of at least $\Delta R_{\text{cr}} = 1.6$ kpc. If we assume that the bar also grows by the same fraction, then:

$$\Delta R_b = \Delta R_{\text{cr}} \frac{R_b}{R_{\text{cr}}} = 1.2 \text{ kpc}, \quad (6.1)$$

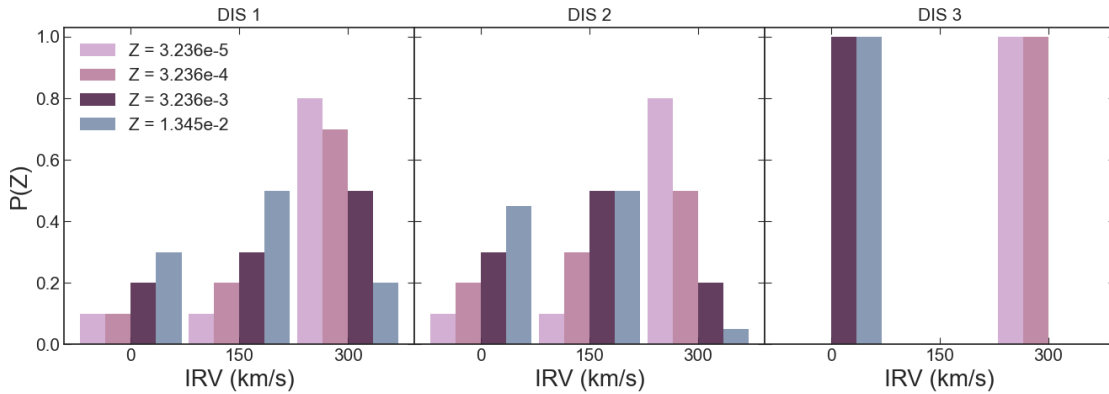


FIGURE 6.1: Probability distributions of initial rotational velocities (IRV) for massive stars as a function of the metallicity (Z).

where $R_b = 5$ kpc is the bar half-length (Wegg et al., 2015) and $R_{cr} = 6.6$ kpc (Chiba et al., 2021b; Clarke et al., 2022). The fraction of stellar mass swept away by the growing bar is then:

$$f = \frac{2\pi\Delta R_b \times R_b \Sigma(R)}{M_b}, \quad (6.2)$$

where $M_b \simeq 10^{10} M_\odot$ is the bar mass (Bland-Hawthorn et al., 2016). Therefore, given a stellar surface mass density predicted by our model at $R_{GC} = 5$ kpc of $\Sigma(5 \text{ kpc}) \simeq 143 M_\odot/\text{pc}^{-2}$, we can compute the fraction of stellar mass which is trapped by the growing bar at 5 kpc, which is $f \simeq 53\%$. This must be considered an upper limit since (i) not all the stars that are trapped into the corotation resonance will also be part of the bar and (ii) only a fraction of stars trapped in the bar will live long enough to populate the Galactic bulge region (which in our model extends until 3 kpc).

6.4 Results without the bar

In the following sections, we present results for the MDF and the abundance patterns as predicted by the best model proposed in Matteucci et al. (2009), but with updated yield from rotating massive stars, alongside results obtained from the newly developed models presented in the last Section (see Table 6.1).

6.4.1 Metallicity distribution function

In Figure 6.2, we report the results of models M19-0, M19-150 and M19-300 obtained with the prescriptions of the best model of Matteucci et al. (2019) (their model D) but with updated yields for rotating massive stars. None of the three models is able to reproduce the MDF observed in the new set of observational data. The predicted MDFs are shifted towards low metallicities, in particular in the case of model M19-0 where the MDF is peaked at $[\text{Fe}/\text{H}] \simeq -0.6$ dex. In the case of models M19-150 and M19-300 the peak is at higher metallicities, at $[\text{Fe}/\text{H}] \simeq -0.3$ dex, since rotation in massive stars increases the production of Fe.

TABLE 6.1: *Input parameters for the chemical evolution models. In the first column we specify the name of the model, in the second we indicate the initial rotational velocity of massive stars, in the third column it is specified the duration of the stop in the SF and in the last column the adopted IMF*

Model	IRV	δt_{SF} (Myr)	IMF
M19-0	0 km/s	250	Salpeter
M19-150	150 km/s	250	Salpeter
M19-300	300 km/s	250	Salpeter
C-0A	0 km/s	250	Chabrier
C-150	150 km/s	250	Chabrier
C-300	300 km/s	250	Chabrier
D-1	DIS 1	250	Chabrier
D-2A	DIS 2	250	Chabrier
D-3A	DIS 3	250	Chabrier
C-0B	0 km/s	0	Chabrier
C-0C	0 km/s	150	Chabrier
C-0D	0 km/s	350	Chabrier
D-2B	DIS 2	0	Chabrier
D-2C	DIS 2	150	Chabrier
D-2D	DIS 2	350	Chabrier
D-3B	DIS 3	0	Chabrier
D-3C	DIS 3	150	Chabrier
D-3D	DIS 3	350	Chabrier

Notes. For the first three models, M19-0, M19-150 and M19-300, the ‘M19’ stands for Matteucci et al. (2019), and the number specifies the adopted initial rotational velocity of massive stars. For the remaining models, the first letter (‘C’ or ‘D’) stands for ‘constant’ or ‘distribution’ for the initial rotational velocity of massive stars. The following number specifies the value of the velocity or the number of the distribution. The second letter, when present, (‘A’, ‘B’, ‘C’ or ‘D’) refers to the main model (with a stop in the SF of 250 Myr), or to its variations corresponding to the different durations of the SF stop. So that, for example, model C-0A has a constant initial rotational velocity of 0 km/s and a stop in the SF of 250 Myr.

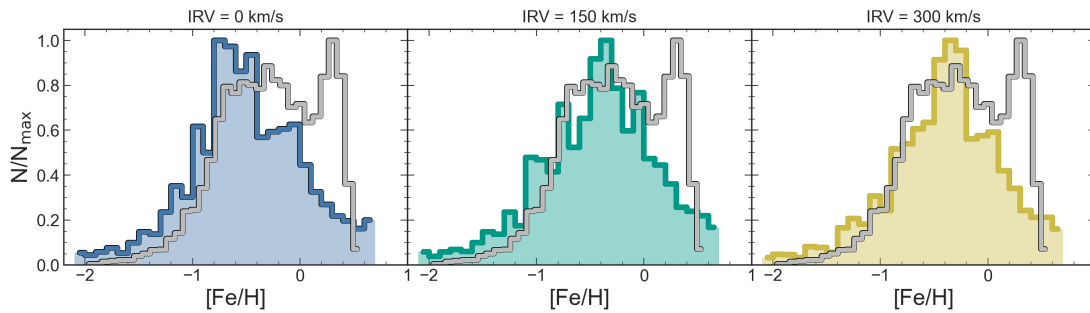


FIGURE 6.2: *MDFs as predicted by models M19-0, M19-150 and M19-300 obtained with the prescriptions of Matteucci et al. (2009) best model with yields of rotating massive stars with initial velocity equal to 0 km/s (left panel), 150 km/s (middle panel) and 300 km/s (right panel).*

However, the observed MR peak is still not reproduced, and, moreover, all of the models overestimate stars in the low metallicity regime.

In Figure 6.3, we present the results of models C-0A, C-150, and C-300 in the first row, and of models D-1, D-2A, and D-3A in the second row. All the models show an improved agreement with data with respect to old models. Specifically, models C-0A, D-2A, and D-3A effectively reproduce the positions of the first and second MDF peaks. In contrast, models C-150, C-300, and D-1 show a less good fit with the data, yielding to similar MDF shapes: the two MP peaks are shifted towards too high metallicities, with a notable underproduction of stars in the intermediate metallicity range ($-1 \leq [\text{Fe}/\text{H}] \leq -0.25$ dex).

The drop produced by all of the models between the MP and the MR peak appears to be slightly too deep with respect to the observed one. The depth of the drop in the MDF increases with the duration of the SF stop. This can be seen in Figure 6.4, where we increase the duration of the SF stop from 0 to 150, 250 and 350 Myr (models C-0(A-D), D-2(A-D) and D-3(A-D)). The longer the SF stop lasts, the deeper the drop will get in the MDF and, as a consequence, a higher second peak in the MDF will be obtained. In the time interval during which the SF is quenched, no star is produced and the production of Fe slows down because of the lack of new massive stars (Type Ia SNe are still active, therefore the production of Fe is not completely stopped). While the SF is quenched, the gas builds up due to the ongoing infall, hence at the end of a longer stop more gas is accumulated. When the SF resumes, since it is proportional to the gas available in the ISM, it will be stronger after a longer stop, and as a consequence the stellar number density will be larger. This can be seen in Figure 6.5, where we report the evolution of the SF, $[\text{Fe}/\text{H}]$ and surface number density of stars as a function of time in case of a stop in the SF of 150, 250 and 350 Myr. Thus, the height of the MR peak can be modelled by changing the duration of the SF stop or, as recently analyzed by Romano et al. (2023) for the chemical enrichment of the bulge fossil Terzan 5, by removal of a major fraction of the gas left over from the first SF episode.

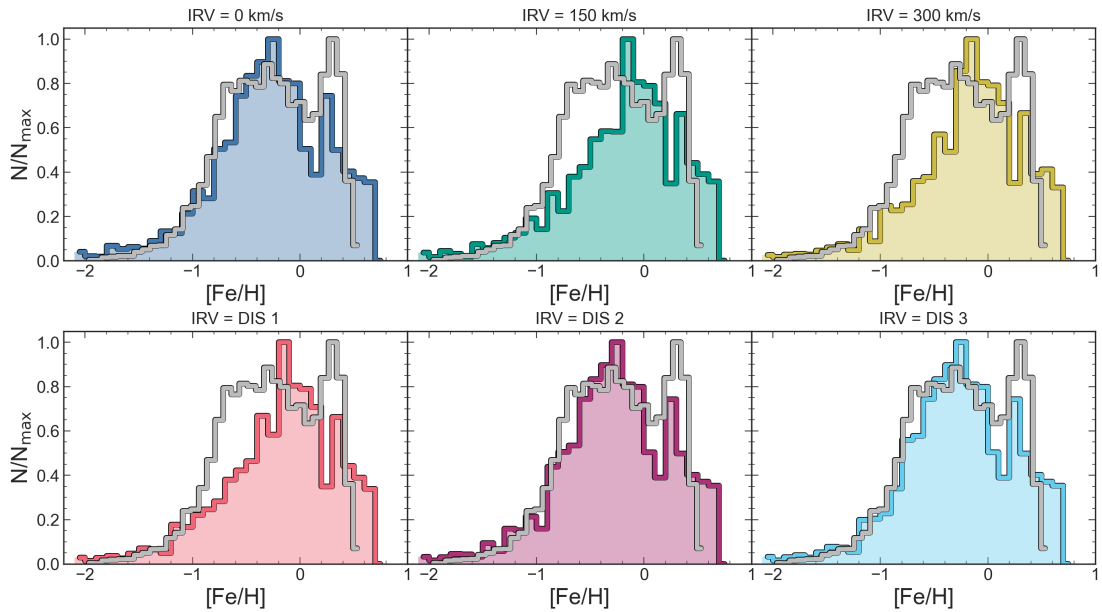


FIGURE 6.3: MDFs predicted with a Chabrier IMF and a stop in the SF lasting 250 Myr. The MDFs differ for the different initial rotational velocities adopted. Models C-0A, C-150 and C-300 in the first row, with constant initial rotational velocities and models D-1-, D-2A and D-3A characterized by a diistribution of the initial rotational velocities (see Table 6.1).

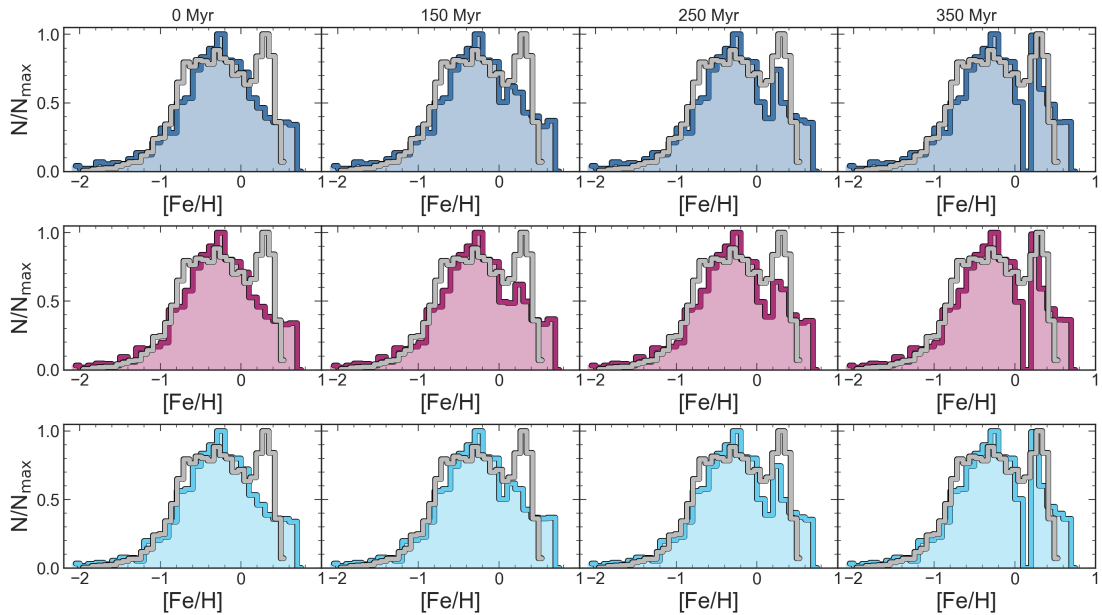


FIGURE 6.4: MDFs predicted by models C-0(A-D) (first row), D-2(A-D) (second row) and D-3(A-D) (third row) characterized by a different duration of the SF stop.

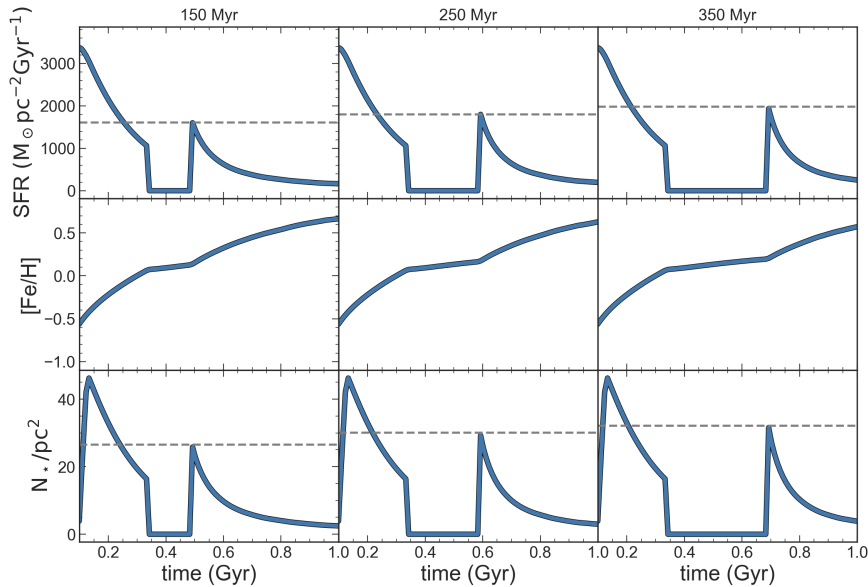


FIGURE 6.5: *SFR, $[Fe/H]$ and surface number density of stars as a function of time predicted by models C-0(A, C, D).*

6.4.2 Abundance patterns

In Figure 6.6, we report the $[\alpha/Fe]$ vs. $[Fe/H]$ abundance patterns of Mg, O, Al and Si as predicted by models C-0(A-D), D-2(A-D) and D-3(A-D). Models with a stop in the SF produce a hole in the $[\alpha/Fe]$ vs. $[Fe/H]$ visible also in the APOGEE data which show indeed two overdensity regions in correspondence of $[Fe/H] \simeq -0.5$ dex and $[Fe/H] \simeq 0.25$ dex. The hole in the abundance patterns occurs because the stop in the SF causes a stop in the production of α -elements from massive stars, while the Fe production continues (even if it is strongly slowed down) thanks to Type Ia SNe and their longer time-delays. The bimodal distribution which is present in the set of data used in this work is also reported by Queiroz et al. (2021) (see also Rojas-Arriagada et al., 2019; Queiroz et al., 2020), although in their case the depression between the two peaks seems to be more pronounced, and the two sequences are more noticeably distinct. However, the different datasets are comparable and their differences are not affecting our conclusions.

Rotation in massive stars increases the production of O and Si, while reduces that of Mg, independently from the metallicity. Only in the case of Al the effects of rotation is different at different metallicity: it enhances Al production at low $[Fe/H]$ but diminishes it at higher $[Fe/H]$. All the models are underestimating the $[Mg/Fe]$ vs. $[Fe/H]$ trend and overestimating the $[Si/Fe]$ one. Model C-0(A-D) is the one which best reproduce the $[Al/Fe]$ vs. $[Fe/H]$ as well as the $[O/Fe]$ vs. $[Fe/H]$, even if deviations at low metallicities are present. The general trend of the observed abundance ratio is however well reproduced by model C-0(A-D), in particular with a stop of 250 Myr (model C-0A). Deviations from the observed pattern are therefore due either to the adopted set of yields or to the IMF, or to a combination of both. A Salpeter (1955) IMF would indeed predict lower abundance patterns for the α -elements, because of a lower production of massive stars. Therefore, by keeping the same set of yields, this would improve the agreement with the $[O/Fe]$ and $[Si/Fe]$ vs. $[Fe/H]$ trends but, at the same time, would worsen the

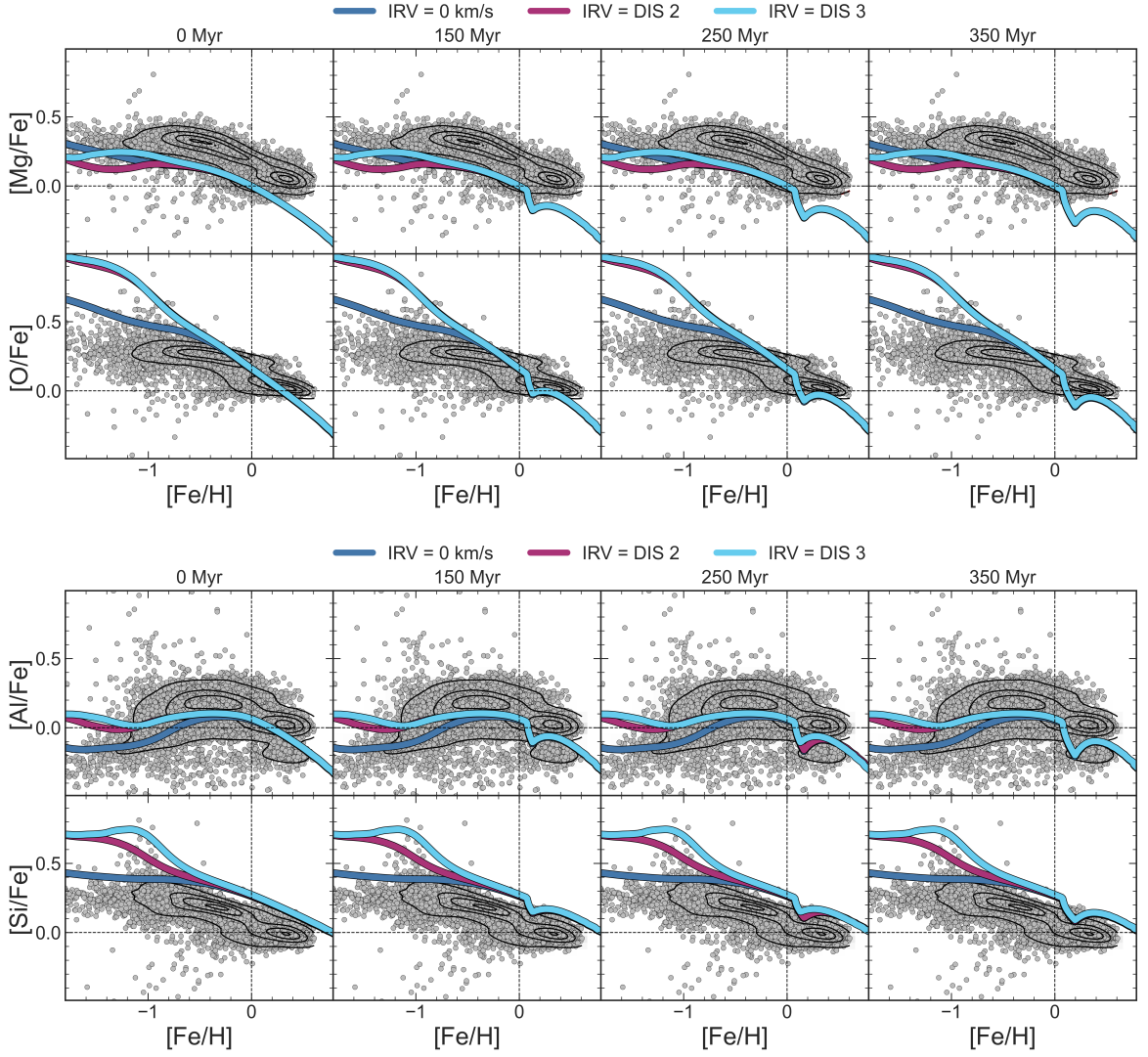


FIGURE 6.6: Predicted $[Mg/Fe]$, $[O/Fe]$, $[Al/Fe]$ and $[Si/Fe]$ vs. $[Fe/H]$ trends for models C-0(A-D), D-2(A-D) and D-3(A-D).

ones with the $[Mg/Fe]$ and $[Al/Fe]$ as well as with the MDF (as shown in the previous section). Concerning the yields variations, adopting the set of Kobayashi et al. (2006) (which accounts for mass loss but not for rotation), produces the results shown in Figure 6.7 for both a Salpeter (1955) and a Chabrier (2003) IMF. The $[Mg/Fe]$ vs. $[Fe/H]$ trend is improved with respect to model C-0A, in particular by adopting a Salpeter (1955) IMF (see Matteucci et al., 2019), but for what it concerns the other elements the fit with the data is poorly improved or gets even worse.

In Figure 6.8, we report results of models C-0(A-D), D-2(A-D) and D-3(A-D) for the $[Ce/Fe]$ vs. $[Fe/H]$ abundance pattern. The characteristic ‘banana’ shape of s-process elements can be seen in the data at $-0.77 \simeq [Fe/H] \simeq 0.60$ dex. At lower $[Fe/H]$, dispersion in the data is also present with mean value $[Ce/Fe] \simeq 0.20$ dex. The bimodal distribution clearly seen in the α -elements is less evident for Ce. Indeed, also in the model results, the different duration of the SF stop has very

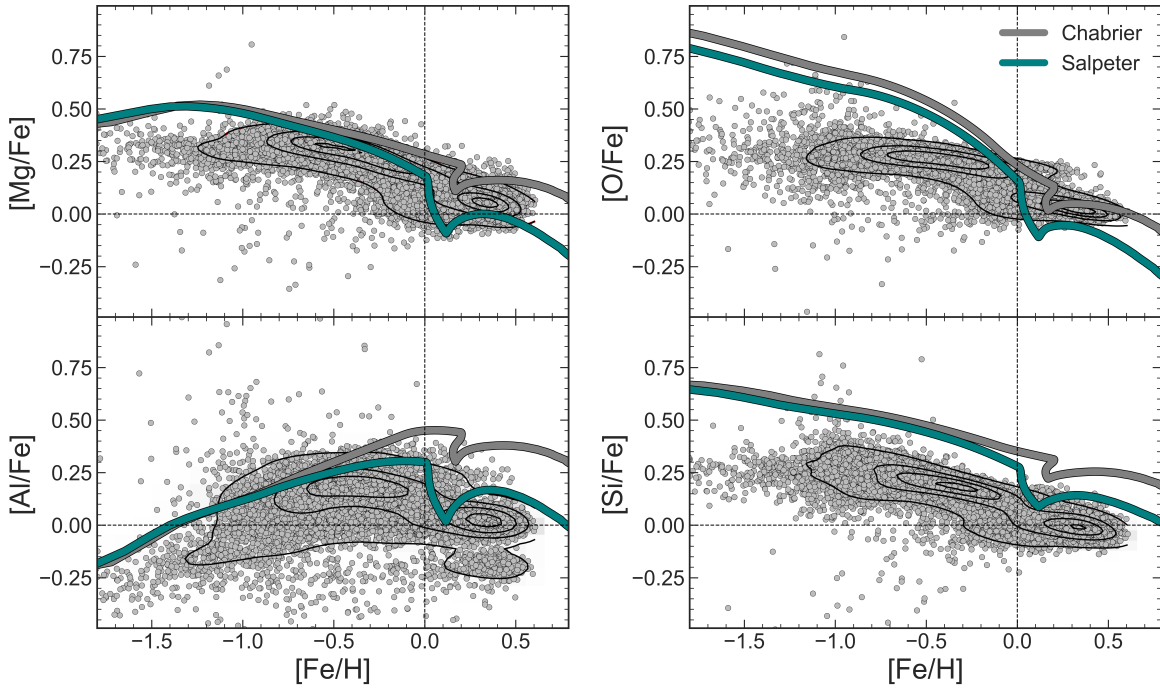


FIGURE 6.7: Predicted $[Mg/Fe]$, $[O/Fe]$, $[Al/Fe]$ and $[Si/Fe]$ vs. $[Fe/H]$ trends with yields set for massive stars from Kobayashi et al. (2006) and different IMFs.

little impact, without affecting too much the comparison with the data. For the s-process elements, such as Ce, rotation in massive stars increases their production, especially at low metallicities (see also Chapter 5). As already discussed in Chapter 5, it is possible to note the strong effect of the MR-SNe at low metallicities responsible for the creation of the plateau visible in models C-0(A-B). When higher rotational velocities for massive stars are considered, then their contribution dominates at low $[Fe/H]$. However, because of the high rotation of massive stars, models D-3(A-D) are overproducing the $[Ce/Fe]$ vs. $[Fe/H]$ trend at low $[Fe/H]$, while models D-2(A-D) and C-0(A-D) are more in agreement with the data. At higher $[Fe/H]$, LIMS dominate the production of s-process elements, creating a bump in the $[Ce/Fe]$. With the adopted sets of yields, however, the production of Ce from LIMS is too strong, and it should be reduced of at least a factor 4 in order to have a better agreement with the data, as shown by the blue dashed line in the Figure, corresponding to models C-0(A-D), but with reduced AGB yields.

6.5 Results with accreted stars

As discussed in the Section 5.1, in this work we are testing the hypothesis put forward by Matteucci et al. (2019), according to which the MR peak of the Galactic bulge is due to both stars which are formed *in situ* and by stars which formed in the innermost part of the Galactic disc and got trapped in the Galactic bar. This can be also supported by the MDF of the innermost part of the Galactic disc obtained by our model which has a peak at a similar value of $[Fe/H]$ of the MR peak of the bulge MDF. This is shown in Figure 3 of Matteucci et al. (2019), where the adopted model for the disc is the one-infall model of Grisoni et al. (2017) with

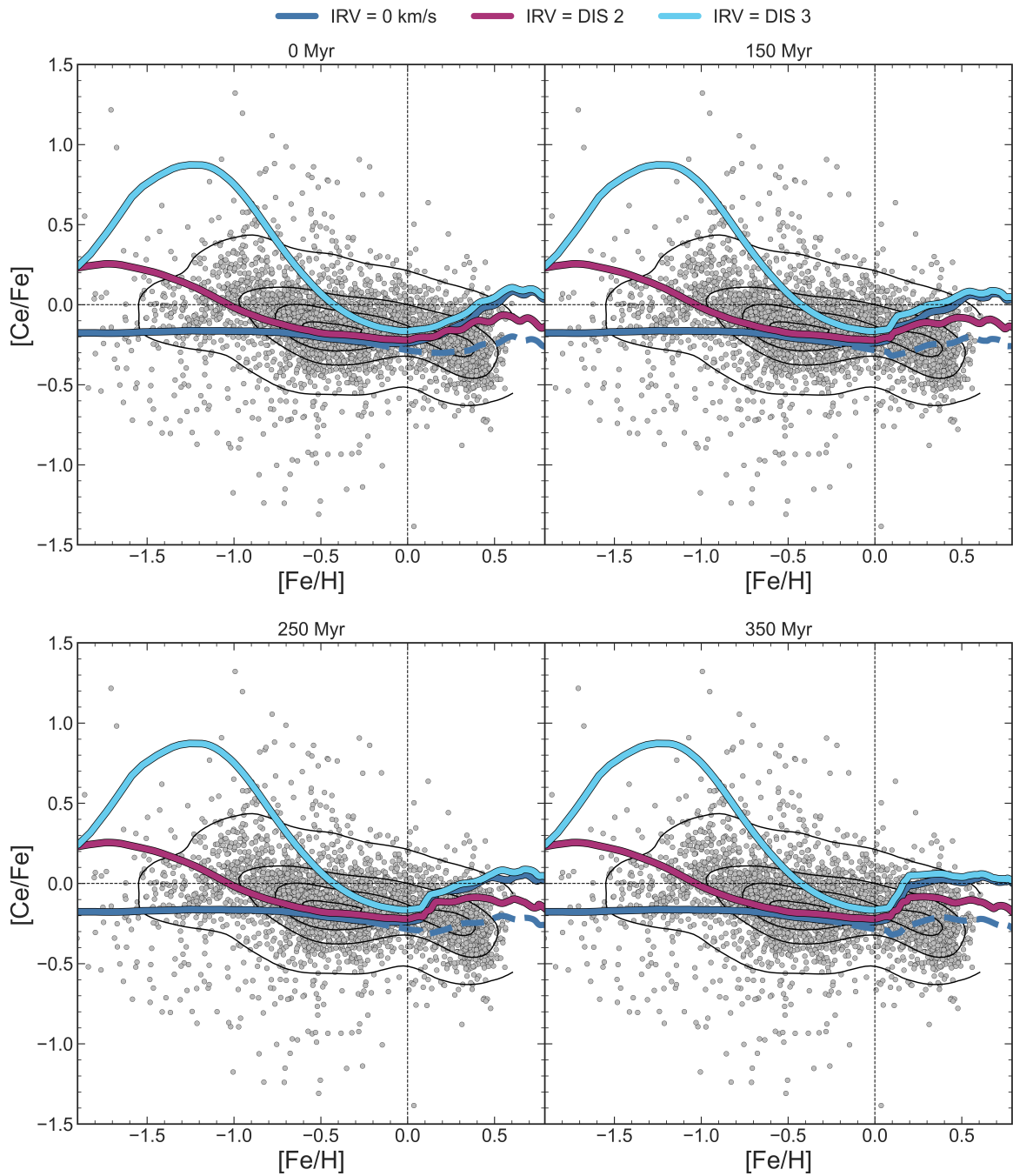


FIGURE 6.8: Same as Figure 6.6 but for Ce. The purple dashed line correspond to model DIS2 but with reduced yields from LIMS.

constant SF efficiency of 1 Gyr^{-1} , a Kroupa et al. (1993) IMF and nucleosynthesis prescriptions from Romano et al. (2010). Here, for consistency with our previous more recent works, we are using the delayed two-infall model presented in Chapter 4 (see Spitoni et al., 2019b; Spitoni et al., 2020; Palla et al., 2020; Molero et al., 2023b) with a SF efficiency of 9 Gyr^{-1} in the inner region of the disc (see e.g., Colavitti et al., 2009), nucleosynthesis prescriptions from Molero et al. (2023b) best model and a Kroupa et al. (1993) IMF.

In Figure 6.9, we present the results of models C-0(A-C) for the MDF, which includes the contribution of stars from the inner disc. To account for the fraction of stars, initially calculated as an upper limit in Section 6.3, we performed tests with varying values, namely $f = 10, 20, 30, 40\%$. As shown in the first row of the figure, when we do not consider any stop in SF, incorporating a certain percentage of stars from the Galactic disc alone does not suffice to replicate the MR peak observed in the MDF. However, assuming a SF stop of 150 Myr leads to an improved agreement with the data. Among the models, it is Model C-0A, with a 250 Myr SF stop and an inclusion of $f = 40\%$ stars from the inner disc, that best reproduces the observed results. Both the MP and the MR peaks within the MDF are notably well-matched, not only in terms of their positions but also in terms of their relative heights.

6.6 Conclusions

In this Chapter, we presented our preliminary study on the chemical evolution of the Galactic bulge. The model for the Galactic bulge is based on the previous model of Matteucci et al. (2019), and it is mainly constrained to the shape of the bulge MDF as observed in the sample of ~ 13000 giant stars coming from the APOGEE DR16 (Rojas-Arriagada et al., 2020). Our main assumption is that the MW bulge has been formed by a strong SF episode, triggered by a fast collapse of primordial gas, which is mainly responsible for the creation of the MP population observed in the MDF as well as in the $[\alpha/\text{Fe}]$ vs. $[\text{Fe}/\text{H}]$ abundance patterns. A second, smaller burst of SF as well as accretion of disc stars from the Galactic bar are the phenomena assumed to be responsible for the creation of the MR stellar population. Our main preliminary conclusions are the following:

- The best model of Matteucci et al. (2019), which assumes a delay between the two SF bursts of 250 Myr, is not able to reproduce the observed MDF function of the bulge represented by the data set of Rojas-Arriagada et al. (2020), if yields for rotating massive stars from Limongi et al. (2018) are considered together with a Salpeter (1955) IMF.
- By adopting a Chabrier (2003) IMF, instead than a Salpeter (1955) one, the agreement with the data is improved. In particular, model which assumes no rotational velocity in massive stars or a distribution of rotational velocities which favours slow rotation at the present time are the ones which better reproduce the observed MDF.

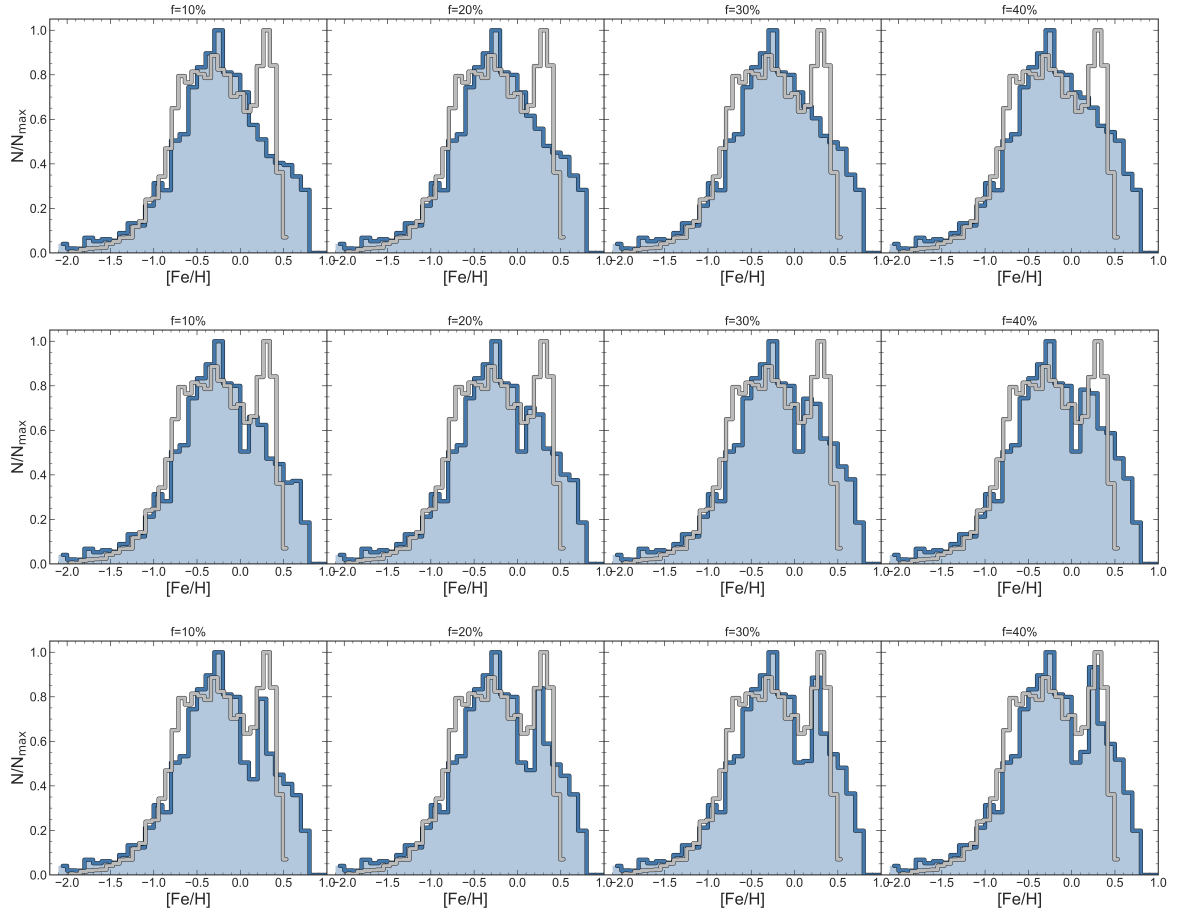


FIGURE 6.9: *MDF of the Galactic bulge predicted by models C-0(A-C) with no stop in the SF (first row, model C-0B), 150 Myr of stop (second row, model C-0C) and 250 Myr (third row, model C-0A) and with different fractions of stars contributing to the bar.*

- The observed abundance trends of α -elements are well reproduced with a delay between the two SF bursts of 250 Myr, but all the models are underproducing the [Mg/Fe] vs. [Fe/H] trend and overproducing the [Si/Fe] one. The model with no rotation of massive stars is the one which best reproduces the [Al/Fe] vs. [Fe/H] as well as the [O/Fe] vs. [Fe/H], even if deviations at low metallicities are present. The situation is slightly improved by using a different set of yields (the one from Kobayashi et al., 2006) only in case of Mg.
- A model with no rotation of massive stars is also the one which best reproduces the [Ce/Fe] vs. [Fe/H] trend, mainly because of the contribution from MR-SNe at low metallicities. However, the abundance pattern is overestimated at high [Fe/H], because of the too strong impact of AGB stars.
- In order to reproduce the MR peak of the MDF we estimate that at least $\sim 40\%$ of stars should get trapped by the growing bar. However, if no stop in the SF is assumed, contamination of stars from the inner disc is not sufficient to fully reproduce the MR peak of the MDF and a stop in the SF of 250 Myr must still be considered.

Elliptical Galaxies - The AGN Feedback

IN this Chapter, I present our study on the formation and evolution of elliptical galaxies and on how they suppress star formation and maintain it quenched. Elliptical galaxies with different infall masses, following a downsizing in star formation scenario are considered, with great emphasis on the feedback processes. We included heating by stellar wind, CC-SNe, Type Ia SNe and active galactic nucleus (AGN), which is a novelty in this kind of models.

The Chapter is organized as follow. In Section 7.1, I introduce the context of this work. In Section 7.2, I present the chemical evolution simulations, the nucleosynthesis prescriptions and the energetic treatment. In Section 7.3, we show results obtained when no AGN feedback is adopted. Section 7.4, is devoted to the description of the adopted treatment for the black hole accretion, luminosity and feedback, and also results obtained with the new energy formulation are presented. Finally, in Section 7.5 I present our discussion and conclusions.

The results presented in this Chapter are described in the published paper Molero et al. (2023a).

7.1 Introduction

Metal abundances are important since they are directly related to stellar mass loss and SNe ejecta, and they can provide constraints on the history of SF, IMF and metal enrichment history of the ISM. Early-type galaxies (ETGs) are metal rich systems characterized by having high $[\alpha/\text{Fe}]$ ratios in their dominant stellar population, with super-solar $[\text{Mg}/\text{Fe}]$ in the nuclei of bright galaxies (Faber et al., 1992; Carollo et al., 1993). This is an important indicator of the fact that elliptical galaxies suffered a short duration of SF, since Type Ia SNe, which occur on a large interval of timescales, should not have had time to pollute significantly the ISM before the end of the SF, and therefore could not contribute to lower the $[\alpha/\text{Fe}]$ ratio (according to the *time-delay model*, Matteucci et al., 2001). Moreover, the increase of the central $[\text{Mg}/\text{Fe}]$ ratio with the stellar velocity dispersion suggests, always on basis of the time-delay model, that the more massive systems evolve faster than the less massive ones. This process is known as *downsizing in star formation* (Cowie et al., 1996; Heavens et al., 2004; Treu et al., 2005).

In order to account for this trend in the SF, the *monolithic model* for the formation and evolution of ellipticals, first suggested by Larson (1975), assumes that ellipticals suffer an intense SF and quickly produce galactic winds when the energy injected into the ISM equates the potential energy of the gas. SF is then quenched and galaxies are evolving passively afterwards. Then, in order to reproduce the increasing trend of the $[\text{Mg}/\text{Fe}]$ with galactic mass, Matteucci (1994) first computed models for ellipticals with a shorter period of SF in larger systems, assuming an increasing efficiency of SF with the galactic mass. As a consequence, galactic winds occur earlier in more massive galaxies (*inverse wind scenario*) and the $[\alpha/\text{Fe}]$ ratio increases with galaxy stellar mass.

Galactic outflows are both theoretically expected (Tomisaka et al., 1988) and observationally detected (Heckman et al., 1990). Physically, they are expected to be driven by the energy released from stars and SNe (Chevalier et al., 1985), as well as from supermassive black holes (SMBH, Begelman et al., 1991). Active galactic nucleus (AGN) feedback is fundamental to control the BH growth and the AGN activity itself, by regulating the evolution of the physical properties of the surrounding gas, and therefore the BH accretion and luminosity. Outflows and feedback are fundamental aspects of galaxy formation and evolution, however the underlying physical mechanisms are complex and it is still debated whether AGN feedback is the main driver of galaxy evolution and to what level it impacts on the physical properties of the bulk of the gas in galaxies (Valentini et al., 2021). Indeed, much more investigation is still needed. There exist many theoretical works which address this important question by adopting different treatments of the feedback processes: the energetic output is usually parametrized by invoking stellar winds, SNe and/or AGNs, or a combination of these.

Results of semi-analytic works, which have been conducted in recent decades, point out that the most important mechanism able to suppress the SF activity is stellar feedback (both in form of stellar winds and SN explosions), at least in relatively low-mass elliptical galaxies (Somerville et al., 1999; Benson et al., 2003; Bower et al., 2006; Bower et al., 2012; Pan et al., 2017). For high mass galaxies instead, AGN feedback can efficiently regulate the SF activity (Silk et al., 2012; Li

et al., 2018). On the other hand, theoretical studies based on large-scale cosmological simulations find that the energy feedback from Type II SNe alone is not enough to quench the SF activity both in low- and in high-mass elliptical galaxies and an energy source from radiation, wind and radio jets from the central AGN is needed (Croton et al., 2006; Lu et al., 2007; Choi et al., 2015; Davé et al., 2016; Taylor et al., 2017; Weinberger et al., 2017). These results are often a consequence of a poor modelling of the energy feedback from SNe, especially from Type Ia SNe, being one of the most difficult processes to model in galaxy-formation simulations (see Kawata et al., 2003 and references therein, but see also Scannapieco et al., 2006; Scannapieco et al., 2008; Jiménez et al., 2015).

However, as also pointed out by Li et al. (2018), the cosmological simulations, compared to analytical models, are better at capturing the environmental effects occurring during the cosmological evolution of galaxies, but the scales on which the feedback processes operate are much smaller than the typical resolution of the simulations and a much higher resolution is needed in order to focus on the relatively small scales of influence of the different feedback processes (even if the situation is improving in recent years: e.g. Curtis et al., 2016; Costa et al., 2020; Anglés-Alcázar et al., 2021).

Many hydrodynamical simulations have been carried out in this direction in order to study the feedback processes in detail, both focusing on the effect of the AGN feedback (Binney et al., 1995; Choi et al., 2012; Gan et al., 2014; Ciotti et al., 2017; Yuan et al., 2018; Ciotti et al., 2022) and on the role of SN feedback (Ciotti et al., 1991; Smith et al., 2018; Lanfranchi et al., 2021). The main advantage of hydrodynamical models is that complex physical effects can be taken into account with high accuracy. However, the computational times of those simulations are long and sometimes it is useful to search for less time-consuming solutions, usually represented by one-zone models. In this work, we adopt a one-zone chemical evolution model. These models are very detailed in computing the chemical abundances and can take into account dynamical processes in a simple way (Sazonov et al., 2005; Ballero et al., 2008; Matteucci, 2008; Lusso et al., 2011). Interesting cases that can be identified by those models can then be simulated in much more detail with hydrodynamical codes.

In this work, we adopt an updated version of Matteucci (1994) chemical evolution model for elliptical galaxies, where the SN rates are computed in details as well as the stellar nucleosynthesis. The main novelty of this model is the inclusion of the AGN feedback, besides that of SNe and stellar winds. In particular, we study the evolution of ETGs with different initial infall of gas mass (between $10^{10} - 5 \times 10^{12} M_{\odot}$). The evolutionary scenario that we consider is the following: ellipticals are formed by infall of gas in a primordial dark matter halo and its evolution is influenced by infall and outflow of gas as well as by stellar nucleosynthesis. The system goes through an early intense burst of SF, which is then quenched when strong galactic winds are produced and the galaxy evolves passively afterwards. This happens when the thermal energy of the gas in the ISM exceeds its binding energy. We study both the case in which the gas is thermalized only by stellar winds and SNe of all types, with particular attention to Type Ia SNe, and the case in which AGN feedback also contributes to the thermal energy of the gas.

7.2 The model

In order to study the chemical evolution of ETGs, we adopt a new model based on the main assumptions presented in Matteucci (1994) and similar to the most recent model of De Masi et al. (2018). The model is one zone but it can be easily extended to be multi-zone. It assumes instantaneous and complete mixing of gas. It is able to follow in detail the evolution of 22 chemical species, from H to Eu, from the beginning of SF up to the present time. It is assumed that galaxies form by infall of primordial gas in a pre-existing diffuse dark matter halo with a mass about 10 times the total mass of the galaxy. Stellar lifetimes are taken into account, thus relaxing the instantaneous recycling approximation (IRA). An early intense burst of star formation is followed by a massive galactic wind. After this main wind the galaxy can continue to loose mass or just stop the wind, depending on the assumptions made on feedback and gravitational potential, as we will describe in the next Sections.

7.2.1 Basic equations

The fundamental equations which describe the temporal evolution of the mass fraction of the generic element i in the gas $X_i(t)$ are the one described by Eq. 2.14, with the addition of an extra term $(-X_i(t)\dot{M}_{\text{BH}}(t))$ due to the presence of a BH in the centre of the galaxy which represents the rate at which the mass fraction of gas in the form of the chemical element i is accreted by the BH (details of this term will be further described in Section 7.4). Here, the SF is assumed to stop as soon as galactic winds are generated. Until that moment, the SF follows a Schmidt-Kennicutt law with $k = 1$, so that:

$$\psi(t) = \begin{cases} \nu G(t)^k & \text{if } t < t_{\text{GW}} \\ 0 & \text{if } t \geq t_{\text{GW}}, \end{cases} \quad (7.1)$$

with ν assumed to increase with the galactic mass in order to reproduce the so called *inverse wind model* (Matteucci, 1994; Matteucci et al., 1998).

For the infall law, we adopt a one-infall scenario described by Eq. 2.10. The reason for the choice of a continuous infall rather than hierarchical mergers to form ellipticals is due to the fact that mergers rise some important problems in reproducing the properties of stellar populations in these galaxies. In particular, in Pipino et al. (2008) it was explored the effect of dry mergers on the chemical properties of stars in elliptical galaxies. It was found that a series of multiple dry mergers (with no star formation in connection with the mergers), involving building blocks that have been created ad hoc to satisfy the [Mg/Fe]-mass relation observed in these galaxies, cannot fit the mass metallicity relation and vice versa. In conclusion, dry mergers alone seem not to explain the need of a more efficient star formation in the more massive galaxies, as suggested by the [Mg/Fe]-mass relation, as well as the late-time assembly suggested in the hierarchical paradigm to recover the galaxy downsizing. In addition, there are also simulations taking into account cosmological infall. In particular, in Colavitti et al. (2008), a cosmological infall law is derived based on dark matter halo properties and this resembles

the exponential infall law predicted for the Galaxy (Chiappini et al., 1997). Therefore, we think that a continuous gas infall is more appropriate to reproduce the chemical properties of ellipticals, as we will see in the next paragraphs.

The outflow rate of the element i due to galactic winds develops when the thermal energy of the gas exceeds its binding energy. The outflow rate has the following law:

$$\dot{G}_{i,w}(t) = \begin{cases} 0 & \text{if } t < t_{GW} \\ \omega_i G(t) & \text{if } t \geq t_{GW} \end{cases} \quad (7.2)$$

where ω_i is the wind parameter (the so called *mass-loading* factor) for the element i (see Chapter 2).

As described in Chapter 2, here we adopt different parametrizations for the IMF, which will be discussed in Section 7.3.1.

7.2.2 Nucleosynthesis prescriptions

For all the stars sufficiently massive to die in a Hubble time, the following stellar yields have been adopted:

- For LIMS we include the metallicity-dependent yields of Van den Hoek et al. (1997).
- For massive stars we assume yields of François et al. (2004).
- For Type Ia SNe we include yields of Iwamoto et al. (1999).

7.2.3 Energy prescriptions

The existence of a wind phase at some stage of evolution of elliptical galaxies is required in order to both explain the observed iron abundance in the intracluster medium and avoid overproducing gas. Galactic winds develop when the thermal energy of the gas, $E_{\text{gas}}^{\text{th}}(t)$, exceeds its binding energy $E_{\text{gas}}^{\text{b}}(t)$ (see Matteucci, 1994; Bradamante et al., 1998):

$$E_{\text{gas}}^{\text{th}}(t) \geq E_{\text{gas}}^{\text{b}}(t). \quad (7.3)$$

In the next Sections we will focus on the description of the different contributions to those two terms.

Gas thermal energy

The gas thermal energy is given by the sum of the thermal energy deposited in the gas by SN explosions, $E_{\text{SN}}^{\text{th}}(t)$, stellar winds $E_{\text{wind}}^{\text{th}}(t)$ and AGN feedback $E_{\text{AGN}}^{\text{th}}(t)$:

$$E_{\text{gas}}^{\text{th}}(t) = E_{\text{SN}}^{\text{th}}(t) + E_{\text{wind}}^{\text{th}}(t) + E_{\text{AGN}}^{\text{th}}(t). \quad (7.4)$$

In this Section we will focus on the contribution by SNe and stellar winds. The AGN feedback is further described in Section 7.4.

In particular, $E_{\text{SN}}^{\text{th}}(t)$ is given by the contribution of both Type II SNe ($E_{\text{II}}^{\text{th}}$, here Type Ib/c SNe are included in the Type II SNe) and Type Ia SNe ($E_{\text{Ia}}^{\text{th}}$), while $E_{\text{wind}}^{\text{th}}(t)$

is given by the contribution of both stellar winds from massive stars (E_W^{th}) and winds from LIMS (E_σ^{th}). So that:

$$\begin{aligned} E_{SN}^{th}(t) &= E_{II}^{th}(t) + E_{Ia}^{th}(t) \\ E_{wind}^{th}(t) &= E_W^{th}(t) + E_\sigma^{th}(t). \end{aligned} \quad (7.5)$$

We have:

$$\begin{aligned} E_{II}^{th}(t) &= \int_0^t \epsilon_{II} R_{II}(t') dt' \\ E_{Ia}^{th}(t) &= \int_0^t \epsilon_{Ia} R_{Ia}(t') dt' \\ E_W^{th}(t) &= \int_0^t \int_8^{m_{up}} \phi(m) \psi(t') \epsilon_W dm dt' \\ E_\sigma^{th}(t) &= \int_0^t \int_{0.8}^8 \phi(m) \psi(t') \sigma^2(t') dm dt', \end{aligned} \quad (7.6)$$

with $\sigma^2 = 0.335GM_*(t)/R_e$ being the stellar velocity dispersion. R_{II} and R_{Ia} are the rates of Type II and Type Ia SNe, respectively (see Chapter 2), and the terms $\epsilon_{II/Ia}$ and ϵ_w are the energies injected into the ISM from supernova explosions and stellar winds from massive stars, respectively. In particular:

$$\begin{aligned} \epsilon_{II} &= \eta_{II} E_0 \\ \epsilon_{Ia} &= \eta_{Ia} E_0 \\ \epsilon_W &= \eta_W E_W, \end{aligned} \quad (7.7)$$

where $E_0 = 10^{51}$ erg is the total energy released by a supernova explosion and $E_{wind} = 10^{49}$ erg is the energy injected into the ISM by a typical massive star during its all lifetime. η_{II} , η_{Ia} and η_W are the efficiencies of energy transfer from supernova Type II, Type Ia and stellar winds into the ISM, respectively. According to Cioffi et al. (1988), due to significant cooling by metal ions, only a few per cent of the initial 10^{51} erg can be provided to the ISM by Type II SNe. On the other hand, since Type Ia SNe explosions occur in a medium already heated by Type II SNe, they can contribute with a higher percentage of their energy budget (Recchi et al., 2001; Matteucci et al., 2001; Pipino et al., 2002; De Masi et al., 2018). In this work we assumed an efficiency of 3% for Type II SNe and stellar winds (see Bradamante et al., 1998; Melioli et al., 2004) and tested three different values for Type Ia SNe: 80%, 30% and 10%, simulating different cooling conditions.

Gas binding energy

Following Bertin et al. (1991), elliptical galaxies have their luminous mass embedded in massive and diffuse dark matter halos. In this context, the binding energy of the gas can be expressed as:

$$E_{gas}^b(t) = W_L(t) + W_{LD}(t), \quad (7.8)$$

where $W_L(t)$ is the gravitational energy of the gas due to the luminous matter, given by

$$W_L(t) = -q_L G \frac{M_{gas}(t) M_L(t)}{R_e}, \quad (7.9)$$

with $M_L(t)$ being the total baryonic mass at the time t , R_e the effective radius and $q_L = 1/2$. $W_{LD}(t)$ is the gravitational energy of the gas due to the interaction of luminous and dark matter:

$$W_{LD}(t) = -\tilde{\omega}_{LD} G \frac{M_{gas}(t) M_{DM}}{R_e}, \quad (7.10)$$

where M_{DM} is the mass of the dark matter halo and

$$\tilde{\omega}_{LD} = \frac{1}{2\pi} \frac{R_e}{R_{DM}} \left[1 + 1.37 \left(\frac{R_e}{R_{DM}} \right) \right] \quad (7.11)$$

is the interaction term, with R_{DM} being the radius of the dark matter halo. According to Bertin et al. (1991), the relations for the gravitational interaction between the gas mass and the total luminous mass of the galaxy, and between the gas mass and the dark matter, are valid for R_e/R_{DM} defined in the range 0.10 – 0.45, at least for massive elliptical galaxies. Here we adopted $R_e/R_{DM} = 0.1$, since that was considered being the best value in previous works (e.g.: Matteucci, 1992; De Masi et al., 2018).

Galaxy binding energy

The binding energy of the galaxy is given by:

$$E_{gal}^b(t) = B_L(t) + B_{LD}(t), \quad (7.12)$$

where $B_L(t)$ is the gravitational energy of the galaxy due to the luminous matter, given by

$$B_L(t) = -q_L G \frac{M_L^2(t)}{R_e} \quad (7.13)$$

and $B_{LD}(t)$ is the gravitational energy of the galaxy due to the interaction between luminous and dark matter:

$$B_{LD}(t) = -\tilde{\omega}_{LD} G \frac{M_L(t) M_{DM}}{R_e}. \quad (7.14)$$

7.3 Results

The model for the chemical evolution of elliptical that we run is similar to one of the best models reported by De Masi et al. (2018) (their model 02b), who used a chemical evolution code similar to the one used here.

The model explores the evolution of elliptical galaxies in the baryonic mass range $10^{10} - 5 \times 10^{12} M_\odot$. The effective radius R_e increases with the baryonic mass and, according to the *inverse wind scenario* (Matteucci, 1994), the star formation efficiency ν increases as well while the infall timescale τ decreases.

TABLE 7.1: *Parameters of the model. We adopted different values for the star formation efficiency ν , the infall timescale τ and the effective radius R_e (columns 2, 3 and 4, respectively) for the different infall masses M_i (column 1). In column 5, 6 and 7 we report the predicted final stellar mass M_{*f} , the predicted time for the onset of the galactic wind t_w and the predicted rate of Type Ia SNe R_{Ia} . Finally, on the last column we specify the adopted IMF*

$M_i (M_\odot)$	$\nu (\text{Gyr}^{-1})$	$\tau_i (\text{Gyr})$	$R_e (\text{kpc})$	$M_{*f} (M_\odot)$	$t_w (\text{Gyr})$	$R_{Ia} (\text{SN/century})$	IMF
1×10^{10}	3.0	0.5	1	1.0×10^9	0.37	0.004	Scalo
5×10^{10}	6.0	0.4	2	1.5×10^{10}	0.35	0.031	Salpeter
1×10^{11}	10	0.4	3	2.0×10^{10}	0.33	0.072	Salpeter
5×10^{11}	15	0.3	6	1.5×10^{11}	0.33	0.524	Arimoto&Yoshii
1×10^{12}	22	0.2	10	2.0×10^{11}	0.25	1.178	Arimoto&Yoshii
5×10^{12}	60	0.1	12	1.5×10^{12}	0.19	5.024	Arimoto&Yoshii

In Table 7.1, we report the adopted parameters. In particular, in the 1st, 2nd, 3rd and 4th columns we report the adopted infall mass, the star formation efficiency, the infall timescale and the effective radius, respectively. In the 5th, 6th and 7th columns we report the predicted final stellar mass, time of the onset of the galactic wind and present day Type Ia SNe rate. In the last column we report the adopted IMF. In particular, according to De Masi et al. (2018), models with constant IMF for galaxies of different mass fail in reproducing the observed trends with galactic mass. They tested a varying IMF and found a better agreement with data by assuming that the IMF goes from being bottom heavy in less massive galaxies to top heavy in more massive ones, producing a downsizing in star formation, favoring massive stars in larger galaxies. As described in Chapter 2, here we adopt a Scalo (1986) IMF for low mass galaxies, a Salpeter (1955) IMF for intermediate mass galaxies and a Yoshii et al. (1987) IMF for high mass galaxies.

As a first step, we try to reproduce the main chemical properties of the stellar populations dominating the spectra of ETGs.

7.3.1 $[\alpha/\text{Fe}]$ ratio and mass-metallicity relations

Our chemical evolution code provides the evolution as a function of time of the abundances of chemical elements in the ISM. For instance, the upper panels in Figure 7.1 show the abundances of different α -elements for an elliptical galaxy of initial infall mass of $10^{11} M_\odot$ (left panel) and the $[\text{O}/\text{Fe}]$ ratios for elliptical galaxies of different infall masses (right panel). As it is possible to see, we infer a higher $[\text{O}/\text{Fe}]$ in the ISM of the more massive galaxies at fixed $[\text{Fe}/\text{H}]$, as a consequence of the effect of the more efficient SFR in the brightest galaxies relative to the smaller ones. The metallicity of ellipticals is measured only by means of metallicity indices obtained from their integrated spectra. The most common metallicity indicators are Mg_2 and $\langle \text{Fe} \rangle$. In order to pass from metallicity indices to $[\text{Fe}/\text{H}]$ (and viceversa) one needs to adopt a suitable calibration. In order to compare the results of our models with the observed averaged stellar abundances of the dominant stellar populations in the galaxies in the dataset, we first need to compute the mean stellar abundance of the element X. This is defined by

Pagel et al. (1975) as:

$$\langle X/H \rangle \equiv \langle Z_X \rangle = \frac{1}{S_0} \int_0^{S_0} Z_X(S) dS, \quad (7.15)$$

where S_0 is the total mass of stars ever born contributing to light at the present time. We recall that the right procedure should be that of averaging on the stellar luminosity at the present time since the observed indices are weighted on V-band luminosity (e.g. Arimoto et al., 1987; Matteucci et al., 1998). However, as it has been shown by Matteucci et al. (1998), results obtained by averaging on luminosity are not significantly different from those obtained by averaging on mass, at least for massive galaxies (see also Pipino et al., 2004; De Masi et al., 2018). Therefore, in this work we will refer only to mass-averaged metallicities. Once the mass-averaged abundances have been determined, we can convert them into spectral indices. This is done by using the calibration relations derived from Tantaló et al. (1998), who consider the Mg/Fe ratios:

$$\begin{cases} Mg_2 = 0.233 + 0.217 \langle Mg/Fe \rangle + (0.153 + 0.120 \langle Mg/Fe \rangle) \langle Fe/H \rangle \\ \langle Fe \rangle = 3.078 + 0.341 \langle Mg/Fe \rangle + (1.654 - 0.307 \langle Mg/Fe \rangle) \langle Fe/H \rangle. \end{cases} \quad (7.16)$$

In Figure 7.1 (lower panels), we compare the predictions of our model with the observational data. In particular, the continuous black and cyan lines are the linear regression of the data points and of the model results, respectively, with the shaded area representing the 1σ uncertainties. The black dotted lines are the boundaries of the 95% confident region. Our model fit reasonably well the observed mass-metallicity relation. In particular, the increasing trend of both $\langle Fe \rangle$ and Mg_2 is successfully reproduced, although the predicted metallicity, especially at high masses, is slightly too high, reflecting in a higher Mg_2 than the observed one. This difference could be due to different assumptions, such as the adopted IMF, the prescriptions for the yields, the adopted calibration or a combination of those factors. For the $\langle Fe \rangle$ we predict a slope of $m_{\langle Fe \rangle}^{\text{model}} = 0.356 \pm 0.084$ to be compared to that of the best fitting line of the observational data equal to $m_{\langle Fe \rangle}^{\text{data}} = 0.301 \pm 0.019$, while for the Mg_2 we predict a slope of $m_{Mg_2}^{\text{model}} = 0.070 \pm 0.035$ to be compared to $m_{Mg_2}^{\text{data}} = 0.062 \pm 0.001$. Therefore, we have shown that our models can well reproduce the chemical properties of ETGs stellar populations, formed before the time at which the galactic wind occurs. At this point, we want to study the passive evolution of ETGs, after the main wind and consequent stop of SF, and the effects of SNIa and AGN feedback.

7.3.2 Energies with no AGN feedback

We start by showing the results of models where the AGN feedback is not considered. In Figure 7.2 we show the evolution as a function of time of the gas thermal energy ($E_{\text{gas}}^{\text{th}}$), the gas binding energy ($E_{\text{gas}}^{\text{b}}$) and the galaxy binding energy ($E_{\text{gal}}^{\text{b}}$) for elliptical galaxies of initial infall mass of $10^{10} M_{\odot}$, $10^{11} M_{\odot}$, $10^{12} M_{\odot}$ and $5 \times 10^{12} M_{\odot}$, as predicted by the model.

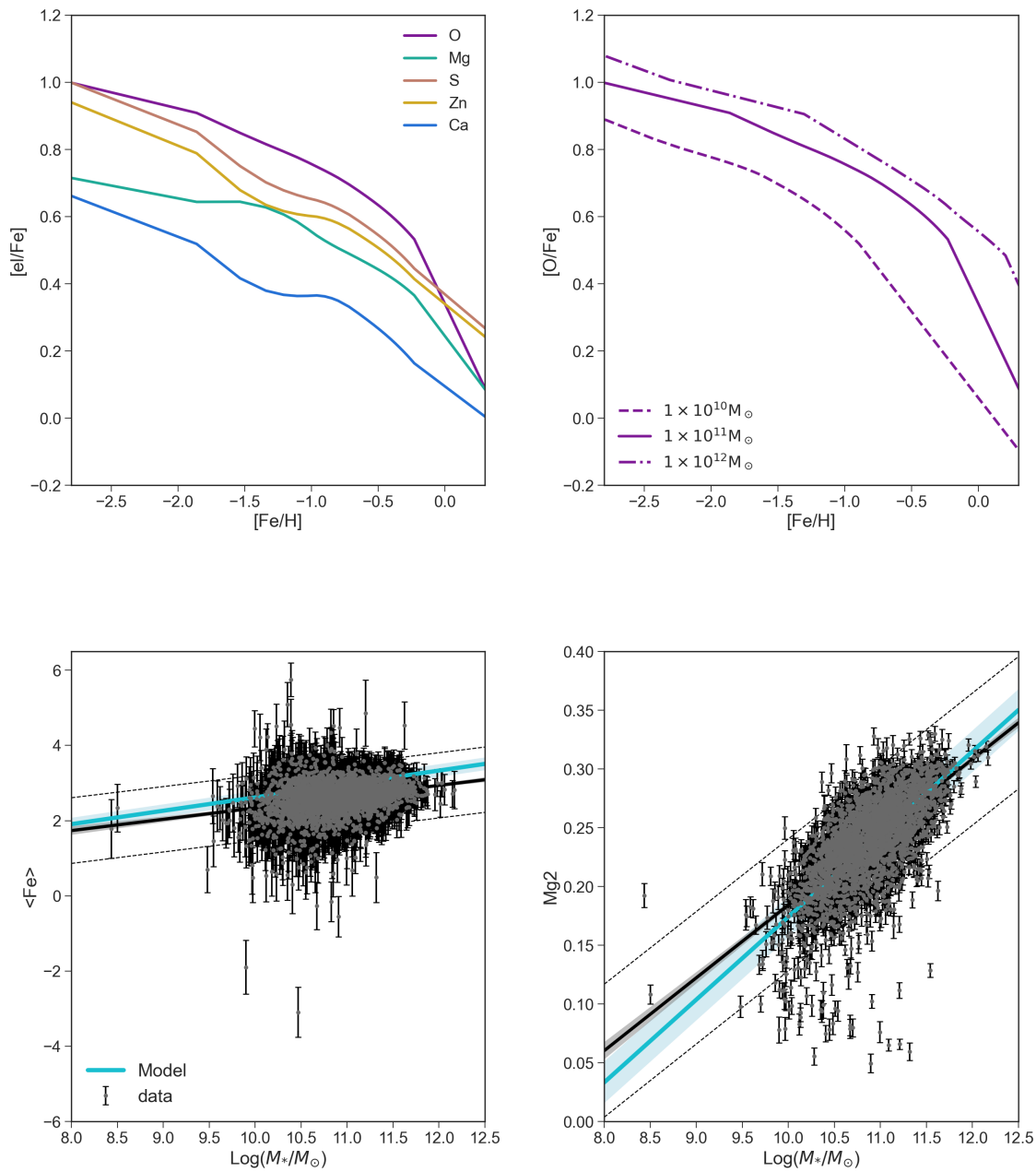


FIGURE 7.1: Upper panels: Predicted abundances ratios in the ISM as functions of $[Fe/H]$ for O, Mg, S, Zn and Ca for an elliptical galaxy with infall gas mass of $M_i = 10^{11} M_{\odot}$ (left). Predicted $[O/Fe]$ abundance ratio in the ISM as a function of $[Fe/H]$ for galaxies with $10^{10} M_{\odot}$ (dashed line), $10^{11} M_{\odot}$ (solid line) and $10^{12} M_{\odot}$ (dash-dotted line) initial infall masses (right). Lower panels: Line-strength indices predicted by the model using Tantalo *et al.* (1998) calibrations together with observational data for both $\langle Fe \rangle$ (left panel) and Mg_2 (right panel). Black dots are the galaxies in the catalogue and the lines are the linear fit to the data (black line) and to the model (cyan line). The shaded area represents the 1σ uncertainties, while the black dotted lines are the boundaries of the 95% confident region.

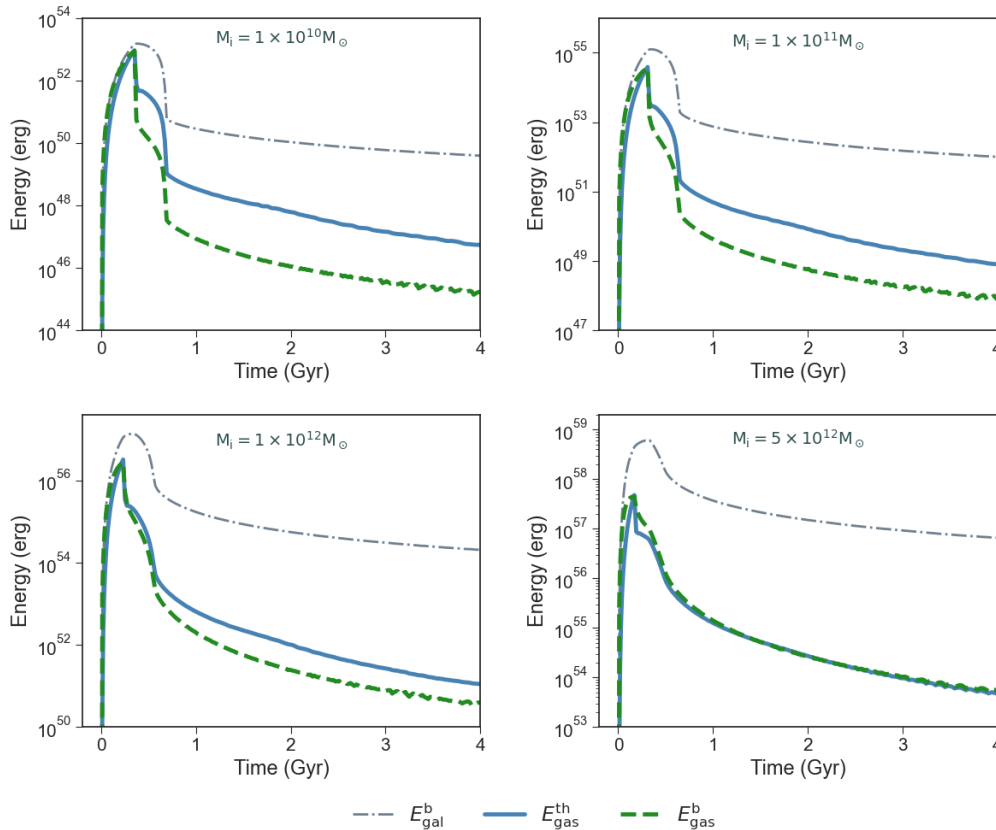


FIGURE 7.2: Energy balance as a function of time for simulated elliptical galaxies with initial infall mass of $10^{10} M_{\odot}$, $10^{11} M_{\odot}$, $10^{12} M_{\odot}$ and $5 \times 10^{12} M_{\odot}$. For each panel, the blue solid line represents the thermal energy of the gas $E_{\text{gas}}^{\text{th}}$, the green dashed line its binding energy, $E_{\text{gas}}^{\text{b}}$, and the grey dash-dotted line the binding energy of the galaxy, $E_{\text{gal}}^{\text{b}}$.

As explained in section 7.2.3, when the thermal energy of the gas heated by SN explosions and stellar winds exceeds its binding energy, the gas present in the galaxy is swept away and the subsequent evolution of the system is determined only by the amount of matter and energy which is restored to the ISM by the dying stellar generations, namely low mass stars, and among SNe, only Type Ia SNe. Therefore, a fundamental point in the evolution of elliptical galaxies is the time of the onset of the galactic wind, t_w . In particular, in each panel of Figure 7.2 it is possible to see the different values of t_w , which coincide to the points at which the gas thermal energy becomes larger than the gas binding energy. With increasing galaxy mass, the value of t_w becomes smaller (as also reported in Table 7.1) according to the *inverse wind scenario* (Matteucci, 1994).

In order for a galaxy to be devoided of gas even after the time of the onset of the galactic wind, the condition $E_{\text{gas}}^{\text{th}} \geq E_{\text{gas}}^{\text{b}}$ must hold until the present time. For galaxies with mass $M \leq 10^{11} M_{\odot}$, this condition is easily reached. However, for systems of larger mass, and in particular for a galaxy of initial infall mass of $5 \times 10^{12} M_{\odot}$ (corresponding to a final stellar mass of $1.5 \times 10^{12} M_{\odot}$), the thermal energy of the gas appears to be comparable to its binding energy for all the evolution of the galaxy, creating a border line situation for the occurrence of a wind.

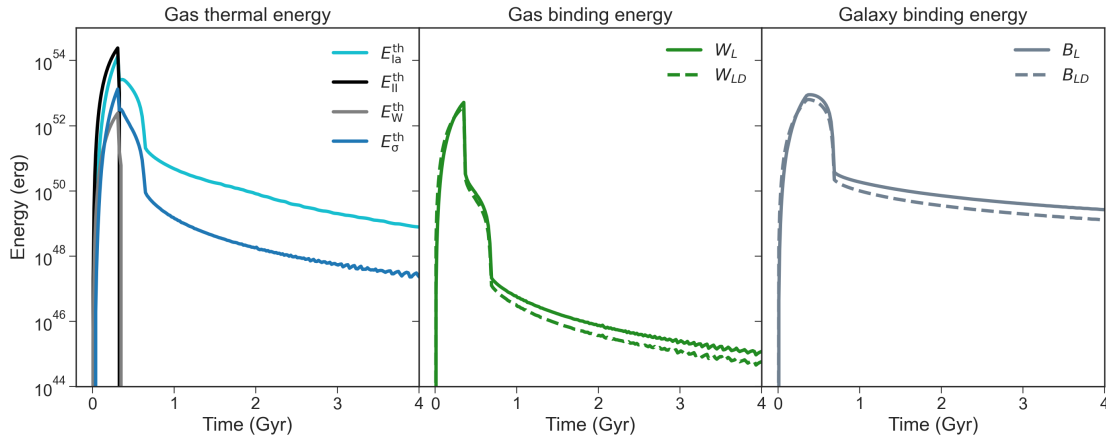


FIGURE 7.3: *Energies for an elliptical galaxies with initial infall mass of $10^{11} M_{\odot}$. Left panel: contribution to the gas thermal energy by Type II SNe ($E_{\text{II}}^{\text{th}}$), Type Ia SNe ($E_{\text{Ia}}^{\text{th}}$) and stellar wind (E_{W}^{th} , E_{σ}^{th}). Central panel: contribution to the total gas binding energy from the gravitational energy of the gas due to luminous matter, W_{L} , and the gravitational energy of the gas due to the interaction between luminous and dark matter, W_{LD} . Right panel: same as central panel, but for the galaxy binding energy.*

In Figure 7.3 we report the evolution as a function of time of the different components of the total energy budget for a galaxy of initial infall mass of $10^{11} M_{\odot}$. As discussed in section 7.2.3, the ISM is heated by the thermalization of stellar motions (E_{W}^{th} and E_{σ}^{th}) and SNe explosions (both Type II, $E_{\text{II}}^{\text{th}}$, and Type Ia, $E_{\text{Ia}}^{\text{th}}$). The contribution from Type II SNe dominates at early times but, as soon as the galactic wind occurs, it stops together with the contribution from stellar wind from massive stars. In fact, star formation halts when the thermal energy of the gas exceeds its binding energy. After the star formation has stopped, the galactic wind is maintained only by Type Ia SNe, which continue to explode until present time, and by the motion of lower mass stars. With a thermal energy of almost 2 orders of magnitude higher than that of stellar winds, Type Ia SNe appears to be the main drivers of the evolution of $E_{\text{gas}}^{\text{th}}$, after the quenching of the SF. Here we assume an efficiency of energy transfer from Type Ia SNe equal to $\eta_{\text{SNIa}} = 80\%$ and justify our assumption by the fact that, since Type Ia SNe explosions occur in a medium already heated by Type II SNe, they should contribute to the total amount of their energy budget with minimal radiative losses (see Recchi et al., 2001). However, we tested also other cases in which $\eta_{\text{SNIa}} = 30\%$ and $\eta_{\text{SNIa}} = 10\%$, whose results are reported in Figure 7.4, for a galaxy of initial infall mass equal to $10^{11} M_{\odot}$. As one can see, when the efficiency of energy transfer of Type Ia SNe gets as low as 10%, the thermal energy of the gas appears to be almost comparable to its binding energy for all the galaxy evolution, so that basically the situation is the same of that illustrated previously in the lower right panel of Figure 7.2 for a high-mass system.

It appears then reasonable to conclude that when no AGN feedback is considered, the thermal energy injected by SNe in the ISM is capable to both drive

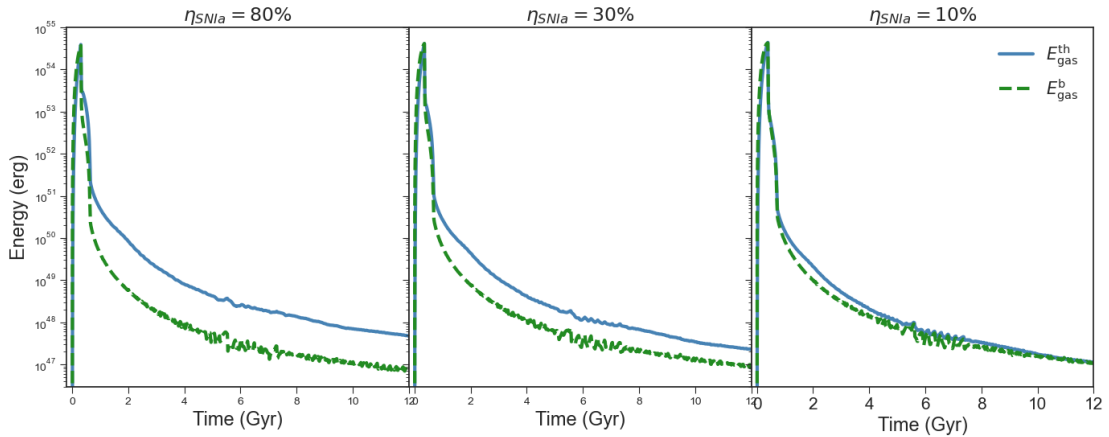


FIGURE 7.4: Comparison between the thermal energy of the gas, $E_{\text{gas}}^{\text{th}}$ (blue solid line), and its binding energy, $E_{\text{gas}}^{\text{b}}$ (green dotted line), for a galaxy of initial mass $M_i = 10^{11} M_{\odot}$, for different values of the efficiency of energy transfer from Type Ia SNe.

galactic winds at early times and to keep the inefficiency of the SF during the subsequent galaxy evolution. This is true at least for systems with $M_i \leq 10^{12} M_{\odot}$, but characterized by a high Type Ia SNe efficiency of energy transfer, or for systems of $M_i \leq 10^{11} M_{\odot}$ but characterized by a low efficiency of energy transfer. Therefore, in the following sections we will focus first on describing the treatment adopted to characterize the BH accretion and the AGN feedback, and then we will show its impact on the evolution and on the energy balance of a high-mass galaxy of $5 \times 10^{12} M_{\odot}$.

7.4 Black hole accretion and AGN feedback

In our phenomenological treatment of the AGN feedback we consider only radiative feedback, thus neglecting other mechanisms as radiation pressure and relativistic particles, as well as mechanical phenomena associated with jets. It is usually assumed that SMBHs are assembled by mergers with other BHs and/or by accretion of the gas from the surrounding medium. Theoretical studies suggest that a seed BH with the mass in the range $10^2 - 10^6 M_{\odot}$ (Valiante et al., 2011) can form either by rapid collapse of Pop III stars (Heger et al., 2002) or by the direct collapse of massive hot and dense gas clouds induced by gravitational instabilities (Bromm et al., 2003; Begelman et al., 2006; Volonteri et al., 2009). In this work, we consider a BH of seed mass equal to $10^6 M_{\odot}$ which suffers spherical accretion of material at the Bondi rate (Bondi, 1952):

$$\dot{M}_B(t) = 4\pi R_B^2 \rho_g c_s \lambda, \quad (7.17)$$

where ρ_g and c_s are the density and sound speed of the gas, respectively, and R_B is the Bondi radius, namely the gravitational radius of influence of the BH, given

by:

$$R_B = \frac{GM_{BH}\mu m_p}{\gamma k_b T_V}, \quad (7.18)$$

with μ being the mean molecular weight of the gas, m_p the mass of the proton, k_b the Boltzmann constant, G the gravitational constant and γ the polytropic index ($\gamma = 1$ in the isothermal case). The parameter λ in equation 7.17 is the dimensionless accretion parameter which, as determined by Ciotti et al. (2018) (see also Mancino et al., 2022), can assume a wide range of values depending on the galaxy structure. Here we set $\lambda = 2 \times 10^4$ for a galaxy of initial infall mass $M_i = 5 \times 10^{12} M_\odot$, even if this choice has a little effect, since the BH growth will be Eddington limited during the entire period of interest. The virial temperature, T_V , is given by:

$$T_V = \frac{1}{3k_B} \mu m_p \sigma^2, \quad (7.19)$$

with σ^2 being the stellar velocity dispersion (see Section 7.2.3).

The accretion is limited to the Eddington rate, namely the accretion rate beyond which radiation pressure overwhelms gravity:

$$\dot{M}_{Edd}(t) = \frac{L_{Edd}}{\eta c^2}, \quad (7.20)$$

where η gives the mass to energy conversion efficiency. In this study we adopt a fixed value of $\eta = 0.1$, which is the mean value for a radiatively efficient Shakura et al. (1973) accretion onto a Schwarzschild BH, ignoring the possibility of radiatively inefficient accretion phases.

The accretion onto the BH is then

$$\dot{M}_{BH}(t) = \begin{cases} \dot{M}_B(t) & \text{if } \dot{M}_B(t) \leq \dot{M}_{Edd}(t) \\ 10^{-3} \dot{M}_{Edd}(t) & \text{if } \dot{M}_B(t) > \dot{M}_{Edd}(t), \end{cases} \quad (7.21)$$

where $\dot{M}_B(t)$ is the rate from eq. 7.17. The corresponding bolometric luminosity is computed as:

$$L_{BH} = \epsilon \dot{M}_{BH} c^2, \quad (7.22)$$

where $\epsilon = 0.1$. As it is possible to see from eq. 7.21, we are using a reduction factor of 10^{-3} to limit the maximum accretion rate. In an ideal simulation, the BH accretion at the Eddington rate limit would fluctuate in time, with shorter and shorter time scales at increasing spatial and temporal resolution, since the feedback time scale would decrease by moving nearer and nearer to the BH. Here, we are using a one-zone model, with a time step limited to 20 Myr. Therefore, in our simulation, in absence of the reduction factor we would actually greatly overestimate the accretion. For what concerns the order of magnitude of the reduction factor, we explored different values in the range $10^{-3} - 1$. As expected, for the value equal to unity, i.e. for an unphysical continuous Eddington accretion lasting 20 Myr, we found unrealistic results for both the BH accretion and, as a consequence, the BH mass M_{BH} and luminosity L_{BH} . Similar results are obtained also for a reduction factor of $\sim 10^{-1}$. Physically reliable solutions are obtained for a reduction factor

in the range $10^{-3} - 10^{-2}$. We then chose the value of 10^{-3} and based our consideration on Ciotti et al. (2017) (see also Ciotti et al., 2007) where a duty-cycle of the order of 10^{-3} is commonly measured. In practice, the reduction factor should not be intended as a reduction of the feedback at the peak values of the AGN luminosity, but as a time-average over the length of the numerical time-step to be adopted in our one-zone simulations.

Finally, we compute the energy per unit time deposited by the BH into the ISM as:

$$\dot{E}_{th}^{AGN}(t) = \xi L_{BH} T_V \bar{n}_p, \quad (7.23)$$

with T_V expressed in K and \bar{n}_p being the average number of particles per cm^3 near the galactic centre. We call the quantity ξ the total absorption coefficient: following Ciotti et al. (2001) (equations 4 and A10) this parameter can be estimated in the optical thin regime with values of the order of $\sim 3 \times 10^{-14}$ for realistic galaxy sizes and ISM properties. For example, when $\xi = 3 \times 10^{-14}$, $T_V = 10^7 \text{ K}$ and $\bar{n}_p = 10^2 \text{ cm}^{-3}$, only $\sim 3 \times 10^{-5}$ is actually deposited as thermal energy in the ISM (see also Binney et al., 1995). Of course, this number can change significantly during the galaxy evolution. Therefore, due to the intrinsic and unavoidable uncertainties on the value of ξ , in this work we test four different values, namely: 3×10^{-14} , 3×10^{-4} , 3×10^{-2} and 1, with this latter two being completely unphysical as they would certainly predict an AGN thermal feedback with an energy deposition larger than the available one. In the simulations we used also these extreme values in order to be sure that we bracketed the true behaviour.

7.4.1 Black hole masses and luminosities

In Figure 7.5 we show the accretion onto the BH evolution as a function of time together with the corresponding bolometric luminosity and BH mass evolution (central and right panel, respectively). As it is possible to see from Figure 7.5, the resulting accretion rate evolution is characterized by a series of spikes, each with a duration of 40 Myr, corresponding to the moments at which $\dot{M}_B \leq \dot{M}_E$. The spikes are reflected into the luminosity, being this latter proportional to \dot{M}_{BH} (see central panel of the same Figure) and, as a consequence, it is characterized by a burst shape representative of the highly intermittent activity that QSOs may exhibit. The predicted final value of the luminosity is $L_{BH} = 2.2 \times 10^{44} \text{ erg/s}$ which is three order of magnitudes lower than the value that it assumes in the last burst, equal to $L_{BH} = 1.43 \times 10^{47} \text{ erg/s}$. It must be noted that with these values we find a very good agreement with several observations of AGN bolometric luminosity both at high and at lower redshift (Dunn et al., 2010; Fiore et al., 2017; Izumi et al., 2021a; Izumi et al., 2021b).

The BH reaches a mass of $2 \times 10^8 M_\odot$ after 1 Gyr of galaxy evolution and a final mass of $3.5 \times 10^9 M_\odot$ at the present time. It is well known that there exist well-defined correlations between the mass of the SMBH, M_{BH} , and the properties (e.g. velocity dispersion, σ , and the stellar mass, M_*) of the spheroidal component of the host galaxy (Magorrian et al., 1998). Even if there have been claims for a non-linear relation between M_{BH} and M_* (Laor, 2001; Wu et al., 2001), Marconi et al. (2003) re-established the tight linear relation: $\langle M_{BH}/M_* \rangle \sim 0.002$, in good agreement also with several other estimates (e.g.: McLure et al., 2002; Dunlop et

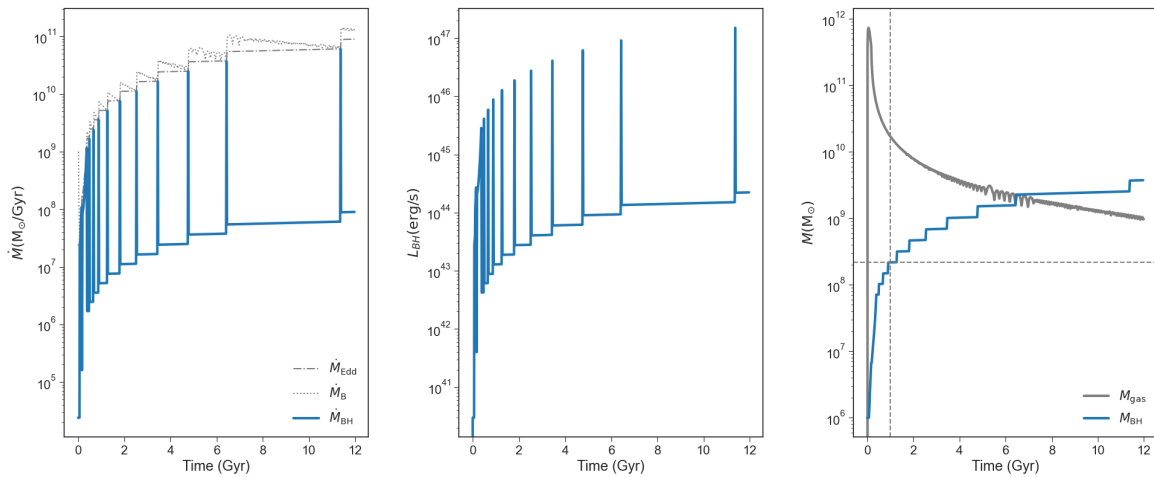


FIGURE 7.5: Evolution of the accretion rate, bolometric luminosity and BH mass for an elliptical galaxy of initial infall mass $5 \times 10^{12} M_{\odot}$. Left panel: evolution of the accretion rate as a function of time. In grey dotted line is reported the Bondi accretion rate, in grey dash-dotted line is reported the Eddington accretion rate and in cyan continuous line the resulting accretion according to equation 7.21. Central panel: bolometric luminosity evolution as a function of time. Right panel: the BH mass evolution as a function of time, with the vertical grey dotted lines indicating the mass reached by the BH after 1 Gyr. The grey continuous line represent the evolution of the mass of gas inside the galaxy.

al., 2003; Häring et al., 2004). In Figure 7.6 we compare predictions of our model for galaxies of initial infall mass in the $10^{10} - 5 \times 10^{12} M_{\odot}$ range with estimates for the M_{BH} vs σ (by Gültekin, 2010) and for the M_{BH} vs M_* (by Marconi et al., 2003) relations. We remind $\sigma^2 = 0.335 GM_*(t)/R_e$ being the stellar velocity dispersion (see Section 7.2.3). The predictions we are showing here have been obtained with the physical expected value of $\xi = 3 \times 10^{-14}$ and show good agreement with observations. We show also what happen when higher values of ξ (3×10^{-2}) are adopted. The results change very little, without affecting the agreement between measurements and predictions. This is a noticeable result, given the simplicity of our model.

7.4.2 Energies with AGN feedback

Figure 7.7 shows the evolution as a function of time of the gas thermal energy ($E_{\text{gas}}^{\text{th}}$), the gas binding energy ($E_{\text{gas}}^{\text{b}}$) and the galaxy binding energy ($E_{\text{gal}}^{\text{b}}$) for an elliptical galaxy of initial infall mass of $5 \times 10^{12} M_{\odot}$ and for four different values of the coefficient ξ (3×10^{-14} , 3×10^{-4} , 3×10^{-2} , 1).

In the upper left panel of Figure 7.7 are reported results for models with $\xi = 3 \times 10^{-14}$. For this model, the effect of the AGN in the evolution of the thermal energy of the gas is totally negligible and there is no difference between this situation and that in which AGN feedback is not considered. The coefficient ξ must be increased by at least ten orders of magnitude before the effect of the AGN on the thermal energy of the gas appears to be visible (upper left panel of Figure 7.7). Even if the contribution from the AGN appears to be no longer negligible, the time at which the galactic wind starts is equal to that of the models with $\xi = 3 \times 10^{-14}$

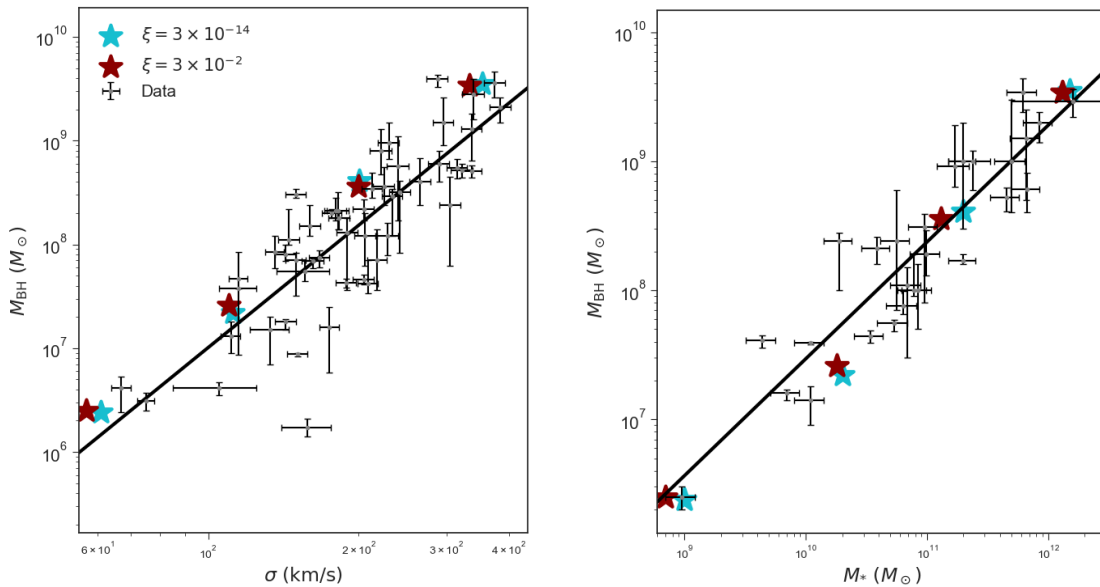


FIGURE 7.6: Comparison between our model predictions and observational data from Gültekin (2010) for the M_{BH} vs σ relation (left panel) and for the M_{BH} vs M_* relation with observational data from Marconi et al. (2003) (right panel). In both panel, the solid black line is the best fit of the observational data and the cyan and red stars are the predictions of our model for galaxies of initial infall mass equal to 10^{10} , 10^{11} , 10^{12} and $5 \times 10^{12} M_{\odot}$ and for an absorption coefficient ξ equal to 3×10^{-14} and 3×10^{-2} , respectively.

and with no AGN feedback ($t_{\text{GW}} = 0.19 \text{ Gyr}$). Therefore, the AGN feedback cannot be the main cause of the formation of a galactic wind. However, since its contribution to the subsequent evolution of $E_{\text{gas}}^{\text{th}}(t)$ cannot be neglected, its role could be crucial in maintaining quenched the galaxy after SF suppression. The situation drastically changes if one adopts a coefficient as high as $\xi = 3 \times 10^{-2}$. In this case, the total thermal energy of the gas, $E_{\text{gas}}^{\text{th}}(t)$, becomes completely dominated by the AGN feedback for all its evolution. In this model, the galactic wind starts also at earlier times, $t_{\text{GW}} = 0.15 \text{ Gyr}$, so that the AGN feedback seems to be its main driver. Finally, in the lower right panel of Figure 7.7 we show the results for the energy evolution in the case in which $\xi = 1$. As one can see, the many bursts that characterize the shape of $E_{\text{gas}}^{\text{th}}$, are so powerful to exceed the binding energy of the galaxy $E_{\text{gal}}^{\text{b}}$. Since the physical consequence of this is a BH which could potentially disrupt entirely the host galaxy or at the very least remove a very large fraction of its gas, it seems physically unreasonable that the AGN feedback process could be so efficient.

The situation is illustrated in more details in the upper left panel of Figure 7.8, where we show the evolution of the different components of the thermal energy. When $\xi = 3 \times 10^{-14}$, the thermal energy due to the AGN is several orders of magnitude lower than that due to the other phenomena. In particular, the thermalization is dominated by the contribution of stellar motions and SN explosions,

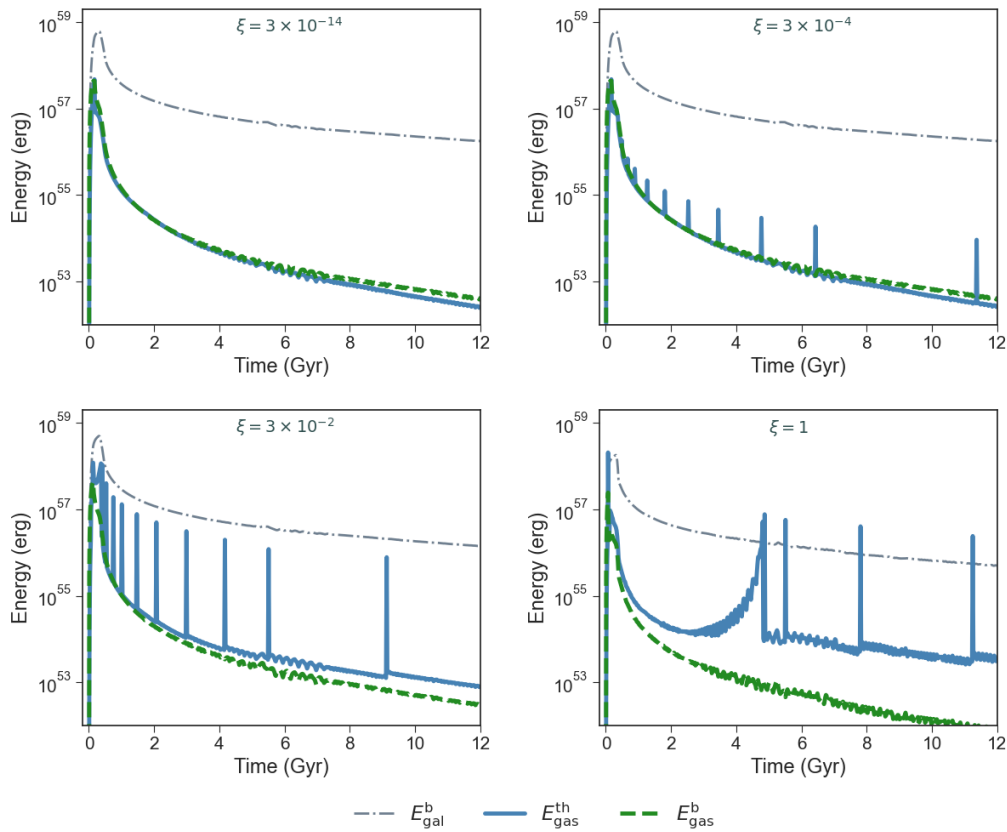


FIGURE 7.7: Energy balance as a function of time for simulated elliptical galaxies with initial infall mass of $5 \times 10^{12} M_{\odot}$ and for different values of the absorption coefficient ξ . For each panel, the blue solid line represents the thermal energy of the gas $E_{\text{gas}}^{\text{th}}$, the green dashed line its binding energy, $E_{\text{gas}}^{\text{b}}$, and the grey dash-dotted line the binding energy of the galaxy, $E_{\text{gal}}^{\text{b}}$.

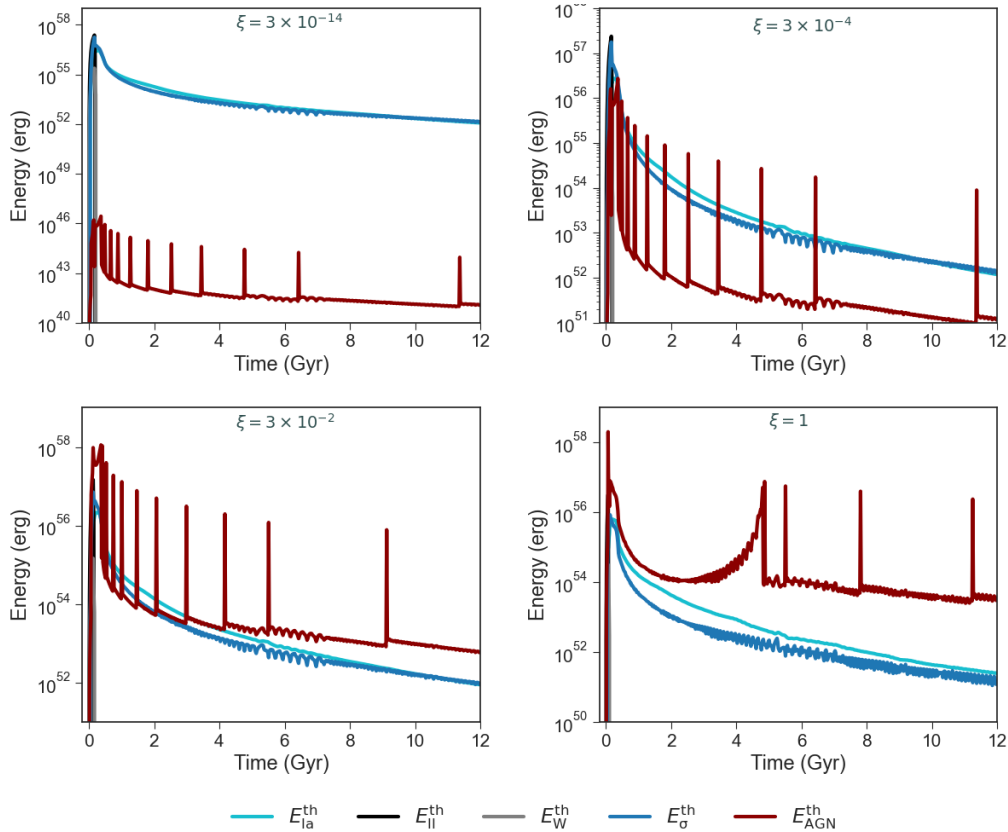


FIGURE 7.8: Contributions to the gas thermal energy by Type II SNe (E_{II}^{th}), Type Ia SNe (E_{Ia}^{th}), stellar wind (E_W^{th} , E_{σ}^{th}) and AGN feedback (E_{AGN}^{th}), for different values of the absorption coefficient ξ .

both at early and at late times (with Type II SNe being the major contributors at early times and Type Ia SNe and stellar motions at late times). The evolution of $E_{AGN}^{th}(t)$ reflects the bursty accretion history of the BH, as expected. Due to the high accretion episodes that we described in the previous section, the BH injects powerful bursts of thermal energy into the surrounding gas. However, the coefficient ξ must be increased of at least ten orders of magnitude before the effect of the AGN on the thermal energy of the gas appears to be visible. In fact, in this case the bursts in the AGN thermal energy appears to be comparable with the energy injected by SNe and stars. Even if the contribution from the AGN is no longer negligible, at early times the thermal energy evolution is still dominated by Type II SNe which continue to be the main driver of the galactic winds. For a coefficient $\xi = 3 \times 10^{-2}$ the thermal energy injected into the ISM by the AGN is larger also than that due to Type II SNe and this causes the AGN feedback to be the main driver of the galactic wind. Finally, for the model with $\xi = 1$, the energy injected by the AGN is much larger than that due to the other phenomena and, as stated above, this cause an unrealistic evolution of the considered galaxy.

In Figure 7.9 we report the evolution of the SFR as a function of time for the four different cases corresponding to the different values of ξ . As it is possible to see, the halt of the SF happens at the same time in the model with $\xi = 1 \times 10^{-14}$ and in the model with $\xi = 1 \times 10^{-4}$, as well as in the model in which we do not

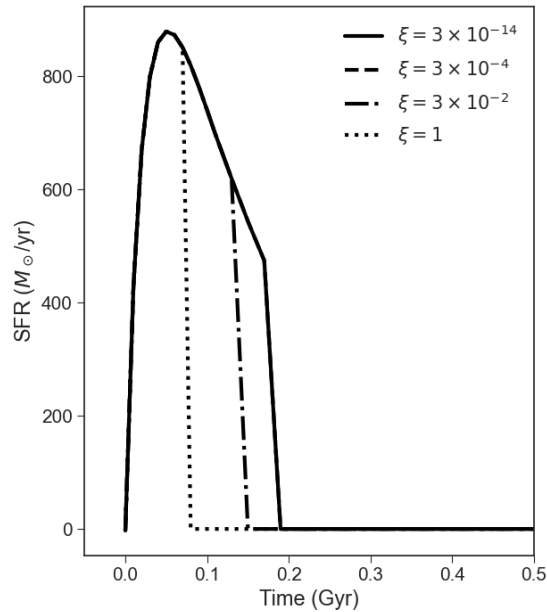


FIGURE 7.9: Evolution of the SFR for a galaxy with initial infall mass of $5 \times 10^{12} M_{\odot}$ and for different values of the absorption coefficient.

consider the effect of the AGN feedback. On the other hand, for the models with $\xi = 1 \times 10^{-2}$ and $\xi = 1$, the SF stops at 150 Myr and 80 Myr, respectively, due to the non negligible affect of the AGN feedback at earlier time.

7.5 Conclusions

In this work, we modelled the evolution of ETGs with initial infall mass in the range $10^{10} - 5 \times 10^{12} M_{\odot}$ by means of a chemical evolution model able to follow the evolution with time of the gas mass and its chemical composition during the entire galactic lifetime. In this first paper, we focused on the effects of stellar and AGN feedback and their role in suppressing the SF in ellipticals at early times. In order to do that, we updated the computation of the energetic budget in our model which now includes, besides core-collapse and Type Ia SNe, both stellar winds from LIMS and AGN feedback. In this way, the ISM is heated by stellar winds (both from massive stars and LIMS), SNe of all types and AGN feedback, and whenever its thermal energy exceeds its binding energy a strong galactic wind is generated and the SF is suppressed. We recall that as far as SMBH accretion (and consequently AGN feedback) is concerned, we also take into account the effect of radiation pressure which stops accretion when the luminosity exceeds the Eddington luminosity. Therefore, even if not directly, radiation pressure influences the ISM thermal energy. We paid particular attention to the role of Type Ia SNe feedback in the suppression of SF and the maintenance of such situation, after the main galactic wind.

7.5.1 Models without AGN feedback

In the first set of simulations presented in this paper we excluded the contribution of AGN feedback from the energetic budget. The thermal energy of the gas depends on SNe (both Type Ia and core-collapse), and on stellar winds (both from massive stars and LIMS). After the occurrence of the first galactic wind and consequent suppression of SF, only Type Ia SNe contribute to the thermal energy of the gas which is restored by low mass stars, with the additional contribution of the thermalization due to the velocity dispersion of the ejecta from the dying low mass stars. We first tested the model without AGN feedback on the chemical properties of the dominant stellar populations in ellipticals (e.g. mass metallicity relation and $[\alpha/\text{Fe}]$ ratios) and selected the parameters that best reproduce observations. From the point of view of the energetic budget, the main conclusions are the following:

- By assuming an efficiency of energy transfer of $\eta_{\text{II}} = 3\%$ and of $\eta_{\text{Ia}} = 80\%$ for core-collapse and Type Ia SNe (see Recchi et al., 2001), respectively, all systems are able to develop a first massive galactic wind, when the condition $E_{\text{gas}}^{\text{th}} \geq E_{\text{gas}}^{\text{b}}$ is satisfied. The time of the onset of the galactic wind, t_{GW} , becomes smaller at increasing galaxy mass, according to the *inverse wind scenario* of Matteucci (1994), and this is due to an assumed increasing efficiency of star formation with galactic mass.
- All systems with final stellar mass $\lesssim 10^{12} M_{\odot}$ can satisfy the condition $E_{\text{gas}}^{\text{th}} \geq E_{\text{gas}}^{\text{b}}$, for the entire galaxy life, when the above SN efficiencies of energy transfer are adopted. In other words, these galaxies are suffering a continuous wind for the remaining $\sim 12\text{Gyr}$, after the main early wind. However, for higher mass systems the thermal energy of the gas, after the main wind, appears to be comparable to its binding energy for all the passive period of the evolution of the galaxy, thus creating a situation in which the gas is not lost from the system.
- If instead the efficiency of energy transfer of Type Ia SNe is assumed to be as low as $\eta_{\text{Ia}} = 10\%$, the situation of comparable thermal and binding energy of the gas, after the main wind, occurs for systems of lower stellar mass ($\sim 10^{10} M_{\odot}$), but for all the smaller galaxies persists the situation of a continuous wind triggered mainly by Type Ia SNe.

Therefore, it appears reasonable to conclude that when AGN feedback is not considered, the thermal energy injected by Type Ia and core-collapse SNe in the ISM is enough for driving global galactic winds at early times as well as to keep the SF quenched for the entire period of passive evolution. In particular, the SF is quenched either in systems with stellar mass $\lesssim 10^{12} M_{\odot}$, but characterized by a high Type Ia SNe efficiency of energy transfer ($\sim 80\%$), or in systems with stellar mass $\lesssim 10^{10} M_{\odot}$, but with an efficiency of energy transfer as low as ($\sim 10\%$). As a consequence, it appears that for high mass galaxies an additional source of energy should be required, in particular if the efficiency of energy transfer by Type Ia SNe is significantly smaller than $\sim 80\%$, and this additional energy should be provided by the AGN feedback.

7.5.2 Models with AGN feedback

In our study we adopted as the additional source of heating the AGN feedback. We considered the effects of radiative feedback on a galaxy with initial infall mass of $5 \times 10^{12} M_{\odot}$ (corresponding to a final stellar mass of $1.5 \times 10^{12} M_{\odot}$), neglecting a direct effect of radiation pressure and/or other mechanisms associated with jets. Radiation pressure (as parametrized by the Eddington luminosity) plays an indirect role on ISM heating, because BH accretion and the associated energy injection are stopped whenever the accretion luminosity is larger than the Eddington one. In the simulation, the central BH is characterized by a seed mass of $10^6 M_{\odot}$ and, as just recalled, it undergoes standard Bondi-Eddington limited accretion. Due to the one-zone nature of our model, we are forced to fix an absorption coefficient ξ , namely the fraction of accretion luminosity actually deposited on the ISM via Compton heating. This number, in hydrodynamical simulations with radiative transport, is found to be time dependent. Here we use the parametrization introduced in Ciotti et al. (1997), but we change the value by orders of magnitude, exploring also some unrealistic cases. As the results change very little even for large variations in the adopted value of ξ , we are confident that our conclusions are quite robust. In particular, we considered four different values for the absorption coefficient ξ , i.e. 3×10^{-14} (the physically expected order of magnitude for a realistic gaseous atmosphere of an elliptical galaxy, see Section 7.4), 3×10^{-4} , 3×10^{-2} and 1 (unrealistically high values used to test the importance of AGN thermal feedback), which allowed us to isolate four different physical situations. We reached the following conclusions:

- As expected, due to the indirect role of the radiation pressure which reduces the BH accretion whenever the accreted luminosity is larger than the Eddington one, the evolution of the BH accretion rate is characterized by a series of spikes, each with a duration of ~ 40 Myr. The spikes are reflected into the luminosity which, as a consequence, is characterized by a bursting shape. The predicted bolometric luminosities are in the range $10^{44} - 10^{47}$ erg/s, in good agreement with observations.
- For absorption coefficients below $\xi = 3 \times 10^{-4}$, the effect of the AGN on the evolution of the thermal energy of the gas is totally negligible, with no difference between this model and the one without AGN feedback.
- For $\xi = 3 \times 10^{-4}$ the effect of the AGN on the thermal energy of the gas becomes detectable, however the time at which the galactic wind starts is unchanged with respect to the model without AGN feedback. Therefore, in this scenario, the AGN cannot be the main cause for the formation of a galactic wind. However, since its contribution for the subsequent evolution of $E_{\text{gas}}^{\text{th}}$ cannot be neglected, its role can be crucial in maintaining the SF quenched.
- For $\xi = 3 \times 10^{-2}$, the total thermal energy of the gas becomes completely dominated by the AGN feedback during the entire evolution. In this model, the galactic wind also sets in at earlier times so that the AGN feedback appears to be its main driver together with core-collapse SNe.

- In the unphysical case in which $\xi = 1$, the many bursts that, due to the AGN feedback, characterize the shape of $E_{\text{gas}}^{\text{th}}$, are so powerful that they can provide an energy exceeding the binding energy of the entire galaxy. Therefore, we are inclined to consider this case physically unacceptable.
- We computed the final BH masses for galaxies of initial infall mass equal to 10^{10} , 10^{11} , 10^{12} and $5 \times 10^{12} M_{\odot}$. We succeeded in reproducing the observed proportionality between the stellar mass of the host galaxy and that of the central black hole as well as the Magorrian relation, without the need of stopping ad hoc the accretion.

In conclusion, the most convincingly scenario is the one in which the ISM is thermalized by both AGN feedback and SNe of all types. When the efficiency of energy transfer of Type Ia SNe is $\sim 80\%$, core-collapse and Type Ia SNe are capable of both driving a global galactic wind at early times and at keeping the SF quenched during the passive evolution for systems with stellar mass $\lesssim 10^{12} M_{\odot}$. If one adopts only an efficiency of $\sim 10\%$ for Type Ia SNe, simulating the strong cooling present in the innermost galaxy regions, then the galaxy stellar mass above which AGN feedback is necessary is $\sim 10^{10} M_{\odot}$. The cooling process is indeed a complex one and depends strongly on the environmental conditions. When SNe explode in a cold and dense medium, the cooling is quite effective. On the other hand, when the environment is warm and rarefied the cooling is negligible. For example Recchi et al. (2001), by means of a dynamical model, suggested that the feedback of Type Ia SNe is more effective than that from Type II SNe (Cioffi et al., 1988; Bradamante et al., 1998; Melioli et al., 2004), since the former explode in an already heated medium. When the contribution from the AGN is added and is characterized by the physically expected value for the absorption coefficient of $\xi = 3 \times 10^{-14}$, the BH feedback appears to be important to regulate the growth of the BH itself but only marginally important for the galaxy evolution. The first effects on the thermalization of the ISM manifest when an absorption coefficient $\xi \simeq 10^{-4}$ is adopted. In that case, the effect of the AGN on the development of the main galactic wind is still negligible when compared to that of SNe, but it can substantially contribute in keeping the SF quenched during the galaxy passive evolution. This result is supported also by recent hydrodynamical simulations. In particular, Lanfranchi et al. (2021) (see also Caproni et al., 2015; Caproni et al., 2017) investigated the effects of outflows from BHs on the gas dynamics in dwarf spheroidal galaxies (dSphs) by means of 3D hydrodynamic simulations, and concluded that, in an inhomogeneous ISM, the impact of the AGN outflow appears to be substantially reduced and its contribution to the removal of gas from the galaxy is almost negligible.

CHAPTER 8

Final Remarks

IN THIS THESIS, we have investigated the chemical evolution of neutron capture elements in different galactic environments, from external galaxies of different morphological type (ellipticals, spirals and irregulars), to Local Group dSph and UFD galaxies and the MW.

To this aim, I focused first on computing the rate of MNS in different galaxies and the CMNSR in different cosmological scenarios. Secondly, I studied the chemical evolution of Eu and Ba in different dSph and UFD galaxies with different prescriptions for the nucleosynthesis and the timescales of production of r-process material. Then, I extended the study on a larger number of neutron capture elements observed with the *Gaia*-ESO survey and focused on their evolution and distribution in the MW galaxy. I then focused on the Bulge of the MW, in which I first developed new model for the formation and evolution of this Galactic component and then I compared their predictions to the Ce abundances observed by the APOGEE survey. Finally, I presented a new formulation for the feedback prescriptions in in early-type galaxy.

In the following Sections, I summarize the main results of this Thesis and outline the future perspectives of this work.

8.1 Summary and conclusions

8.1.1 External galaxies and the cosmic merging neutron stars rate

In Chapter 3, I computed models for the chemical evolution of external galaxies of different morphological type (ellipticals, spirals and irregulars) in order to give predictions for the MNS rates in different environments. In the model, galaxies are formed by infall of primordial gas in a pre-existing diffuse dark matter halo. The infalling mass of gas, the infall timescale and the efficiency of SF, have been fine tuned in order to reproduce the measured present day SFR in the solar neighbourhood (for spiral galaxies) and in the Small Magellanic Cloud (for irregular galaxies). For ellipticals we traced their typical SF behaviour, with a quenching of the SF determined by the action of galactic winds.

The rate of MNS in the different galaxies has been computed as the convolution between the SF of the studied galaxy with different DTDs (we adopted the prescriptions of Simonetti et al., 2019, with different values of the β parameter which shapes the distribution of the systems initial separation). It has been tested also the case in which all NS binary systems are merging with the same short delay time (10 Myr, as suggested by Matteucci et al., 2014). The rate of MNS in spiral galaxies has been fine tuned to reproduce the one suggested by Kalogera et al. (2004) in the MW, of $\sim 80_{-60}^{+200}$ events/Myr. The [Eu/Fe] vs. [Fe/H] abundance pattern in spiral galaxies has also been considered as an observational constraint. We considered scenarios in which either MNS are the only producers of Eu or in which also massive stars contribute to its production. Results have been compared with observations in the MW.

The main results are the following:

- Concerning spiral galaxies, in order to reproduce at the same time the observed present day rate of MNS, the [Eu/Fe] vs. [Fe/H] trend and the observed solar Eu abundances in the Galaxy, we can assume either a DTD with $\beta = -0.9$ or a constant delay time of 10 Myr. In the first case, the occurrence probability of MNS is 5.42% and the Eu should be co-produced by both MNS (with a yield of $0.5 \times 10^{-6} M_{\odot}$ per merging event) and massive stars. In the second case, the occurrence probability of MNS is found to be 6.15% and the yield of Eu should be $2.0 \times 10^{-6} M_{\odot}$. In both cases the yield of Eu is well inside the theoretical range predicted by Korobkin et al. (2012).
- Concerning elliptical galaxies, we should not be able to see any merging event at the present time if a short and constant total delay for merging is assumed. In fact, in this case the dependence of the MNS rate with the SF is stronger than in the case with a DTD, and the rate will follow the evolution of the SF (as it happens for massive stars). If, on the other hand, we assume a DTD then the present day rate of MNS will be different from zero (as in the case of Type Ia SNe), in agreement with the probability that the event GW170817 has happened in an early-type galaxy.

- When comparing the predicted [Eu/Fe] vs. [Fe/H] trend in galaxies of different morphological type the time-delay model is found, as expected. Ellipticals, with higher SF, are producing a longer plateau than spirals and irregulars, with weaker SF.

The cosmic evolution of the MNS rate (cosmic MNS rate, CMNSR) has been computed in three different cosmological scenarios: i) a simple PLE scenario, in which the number density of different galaxies is assumed to be constant with redshift; ii) a DE scenario, which simulates a typical hierarchical galaxy formation; iii) an alternative scenario, observationally derived. The CMNSR has been computed both in the case of DTD with $\beta = -0.9$ and in the case of a constant and short delay time for merging and it has been compared with the redshift distributions of SGRBs as derived by Ghirlanda et al. (2016). Our main conclusions are the following:

- In the PLE, the CMNSR computed with a short and constant delay time is characterized by two peaks. The first peak, at $z \sim 8$, is due to the formation at high redshift of elliptical galaxies, while the second peak, at $z \sim 2$ is due to spirals. The CMNSR decreases abruptly after the first peak, because of the quenching of the SF of early-type galaxies. On the contrary, if a DTD for MNS is considered, the decrease after the high-redshift peak is smoother, because the rate of MNS in ellipticals does not stop with the stop of the SF and, therefore, early-type galaxies can contribute to the CMNSR for the whole range of redshift. Independently of adopting a DTD, the contribution from elliptical galaxies is dominant at high redshift, whereas that from spirals is dominant at lower redshift. The present time CMNSR predicted is in agreement with the one observed by LIGO/Virgo as well as the one estimated by Della Valle et al. (2018).
- In the DE and in the alternative scenario, the contribution to the CMNSR from elliptical galaxies has a lower impact with respect to spirals, for the whole range of redshift, and using a DTD or a constant delay time for merging has almost no consequences on the overall behavior. Also in these scenarios, our predictions for the present day CMNSR are in good agreement with the observations.
- The alternative scenario can be considered the best one because it nicely reproduces the cosmic stellar mass density observed by Madau et al. (2014). Gioannini et al. (2017) also proposed the alternative scenario as the best one, because of the agreement with the cosmic star formation rate of Madau et al. (2014). If we assume the alternative scenario as the best one, the SGRBs redshift distribution proposed by Ghirlanda et al. (2016) is best represented by a model with a DTD for MNS, otherwise too many events at high redshift are produced.

8.1.2 Dwarf spheroidal and ultra-faint dwarf galaxies

In Chapter 4, I focused on the chemical evolution of both Eu and Ba in 6 dSph and 2 UFD galaxies. I presented results for Sculptor and Fornax, as representative

of those obtained for the other dSphs, and of Reticulum II because of its peculiar abundance patterns. Results for the other galaxies are provided as Supplementary Material online of the paper Molero et al. (2021a).

For each galaxy, we first fine tuned the model in order to reproduce the observed SFR, the [Mg/Fe] vs. [Fe/H] abundance pattern, the MDF and the present day observed number of stars. Then, we focused on the evolution of the neutron capture elements.

We compared our model with the observational data of Reichert et al. (2020). Except that for Reticulum II, for all the dwarf galaxies in the sample the observed [Eu/Fe] vs. [Fe/H] shows a pattern very similar to that observed in the MW, characterized by a plateau at low-intermediate metallicities followed by a decrease. On the other hand, the [Ba/Fe] vs. [Fe/H] trend is characterized by a low abundance of Ba at low metallicities and by almost solar values from intermediate to high metallicities. The abundances of Eu and Ba in Reticulum II, on the contrary, are concentrated only at really low metallicity and are 1-2 order of magnitude higher than those observed in the other dwarfs.

Concerning the nucleosynthesis of neutron capture elements, we adopted MNS and/or MR-SNe as r-process producers and LIMS as s-process ones. The yields of Eu and Ba from MNS have been obtained by scaling them with the one of Sr observed by Watson et al. (2019) in the reanalysis of the spectra of the kilonova AT2017gfo which followed the neutron-star merger GW170817. For MR-SNe, we tested different sets of yields from the literature and for LIMS we adopted yields of Busso et al. (2001) for stars in the mass range of $1.0 - 3.0 M_{\odot}$. MR-SNe are a quick source for the production of r-process material, while MNS are considered a delayed one if proper DTDs are adopted. On the contrary, if MNS are assumed to merge on a short and constant timescales, they are a quick source.

Our main results for Sculptor and Fornax can be summarized as follows:

- Models in which r-process material is produced only by a quick source are able to produce the [Eu/Fe] vs. [Fe/H] abundance pattern, but fails in reproducing the low-metallicity data of the [Ba/Fe] vs. [Fe/H]. This happens also when r-process is co-produced by both a quick and a delayed source (such as MR-SNe + MNS with a DTD).
- On the contrary, models in which r-process material is produced only with longer delays can reproduce the [Ba/Fe] vs. [Fe/H] trend, but fails to reproduce the [Eu/Fe] one.

Therefore, a scenario in which both MR-SNe and MNS with a DTD produce r-process material is certainly able to reproduce the observed [Eu/Fe] vs. [Fe/H] in dwarf galaxies as it happens in the MW (in the MW this has already been confirmed by several studies, e.g., Matteucci et al., 2014; Cescutti et al., 2015; Côté et al., 2019; Simonetti et al., 2019). Here, we found that the Eu produced by each MNS event should be in the range $(3.0 \times 10^{-6} - 1.5 \times 10^{-5} M_{\odot})$ range, slightly higher than the one estimated from the kilonova AT2017gfo, but in agreement with the one estimated by Korobkin et al. (2012). For MR-SNe, their yields is in the range of the theoretical calculations of Nishimura et al. (2017), if only 1-2% of

stars with initial mass in the (10-80) M_{\odot} range would die as a MR-SNe. However, when compared to the observed data of the [Ba/Fe] vs. [Fe/H], this model struggles in reproducing the low-metallicity data, because of the too strong production from MR-SNe. When only a delayed source is adopted as r-process site, the agreement with the low-metallicity data of Ba improves, but the model slightly underestimate the data at intermediate [Fe/H], proving that the contribution to the s-process nucleosynthesis from rotating massive stars can not be excluded (see e.g., Rizzuti et al., 2019; Rizzuti et al., 2021).

On the other hand, results for the Reticulum II UFD galaxy are different from those of the other dwarfs, because of its peculiar abundance patterns. We can summarize them as follows:

- The low-metallicity high-enhanced data of both the Ba and the Eu abundances can be explained only if a quick source is active for the r-process production. It can be represented either by MR-SNe or by MNS with a short delay time for merging, but in any case it should pollute the ISM really fast. It can be represented by a single event with the same yields adopted in the other environments (but lower than the ones estimated by Ji et al., 2016). If the single event coincide with a MNS then, because of the low SF of Reticulum II, the α_{MNS} parameter should be set to 1.

8.1.3 Milky Way - the disc

In Chapter 5, I extended our study on the origin of neutron capture elements by analyzing both the abundance patterns and radial gradients of the 9 chemical species (Y, Zr, Ba, La, Ce, Eu, Mo, Nd, Pr) observed by the *Gaia*-ESO survey in the MW disc. Gradients can indeed provide important informations about both the nucleosynthesis and the timescales of production of the different chemical elements which, in the case of neutron capture elements, can still be very uncertain. In order to study the chemical evolution of the disc, we adopted a delayed two-infall model with an inside-out scenario of formation and with a variable SF efficiency. The model has been previously tested (Palla et al., 2020) and it is able to reproduce the main observational constraints of the MW disc. For the nucleosynthesis and timescales of production of the neutron capture elements we adopted the most up to date prescriptions. The r-process sites are:

- MNS with a DTD with $\beta = -0.9$. Their rate has been fine tuned in order to reproduce the latest estimation of the MNS rate of Abbott et al. (2021) after having converted it in a Galactic one, equal to $32_{-24}^{+49} \text{ Myr}^{-1}$ (consistent in the error bars with that from Kalogera et al., 2004). The yields of the different neutron capture elements from MNS have been obtained as in Chapter 4, by scaling the one of Sr observed by Watson et al. (2019) according to the solar system r-process contribution, as determined by Simmerer et al. (2004).
- MR-SNe, which are assumed to be 20% of stars with initial mass in the 10-25 M_{\odot} with yields by Nishimura et al. (2017). The mass range has been fixed in order to be consistent with the adopted model for the yields of normal

CC-SNe. The assumed yields are the same of our best model of Chapter 4 and the percentage of stars dying as a MR-SNe has been fixed by fine tuning it to the observed [Eu/Fe] vs. [Fe/H] pattern in the solar neighborhood.

The s-process sites are:

- LIMS with yields from the non-rotational set available on the FRUITY data base (Cristallo et al., 2009; Cristallo et al., 2011; Cristallo et al., 2015).
- Rotating massive stars for which we tested the three different sets of yields corresponding to three different initial rotational velocities from Limongi et al. (2018).

Our main results are the following:

- With the previously mentioned prescriptions, the [Eu/Fe] vs. [Fe/H] is well reproduced both in the inner and in the solar and outer regions, in agreement with the past studies on the subject (e.g., Van der Swaelmen et al., 2023). However, the quick source completely dominates the production of Eu. The other neutron capture abundance patterns observed in the adopted OCs sample are also well reproduced in the three disc regions, but yields from LIMS must be reduced of at least a factor of two (in agreement with Rizzuti et al., 2019) and, once MR-SNe contribute to their production, differences between different initial rotational velocities of massive stars becomes negligible (except that for velocities higher than 150 km/s).
- The present day slope of the [Fe/H] gradient predicted by our model is -0.067 ± 0.003 dex kpc^{-1} , which is slightly steeper than the one of the OCs sample, but in agreement with other recent slopes from OC samples (Carrera et al., 2019; Donor et al., 2020; Zhang et al., 2021; Spina et al., 2021; Spina et al., 2022). Moreover, if the observed slope is recomputed by adopting the guiding radii (R_{mean}) instead that the observed galactocentric distance (R_{GC}), then the agreement with the model improves noticeable, suggesting that radial migration might have played a non negligible role.
- The observed [Eu/H] gradient is characterized by a very flat slope. In general, we remind that the flatter is the slope of a certain chemical element, the quicker it is its production. The flat slope observed in the [Eu/H] agrees well with its presumable quick production from MR-SNe (or any other quick source). However, our best model with both a quick and a delayed source (MR-SNe + MNS) is not able to reproduce such a flat slope and even scenarios in which there is no delayed source are not able to improve the fit to the data. If the observed [Eu/H] gradient is recomputed by adopting R_{mean} instead of R_{GC} the agreement with our model does not change.
- Concerning the time evolution of the [Fe/H] and the [Eu/H] gradients, results of our model at Age=0.5, 2 and 5 Gyr are in agreement with the observed trend, with a really limited time evolution of the gradients between the considered ages. However, as for the present day gradient, also at different ages the [Eu/H] gradients obtained by our model is too steep with

respect to the observed ones. Finally, for all the elements belonging to the second s-process peak, our model produces a plateau at low Galactocentric distances most probably due to the effect of LIMS, whose production reaches an equilibrium value before in the inner regions than in the outer one, because of a faster SF and a strong production from LIMS.

8.1.4 Milky Way - the bulge

In Chapter 6, I present our study on the chemical evolution of the Galactic bulge. We mainly constrained our model such that it would reproduce the shape of the MDF observed in the sample of APOGEE stars of Rojas-Arriagada et al. (2020). The observed MDF is characterized by two peaks with different metallicities, a MP one and a MR one. We assume that the MW bulge has been formed by a strong SF episode, mainly responsible for the creation of the MP population, and suffered a second burst of SF as well as accretion of stars from the innermost part of the MW disc, responsible for the creation of the stellar population of the MR peak. Our main preliminary results are the following:

- Previous chemical evolution models (Matteucci et al., 2019) are not able to reproduce the bulge MDF of the sample of Rojas-Arriagada et al. (2020) if rotating massive stars are included, unless a Chabrier (2003) IMF is adopted. In that case, the agreement is improved but models still underproduce the observed MR peak. Among the sets of rotating massive stars yields from Limongi et al. (2018), the ones which best reproduce the observed MDF are those which favour slow or no rotation at the present time. In order to reproduce the MR peak, we estimate an upper limit for the fraction of stars which might have been trapped by the growing bar, which is $f \sim 50\%$. We tested different values of f and found that at least 40% of stars from the inner disc might have contributed to the bulge population.
- The observed abundance patterns for α -elements and for the neutron capture element Ce is best reproduced by assuming a delay of 250 Myr between the two SF episodes. However, even if the model fits the general trend, some deviations are still presents in particular in the case of the [Mg/Fe] and the [Si/Fe] vs. [Fe/H] patterns. On the contrary, the [Ce/Fe] vs. [Fe/H] is nicely reproduced at low metallicities by model with no rotation in massive stars (mainly because of the contribution from MR-SNe), however, at high [Fe/H], the contribution from AGB stars must be reduced in order to fit the data, similarly to what we did in Chapter 5. The chemical contribution of stars accreted by the bar still have to be included in our model and will be subject of future work on the subject.

8.1.5 Elliptical galaxies - the AGN feedback

In Chapter 7, I presented our study on the formation and evolution of early-type galaxies and on how they suppress SF. We adopt an updated version of Matteucci (1994) chemical evolution model for elliptical galaxies, where SN rates were computed in details. The main novelty of this work has been the inclusion of the AGN

feedback, besides that of SNe and stellar winds. The evolutionary scenario considered is the following: ellipticals are formed by infall of gas in a primordial dark matter halo. The gas evolution is influenced by infall and outflow as well as by stellar nucleosynthesis. The system goes through an early intense burst of SF, which is then quenched when strong galactic winds are produced and the galaxy evolves passively afterwards. This happens when the thermal energy of the gas in the ISM exceeds its binding energy. The thermal energy of the gas is given by the sum of the thermal energy deposited in the gas by SN explosions, stellar winds and AGN feedback.

We first presented a set of simulations without the contribution of AGN feedback from the energetic budget. In that case, the thermal energy of the gas depends on SNe (of all types) and on stellar winds. In particular, after the development of the first main galactic wind episode, only Type Ia SNe contribute to the thermal energy of the gas, together with the low contribution due to the velocity dispersion of the ejecta from low mass stars. Our main conclusions are the following:

- By assuming an efficiency of energy transfer of $\eta_{\text{II}} = 3\%$ and of $\eta_{\text{Ia}} = 80\%$ for core-collapse and Type Ia SNe, respectively, all systems with final stellar mass $\leq 10^{12} M_{\odot}$ can satisfy the condition $E_{\text{gas}}^{\text{th}} \geq E_{\text{gas}}^{\text{b}}$, for the entire galaxy life, and therefore are suffering a continuous wind after the main early wind episode. On the contrary, for higher mass system, after the main wind, the gas is hardly lost from the galaxy. If the efficiency of energy transfer of Type Ia SNe is assumed to be as low as $\eta_{\text{Ia}} = 10\%$, also systems with lower stellar mass ($\sim 10^{10} M_{\odot}$) struggle to get rid of the gas after the main wind episode.

Therefore, we can conclude that when the AGN feedback is not considered, the thermal energy injected by Type Ia and core-collapse SNe in the ISM is enough for driving a global galactic winds at early times as well as to keep the SF quenched for the entire period of passive evolution. This is valid for system with a stellar mass $\leq 10^{12} M_{\odot}$ ($\leq 10^{10} M_{\odot}$) with an efficiency of energy transfer of Type Ia SNe of $\eta_{\text{Ia}} = 80\%$ ($\eta_{\text{Ia}} = 10\%$). For higher mass galaxies an additional source of energy should be required.

In our study the additional source of heating adopted has been the AGN feedback. In particular, we considered the effect of radiative feedback on a galaxy with initial infall mass of gas of $5 \times 10^{12} M_{\odot}$. The central BH is characterized by a seed mass of $10^6 M_{\odot}$ and it undergoes standard Bondi-Eddington limited accretion. We fix an absorption coefficient ξ , which represents the fraction of accretion luminosity actually deposited in the ISM via Compton heating, for which we explored different values. Our main conclusions are the following:

- For absorption coefficients below $\xi = 3 \times 10^{-4}$, the effect of the AGN on the evolution of the thermal energy of the gas is negligible. For $\xi = 3 \times 10^{-4}$, the role of the AGN becomes crucial in maintaining the SF quenched, but it is not the main cause of formation of a galactic wind. For $\xi = 3 \times 10^{-2}$, the total thermal energy of the gas is dominated by the AGN feedback for the entire evolution of the galaxy, with the AGN being also the main cause of the development of the main wind episode. The case in which $\xi = 1$ is

unphysical and this is reflected by the results of the simulations in which the many bursts which characterize the shape of $E_{\text{gas}}^{\text{th}}$ are so powerful that they can provide an energy exceeding the binding energy of the entire galaxy.

In conclusion, the most convincing scenario is the one in which the ISM is thermalized by both AGN feedback and SNe of all types. In particular, when the contribution from the AGN is added and is characterized by the physically expected value for the absorption coefficient of $\xi = 3 \times 10^{-14}$, the BH feedback appears to be important to regulate the growth of the BH itself, but only marginally important for the galaxy evolution. The first effects on the thermalization of the ISM manifest when an absorption coefficient $\xi \simeq 10^{-4}$ is adopted. In that case, the effect of the AGN on the development of the main galactic wind is still negligible when compared to that of SNe, but it can substantially contribute in keeping the SF quenched during the galaxy passive evolution.

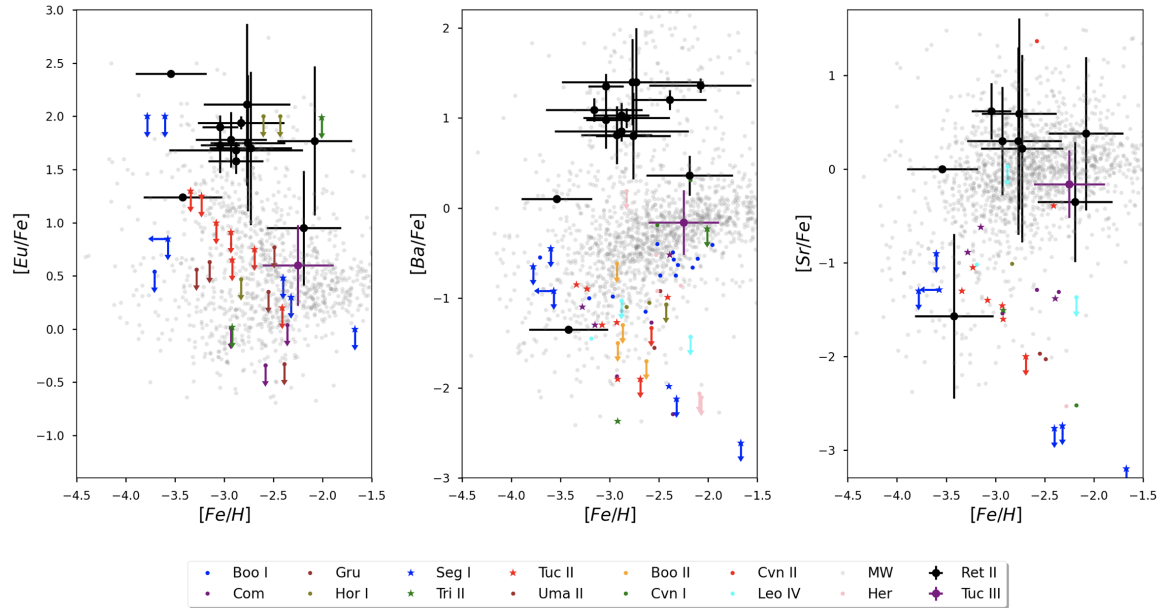


FIGURE 8.1: Observed $[Eu/Fe]$, $[Ba/Fe]$ and $[Sr/Fe]$ vs. $[Fe/H]$ of Reticulum II (black dots) and Tucana III (purple dots) compared to those of other UFDs (colored points) and the MW halo (grey dots). Data are a collection from SAGA database (Suda et al., 2008; Suda et al., 2011; Yamada et al., 2013; Suda et al., 2017).

8.2 Future prospects

There are still several open questions about the evolution of neutron capture elements which can be further explored in order to better understand their production and distribution. In the following, I propose some future perspectives to my work.

In Chapter 4, I show the enhanced r-process elements pattern observed in Reticulum II. However, recent observations show that Reticulum II is not the only UFD galaxy with a stellar population with such a peculiar elemental abundances. Indeed, some stars in Tucana III show high Eu, Sr and Ba abundances as well. In Figure 8.1, we report the observed $[Eu/Fe]$, $[Ba/Fe]$ and $[Sr/Fe]$ vs. $[Fe/H]$ abundances pattern for both Reticulum II and Tucana III compared to those of other UFDs and MW halo stars. We were able to reproduce such a trend in the Reticulum II UFD by assuming that a single and rare r-process event polluted the galaxy very fast at early times. However, why such a rare event would happen in a galaxy as small as Reticulum II? And why the Tucana III stars are less r-process enhanced than the one in Reticulum II? As also pointed out by Hansen et al. (2017), r -I stars have mostly been identified in more luminous dwarf galaxies which probably had more gas content at early times and therefore the ejecta from a MNS or a MR-SNe would have been diluted. Also, the spread in these galaxies similar to the one of MW halo stars, would point towards an inhomogeneous mixing scenario, which can be better investigated by stochastic chemical evolution models (Cescutti et al., 2015).

In Chapter 5 one question remains open. Why we can not reproduce the flat [Eu/H] gradient in the disc of the MW as observed in the young OCs sample? As we discussed, the flatter is the gradient of a chemical element, the quicker is its production. However, even by imposing a quick production of Eu from MR-SNe (or MNS with a constant and short delay time for merging), the predicted gradient is too steep with respect to the observed one. Therefore, the disagreement between model predictions and data is not to be attributed to the nucleosynthesis prescriptions, but rather to different Galaxy formation mechanisms and/or radial migration (if clusters are affected by it). A constant SF efficiency for all Galactocentric distances indeed improved our results. However, this choice has already been discarded by previous chemical evolution models (see e.g., Grisoni et al., 2018; Palla et al., 2020). However, the possibility of having a constant SF efficiency only in the outer part of the MW should still be tested and can be supported by the fact that our model predicts a better agreement with the data in the inner region than in the outer ones. If that is the case, then in the future it would first be needed to test the model on the observed MDFs, on the abundance patterns and on the gradients of also lighter elements in the outer region.

Some of the main uncertainties in the production of r-process elements in chemical evolution models are the adopted prescriptions for MR-SNe. While for MNS we can rely on observations for the yields (Watson et al., 2019), for the DTDs (from observations of sGRBs, e.g., Ghirlanda et al., 2016) and for the rate (Kalogera et al., 2004; Abbott et al., 2021), for MR-SNe we have to arbitrarily choose (i) the fraction of normal CC-SNe which can die as a MR-SNe, (ii) the mass range and (iii) the yields (since different authors often obtain different results). In Chapters 4 and 5, we show some possibilities in which these free parameters can be fixed in a self-consistent manner. Nevertheless, ambiguities persist, and the possibility of a substantial level of degeneracy remains a significant consideration. One of the improvements which should be addressed in the future is the computation of the yields for different masses. In the actual chemical evolution models, in fact, the prescription for one single stellar mass (e.g., $35 M_{\odot}$) is interpolated to all the range of masses considered. Computing yields of MR-SNe for stars of different masses is not an easy task and it often depends on the limited computational power. However, different stars would produce different amount of r-process material and, depending on their mass, on different timescales as well. A similar approach was done in Cescutti et al. (2006), where different yields of Eu and Ba from massive stars were assumed *ad hoc* for different masses (12, 15, $30 M_{\odot}$). However, in the future a proper computation of the yields should be achieved and then it would be natural to prove it in chemical evolution models.

A second improvement in the nucleosynthesis of neutron capture elements is to be related to AGB stars. In Chapters 5 and 6, we adopt the yields from the FRUITY database (Cristallo et al., 2009; Cristallo et al., 2011; Cristallo et al., 2015). However, extremely precise isotopic ratio measurements in presolar SiC grains (Liu et al., 2018) demonstrated that the neutron density of FRUITY models is probably overestimated. Indeed, in chemical evolution models, yields of AGB from FRUITY are usually reduced by a factor of two or more (see Chapters 5 and 6 as well as

Rizzuti et al., 2019; Rizzuti et al., 2021). Models for AGB stars have been recently revised by considering the mixing triggered by magnetic fields (see Vescovi et al., 2020 for details) for a star of $M = 2 M_{\odot}$ at metallicities $Z = 10^{-2}$, Z_{\odot} , 2×10^{-2} . Extensions of these models also to 1.5, 2.5, 3 M_{\odot} as well as to more metallicities are in preparation (Vescovi et al., in prep.). Following the work of Magrini et al. (2021) and of Viscasillas Vázquez et al. (2022b), we are planning to adopt the new magnetic yields from AGB stars to model the evolution of the $[s/\alpha]$ vs. Age patterns in the Galactic disc in the range $R_{GC} \sim 6 - 20$ kpc and to compare them to the sample of OCs presented in Chapter 5, in order to investigate on the possibility of using such relations as chemical clocks in the Galactic disc.

The study on the bulge presented in Chapter 6 still needs to be further developed. As a first approach we are assuming that the two peaks MDF observed in the bulge region ($R_{GC} \leq 3.5$ kpc) can be reproduced by an early fast and violent star formation event, mainly responsible for the creation of the MP peak, combined with a stop in the SF of 250 Myr (Matteucci et al., 2019) and a fraction of disc stars being trapped by a growing bar (with these two last phenomena responsible for the creation of the MR peak). Although we successfully reproduce the observed MDF, we still need to investigate on the abundance patterns of both the α -elements and the neutron capture element Ce. Whether or not stars being trapped by the bar are then accreted by the bulge can depend on their radial velocity. If that is the case then, depending on the assumed radial velocity and on where stars are being trapped, only stars with a certain mass will die in the bulge and will pollute that region. These would then be *active agents* of chemical evolution (see also Prantzos et al., 2023), namely long-lived nucleosynthesis sources, such as low mass AGB stars as well as Type Ia SNe. In that case, from the chemical evolution point of view, we would expect variations in the $[\alpha/Fe]$ vs. $[Fe/H]$ abundance patterns for elements which have a strong contribution from Type Ia SNe (for example we would not expect any change in the O abundance pattern), and in particular in the $[Ce/Fe]$ vs. $[Fe/H]$ trend because of the contribution from AGB stars, probably enhancing it towards higher metallicities. A second ingredient which can be taken into account, is the presence of cold gas inflows driven by the Galactic bar from the disc towards the centre (see e.g., Sormani et al., 2023). If such a gas transport is present, then it can fuel SF activity. Moreover, its chemical composition will be that of the inner disc, with potential consequences on the abundance patterns predicted by our model. In the future, different prescriptions will be tested.

Bibliography

- (N.d.[b]). In: ().
- Abadi, Mario G. et al. (July 2003a). “Simulations of Galaxy Formation in a Λ Cold Dark Matter Universe. I. Dynamical and Photometric Properties of a Simulated Disk Galaxy”. In: 591.2, pp. 499–514. DOI: [10.1086/375512](https://doi.org/10.1086/375512). arXiv: [astro-ph/0211331](https://arxiv.org/abs/astro-ph/0211331) [[astro-ph](#)].
- (Nov. 2003b). “Simulations of Galaxy Formation in a Λ Cold Dark Matter Universe. II. The Fine Structure of Simulated Galactic Disks”. In: 597.1, pp. 21–34. DOI: [10.1086/378316](https://doi.org/10.1086/378316). arXiv: [astro-ph/0212282](https://arxiv.org/abs/astro-ph/0212282) [[astro-ph](#)].
- Abbott, B. P. et al. (Oct. 2017). “GW170817: Observation of Gravitational Waves from a Binary Neutron Star Inspiral”. In: 119.16, 161101, p. 161101. DOI: [10.1103/PhysRevLett.119.161101](https://doi.org/10.1103/PhysRevLett.119.161101). arXiv: [1710.05832](https://arxiv.org/abs/1710.05832) [[gr-qc](#)].
- Abbott, R. et al. (May 2021). “Population Properties of Compact Objects from the Second LIGO-Virgo Gravitational-Wave Transient Catalog”. In: 913.1, L7, p. L7. DOI: [10.3847/2041-8213/abe94910.48550/arXiv.2010.14533](https://doi.org/10.3847/2041-8213/abe94910.48550/arXiv.2010.14533). arXiv: [2010.14533](https://arxiv.org/abs/2010.14533) [[astro-ph.HE](#)].
- Amati, L. et al. (July 2018). “The THESEUS space mission concept: science case, design and expected performances”. In: *Advances in Space Research* 62.1, pp. 191–244. DOI: [10.1016/j.asr.2018.03.010](https://doi.org/10.1016/j.asr.2018.03.010). arXiv: [1710.04638](https://arxiv.org/abs/1710.04638) [[astro-ph.IM](#)].
- Anderson, L. D. et al. (Sept. 2020). “Unusual Galactic H II Regions at the Intersection of the Central Molecular Zone and the Far Dust Lane”. In: 901.1, 51, p. 51. DOI: [10.3847/1538-4357/abadf6](https://doi.org/10.3847/1538-4357/abadf6). arXiv: [2008.04258](https://arxiv.org/abs/2008.04258) [[astro-ph.GA](#)].
- Anglés-Alcázar, Daniel et al. (Aug. 2021). “Cosmological Simulations of Quasar Fueling to Subparsec Scales Using Lagrangian Hyper-refinement”. In: 917.2, 53, p. 53. DOI: [10.3847/1538-4357/ac09e8](https://doi.org/10.3847/1538-4357/ac09e8). arXiv: [2008.12303](https://arxiv.org/abs/2008.12303) [[astro-ph.GA](#)].
- Arcones, A., H. Th. Janka, and L. Scheck (June 2007). “Nucleosynthesis-relevant conditions in neutrino-driven supernova outflows. I. Spherically symmetric hydrodynamic simulations”. In: 467.3, pp. 1227–1248. DOI: [10.1051/0004-6361:20066983](https://doi.org/10.1051/0004-6361:20066983). arXiv: [astro-ph/0612582](https://arxiv.org/abs/astro-ph/0612582) [[astro-ph](#)].
- Arcones, A. and F. K. Thielemann (Jan. 2013). “Neutrino-driven wind simulations and nucleosynthesis of heavy elements”. In: *Journal of Physics G Nuclear Physics*

- 40.1, 013201, p. 013201. DOI: [10.1088/0954-3899/40/1/013201](https://doi.org/10.1088/0954-3899/40/1/013201). arXiv: [1207.2527](https://arxiv.org/abs/1207.2527) [astro-ph.SR].
- Arcones, Almudena and Friedrich-Karl Thielemann (Dec. 2023). “Origin of the elements”. In: 31.1, 1, p. 1. DOI: [10.1007/s00159-022-00146-x](https://doi.org/10.1007/s00159-022-00146-x).
- Argast, D. et al. (Mar. 2004). “Neutron star mergers versus core-collapse supernovae as dominant r-process sites in the early Galaxy”. In: 416, pp. 997–1011. DOI: [10.1051/0004-6361:20034265](https://doi.org/10.1051/0004-6361:20034265). arXiv: [astro-ph/0309237](https://arxiv.org/abs/astro-ph/0309237) [astro-ph].
- Arimoto, N. and Y. Yoshii (Feb. 1987). “Chemical and photometric properties of a galactic wind model for elliptical galaxies.” In: 173, pp. 23–38.
- Arnett, W. David (Jan. 1966). “Gravitational collapse and weak interactions”. In: *Canadian Journal of Physics* 44, pp. 2553–2594. DOI: [10.1139/p66-210](https://doi.org/10.1139/p66-210).
- Asplund, Martin et al. (Sept. 2009). “The Chemical Composition of the Sun”. In: 47.1, pp. 481–522. DOI: [10.1146/annurev.astro.46.060407.145222](https://doi.org/10.1146/annurev.astro.46.060407.145222). arXiv: [0909.0948](https://arxiv.org/abs/0909.0948) [astro-ph.SR].
- Athanassoula, E. (Jan. 2005). “Dynamical Evolution of Barred Galaxies”. In: *Celestial Mechanics and Dynamical Astronomy* 91.1-2, pp. 9–31. DOI: [10.1007/s10569-004-4947-7](https://doi.org/10.1007/s10569-004-4947-7). arXiv: [astro-ph/0501196](https://arxiv.org/abs/astro-ph/0501196) [astro-ph].
- Baba, Junichi and Daisuke Kawata (Mar. 2020). “Age dating the Galactic bar with the nuclear stellar disc”. In: 492.3, pp. 4500–4511. DOI: [10.1093/mnras/staa140](https://doi.org/10.1093/mnras/staa140). arXiv: [1909.07548](https://arxiv.org/abs/1909.07548) [astro-ph.GA].
- Babusiaux, C. et al. (Sept. 2010). “Insights on the Milky Way bulge formation from the correlations between kinematics and metallicity”. In: 519, A77, A77. DOI: [10.1051/0004-6361/201014353](https://doi.org/10.1051/0004-6361/201014353). arXiv: [1005.3919](https://arxiv.org/abs/1005.3919) [astro-ph.GA].
- Ballero, S. K. et al. (May 2007). “Formation and evolution of the Galactic bulge: constraints from stellar abundances”. In: 467.1, pp. 123–136. DOI: [10.1051/0004-6361:20066596](https://doi.org/10.1051/0004-6361:20066596). arXiv: [astro-ph/0702137](https://arxiv.org/abs/astro-ph/0702137) [astro-ph].
- Ballero, S. K. et al. (Feb. 2008). “Evolution of chemical abundances in Seyfert galaxies”. In: 478.2, pp. 335–351. DOI: [10.1051/0004-6361:20078663](https://doi.org/10.1051/0004-6361:20078663). arXiv: [0710.4129](https://arxiv.org/abs/0710.4129) [astro-ph].
- Baratella, M. et al. (Feb. 2020). “The Gaia-ESO Survey: a new approach to chemically characterising young open clusters. I. Stellar parameters, and iron-peak, α -, and proton-capture elements”. In: 634, A34, A34. DOI: [10.1051/0004-6361/201937055](https://doi.org/10.1051/0004-6361/201937055). arXiv: [2001.03179](https://arxiv.org/abs/2001.03179) [astro-ph.SR].
- Baratella, M. et al. (Sept. 2021). “The Gaia-ESO Survey: a new approach to chemically characterising young open clusters. II. Abundances of the neutron-capture elements Cu, Sr, Y, Zr, Ba, La, and Ce”. In: 653, A67, A67. DOI: [10.1051/0004-6361/202141069](https://doi.org/10.1051/0004-6361/202141069). arXiv: [2107.12381](https://arxiv.org/abs/2107.12381) [astro-ph.SR].
- Barbuy, Beatriz, Cristina Chiappini, and Ortwin Gerhard (Sept. 2018). “Chemodynamical History of the Galactic Bulge”. In: 56, pp. 223–276. DOI: [10.1146/annurev-astro-081817-051826](https://doi.org/10.1146/annurev-astro-081817-051826). arXiv: [1805.01142](https://arxiv.org/abs/1805.01142) [astro-ph.GA].
- Battaglia, G. et al. (July 2008). “The Kinematic Status and Mass Content of the Sculptor Dwarf Spheroidal Galaxy”. In: 681.1, p. L13. DOI: [10.1086/590179](https://doi.org/10.1086/590179). arXiv: [0802.4220](https://arxiv.org/abs/0802.4220) [astro-ph].
- Battistini, Chiara and Thomas Bensby (Feb. 2016). “The origin and evolution of r- and s-process elements in the Milky Way stellar disk”. In: 586, A49, A49. DOI: [10.1051/0004-6361/201527385](https://doi.org/10.1051/0004-6361/201527385). arXiv: [1511.00966](https://arxiv.org/abs/1511.00966) [astro-ph.SR].

- Baugh, C. M., S. Cole, and C. S. Frenk (Dec. 1996). “Evolution of the Hubble sequence in hierarchical models for galaxy formation”. In: 283.4, pp. 1361–1378. DOI: [10.1093/mnras/283.4.1361](https://doi.org/10.1093/mnras/283.4.1361). arXiv: [astro-ph/9602085](https://arxiv.org/abs/astro-ph/9602085) [astro-ph].
- Bechtol, K. et al. (July 2015). “Eight New Milky Way Companions Discovered in First-year Dark Energy Survey Data”. In: 807.1, 50, p. 50. DOI: [10.1088/0004-637X/807/1/50](https://doi.org/10.1088/0004-637X/807/1/50). arXiv: [1503.02584](https://arxiv.org/abs/1503.02584) [astro-ph.GA].
- Begelman, Mitchell, Martijn de Kool, and Marek Sikora (Dec. 1991). “Outflows Driven by Cosmic-Ray Pressure in Broad Absorption Line QSOs”. In: 382, p. 416. DOI: [10.1086/170731](https://doi.org/10.1086/170731).
- Begelman, Mitchell C., Marta Volonteri, and Martin J. Rees (July 2006). “Formation of supermassive black holes by direct collapse in pre-galactic haloes”. In: 370.1, pp. 289–298. DOI: [10.1111/j.1365-2966.2006.10467.x](https://doi.org/10.1111/j.1365-2966.2006.10467.x). arXiv: [astro-ph/0602363](https://arxiv.org/abs/astro-ph/0602363) [astro-ph].
- Beniamini, Paz, Irina Dvorkin, and Joe Silk (Aug. 2018). “Retention of r-process material in dwarf galaxies”. In: 478.2, pp. 1994–2005. DOI: [10.1093/mnras/sty1035](https://doi.org/10.1093/mnras/sty1035). arXiv: [1711.02683](https://arxiv.org/abs/1711.02683) [astro-ph.HE].
- Bensby, T. et al. (Sept. 2011). “Chemical evolution of the Galactic bulge as traced by microlensed dwarf and subgiant stars. IV. Two bulge populations”. In: 533, A134, A134. DOI: [10.1051/0004-6361/201117059](https://doi.org/10.1051/0004-6361/201117059). arXiv: [1107.5606](https://arxiv.org/abs/1107.5606) [astro-ph.GA].
- Benson, A. J. et al. (Dec. 2003). “What Shapes the Luminosity Function of Galaxies?” In: 599.1, pp. 38–49. DOI: [10.1086/379160](https://doi.org/10.1086/379160). arXiv: [astro-ph/0302450](https://arxiv.org/abs/astro-ph/0302450) [astro-ph].
- Berger, Edo (Aug. 2014). “Short-Duration Gamma-Ray Bursts”. In: 52, pp. 43–105. DOI: [10.1146/annurev-astro-081913-035926](https://doi.org/10.1146/annurev-astro-081913-035926). arXiv: [1311.2603](https://arxiv.org/abs/1311.2603) [astro-ph.HE].
- Bertin, G. et al. (Jan. 1991). “Gaseous Disks in Elliptical Galaxies”. In: *Dynamics of Galaxies and Their Molecular Cloud Distributions*. Ed. by F. Combes and Fabienne Casoli. Vol. 146, p. 43.
- Bhattarai, Binod et al. (May 2022). “Resonance Sweeping in Barred Galaxy Simulations”. In: *AAS/Division of Dynamical Astronomy Meeting*. Vol. 54. AAS/Division of Dynamical Astronomy Meeting, 400.03, p. 400.03.
- Bilitewski, Thomas and Ralph Schönrich (Nov. 2012). “Radial flows and angular momentum conservation in Galactic chemical evolution”. In: 426.3, pp. 2266–2282. DOI: [10.1111/j.1365-2966.2012.21827.x](https://doi.org/10.1111/j.1365-2966.2012.21827.x). arXiv: [1208.0003](https://arxiv.org/abs/1208.0003) [astro-ph.GA].
- Binney, J. and G. Tabor (Sept. 1995). “Evolving cooling flows.” In: 276, pp. 663–678. DOI: [10.1093/mnras/276.2.663](https://doi.org/10.1093/mnras/276.2.663).
- Binney, James et al. (Sept. 1991). “Understanding the kinematics of Galactic Centre gas.” In: 252, p. 210. DOI: [10.1093/mnras/252.2.210](https://doi.org/10.1093/mnras/252.2.210).
- Bissantz, Nicolai and Ortwin Gerhard (Mar. 2002). “Spiral arms, bar shape and bulge microlensing in the Milky Way”. In: 330.3, pp. 591–608. DOI: [10.1046/j.1365-8711.2002.05116.x](https://doi.org/10.1046/j.1365-8711.2002.05116.x). arXiv: [astro-ph/0110368](https://arxiv.org/abs/astro-ph/0110368) [astro-ph].
- Bisterzo, S. et al. (May 2014). “Galactic Chemical Evolution and Solar s-process Abundances: Dependence on the ^{13}C -pocket Structure”. In: 787.1, 10, p. 10. DOI: [10.1088/0004-637X/787/1/10](https://doi.org/10.1088/0004-637X/787/1/10). arXiv: [1403.1764](https://arxiv.org/abs/1403.1764) [astro-ph.SR].
- Bland-Hawthorn, Joss and Ortwin Gerhard (Sept. 2016). “The Galaxy in Context: Structural, Kinematic, and Integrated Properties”. In: 54, pp. 529–596. DOI: [10.1146/annurev-astro-081915-023441](https://doi.org/10.1146/annurev-astro-081915-023441). arXiv: [1602.07702](https://arxiv.org/abs/1602.07702) [astro-ph.GA].

- Bliss, J., A. Arcones, and Y. Z. Qian (Oct. 2018). “Production of Mo and Ru Isotopes in Neutrino-driven Winds: Implications for Solar Abundances and Presolar Grains”. In: 866.2, 105, p. 105. DOI: [10.3847/1538-4357/aade8d](https://doi.org/10.3847/1538-4357/aade8d). arXiv: [1804.03947](https://arxiv.org/abs/1804.03947) [astro-ph.HE].
- Bliss, J. et al. (May 2020). “Nuclear physics uncertainties in neutrino-driven, neutron-rich supernova ejecta”. In: 101.5, 055807, p. 055807. DOI: [10.1103/PhysRevC.101.055807](https://doi.org/10.1103/PhysRevC.101.055807). arXiv: [2001.02085](https://arxiv.org/abs/2001.02085) [nucl-ex].
- Bondi, H. (Jan. 1952). “On spherically symmetrical accretion”. In: 112, p. 195. DOI: [10.1093/mnras/112.2.195](https://doi.org/10.1093/mnras/112.2.195).
- Bonetti, Matteo et al. (Nov. 2019). “Neutron star binary orbits in their host potential: effect on early r-process enrichment”. In: 490.1, pp. 296–311. DOI: [10.1093/mnras/stz2554](https://doi.org/10.1093/mnras/stz2554). arXiv: [1905.12016](https://arxiv.org/abs/1905.12016) [astro-ph.HE].
- Bovy, Jo (Feb. 2015). “galpy: A python Library for Galactic Dynamics”. In: 216.2, 29, p. 29. DOI: [10.1088/0067-0049/216/2/29](https://doi.org/10.1088/0067-0049/216/2/29). arXiv: [1412.3451](https://arxiv.org/abs/1412.3451) [astro-ph.GA].
- Bovy, Jo and Hans-Walter Rix (Dec. 2013). “A Direct Dynamical Measurement of the Milky Way’s Disk Surface Density Profile, Disk Scale Length, and Dark Matter Profile at $4 \text{ kpc} < R < 9 \text{ kpc}$ ”. In: 779.2, 115, p. 115. DOI: [10.1088/0004-637X/779/2/115](https://doi.org/10.1088/0004-637X/779/2/115). arXiv: [1309.0809](https://arxiv.org/abs/1309.0809) [astro-ph.GA].
- Bower, R. G., A. J. Benson, and Robert A. Crain (June 2012). “What shapes the galaxy mass function? Exploring the roles of supernova-driven winds and active galactic nuclei”. In: 422.4, pp. 2816–2840. DOI: [10.1111/j.1365-2966.2012.20516.x](https://doi.org/10.1111/j.1365-2966.2012.20516.x). arXiv: [1112.2712](https://arxiv.org/abs/1112.2712) [astro-ph.CO].
- Bower, R. G. et al. (Aug. 2006). “Breaking the hierarchy of galaxy formation”. In: 370.2, pp. 645–655. DOI: [10.1111/j.1365-2966.2006.10519.x](https://doi.org/10.1111/j.1365-2966.2006.10519.x). arXiv: [astro-ph/0511338](https://arxiv.org/abs/astro-ph/0511338) [astro-ph].
- Bradamante, F., F. Matteucci, and A. D’Ercole (Sept. 1998). “The influence of stellar energetics and dark matter on the chemical evolution of dwarf irregulars”. In: 337, pp. 338–348. arXiv: [astro-ph/9801131](https://arxiv.org/abs/astro-ph/9801131) [astro-ph].
- Bromm, Volker and Abraham Loeb (Oct. 2003). “Formation of the First Supermassive Black Holes”. In: 596.1, pp. 34–46. DOI: [10.1086/377529](https://doi.org/10.1086/377529). arXiv: [astro-ph/0212400](https://arxiv.org/abs/astro-ph/0212400) [astro-ph].
- Brott, I. et al. (June 2011). “Rotating massive main-sequence stars. I. Grids of evolutionary models and isochrones”. In: 530, A115, A115. DOI: [10.1051/0004-6361/201016113](https://doi.org/10.1051/0004-6361/201016113). arXiv: [1102.0530](https://arxiv.org/abs/1102.0530) [astro-ph.SR].
- Brown, Thomas M. et al. (Dec. 2014). “The Quenching of the Ultra-faint Dwarf Galaxies in the Reionization Era”. In: 796.2, 91, p. 91. DOI: [10.1088/0004-637X/796/2/91](https://doi.org/10.1088/0004-637X/796/2/91). arXiv: [1410.0681](https://arxiv.org/abs/1410.0681) [astro-ph.GA].
- Bruenn, Stephen W. (May 1989a). “The Prompt-Shock Supernova Mechanism. I. The Effect of the Free-Proton Mass Fraction and the Neutrino Transport Algorithm”. In: 340, p. 955. DOI: [10.1086/167450](https://doi.org/10.1086/167450).
- (June 1989b). “The Prompt-Shock Supernova Mechanism. II. Supranuclear EOS Behavior and the Precollapse Model”. In: 341, p. 385. DOI: [10.1086/167502](https://doi.org/10.1086/167502).
- Buder, Sven et al. (Sept. 2021). “The GALAH+ survey: Third data release”. In: 506.1, pp. 150–201. DOI: [10.1093/mnras/stab1242](https://doi.org/10.1093/mnras/stab1242). arXiv: [2011.02505](https://arxiv.org/abs/2011.02505) [astro-ph.GA].
- Burbidge, E. Margaret et al. (Jan. 1957). “Synthesis of the Elements in Stars”. In: *Reviews of Modern Physics* 29.4, pp. 547–650. DOI: [10.1103/RevModPhys.29.547](https://doi.org/10.1103/RevModPhys.29.547).

- Burrows, A. and D. Vartanyan (Jan. 2021). “Core-collapse supernova explosion theory”. In: 589.7840, pp. 29–39. DOI: [10.1038/s41586-020-03059-w](https://doi.org/10.1038/s41586-020-03059-w). arXiv: [2009.14157](https://arxiv.org/abs/2009.14157) [astro-ph.SR].
- Busso, M., R. Gallino, and G. J. Wasserburg (Jan. 1999). “Nucleosynthesis in Asymptotic Giant Branch Stars: Relevance for Galactic Enrichment and Solar System Formation”. In: 37, pp. 239–309. DOI: [10.1146/annurev.astro.37.1.239](https://doi.org/10.1146/annurev.astro.37.1.239).
- Busso, Maurizio et al. (Aug. 2001). “Nucleosynthesis and Mixing on the Asymptotic Giant Branch. III. Predicted and Observed s-Process Abundances”. In: 557.2, pp. 802–821. DOI: [10.1086/322258](https://doi.org/10.1086/322258). arXiv: [astro-ph/0104424](https://arxiv.org/abs/astro-ph/0104424) [astro-ph].
- Caffau, E. et al. (Oct. 2005). “Sulphur abundance in Galactic stars”. In: 441.2, pp. 533–548. DOI: [10.1051/0004-6361:20052905](https://doi.org/10.1051/0004-6361:20052905). arXiv: [astro-ph/0507030](https://arxiv.org/abs/astro-ph/0507030) [astro-ph].
- Calura, Francesco and Francesca Matteucci (Apr. 2003). “The evolution of cosmic star formation, metals and gas”. In: 284.2, pp. 429–432. DOI: [10.1023/A:1024023320657](https://doi.org/10.1023/A:1024023320657). arXiv: [astro-ph/0211163](https://arxiv.org/abs/astro-ph/0211163) [astro-ph].
- Cameron, A. G. W. (June 1957). “Nuclear Reactions in Stars and Nucleogenesis”. In: 69.408, p. 201. DOI: [10.1086/127051](https://doi.org/10.1086/127051).
- Cantat-Gaudin, T. et al. (Aug. 2020). “Painting a portrait of the Galactic disc with its stellar clusters”. In: 640, A1, A1. DOI: [10.1051/0004-6361/202038192](https://doi.org/10.1051/0004-6361/202038192). arXiv: [2004.07274](https://arxiv.org/abs/2004.07274) [astro-ph.GA].
- Cappellaro, E., R. Evans, and M. Turatto (Nov. 1999a). “A new determination of supernova rates and a comparison with indicators for galactic star formation”. In: 351, pp. 459–466. DOI: [10.48550/arXiv.astro-ph/9904225](https://doi.org/10.48550/arXiv.astro-ph/9904225). arXiv: [astro-ph/9904225](https://arxiv.org/abs/astro-ph/9904225) [astro-ph].
- (Nov. 1999b). “A new determination of supernova rates and a comparison with indicators for galactic star formation”. In: 351, pp. 459–466. arXiv: [astro-ph/9904225](https://arxiv.org/abs/astro-ph/9904225) [astro-ph].
- Caproni, A. et al. (June 2015). “Three-dimensional Hydrodynamical Simulations of the Supernovae-driven Gas Loss in the Dwarf Spheroidal Galaxy Ursa Minor”. In: 805.2, 109, p. 109. DOI: [10.1088/0004-637X/805/2/109](https://doi.org/10.1088/0004-637X/805/2/109). arXiv: [1504.07653](https://arxiv.org/abs/1504.07653) [astro-ph.GA].
- Caproni, A. et al. (July 2017). “Gas depletion driven by supernovae in dwarf spheroidal galaxy Ursa Minor: hydrodynamical results”. In: *Revista Mexicana de Astronomia y Astrofisica Conference Series*. Vol. 49. Revista Mexicana de Astronomia y Astrofisica Conference Series, pp. 175–175.
- Carollo, C. M., I. J. Danziger, and L. Buson (Dec. 1993). “Metallicity gradients in early-type galaxies.” In: 265, pp. 553–580. DOI: [10.1093/mnras/265.3.553](https://doi.org/10.1093/mnras/265.3.553).
- Carrera, R. et al. (Mar. 2019). “Open clusters in APOGEE and GALAH. Combining Gaia and ground-based spectroscopic surveys”. In: 623, A80, A80. DOI: [10.1051/0004-6361/201834546](https://doi.org/10.1051/0004-6361/201834546). arXiv: [1901.09302](https://arxiv.org/abs/1901.09302) [astro-ph.GA].
- Casali, G. et al. (May 2023). “Time evolution of Ce as traced by APOGEE using giant stars observed with the Kepler, TESS and K2 missions”. In: *arXiv e-prints*, arXiv:2305.06396, arXiv:2305.06396. DOI: [10.48550/arXiv.2305.06396](https://doi.org/10.48550/arXiv.2305.06396). arXiv: [2305.06396](https://arxiv.org/abs/2305.06396) [astro-ph.GA].
- Cavallo, L., G. Cescutti, and F. Matteucci (May 2021). “Neutron stars mergers in a stochastic chemical evolution model: impact of time delay distributions”. In: 503.1, pp. 1–12. DOI: [10.1093/mnras/stab281](https://doi.org/10.1093/mnras/stab281). arXiv: [2009.09534](https://arxiv.org/abs/2009.09534) [astro-ph.GA].

- Cavichia, O. et al. (Feb. 2014). “The role of the Galactic bar in the chemical evolution of the Milky Way”. In: 437.4, pp. 3688–3701. DOI: [10.1093/mnras/stt2164](https://doi.org/10.1093/mnras/stt2164). arXiv: [1311.1518](https://arxiv.org/abs/1311.1518) [astro-ph.GA].
- Cayrel, F. et al. (Feb. 2004). “A simple model for boron trapping by He implantation extended defects in Si: the role of boron diffusivity”. In: *Nuclear Instruments and Methods in Physics Research B* 216, pp. 291–296. DOI: [10.1016/j.nimb.2003.11.049](https://doi.org/10.1016/j.nimb.2003.11.049).
- Cescutti, G. (Apr. 2008). “An inhomogeneous model for the Galactic halo: a possible explanation for the spread observed in s- and r-process elements”. In: 481.3, pp. 691–699. DOI: [10.1051/0004-6361:20078571](https://doi.org/10.1051/0004-6361:20078571). arXiv: [0802.0678](https://arxiv.org/abs/0802.0678) [astro-ph].
- Cescutti, G. and C. Chiappini (May 2014a). “Explaining the Ba, Y, Sr, and Eu abundance scatter in metal-poor halo stars: constraints to the r-process”. In: 565, A51, A51. DOI: [10.1051/0004-6361/201423432](https://doi.org/10.1051/0004-6361/201423432). arXiv: [1403.8070](https://arxiv.org/abs/1403.8070) [astro-ph.GA].
- (May 2014b). “Explaining the Ba, Y, Sr, and Eu abundance scatter in metal-poor halo stars: constraints to the r-process”. In: 565, A51, A51. DOI: [10.1051/0004-6361/201423432](https://doi.org/10.1051/0004-6361/201423432). arXiv: [1403.8070](https://arxiv.org/abs/1403.8070) [astro-ph.GA].
- Cescutti, G. and F. Matteucci (Jan. 2011a). “Galactic astroarchaeology: reconstructing the bulge history by means of the newest data”. In: 525, A126, A126. DOI: [10.1051/0004-6361/201015665](https://doi.org/10.1051/0004-6361/201015665). arXiv: [1010.1469](https://arxiv.org/abs/1010.1469) [astro-ph.GA].
- (Jan. 2011b). “Galactic astroarchaeology: reconstructing the bulge history by means of the newest data”. In: 525, A126, A126. DOI: [10.1051/0004-6361/201015665](https://doi.org/10.1051/0004-6361/201015665). arXiv: [1010.1469](https://arxiv.org/abs/1010.1469) [astro-ph.GA].
- Cescutti, G. et al. (Mar. 2006). “The chemical evolution of barium and europium in the Milky Way”. In: 448.2, pp. 557–569. DOI: [10.1051/0004-6361:20053622](https://doi.org/10.1051/0004-6361:20053622). arXiv: [astro-ph/0510496](https://arxiv.org/abs/astro-ph/0510496) [astro-ph].
- Cescutti, G. et al. (Feb. 2007). “Abundance gradients in the Milky Way for α elements, iron peak elements, barium, lanthanum, and europium”. In: 462.3, pp. 943–951. DOI: [10.1051/0004-6361:20065403](https://doi.org/10.1051/0004-6361:20065403). arXiv: [astro-ph/0609813](https://arxiv.org/abs/astro-ph/0609813) [astro-ph].
- Cescutti, G. et al. (May 2013). “The s-process in the Galactic halo: the fifth signature of spinstars in the early Universe?” In: 553, A51, A51. DOI: [10.1051/0004-6361/201220809](https://doi.org/10.1051/0004-6361/201220809). arXiv: [1302.4354](https://arxiv.org/abs/1302.4354) [astro-ph.GA].
- Cescutti, G. et al. (May 2015). “The role of neutron star mergers in the chemical evolution of the Galactic halo”. In: 577, A139, A139. DOI: [10.1051/0004-6361/201525698](https://doi.org/10.1051/0004-6361/201525698). arXiv: [1503.02954](https://arxiv.org/abs/1503.02954) [astro-ph.GA].
- Chabrier, Gilles (July 2003). “Galactic Stellar and Substellar Initial Mass Function”. In: 115.809, pp. 763–795. DOI: [10.1086/376392](https://doi.org/10.1086/376392). arXiv: [astro-ph/0304382](https://arxiv.org/abs/astro-ph/0304382) [astro-ph].
- Chen, L., J. L. Hou, and J. J. Wang (Mar. 2003). “On the Galactic Disk Metallicity Distribution from Open Clusters. I. New Catalogs and Abundance Gradient”. In: 125.3, pp. 1397–1406. DOI: [10.1086/367911](https://doi.org/10.1086/367911). arXiv: [astro-ph/0212542](https://arxiv.org/abs/astro-ph/0212542) [astro-ph].
- Chevalier, R. A. and A. W. Clegg (Sept. 1985). “Wind from a starburst galaxy nucleus”. In: 317.6032, pp. 44–45. DOI: [10.1038/317044a0](https://doi.org/10.1038/317044a0).

- Chiappini, C., F. Matteucci, and R. Gratton (Mar. 1997). “The Chemical Evolution of the Galaxy: The Two-Infall Model”. In: 477.2, pp. 765–780. DOI: [10.1086/303726](https://doi.org/10.1086/303726). arXiv: [astro-ph/9609199](https://arxiv.org/abs/astro-ph/9609199) [astro-ph].
- Chiappini, C., F. Matteucci, and P. Padoan (Jan. 2000). “The Chemical Evolution of the Galaxy with Variable Initial Mass Functions”. In: 528.2, pp. 711–722. DOI: [10.1086/308185](https://doi.org/10.1086/308185). arXiv: [astro-ph/9908207](https://arxiv.org/abs/astro-ph/9908207) [astro-ph].
- Chiappini, Cristina, Francesca Matteucci, and Donatella Romano (June 2001). “Abundance Gradients and the Formation of the Milky Way”. In: 554.2, pp. 1044–1058. DOI: [10.1086/321427](https://doi.org/10.1086/321427). arXiv: [astro-ph/0102134](https://arxiv.org/abs/astro-ph/0102134) [astro-ph].
- Chiappini, Cristina et al. (Apr. 1999). “The Earliest Phases of Galaxy Evolution”. In: 515.1, pp. 226–238. DOI: [10.1086/307006](https://doi.org/10.1086/307006). arXiv: [astro-ph/9810422](https://arxiv.org/abs/astro-ph/9810422) [astro-ph].
- Chiappini, Cristina et al. (Apr. 2011). “Imprints of fast-rotating massive stars in the Galactic Bulge”. In: 472.7344, pp. 454–457. DOI: [10.1038/nature10000](https://doi.org/10.1038/nature10000).
- Chiba, Rimpei, Jennifer K. S. Friske, and Ralph Schönrich (Jan. 2021a). “Resonance sweeping by a decelerating Galactic bar”. In: 500.4, pp. 4710–4729. DOI: [10.1093/mnras/staa3585](https://doi.org/10.1093/mnras/staa3585). arXiv: [1912.04304](https://arxiv.org/abs/1912.04304) [astro-ph.GA].
- Chiba, Rimpei and Ralph Schönrich (Aug. 2021b). “Tree-ring structure of Galactic bar resonance”. In: 505.2, pp. 2412–2426. DOI: [10.1093/mnras/stab1094](https://doi.org/10.1093/mnras/stab1094). arXiv: [2102.08388](https://arxiv.org/abs/2102.08388) [astro-ph.GA].
- (June 2022). “Oscillating dynamical friction on galactic bars by trapped dark matter”. In: 513.1, pp. 768–787. DOI: [10.1093/mnras/stac697](https://doi.org/10.1093/mnras/stac697). arXiv: [2109.10910](https://arxiv.org/abs/2109.10910) [astro-ph.GA].
- Choi, Ena et al. (Aug. 2012). “Radiative and Momentum-based Mechanical Active Galactic Nucleus Feedback in a Three-dimensional Galaxy Evolution Code”. In: 754.2, 125, p. 125. DOI: [10.1088/0004-637X/754/2/125](https://doi.org/10.1088/0004-637X/754/2/125). arXiv: [1205.2082](https://arxiv.org/abs/1205.2082) [astro-ph.GA].
- Choi, Ena et al. (June 2015). “The impact of mechanical AGN feedback on the formation of massive early-type galaxies”. In: 449.4, pp. 4105–4116. DOI: [10.1093/mnras/stv575](https://doi.org/10.1093/mnras/stv575). arXiv: [1403.1257](https://arxiv.org/abs/1403.1257) [astro-ph.CO].
- Chomiuk, Laura and Matthew S. Povich (Dec. 2011). “Toward a Unification of Star Formation Rate Determinations in the Milky Way and Other Galaxies”. In: 142.6, 197, p. 197. DOI: [10.1088/0004-6256/142/6/197](https://doi.org/10.1088/0004-6256/142/6/197). arXiv: [1110.4105](https://arxiv.org/abs/1110.4105) [astro-ph.GA].
- Ciambur, Bogdan C. et al. (May 2021). “Double X/Peanut structures in barred galaxies - insights from an N-body simulation”. In: 503.2, pp. 2203–2214. DOI: [10.1093/mnras/staa3814](https://doi.org/10.1093/mnras/staa3814). arXiv: [2003.00015](https://arxiv.org/abs/2003.00015) [astro-ph.GA].
- Cioffi, Denis F., Christopher F. McKee, and Edmund Bertschinger (Nov. 1988). “Dynamics of Radiative Supernova Remnants”. In: 334, p. 252. DOI: [10.1086/166834](https://doi.org/10.1086/166834).
- Ciotti, Luca and Jeremiah P. Ostriker (Oct. 1997). “Cooling Flows and Quasars: Different Aspects of the Same Phenomenon? I. Concepts”. In: 487.2, pp. L105–L108. DOI: [10.1086/310902](https://doi.org/10.1086/310902). arXiv: [astro-ph/9706281](https://arxiv.org/abs/astro-ph/9706281) [astro-ph].
- (Apr. 2001). “Cooling Flows and Quasars. II. Detailed Models of Feedback-modulated Accretion Flows”. In: 551.1, pp. 131–152. DOI: [10.1086/320053](https://doi.org/10.1086/320053). arXiv: [astro-ph/9912064](https://arxiv.org/abs/astro-ph/9912064) [astro-ph].

- Ciotti, Luca and Jeremiah P. Ostriker (Aug. 2007). “Radiative Feedback from Massive Black Holes in Elliptical Galaxies: AGN Flaring and Central Starburst Fueled by Recycled Gas”. In: 665.2, pp. 1038–1056. DOI: [10.1086/519833](https://doi.org/10.1086/519833). arXiv: [astro-ph/0703057](https://arxiv.org/abs/astro-ph/0703057) [astro-ph].
- Ciotti, Luca and Silvia Pellegrini (Dec. 2018). “Isothermal Bondi Accretion in Two-component Jaffe Galaxies with a Central Black Hole”. In: 868.2, 91, p. 91. DOI: [10.3847/1538-4357/aae97d](https://doi.org/10.3847/1538-4357/aae97d). arXiv: [1808.00871](https://arxiv.org/abs/1808.00871) [astro-ph.HE].
- Ciotti, Luca et al. (Aug. 1991). “Winds, Outflows, and Inflows in X-Ray Elliptical Galaxies. I.” In: 376, p. 380. DOI: [10.1086/170289](https://doi.org/10.1086/170289).
- Ciotti, Luca et al. (Jan. 2017). “The Effect of the AGN Feedback on the Interstellar Medium of Early-Type Galaxies: 2D Hydrodynamical Simulations of the Low-Rotation Case.” In: 835.1, 15, p. 15. DOI: [10.3847/1538-4357/835/1/15](https://doi.org/10.3847/1538-4357/835/1/15). arXiv: [1608.03403](https://arxiv.org/abs/1608.03403) [astro-ph.GA].
- Ciotti, Luca et al. (Jan. 2022). “A Parameter Space Exploration of High Resolution Numerically Evolved Early Type Galaxies Including AGN Feedback and Accurate Dynamical Treatment of Stellar Orbits”. In: *arXiv e-prints*, arXiv:2201.03909, arXiv:2201.03909. arXiv: [2201.03909](https://arxiv.org/abs/2201.03909) [astro-ph.GA].
- Clarke, Jonathan P. and Ortwin Gerhard (May 2022). “The pattern speed of the Milky Way bar/bulge from VIRAC and Gaia”. In: 512.2, pp. 2171–2188. DOI: [10.1093/mnras/stac603](https://doi.org/10.1093/mnras/stac603). arXiv: [2107.10875](https://arxiv.org/abs/2107.10875) [astro-ph.GA].
- Colavitti, E., F. Matteucci, and G. Murante (May 2008). “The chemical evolution of a Milky Way-like galaxy: the importance of a cosmologically motivated infall law”. In: 483.2, pp. 401–413. DOI: [10.1051/0004-6361:200809413](https://doi.org/10.1051/0004-6361:200809413). arXiv: [0802.1847](https://arxiv.org/abs/0802.1847) [astro-ph].
- Colavitti, E. et al. (Mar. 2009). “The origin of abundance gradients in the Milky Way: the predictions of different models”. In: 496.2, pp. 429–439. DOI: [10.1051/0004-6361:200810891](https://doi.org/10.1051/0004-6361:200810891). arXiv: [0811.3505](https://arxiv.org/abs/0811.3505) [astro-ph].
- Cole, Andrew A. and Martin D. Weinberg (July 2002). “An Upper Limit to the Age of the Galactic Bar”. In: 574.1, pp. L43–L46. DOI: [10.1086/342278](https://doi.org/10.1086/342278). arXiv: [astro-ph/0206199](https://arxiv.org/abs/astro-ph/0206199) [astro-ph].
- Coleman, Matthew G. and Jelte T. A. de Jong (Oct. 2008). “A Deep Survey of the Fornax dSph. I. Star Formation History”. In: 685.2, pp. 933–946. DOI: [10.1086/589992](https://doi.org/10.1086/589992). arXiv: [0805.1365](https://arxiv.org/abs/0805.1365) [astro-ph].
- Colgate, Stirling A. and Richard H. White (Mar. 1966). “The Hydrodynamic Behavior of Supernovae Explosions”. In: 143, p. 626. DOI: [10.1086/148549](https://doi.org/10.1086/148549).
- Combes, F. et al. (July 1990). “Box and peanut shapes generated by stellar bars.” In: 233, p. 82.
- Contursi, G. et al. (Feb. 2023). “The cerium content of the Milky Way as revealed by Gaia DR3 GSP-Spec abundances”. In: 670, A106, A106. DOI: [10.1051/0004-6361/202244469](https://doi.org/10.1051/0004-6361/202244469). arXiv: [2207.05368](https://arxiv.org/abs/2207.05368) [astro-ph.GA].
- Costa, Tiago, Rüdiger Pakmor, and Volker Springel (Oct. 2020). “Powering galactic superwinds with small-scale AGN winds”. In: 497.4, pp. 5229–5255. DOI: [10.1093/mnras/staa2321](https://doi.org/10.1093/mnras/staa2321). arXiv: [2006.05997](https://arxiv.org/abs/2006.05997) [astro-ph.GA].
- Côté, Benoit and Christian Ritter (June 2018). *OMEGA: One-zone Model for the Evolution of Galaxies*. Astrophysics Source Code Library, record ascl:1806.018. ascl: [1806.018](https://ascl.net/1806.018).

- Côté, Benoit et al. (Feb. 2017). “Advanced LIGO Constraints on Neutron Star Mergers and r-process Sites”. In: 836.2, 230, p. 230. DOI: [10.3847/1538-4357/aa5c8d](https://doi.org/10.3847/1538-4357/aa5c8d). arXiv: [1610.02405](https://arxiv.org/abs/1610.02405) [astro-ph.GA].
- Côté, Benoit et al. (Apr. 2019). “Neutron Star Mergers Might Not Be the Only Source of r-process Elements in the Milky Way”. In: 875.2, 106, p. 106. DOI: [10.3847/1538-4357/ab10db](https://doi.org/10.3847/1538-4357/ab10db). arXiv: [1809.03525](https://arxiv.org/abs/1809.03525) [astro-ph.HE].
- Côté, Benoit et al. (June 2020). “Constraining the Rapid Neutron-Capture Process with Meteoritic I-129 and Cm-247”. In: *arXiv e-prints*, arXiv:2006.04833, arXiv:2006.04833. arXiv: [2006.04833](https://arxiv.org/abs/2006.04833) [astro-ph.SR].
- Coulter, D. A. et al. (Dec. 2017). “Swope Supernova Survey 2017a (SSS17a), the optical counterpart to a gravitational wave source”. In: *Science* 358.6370, pp. 1556–1558. DOI: [10.1126/science.aap9811](https://doi.org/10.1126/science.aap9811). arXiv: [1710.05452](https://arxiv.org/abs/1710.05452) [astro-ph.HE].
- Cowan, John J. et al. (Jan. 2019). “Origin of the Heaviest Elements: the Rapid Neutron-Capture Process”. In: *arXiv e-prints*, arXiv:1901.01410, arXiv:1901.01410. arXiv: [1901.01410](https://arxiv.org/abs/1901.01410) [astro-ph.HE].
- (Jan. 2021). “Origin of the heaviest elements: The rapid neutron-capture process”. In: *Reviews of Modern Physics* 93.1, 015002, p. 015002. DOI: [10.1103/RevModPhys.93.015002](https://doi.org/10.1103/RevModPhys.93.015002). arXiv: [1901.01410](https://arxiv.org/abs/1901.01410) [astro-ph.HE].
- Cowie, Lennox L. et al. (Sept. 1996). “New Insight on Galaxy Formation and Evolution From Keck Spectroscopy of the Hawaii Deep Fields”. In: 112, p. 839. DOI: [10.1086/118058](https://doi.org/10.1086/118058). arXiv: [astro-ph/9606079](https://arxiv.org/abs/astro-ph/9606079) [astro-ph].
- Cristallo, S. et al. (May 2009). “Evolution, Nucleosynthesis, and Yields of Low-Mass Asymptotic Giant Branch Stars at Different Metallicities”. In: 696.1, pp. 797–820. DOI: [10.1088/0004-637X/696/1/797](https://doi.org/10.1088/0004-637X/696/1/797). arXiv: [0902.0243](https://arxiv.org/abs/0902.0243) [astro-ph.SR].
- Cristallo, S. et al. (Dec. 2011). “Evolution, Nucleosynthesis, and Yields of Low-mass Asymptotic Giant Branch Stars at Different Metallicities. II. The FRUITY Database”. In: 197.2, 17, p. 17. DOI: [10.1088/0067-0049/197/2/17](https://doi.org/10.1088/0067-0049/197/2/17). arXiv: [1109.1176](https://arxiv.org/abs/1109.1176) [astro-ph.SR].
- Cristallo, S. et al. (Aug. 2015). “Evolution, Nucleosynthesis, and Yields of AGB Stars at Different Metallicities. III. Intermediate-mass Models, Revised Low-mass Models, and the ph-FRUITY Interface”. In: 219.2, 40, p. 40. DOI: [10.1088/0067-0049/219/2/40](https://doi.org/10.1088/0067-0049/219/2/40). arXiv: [1507.07338](https://arxiv.org/abs/1507.07338) [astro-ph.SR].
- Croton, Darren J. et al. (Jan. 2006). “The many lives of active galactic nuclei: cooling flows, black holes and the luminosities and colours of galaxies”. In: 365.1, pp. 11–28. DOI: [10.1111/j.1365-2966.2005.09675.x](https://doi.org/10.1111/j.1365-2966.2005.09675.x). arXiv: [astro-ph/0508046](https://arxiv.org/abs/astro-ph/0508046) [astro-ph].
- Cunha, K. et al. (Sept. 2016). “Chemical abundance gradients from open clusters in the Milky Way disk: Results from the APOGEE survey”. In: *Astronomische Nachrichten* 337.8-9, p. 922. DOI: [10.1002/asna.201612398](https://doi.org/10.1002/asna.201612398). arXiv: [1601.03099](https://arxiv.org/abs/1601.03099) [astro-ph.GA].
- Cunha, Katia et al. (Aug. 2017). “Adding the s-Process Element Cerium to the APOGEE Survey: Identification and Characterization of Ce II Lines in the H-band Spectral Window”. In: 844.2, 145, p. 145. DOI: [10.3847/1538-4357/aa7beb](https://doi.org/10.3847/1538-4357/aa7beb).
- Curtis, Michael and Debora Sijacki (Nov. 2016). “Resolving flows around black holes: the impact of gas angular momentum”. In: 463.1, pp. 63–77. DOI: [10.1093/mnras/stw1944](https://doi.org/10.1093/mnras/stw1944). arXiv: [1606.02729](https://arxiv.org/abs/1606.02729) [astro-ph.GA].

- D'Avanzo, P. (Sept. 2015). "Short gamma-ray bursts: A review". In: *Journal of High Energy Astrophysics* 7, pp. 73–80. DOI: [10.1016/j.jheap.2015.07.002](https://doi.org/10.1016/j.jheap.2015.07.002).
- Davé, Romeel, Robert Thompson, and Philip F. Hopkins (Nov. 2016). "MUFASA: galaxy formation simulations with meshless hydrodynamics". In: 462.3, pp. 3265–3284. DOI: [10.1093/mnras/stw1862](https://doi.org/10.1093/mnras/stw1862). arXiv: [1604.01418](https://arxiv.org/abs/1604.01418) [astro-ph.GA].
- de Boer, T. J. L., V. Belokurov, and S. Koposov (Aug. 2015). "The star formation history of the Sagittarius stream". In: 451.4, pp. 3489–3503. DOI: [10.1093/mnras/stv946](https://doi.org/10.1093/mnras/stv946). arXiv: [1505.00787](https://arxiv.org/abs/1505.00787) [astro-ph.GA].
- de Boer, T. J. L. et al. (Aug. 2012a). "The star formation and chemical evolution history of the Fornax dwarf spheroidal galaxy". In: 544, A73, A73. DOI: [10.1051/0004-6361/201219547](https://doi.org/10.1051/0004-6361/201219547). arXiv: [1206.6968](https://arxiv.org/abs/1206.6968) [astro-ph.GA].
- de Boer, T. J. L. et al. (Mar. 2012b). "The star formation and chemical evolution history of the sculptor dwarf spheroidal galaxy". In: 539, A103, A103. DOI: [10.1051/0004-6361/201118378](https://doi.org/10.1051/0004-6361/201118378). arXiv: [1201.2408](https://arxiv.org/abs/1201.2408) [astro-ph.CO].
- De Lucia, Gabriella and Amina Helmi (Nov. 2008). "The Galaxy and its stellar halo: insights on their formation from a hybrid cosmological approach". In: 391.1, pp. 14–31. DOI: [10.1111/j.1365-2966.2008.13862.x](https://doi.org/10.1111/j.1365-2966.2008.13862.x). arXiv: [0804.2465](https://arxiv.org/abs/0804.2465) [astro-ph].
- De Masi, Carlo, F. Matteucci, and F. Vincenzo (Mar. 2018). "The effects of the initial mass function on the chemical evolution of elliptical galaxies". In: 474.4, pp. 5259–5271. DOI: [10.1093/mnras/stx3044](https://doi.org/10.1093/mnras/stx3044). arXiv: [1710.04439](https://arxiv.org/abs/1710.04439) [astro-ph.GA].
- De Silva, G. M. et al. (May 2015). "The GALAH survey: scientific motivation". In: 449.3, pp. 2604–2617. DOI: [10.1093/mnras/stv327](https://doi.org/10.1093/mnras/stv327). arXiv: [1502.04767](https://arxiv.org/abs/1502.04767) [astro-ph.GA].
- Debattista, Victor P. and J. A. Sellwood (Nov. 2000). "Constraints from Dynamical Friction on the Dark Matter Content of Barred Galaxies". In: 543.2, pp. 704–721. DOI: [10.1086/317148](https://doi.org/10.1086/317148). arXiv: [astro-ph/0006275](https://arxiv.org/abs/astro-ph/0006275) [astro-ph].
- deBoer, R. J. et al. (July 2017). "The $^{12}\text{C}(\alpha, \gamma)^{16}\text{O}$ reaction and its implications for stellar helium burning". In: *Reviews of Modern Physics* 89.3, 035007, p. 035007. DOI: [10.1103/RevModPhys.89.035007](https://doi.org/10.1103/RevModPhys.89.035007). arXiv: [1709.03144](https://arxiv.org/abs/1709.03144) [nucl-ex].
- Della Valle, M. et al. (Dec. 2018). "GW170817: implications for the local kilonova rate and for surveys from ground-based facilities". In: 481.4, pp. 4355–4360. DOI: [10.1093/mnras/sty2541](https://doi.org/10.1093/mnras/sty2541). arXiv: [1809.04295](https://arxiv.org/abs/1809.04295) [astro-ph.HE].
- Denissenkov, Pavel A. et al. (Sept. 2019). "The i-process yields of rapidly accreting white dwarfs from multicycle He-shell flash stellar evolution models with mixing parametrizations from 3D hydrodynamics simulations". In: 488.3, pp. 4258–4270. DOI: [10.1093/mnras/stz1921](https://doi.org/10.1093/mnras/stz1921). arXiv: [1809.03666](https://arxiv.org/abs/1809.03666) [astro-ph.SR].
- Doherty, Carolyn L. et al. (June 2014). "Super and massive AGB stars - III. Nucleosynthesis in metal-poor and very metal-poor stars - $Z = 0.001$ and 0.0001 ". In: 441.1, pp. 582–598. DOI: [10.1093/mnras/stu571](https://doi.org/10.1093/mnras/stu571). arXiv: [1403.5054](https://arxiv.org/abs/1403.5054) [astro-ph.SR].
- Dolphin, A. E. (May 2002). "Numerical methods of star formation history measurement and applications to seven dwarf spheroidals". In: 332.1, pp. 91–108. DOI: [10.1046/j.1365-8711.2002.05271.x](https://doi.org/10.1046/j.1365-8711.2002.05271.x). arXiv: [astro-ph/0112331](https://arxiv.org/abs/astro-ph/0112331) [astro-ph].
- Donor, John et al. (May 2020). "The Open Cluster Chemical Abundances and Mapping Survey. IV. Abundances for 128 Open Clusters Using SDSS/APOGEE DR16". In: 159.5, 199, p. 199. DOI: [10.3847/1538-3881/ab77bc](https://doi.org/10.3847/1538-3881/ab77bc). arXiv: [2002.08980](https://arxiv.org/abs/2002.08980) [astro-ph.GA].

- Dunlop, J. S. et al. (Apr. 2003). “Quasars, their host galaxies and their central black holes”. In: 340.4, pp. 1095–1135. DOI: [10.1046/j.1365-8711.2003.06333.x](https://doi.org/10.1046/j.1365-8711.2003.06333.x). arXiv: [astro-ph/0108397](https://arxiv.org/abs/astro-ph/0108397) [astro-ph].
- Dunn, Jay P. et al. (Feb. 2010). “The Quasar Outflow Contribution to AGN Feedback: VLT Measurements of SDSS J0318-0600”. In: 709.2, pp. 611–631. DOI: [10.1088/0004-637X/709/2/611](https://doi.org/10.1088/0004-637X/709/2/611). arXiv: [0911.3896](https://arxiv.org/abs/0911.3896) [astro-ph.CO].
- Ebrova, I. et al. (Feb. 2020). “NGC 4993, the shell galaxy host of GW170817: constraints on the recent galactic merger”. In: 634, A73, A73. DOI: [10.1051/0004-6361/201935219](https://doi.org/10.1051/0004-6361/201935219).
- Emerick, Andrew, Greg L. Bryan, and Mordecai-Mark Mac Low (Feb. 2020). “Simulating Metal Mixing of Both Common and Rare Enrichment Sources in a Low-mass Dwarf Galaxy”. In: 890.2, 155, p. 155. DOI: [10.3847/1538-4357/ab6efc](https://doi.org/10.3847/1538-4357/ab6efc). arXiv: [1909.04695](https://arxiv.org/abs/1909.04695) [astro-ph.GA].
- Faber, S. M., G. Worthey, and J. J. Gonzales (Jan. 1992). “Absorption-Line Spectra of Elliptical Galaxies and Their Relation to Elliptical Formation”. In: *The Stellar Populations of Galaxies*. Ed. by Beatriz Barbuy and Alvio Renzini. Vol. 149, p. 255.
- Fernandez, Rodrigo et al. (July 2023). “Viscous hydrodynamic evolution of neutron star merger accretion disks: a code comparison”. In: *arXiv e-prints*, arXiv:2307.02554, arXiv:2307.02554. DOI: [10.48550/arXiv.2307.02554](https://doi.org/10.48550/arXiv.2307.02554). arXiv: [2307.02554](https://arxiv.org/abs/2307.02554) [astro-ph.HE].
- Fiore, F. et al. (May 2017). “AGN wind scaling relations and the co-evolution of black holes and galaxies”. In: 601, A143, A143. DOI: [10.1051/0004-6361/201629478](https://doi.org/10.1051/0004-6361/201629478). arXiv: [1702.04507](https://arxiv.org/abs/1702.04507) [astro-ph.GA].
- Fischer, T., F. K. Thielemann, and M. Liebendorfer (Aug. 2010). “Explosions of massive stars and the neutrino-driven wind in simulations using Boltzmann neutrino transport”. In: *10th International Symposium on Origin of Matter and Evolution of Galaxies: OMEG - 2010*. Ed. by Isao Tanihara et al. Vol. 1269. American Institute of Physics Conference Series, pp. 181–188. DOI: [10.1063/1.3485132](https://doi.org/10.1063/1.3485132).
- Fishlock, Cherie K. et al. (Dec. 2014). “Evolution and Nucleosynthesis of Asymptotic Giant Branch Stellar Models of Low Metallicity”. In: 797.1, 44, p. 44. DOI: [10.1088/0004-637X/797/1/44](https://doi.org/10.1088/0004-637X/797/1/44). arXiv: [1410.7457](https://arxiv.org/abs/1410.7457) [astro-ph.SR].
- Fong, W. et al. (Sept. 2012). “A Jet Break in the X-Ray Light Curve of Short GRB 111020A: Implications for Energetics and Rates”. In: 756.2, 189, p. 189. DOI: [10.1088/0004-637X/756/2/189](https://doi.org/10.1088/0004-637X/756/2/189). arXiv: [1204.5475](https://arxiv.org/abs/1204.5475) [astro-ph.HE].
- Fong, W. et al. (Oct. 2017). “The Electromagnetic Counterpart of the Binary Neutron Star Merger LIGO/Virgo GW170817. VIII. A Comparison to Cosmological Short-duration Gamma-Ray Bursts”. In: 848.2, L23, p. L23. DOI: [10.3847/2041-8213/aa9018](https://doi.org/10.3847/2041-8213/aa9018). arXiv: [1710.05438](https://arxiv.org/abs/1710.05438) [astro-ph.HE].
- Francois, P. et al. (July 2004). “The evolution of the Milky Way from its earliest phases: Constraints on stellar nucleosynthesis”. In: 421, pp. 613–621. DOI: [10.1051/0004-6361:20034140](https://doi.org/10.1051/0004-6361:20034140). arXiv: [astro-ph/0401499](https://arxiv.org/abs/astro-ph/0401499) [astro-ph].
- Fraser, Jack and Ralph Schonrich (Feb. 2022). “Metallicity-suppressed collapsars cannot be the dominant r-process source in the milky way”. In: 509.4, pp. 6008–6027. DOI: [10.1093/mnras/stab3385](https://doi.org/10.1093/mnras/stab3385). arXiv: [2111.11464](https://arxiv.org/abs/2111.11464) [astro-ph.GA].
- Freeman, K. et al. (Feb. 2013). “ARGOS - II. The Galactic bulge survey”. In: 428.4, pp. 3660–3670. DOI: [10.1093/mnras/sts305](https://doi.org/10.1093/mnras/sts305). arXiv: [1212.1541](https://arxiv.org/abs/1212.1541) [astro-ph.GA].

- Friel, Eileen D. et al. (Nov. 2002). “Metallicities of Old Open Clusters”. In: 124.5, pp. 2693–2720. DOI: [10.1086/344161](https://doi.org/10.1086/344161).
- Frischknecht, Urs et al. (Feb. 2016). “s-process production in rotating massive stars at solar and low metallicities”. In: 456.2, pp. 1803–1825. DOI: [10.1093/mnras/stv2723](https://doi.org/10.1093/mnras/stv2723). arXiv: [1511.05730](https://arxiv.org/abs/1511.05730) [astro-ph.SR].
- Fröhlich, C. et al. (Oct. 2006). “Nucleosynthesis in neutrino-driven supernovae”. In: 50.7-8, pp. 496–499. DOI: [10.1016/j.newar.2006.06.003](https://doi.org/10.1016/j.newar.2006.06.003). arXiv: [astro-ph/0511584](https://arxiv.org/abs/astro-ph/0511584) [astro-ph].
- Fujibayashi, Sho et al. (Sept. 2017). “Properties of Neutrino-driven Ejecta from the Remnant of a Binary Neutron Star Merger: Pure Radiation Hydrodynamics Case”. In: 846.2, 114, p. 114. DOI: [10.3847/1538-4357/aa8039](https://doi.org/10.3847/1538-4357/aa8039). arXiv: [1703.10191](https://arxiv.org/abs/1703.10191) [astro-ph.HE].
- Fujibayashi, Sho et al. (Jan. 2023). “Comprehensive Study of Mass Ejection and Nucleosynthesis in Binary Neutron Star Mergers Leaving Short-lived Massive Neutron Stars”. In: 942.1, 39, p. 39. DOI: [10.3847/1538-4357/ac9ce0](https://doi.org/10.3847/1538-4357/ac9ce0). arXiv: [2205.05557](https://arxiv.org/abs/2205.05557) [astro-ph.HE].
- Gaia Collaboration et al. (May 2021). “Gaia Early Data Release 3. Summary of the contents and survey properties”. In: 649, A1, A1. DOI: [10.1051/0004-6361/202039657](https://doi.org/10.1051/0004-6361/202039657). arXiv: [2012.01533](https://arxiv.org/abs/2012.01533) [astro-ph.GA].
- Gan, Zhaoming et al. (July 2014). “Active Galactic Nucleus Feedback in an Isolated Elliptical Galaxy: The Effect of Strong Radiative Feedback in the Kinetic Mode”. In: 789.2, 150, p. 150. DOI: [10.1088/0004-637X/789/2/150](https://doi.org/10.1088/0004-637X/789/2/150). arXiv: [1403.0670](https://arxiv.org/abs/1403.0670) [astro-ph.GA].
- García Pérez, Ana E. et al. (June 2016). “ASPCAP: The APOGEE Stellar Parameter and Chemical Abundances Pipeline”. In: 151.6, 144, p. 144. DOI: [10.3847/0004-6256/151/6/144](https://doi.org/10.3847/0004-6256/151/6/144). arXiv: [1510.07635](https://arxiv.org/abs/1510.07635) [astro-ph.SR].
- Genovali, K. et al. (Aug. 2015). “On the α -element gradients of the Galactic thin disk using Cepheids”. In: 580, A17, A17. DOI: [10.1051/0004-6361/201525894](https://doi.org/10.1051/0004-6361/201525894). arXiv: [1503.03758](https://arxiv.org/abs/1503.03758) [astro-ph.SR].
- Ghirlanda, G. et al. (Oct. 2016). “Short gamma-ray bursts at the dawn of the gravitational wave era”. In: 594, A84, A84. DOI: [10.1051/0004-6361/201628993](https://doi.org/10.1051/0004-6361/201628993). arXiv: [1607.07875](https://arxiv.org/abs/1607.07875) [astro-ph.HE].
- Ghosh, Soumavo et al. (June 2023). “Bars and boxy/peanut bulges in thin and thick discs. II. Can bars form in hot thick discs?” In: 674, A128, A128. DOI: [10.1051/0004-6361/202245275](https://doi.org/10.1051/0004-6361/202245275). arXiv: [2210.14244](https://arxiv.org/abs/2210.14244) [astro-ph.GA].
- Gibson, B. K. (Sept. 1997). “Galactic winds and the photochemical evolution of elliptical galaxies: the classic model revisited”. In: 290.3, pp. 471–489. DOI: [10.1093/mnras/290.3.471](https://doi.org/10.1093/mnras/290.3.471). arXiv: [astro-ph/9705104](https://arxiv.org/abs/astro-ph/9705104) [astro-ph].
- Gilmore, G. et al. (Mar. 2012). “The Gaia-ESO Public Spectroscopic Survey”. In: *The Messenger* 147, pp. 25–31.
- Gilmore, G. et al. (Oct. 2022). “The Gaia-ESO Public Spectroscopic Survey: Motivation, implementation, GIRAFFE data processing, analysis, and final data products”. In: 666, A120, A120. DOI: [10.1051/0004-6361/202243134](https://doi.org/10.1051/0004-6361/202243134). arXiv: [2208.05432](https://arxiv.org/abs/2208.05432) [astro-ph.SR].
- Gioannini, L., F. Matteucci, and F. Calura (Nov. 2017). “The cosmic dust rate across the Universe”. In: 471.4, pp. 4615–4627. DOI: [10.1093/mnras/stx1914](https://doi.org/10.1093/mnras/stx1914). arXiv: [1707.06784](https://arxiv.org/abs/1707.06784) [astro-ph.GA].

- Gonzalez, O. A. et al. (Dec. 2015). “The GIRAFFE Inner Bulge Survey (GIBS). II. Metallicity distributions and alpha element abundances at fixed Galactic latitude”. In: 584, A46, A46. DOI: [10.1051/0004-6361/201526737](https://doi.org/10.1051/0004-6361/201526737). arXiv: [1508.02576](https://arxiv.org/abs/1508.02576) [astro-ph.GA].
- Grado, A. et al. (Feb. 2020). “Search for the optical counterpart of the GW170814 gravitational wave event with the VLT Survey Telescope”. In: 492.2, pp. 1731–1754. DOI: [10.1093/mnras/stz3536](https://doi.org/10.1093/mnras/stz3536). arXiv: [2001.09905](https://arxiv.org/abs/2001.09905) [astro-ph.HE].
- Grady, J., V. Belokurov, and N. W. Evans (Feb. 2020). “Age demographics of the Milky Way disc and bulge”. In: 492.3, pp. 3128–3142. DOI: [10.1093/mnras/stz3617](https://doi.org/10.1093/mnras/stz3617). arXiv: [1912.02816](https://arxiv.org/abs/1912.02816) [astro-ph.GA].
- Gratton, R. G. et al. (July 2003). “Abundances for metal-poor stars with accurate parallaxes. II. alpha -elements in the halo”. In: 406, pp. 131–140. DOI: [10.1051/0004-6361:20030754](https://doi.org/10.1051/0004-6361:20030754). arXiv: [astro-ph/0305358](https://arxiv.org/abs/astro-ph/0305358) [astro-ph].
- Greggio, L. (Oct. 2005). “The rates of type Ia supernovae. I. Analytical formulations”. In: 441.3, pp. 1055–1078. DOI: [10.1051/0004-6361:20052926](https://doi.org/10.1051/0004-6361:20052926). arXiv: [astro-ph/0504376](https://arxiv.org/abs/astro-ph/0504376) [astro-ph].
- Greggio, Laura, Paolo Simonetti, and Francesca Matteucci (Jan. 2021). “On the delay times of merging double neutron stars”. In: 500.2, pp. 1755–1771. DOI: [10.1093/mnras/staa3312](https://doi.org/10.1093/mnras/staa3312). arXiv: [2009.13138](https://arxiv.org/abs/2009.13138) [astro-ph.HE].
- Grieco, V. et al. (Dec. 2012a). “Chemical evolution of the Galactic bulge: different stellar populations and possible gradients”. In: 548, A60, A60. DOI: [10.1051/0004-6361/201219761](https://doi.org/10.1051/0004-6361/201219761). arXiv: [1209.4462](https://arxiv.org/abs/1209.4462) [astro-ph.GA].
- Grieco, V. et al. (July 2012b). “Metallicity effects on cosmic Type Ib/c supernovae and gamma-ray burst rates”. In: 423.4, pp. 3049–3057. DOI: [10.1111/j.1365-2966.2012.21052.x](https://doi.org/10.1111/j.1365-2966.2012.21052.x).
- Grieco, V. et al. (June 2015). “Chemical evolution of the Galactic Centre”. In: 450.2, pp. 2094–2103. DOI: [10.1093/mnras/stv729](https://doi.org/10.1093/mnras/stv729). arXiv: [1503.08949](https://arxiv.org/abs/1503.08949) [astro-ph.GA].
- Grisoni, V., E. Spitoni, and F. Matteucci (Dec. 2018). “Abundance gradients along the Galactic disc from chemical evolution models”. In: 481.2, pp. 2570–2580. DOI: [10.1093/mnras/sty2444](https://doi.org/10.1093/mnras/sty2444). arXiv: [1805.11415](https://arxiv.org/abs/1805.11415) [astro-ph.GA].
- Grisoni, V. et al. (Dec. 2017). “The AMBRE project: chemical evolution models for the Milky Way thick and thin discs”. In: 472.3, pp. 3637–3647. DOI: [10.1093/mnras/stx2201](https://doi.org/10.1093/mnras/stx2201). arXiv: [1706.02614](https://arxiv.org/abs/1706.02614) [astro-ph.GA].
- Grisoni, V. et al. (Feb. 2020). “Modelling the chemical evolution of Zr, La, Ce, and Eu in the Galactic discs and bulge”. In: 492.2, pp. 2828–2834. DOI: [10.1093/mnras/staa051](https://doi.org/10.1093/mnras/staa051). arXiv: [1911.04271](https://arxiv.org/abs/1911.04271) [astro-ph.GA].
- Guesten, R. and P. G. Mezger (Jan. 1982). “Star formation and abundance gradients in the galaxy”. In: *Vistas in Astronomy* 26.3, pp. 159–224. DOI: [10.1016/0083-6656\(82\)90005-8](https://doi.org/10.1016/0083-6656(82)90005-8).
- Gültekin, Kayhan (May 2010). “Determination of the Intrinsic Scatter in the $M_{BH}-\sigma$ and $M_{BH}-L_{bulge}$ Relations”. In: *Co-Evolution of Central Black Holes and Galaxies*. Ed. by Bradley M. Peterson, Rachel S. Somerville, and Thaisa Storchi-Bergmann. Vol. 267, pp. 189–194. DOI: [10.1017/S1743921310006149](https://doi.org/10.1017/S1743921310006149).
- Hansen, C. J., A. C. Andersen, and N. Christlieb (Aug. 2014). “Stellar abundances and presolar grains trace the nucleosynthetic origin of molybdenum and ruthenium”. In: 568, A47, A47. DOI: [10.1051/0004-6361/201423535](https://doi.org/10.1051/0004-6361/201423535). arXiv: [1406.6686](https://arxiv.org/abs/1406.6686) [astro-ph.SR].

- Hansen, T. T. et al. (Mar. 2017). “An r-process Enhanced Star in the Dwarf Galaxy Tucana III”. In: 838.1, 44, p. 44. DOI: [10.3847/1538-4357/aa634a](https://doi.org/10.3847/1538-4357/aa634a). arXiv: [1702.07430](https://arxiv.org/abs/1702.07430) [astro-ph.SR].
- Häring, Nadine and Hans-Walter Rix (Apr. 2004). “On the Black Hole Mass-Bulge Mass Relation”. In: 604.2, pp. L89–L92. DOI: [10.1086/383567](https://doi.org/10.1086/383567). arXiv: [astro-ph/0402376](https://arxiv.org/abs/astro-ph/0402376) [astro-ph].
- Hayden, Michael R. et al. (May 2014). “Chemical Cartography with APOGEE: Large-scale Mean Metallicity Maps of the Milky Way Disk”. In: 147.5, 116, p. 116. DOI: [10.1088/0004-6256/147/5/116](https://doi.org/10.1088/0004-6256/147/5/116). arXiv: [1311.4569](https://arxiv.org/abs/1311.4569) [astro-ph.GA].
- Hayden, Michael R. et al. (Aug. 2015). “Chemical Cartography with APOGEE: Metallicity Distribution Functions and the Chemical Structure of the Milky Way Disk”. In: 808.2, 132, p. 132. DOI: [10.1088/0004-637X/808/2/132](https://doi.org/10.1088/0004-637X/808/2/132). arXiv: [1503.02110](https://arxiv.org/abs/1503.02110) [astro-ph.GA].
- Hayes, Christian R. et al. (Sept. 2022). “BACCHUS Analysis of Weak Lines in APOGEE Spectra (BAWLAS)”. In: 262.1, 34, p. 34. DOI: [10.3847/1538-4365/ac839f](https://doi.org/10.3847/1538-4365/ac839f). arXiv: [2208.00071](https://arxiv.org/abs/2208.00071) [astro-ph.GA].
- Haywood, M. et al. (July 2015). “Clues to the formation of the Milky Way’s thick disk”. In: 579, A5, A5. DOI: [10.1051/0004-6361/201425459](https://doi.org/10.1051/0004-6361/201425459). arXiv: [1504.02019](https://arxiv.org/abs/1504.02019) [astro-ph.GA].
- Heavens, Alan et al. (Apr. 2004). “The star-formation history of the Universe from the stellar populations of nearby galaxies”. In: 428.6983, pp. 625–627. DOI: [10.1038/nature02474](https://doi.org/10.1038/nature02474). arXiv: [astro-ph/0403293](https://arxiv.org/abs/astro-ph/0403293) [astro-ph].
- Heckman, Timothy M., Lee Armus, and George K. Miley (Dec. 1990). “On the Nature and Implications of Starburst-driven Galactic Superwinds”. In: 74, p. 833. DOI: [10.1086/191522](https://doi.org/10.1086/191522).
- Heger, A. and S. E. Woosley (Mar. 2002). “The Nucleosynthetic Signature of Population III”. In: 567.1, pp. 532–543. DOI: [10.1086/338487](https://doi.org/10.1086/338487). arXiv: [astro-ph/0107037](https://arxiv.org/abs/astro-ph/0107037) [astro-ph].
- Hernandez, X., Gerard Gilmore, and David Valls-Gabaud (Oct. 2000). “Non-parametric star formation histories for four dwarf spheroidal galaxies of the Local Group”. In: 317.4, pp. 831–842. DOI: [10.1046/j.1365-8711.2000.03809.x](https://doi.org/10.1046/j.1365-8711.2000.03809.x). arXiv: [astro-ph/0001337](https://arxiv.org/abs/astro-ph/0001337) [astro-ph].
- Hernquist, Lars and Martin D. Weinberg (Nov. 1992). “Bar-Spheroid Interaction in Galaxies”. In: 400, p. 80. DOI: [10.1086/171975](https://doi.org/10.1086/171975).
- Hertzsprung, Ejnar (1976). *Zur Strahlung der Sterne. Drei Arbeiten von Ejnar Hertzsprung*.
- Hill, V. et al. (Oct. 2011). “The metallicity distribution of bulge clump giants in Baade’s window”. In: 534, A80, A80. DOI: [10.1051/0004-6361/200913757](https://doi.org/10.1051/0004-6361/200913757). arXiv: [1107.5199](https://arxiv.org/abs/1107.5199) [astro-ph.GA].
- Holmbeck, E. M., T. M. Sprouse, and M. R. Mumpower (Feb. 2023). “Nucleosynthesis and observation of the heaviest elements”. In: *European Physical Journal A* 59.2, 28, p. 28. DOI: [10.1140/epja/s10050-023-00927-7](https://doi.org/10.1140/epja/s10050-023-00927-7). arXiv: [2304.01850](https://arxiv.org/abs/2304.01850) [nucl-th].
- Horowitz, C. J. et al. (Aug. 2019). “r-process nucleosynthesis: connecting rare-isotope beam facilities with the cosmos”. In: *Journal of Physics G Nuclear Physics* 46.8, p. 083001. DOI: [10.1088/1361-6471/ab0849](https://doi.org/10.1088/1361-6471/ab0849). arXiv: [1805.04637](https://arxiv.org/abs/1805.04637) [astro-ph.SR].

- Hotokezaka, Kenta, Paz Beniamini, and Tsvi Piran (Jan. 2018). “Neutron star mergers as sites of r-process nucleosynthesis and short gamma-ray bursts”. In: *International Journal of Modern Physics D* 27.13, 1842005, p. 1842005. DOI: [10.1142/S0218271818420051](https://doi.org/10.1142/S0218271818420051). arXiv: [1801.01141](https://arxiv.org/abs/1801.01141) [astro-ph.HE].
- Hubble, E. P. (Dec. 1926). “Extragalactic nebulae.” In: 64, pp. 321–369. DOI: [10.1086/143018](https://doi.org/10.1086/143018).
- Hunter, I. et al. (Feb. 2008). “The VLT-FLAMES survey of massive stars: atmospheric parameters and rotational velocity distributions for B-type stars in the Magellanic Clouds”. In: 479.2, pp. 541–555. DOI: [10.1051/0004-6361:20078511](https://doi.org/10.1051/0004-6361:20078511). arXiv: [0711.2264](https://arxiv.org/abs/0711.2264) [astro-ph].
- Iben Icko, Jr. (Jan. 1967). “Stellar Evolution Within and off the Main Sequence”. In: 5, p. 571. DOI: [10.1146/annurev.aa.05.090167.003035](https://doi.org/10.1146/annurev.aa.05.090167.003035).
- Iwamoto, Koichi et al. (Dec. 1999). “Nucleosynthesis in Chandrasekhar Mass Models for Type IA Supernovae and Constraints on Progenitor Systems and Burning-Front Propagation”. In: 125.2, pp. 439–462. DOI: [10.1086/313278](https://doi.org/10.1086/313278). arXiv: [astro-ph/0002337](https://arxiv.org/abs/astro-ph/0002337) [astro-ph].
- Izumi, Takuma et al. (Feb. 2021a). “Subaru High-z Exploration of Low-luminosity Quasars (SHELLQs). XII. Extended [C II] Structure (Merger or Outflow) in a $z = 6.72$ Red Quasar”. In: 908.2, 235, p. 235. DOI: [10.3847/1538-4357/abd7ef](https://doi.org/10.3847/1538-4357/abd7ef). arXiv: [2101.01199](https://arxiv.org/abs/2101.01199) [astro-ph.GA].
- Izumi, Takuma et al. (June 2021b). “Subaru High-z Exploration of Low-luminosity Quasars (SHELLQs). XIII. Large-scale Feedback and Star Formation in a Low-luminosity Quasar at $z = 7.07$ on the Local Black Hole to Host Mass Relation”. In: 914.1, 36, p. 36. DOI: [10.3847/1538-4357/abf6dc](https://doi.org/10.3847/1538-4357/abf6dc). arXiv: [2104.05738](https://arxiv.org/abs/2104.05738) [astro-ph.GA].
- Janka, H. Th. et al. (Apr. 2007). “Theory of core-collapse supernovae”. In: 442.1-6, pp. 38–74. DOI: [10.1016/j.physrep.2007.02.002](https://doi.org/10.1016/j.physrep.2007.02.002). arXiv: [astro-ph/0612072](https://arxiv.org/abs/astro-ph/0612072) [astro-ph].
- Janka, Hans-Thomas, Tobias Melson, and Alexander Summa (Oct. 2016). “Physics of Core-Collapse Supernovae in Three Dimensions: A Sneak Preview”. In: *Annual Review of Nuclear and Particle Science* 66.1, pp. 341–375. DOI: [10.1146/annurev-nucl-102115-044747](https://doi.org/10.1146/annurev-nucl-102115-044747). arXiv: [1602.05576](https://arxiv.org/abs/1602.05576) [astro-ph.SR].
- Ji, Alexander P. et al. (Mar. 2016). “R-process enrichment from a single event in an ancient dwarf galaxy”. In: 531.7596, pp. 610–613. DOI: [10.1038/nature17425](https://doi.org/10.1038/nature17425). arXiv: [1512.01558](https://arxiv.org/abs/1512.01558) [astro-ph.GA].
- Jiménez, Noelia, Patricia B. Tissera, and Francesca Matteucci (Sept. 2015). “Type Ia Supernova Progenitors and Chemical Enrichment in Hydrodynamical Simulations. I. The Single-degenerate Scenario”. In: 810.2, 137, p. 137. DOI: [10.1088/0004-637X/810/2/137](https://doi.org/10.1088/0004-637X/810/2/137). arXiv: [1402.4137](https://arxiv.org/abs/1402.4137) [astro-ph.GA].
- Johnson, Christian I. et al. (Sept. 2022). “Blanco DECam Bulge Survey (BDBS) IV: Metallicity distributions and bulge structure from 2.6 million red clump stars”. In: 515.1, pp. 1469–1491. DOI: [10.1093/mnras/stac1840](https://doi.org/10.1093/mnras/stac1840). arXiv: [2206.14851](https://arxiv.org/abs/2206.14851) [astro-ph.GA].
- Johnston, Simon et al. (Mar. 1992). “PSR 1259-63: A Binary Radio Pulsar with a Be Star Companion”. In: 387, p. L37. DOI: [10.1086/186300](https://doi.org/10.1086/186300).

- José, Jordi and Margarita Hernanz (Dec. 2007). “TOPICAL REVIEW: Nucleosynthesis in classical nova explosions”. In: *Journal of Physics G Nuclear Physics* 34.12, R431–R458. DOI: [10.1088/0954-3899/34/12/R01](https://doi.org/10.1088/0954-3899/34/12/R01).
- Kalogera, V. et al. (Feb. 2004). “The Cosmic Coalescence Rates for Double Neutron Star Binaries”. In: 601.2, pp. L179–L182. DOI: [10.1086/382155](https://doi.org/10.1086/382155).
- Karakas, A. I. (Apr. 2010). “Updated stellar yields from asymptotic giant branch models”. In: 403.3, pp. 1413–1425. DOI: [10.1111/j.1365-2966.2009.16198.x](https://doi.org/10.1111/j.1365-2966.2009.16198.x). arXiv: [0912.2142](https://arxiv.org/abs/0912.2142) [astro-ph.SR].
- Kaspi, V. M. et al. (Mar. 1994). “A Massive Radio Pulsar Binary in the Small Magellanic Cloud”. In: 423, p. L43. DOI: [10.1086/187231](https://doi.org/10.1086/187231).
- Kawata, D. and C. Chiappini (Sept. 2016). “Milky Way’s thick and thin disk: Is there a distinct thick disk?” In: *Astronomische Nachrichten* 337.8-9, p. 976. DOI: [10.1002/asna.201612421](https://doi.org/10.1002/asna.201612421). arXiv: [1608.01698](https://arxiv.org/abs/1608.01698) [astro-ph.GA].
- Kawata, D. and B. K. Gibson (Nov. 2003). “Multiwavelength cosmological simulations of elliptical galaxies”. In: 346.1, pp. 135–152. DOI: [10.1046/j.1365-2966.2003.07080.x](https://doi.org/10.1046/j.1365-2966.2003.07080.x). arXiv: [astro-ph/0308168](https://arxiv.org/abs/astro-ph/0308168) [astro-ph].
- Kennicutt Robert C., Jr. (May 1998). “The Global Schmidt Law in Star-forming Galaxies”. In: 498.2, pp. 541–552. DOI: [10.1086/305588](https://doi.org/10.1086/305588). arXiv: [astro-ph/9712213](https://arxiv.org/abs/astro-ph/9712213) [astro-ph].
- Kobayashi, Chiaki, Amanda I. Karakas, and Maria Lugaro (Sept. 2020). “The Origin of Elements from Carbon to Uranium”. In: 900.2, 179, p. 179. DOI: [10.3847/1538-4357/abae65](https://doi.org/10.3847/1538-4357/abae65). arXiv: [2008.04660](https://arxiv.org/abs/2008.04660) [astro-ph.GA].
- Kobayashi, Chiaki and Naohito Nakasato (Mar. 2011). “Chemodynamical Simulations of the Milky Way Galaxy”. In: 729.1, 16, p. 16. DOI: [10.1088/0004-637X/729/1/16](https://doi.org/10.1088/0004-637X/729/1/16). arXiv: [1012.5144](https://arxiv.org/abs/1012.5144) [astro-ph.GA].
- Kobayashi, Chiaki et al. (Dec. 2006). “Galactic Chemical Evolution: Carbon through Zinc”. In: 653.2, pp. 1145–1171. DOI: [10.1086/508914](https://doi.org/10.1086/508914). arXiv: [astro-ph/0608688](https://arxiv.org/abs/astro-ph/0608688) [astro-ph].
- Koch, Andreas (Jan. 2009). “Complexity in small-scale dwarf spheroidal galaxies”. In: *Reviews in Modern Astronomy* 21, pp. 39–69. DOI: [10.1002/9783527629190.ch2](https://doi.org/10.1002/9783527629190.ch2). arXiv: [0905.0557](https://arxiv.org/abs/0905.0557) [astro-ph.GA].
- Korobkin, O. et al. (Nov. 2012). “On the astrophysical robustness of the neutron star merger r-process”. In: 426.3, pp. 1940–1949. DOI: [10.1111/j.1365-2966.2012.21859.x](https://doi.org/10.1111/j.1365-2966.2012.21859.x). arXiv: [1206.2379](https://arxiv.org/abs/1206.2379) [astro-ph.SR].
- Kraljic, Katarina, Frédéric Bournaud, and Marie Martig (Sept. 2012). “The Two-phase Formation History of Spiral Galaxies Traced by the Cosmic Evolution of the Bar Fraction”. In: 757.1, 60, p. 60. DOI: [10.1088/0004-637X/757/1/60](https://doi.org/10.1088/0004-637X/757/1/60). arXiv: [1207.0351](https://arxiv.org/abs/1207.0351) [astro-ph.GA].
- Kroupa, Pavel, Christopher A. Tout, and Gerard Gilmore (June 1993). “The Distribution of Low-Mass Stars in the Galactic Disc”. In: 262, pp. 545–587. DOI: [10.1093/mnras/262.3.545](https://doi.org/10.1093/mnras/262.3.545).
- Landau, Lev Davidovich and E. M. Lifshitz (1966). *Klassische Feldtheorie*.
- Lanfranchi, G. A., F. Matteucci, and G. Cescutti (July 2006). “Detailed chemical evolution of Carina and Sagittarius dwarf spheroidal galaxies”. In: 453.1, pp. 67–75. DOI: [10.1051/0004-6361:20054627](https://doi.org/10.1051/0004-6361:20054627). arXiv: [astro-ph/0603577](https://arxiv.org/abs/astro-ph/0603577) [astro-ph].

- (Apr. 2008). “A comparison of the s- and r-process element evolution in local dwarf spheroidal galaxies and in the Milky Way”. In: 481.3, pp. 635–644. DOI: [10.1051/0004-6361:20078696](https://doi.org/10.1051/0004-6361:20078696). arXiv: [0802.3368](https://arxiv.org/abs/0802.3368) [astro-ph].
- Lanfranchi, Gustavo A. and Francesca Matteucci (July 2004). “The predicted metallicity distribution of stars in dwarf spheroidal galaxies”. In: 351.4, pp. 1338–1348. DOI: [10.1111/j.1365-2966.2004.07877.x](https://doi.org/10.1111/j.1365-2966.2004.07877.x). arXiv: [astro-ph/0403602](https://arxiv.org/abs/astro-ph/0403602) [astro-ph].
- Lanfranchi, Gustavo A., Francesca Matteucci, and Gabriele Cescutti (Mar. 2010). “Chemical evolution models for local group dwarf spheroidal galaxies: the evolution of Fe-peak elements”. In: *Chemical Abundances in the Universe: Connecting First Stars to Planets*. Ed. by Katia Cunha, Monique Spite, and Beatriz Barbuy. Vol. 265, pp. 245–246. DOI: [10.1017/S1743921310000669](https://doi.org/10.1017/S1743921310000669).
- Lanfranchi, Gustavo A. et al. (June 2021). “Parameterizing the Outflow from a Central Black Hole in Dwarf Spheroidal Galaxies: A 3D Hydrodynamic Simulation”. In: 914.1, 32, p. 32. DOI: [10.3847/1538-4357/abf6d2](https://doi.org/10.3847/1538-4357/abf6d2). arXiv: [2201.08172](https://arxiv.org/abs/2201.08172) [astro-ph.GA].
- Langer, N., J. P. Arcoragi, and M. Arnould (Feb. 1989). “Neutron capture nucleosynthesis and the evolution of 15 and 30 M stars. I. The core helium burning phase.” In: 210, pp. 187–197.
- Laor, Ari (June 2001). “On the Linearity of the Black Hole-Bulge Mass Relation in Active and in Nearby Galaxies”. In: 553.2, pp. 677–682. DOI: [10.1086/320989](https://doi.org/10.1086/320989). arXiv: [astro-ph/0101405](https://arxiv.org/abs/astro-ph/0101405) [astro-ph].
- Larson, R. B. (Dec. 1975). “Models for the formation of elliptical galaxies.” In: 173, pp. 671–699. DOI: [10.1093/mnras/173.3.671](https://doi.org/10.1093/mnras/173.3.671).
- LeBlanc, J. M. and J. R. Wilson (Aug. 1970). “A Numerical Example of the Collapse of a Rotating Magnetized Star”. In: 161, p. 541. DOI: [10.1086/150558](https://doi.org/10.1086/150558).
- Leung, Henry W. and Jo Bovy (Oct. 2019). “Simultaneous calibration of spectrophotometric distances and the Gaia DR2 parallax zero-point offset with deep learning”. In: 489.2, pp. 2079–2096. DOI: [10.1093/mnras/stz2245](https://doi.org/10.1093/mnras/stz2245). arXiv: [1902.08634](https://arxiv.org/abs/1902.08634) [astro-ph.GA].
- Li, Ya-Ping et al. (Oct. 2018). “Stellar and AGN Feedback in Isolated Early-type Galaxies: The Role in Regulating Star Formation and ISM Properties”. In: 866.1, 70, p. 70. DOI: [10.3847/1538-4357/aade8b](https://doi.org/10.3847/1538-4357/aade8b). arXiv: [1803.01444](https://arxiv.org/abs/1803.01444) [astro-ph.HE].
- Limongi, Marco and Alessandro Chieffi (July 2003). “Evolution, Explosion, and Nucleosynthesis of Core-Collapse Supernovae”. In: 592.1, pp. 404–433. DOI: [10.1086/375703](https://doi.org/10.1086/375703). arXiv: [astro-ph/0304185](https://arxiv.org/abs/astro-ph/0304185) [astro-ph].
- (July 2018). “Presupernova Evolution and Explosive Nucleosynthesis of Rotating Massive Stars in the Metallicity Range $-3 \leq [\text{Fe}/\text{H}] \leq 0$ ”. In: 237.1, 13, p. 13. DOI: [10.3847/1538-4365/aacb24](https://doi.org/10.3847/1538-4365/aacb24). arXiv: [1805.09640](https://arxiv.org/abs/1805.09640) [astro-ph.SR].
- Liu, Nan et al. (Oct. 2018). “New Constraints on the Major Neutron Source in Low-mass AGB Stars”. In: 865.2, 112, p. 112. DOI: [10.3847/1538-4357/aad9f3](https://doi.org/10.3847/1538-4357/aad9f3). arXiv: [1808.03614](https://arxiv.org/abs/1808.03614) [astro-ph.SR].
- Lodders, K., H. Palme, and H. P. Gail (Jan. 2009). “Abundances of the Elements in the Solar System”. In: *Landolt & Bornstein* 4B, p. 712. DOI: [10.1007/978-3-540-88055-4_34](https://doi.org/10.1007/978-3-540-88055-4_34). arXiv: [0901.1149](https://arxiv.org/abs/0901.1149) [astro-ph.EP].

- Longland, R., C. Iliadis, and A. I. Karakas (June 2012). “Reaction rates for the s-process neutron source $^{22}\text{Ne} + \alpha$ ”. In: 85.6, 065809, p. 065809. DOI: [10.1103/PhysRevC.85.065809](https://doi.org/10.1103/PhysRevC.85.065809). arXiv: [1206.3871](https://arxiv.org/abs/1206.3871) [astro-ph.SR].
- López-Corredoira, M., A. Cabrera-Lavers, and O. E. Gerhard (Aug. 2005). “A boxy bulge in the Milky Way. Inversion of the stellar statistics equation with 2MASS data”. In: 439.1, pp. 107–110. DOI: [10.1051/0004-6361:20053075](https://doi.org/10.1051/0004-6361:20053075). arXiv: [astro-ph/0504608](https://arxiv.org/abs/astro-ph/0504608) [astro-ph].
- Lu, Yu and H. J. Mo (May 2007). “The accretion and cooling of pre-heated gas in dark matter haloes”. In: 377.2, pp. 617–629. DOI: [10.1111/j.1365-2966.2007.11627.x](https://doi.org/10.1111/j.1365-2966.2007.11627.x). arXiv: [astro-ph/0609640](https://arxiv.org/abs/astro-ph/0609640) [astro-ph].
- Luck, R. Earle and David L. Lambert (Oct. 2011). “The Distribution of the Elements in the Galactic Disk. III. A Reconsideration of Cepheids from $l = 30^\circ$ to 250° ”. In: 142.4, 136, p. 136. DOI: [10.1088/0004-6256/142/4/136](https://doi.org/10.1088/0004-6256/142/4/136). arXiv: [1108.1947](https://arxiv.org/abs/1108.1947) [astro-ph.GA].
- Lusso, E. and L. Ciotti (Jan. 2011). “One-zone models for spheroidal galaxies with a central supermassive black-hole. Self-regulated Bondi accretion”. In: 525, A115, A115. DOI: [10.1051/0004-6361/201015189](https://doi.org/10.1051/0004-6361/201015189). arXiv: [1009.5292](https://arxiv.org/abs/1009.5292) [astro-ph.GA].
- Lynden-Bell, D. (Jan. 1975). “The chemical evolution of galaxies”. In: *Vistas in Astronomy* 19.3, pp. 299–316. DOI: [10.1016/0083-6656\(75\)90005-7](https://doi.org/10.1016/0083-6656(75)90005-7).
- Mackereth, J. Ted et al. (Jan. 2019). “The origin of accreted stellar halo populations in the Milky Way using APOGEE, Gaia, and the EAGLE simulations”. In: 482.3, pp. 3426–3442. DOI: [10.1093/mnras/sty2955](https://doi.org/10.1093/mnras/sty2955). arXiv: [1808.00968](https://arxiv.org/abs/1808.00968) [astro-ph.GA].
- Madau, Piero and Mark Dickinson (Aug. 2014). “Cosmic Star-Formation History”. In: 52, pp. 415–486. DOI: [10.1146/annurev-astro-081811-125615](https://doi.org/10.1146/annurev-astro-081811-125615). arXiv: [1403.0007](https://arxiv.org/abs/1403.0007) [astro-ph.CO].
- Magorrian, John et al. (June 1998). “The Demography of Massive Dark Objects in Galaxy Centers”. In: 115.6, pp. 2285–2305. DOI: [10.1086/300353](https://doi.org/10.1086/300353). arXiv: [astro-ph/9708072](https://arxiv.org/abs/astro-ph/9708072) [astro-ph].
- Magrini, L. et al. (Jan. 2009). “The evolution of the Galactic metallicity gradient from high-resolution spectroscopy of open clusters”. In: 494.1, pp. 95–108. DOI: [10.1051/0004-6361:200810634](https://doi.org/10.1051/0004-6361:200810634). arXiv: [0812.0854](https://arxiv.org/abs/0812.0854) [astro-ph].
- Magrini, L. et al. (Feb. 2021). “Magnetic-buoyancy-induced mixing in AGB stars: a theoretical explanation of the non-universal relation of $[Y/Mg]$ to age”. In: 646, L2, p. L2. DOI: [10.1051/0004-6361/202040115](https://doi.org/10.1051/0004-6361/202040115). arXiv: [2101.04429](https://arxiv.org/abs/2101.04429) [astro-ph.GA].
- Magrini, L. et al. (Jan. 2023). “The Gaia-ESO survey: Mapping the shape and evolution of the radial abundance gradients with open clusters”. In: 669, A119, A119. DOI: [10.1051/0004-6361/202244957](https://doi.org/10.1051/0004-6361/202244957). arXiv: [2210.15525](https://arxiv.org/abs/2210.15525) [astro-ph.GA].
- Majewski, Steven R. et al. (Sept. 2017a). “The Apache Point Observatory Galactic Evolution Experiment (APOGEE)”. In: 154.3, 94, p. 94. DOI: [10.3847/1538-3881/aa784d](https://doi.org/10.3847/1538-3881/aa784d). arXiv: [1509.05420](https://arxiv.org/abs/1509.05420) [astro-ph.IM].
- (Sept. 2017b). “The Apache Point Observatory Galactic Evolution Experiment (APOGEE)”. In: 154.3, 94, p. 94. DOI: [10.3847/1538-3881/aa784d](https://doi.org/10.3847/1538-3881/aa784d). arXiv: [1509.05420](https://arxiv.org/abs/1509.05420) [astro-ph.IM].

- Mancino, Antonio, Luca Ciotti, and Silvia Pellegrini (May 2022). “On the polytropic Bondi accretion in two-component galaxy models with a central massive BH”. In: 512.2, pp. 2474–2488. DOI: [10.1093/mnras/stac612](https://doi.org/10.1093/mnras/stac612). arXiv: [2203.05050](https://arxiv.org/abs/2203.05050) [astro-ph.GA].
- Marconi, Alessandro and Leslie K. Hunt (May 2003). “The Relation between Black Hole Mass, Bulge Mass, and Near-Infrared Luminosity”. In: 589.1, pp. L21–L24. DOI: [10.1086/375804](https://doi.org/10.1086/375804). arXiv: [astro-ph/0304274](https://arxiv.org/abs/astro-ph/0304274) [astro-ph].
- Martayan, C. et al. (Sept. 2007a). “Be stars and binaries in the field of the SMC open cluster NGC 330 with VLT-FLAMES”. In: 472.2, pp. 577–586. DOI: [10.1051/0004-6361:20077390](https://doi.org/10.1051/0004-6361:20077390). arXiv: [0706.4426](https://arxiv.org/abs/0706.4426) [astro-ph].
- Martayan, C. et al. (Feb. 2007b). “Effects of metallicity, star-formation conditions, and evolution in B and Be stars. II. Small Magellanic Cloud, field of NGC 330”. In: 462.2, pp. 683–694. DOI: [10.1051/0004-6361:20065076](https://doi.org/10.1051/0004-6361:20065076). arXiv: [astro-ph/0609677](https://arxiv.org/abs/astro-ph/0609677) [astro-ph].
- Martinez-Valpuesta, Inma, Isaac Shlosman, and Clayton Heller (Jan. 2006a). “Evolution of Stellar Bars in Live Axisymmetric Halos: Recurrent Buckling and Secular Growth”. In: 637.1, pp. 214–226. DOI: [10.1086/498338](https://doi.org/10.1086/498338). arXiv: [astro-ph/0507219](https://arxiv.org/abs/astro-ph/0507219) [astro-ph].
- (Jan. 2006b). “Evolution of Stellar Bars in Live Axisymmetric Halos: Recurrent Buckling and Secular Growth”. In: 637.1, pp. 214–226. DOI: [10.1086/498338](https://doi.org/10.1086/498338). arXiv: [astro-ph/0507219](https://arxiv.org/abs/astro-ph/0507219) [astro-ph].
- Marzke, Ronald O. et al. (Aug. 1998). “The Galaxy Luminosity Function at $Z \approx 0.05$: Dependence on Morphology”. In: 503.2, pp. 617–631. DOI: [10.1086/306011](https://doi.org/10.1086/306011). arXiv: [astro-ph/9805218](https://arxiv.org/abs/astro-ph/9805218) [astro-ph].
- Matsumoto, J. et al. (Oct. 2022). “Magnetic support for neutrino-driven explosion of 3D non-rotating core-collapse supernova models”. In: 516.2, pp. 1752–1767. DOI: [10.1093/mnras/stac2335](https://doi.org/10.1093/mnras/stac2335). arXiv: [2202.07967](https://arxiv.org/abs/2202.07967) [astro-ph.HE].
- Matteucci, F. and P. Francois (Aug. 1989). “Galactic chemical evolution : abundance gradients of individual elements.” In: 239, pp. 885–904. DOI: [10.1093/mnras/239.3.885](https://doi.org/10.1093/mnras/239.3.885).
- Matteucci, F. and L. Greggio (Jan. 1986). “Relative roles of type I and II supernovae in the chemical enrichment of the interstellar gas”. In: 154.1-2, pp. 279–287.
- Matteucci, F. et al. (July 2009). “The effect of different type Ia supernova progenitors on Galactic chemical evolution”. In: 501.2, pp. 531–538. DOI: [10.1051/0004-6361/200911869](https://doi.org/10.1051/0004-6361/200911869). arXiv: [0905.0272](https://arxiv.org/abs/0905.0272) [astro-ph.GA].
- Matteucci, F. et al. (Mar. 2014). “Europium production: neutron star mergers versus core-collapse supernovae”. In: 438.3, pp. 2177–2185. DOI: [10.1093/mnras/stt2350](https://doi.org/10.1093/mnras/stt2350). arXiv: [1311.6980](https://arxiv.org/abs/1311.6980) [astro-ph.GA].
- Matteucci, F. et al. (Aug. 2019). “The origin of stellar populations in the Galactic bulge from chemical abundances”. In: 487.4, pp. 5363–5371. DOI: [10.1093/mnras/stz1647](https://doi.org/10.1093/mnras/stz1647). arXiv: [1903.12440](https://arxiv.org/abs/1903.12440) [astro-ph.GA].
- Matteucci, Francesca (Sept. 1992). “The Influence of Dark Matter on the Chemical Evolution of Elliptical Galaxies”. In: 397, p. 32. DOI: [10.1086/171762](https://doi.org/10.1086/171762).
- (Aug. 1994). “Abundance ratios in ellipticals and galaxy formation.” In: 288, pp. 57–64.
- (Dec. 2008). “Chemical enrichment and feedback in low metallicity environments: constraints on galaxy formation”. In: *Low-Metallicity Star Formation:*

- From the First Stars to Dwarf Galaxies*. Ed. by Leslie K. Hunt, Suzanne C. Madden, and Raffaella Schneider. Vol. 255, pp. 134–141. DOI: [10.1017/S1743921308024708](https://doi.org/10.1017/S1743921308024708).
- Matteucci, Francesca (2012). *Chemical Evolution of Galaxies*. DOI: [10.1007/978-3-642-22491-1](https://doi.org/10.1007/978-3-642-22491-1).
- (Dec. 2021). “Modelling the chemical evolution of the Milky Way”. In: 29.1, 5, p. 5. DOI: [10.1007/s00159-021-00133-8](https://doi.org/10.1007/s00159-021-00133-8). arXiv: [2106.13145](https://arxiv.org/abs/2106.13145) [astro-ph.GA].
- Matteucci, Francesca and Enzo Brocato (Dec. 1990). “Metallicity Distribution and Abundance Ratios in the Stars of the Galactic Bulge”. In: 365, p. 539. DOI: [10.1086/169508](https://doi.org/10.1086/169508).
- Matteucci, Francesca, Raffaella Ponzoni, and Brad K. Gibson (July 1998). “On the trend of [Mg/Fe] among giant elliptical galaxies”. In: 335, pp. 855–866. arXiv: [astro-ph/9803126](https://arxiv.org/abs/astro-ph/9803126) [astro-ph].
- Matteucci, Francesca and Simone Recchi (Sept. 2001). “On the Typical Timescale for the Chemical Enrichment from Type Ia Supernovae in Galaxies”. In: 558.1, pp. 351–358. DOI: [10.1086/322472](https://doi.org/10.1086/322472). arXiv: [astro-ph/0105074](https://arxiv.org/abs/astro-ph/0105074) [astro-ph].
- McConnachie, Alan W. (July 2012). “The Observed Properties of Dwarf Galaxies in and around the Local Group”. In: 144.1, 4, p. 4. DOI: [10.1088/0004-6256/144/1/4](https://doi.org/10.1088/0004-6256/144/1/4). arXiv: [1204.1562](https://arxiv.org/abs/1204.1562) [astro-ph.CO].
- McLure, R. J. and J. S. Dunlop (Apr. 2002). “On the black hole-bulge mass relation in active and inactive galaxies”. In: 331.3, pp. 795–804. DOI: [10.1046/j.1365-8711.2002.05236.x](https://doi.org/10.1046/j.1365-8711.2002.05236.x). arXiv: [astro-ph/0108417](https://arxiv.org/abs/astro-ph/0108417) [astro-ph].
- McWilliam, Andrew and R. Michael Rich (Apr. 1994). “The First Detailed Abundance Analysis of Galactic Bulge K Giants in Baade’s Window”. In: 91, p. 749. DOI: [10.1086/191954](https://doi.org/10.1086/191954).
- Melioli, C. and E. M. de Gouveia Dal Pino (Sept. 2004). “Evolution of the ISM of starburst galaxies: The SN heating efficiency”. In: 424, pp. 817–831. DOI: [10.1051/0004-6361:20035750](https://doi.org/10.1051/0004-6361:20035750). arXiv: [astro-ph/0311628](https://arxiv.org/abs/astro-ph/0311628) [astro-ph].
- Melioli, C. et al. (Nov. 2009). “Hydrodynamical simulations of Galactic fountains - II. Evolution of multiple fountains”. In: 399.3, pp. 1089–1105. DOI: [10.1111/j.1365-2966.2009.14725.x](https://doi.org/10.1111/j.1365-2966.2009.14725.x). arXiv: [0903.0720](https://arxiv.org/abs/0903.0720) [astro-ph.GA].
- Méndez-Delgado, J. E. et al. (Mar. 2022). “Gradients of chemical abundances in the Milky Way from H II regions: distances derived from Gaia EDR3 parallaxes and temperature inhomogeneities”. In: 510.3, pp. 4436–4455. DOI: [10.1093/mnras/stab3782](https://doi.org/10.1093/mnras/stab3782). arXiv: [2112.12600](https://arxiv.org/abs/2112.12600) [astro-ph.GA].
- Mikolaitis, Š. et al. (Apr. 2017). “The AMBRE project: Iron-peak elements in the solar neighbourhood”. In: 600, A22, A22. DOI: [10.1051/0004-6361/201629629](https://doi.org/10.1051/0004-6361/201629629). arXiv: [1612.07622](https://arxiv.org/abs/1612.07622) [astro-ph.SR].
- Minchev, I., C. Chiappini, and M. Martig (Sept. 2016). “Milky Way chemo-dynamics in the era of Gaia”. In: *Astronomische Nachrichten* 337.8-9, p. 944. DOI: [10.1002/asna.201612404](https://doi.org/10.1002/asna.201612404). arXiv: [1601.01313](https://arxiv.org/abs/1601.01313) [astro-ph.GA].
- Minchev, I. et al. (Dec. 2018). “Estimating stellar birth radii and the time evolution of Milky Way’s ISM metallicity gradient”. In: 481.2, pp. 1645–1657. DOI: [10.1093/mnras/sty2033](https://doi.org/10.1093/mnras/sty2033). arXiv: [1804.06856](https://arxiv.org/abs/1804.06856) [astro-ph.GA].
- Minniti, D. et al. (July 2010). “VISTA Variables in the Via Lactea (VVV): The public ESO near-IR variability survey of the Milky Way”. In: 15.5, pp. 433–443. DOI: [10.1016/j.newast.2009.12.002](https://doi.org/10.1016/j.newast.2009.12.002). arXiv: [0912.1056](https://arxiv.org/abs/0912.1056) [astro-ph.GA].

- Mishenina, T. et al. (Oct. 2019). “Enrichment of the Galactic disc with neutron-capture elements: Mo and Ru”. In: 489.2, pp. 1697–1708. DOI: [10.1093/mnras/stz2202](https://doi.org/10.1093/mnras/stz2202). arXiv: [1908.02992](https://arxiv.org/abs/1908.02992) [astro-ph.GA].
- Molero, Marta, Francesca Matteucci, and Luca Ciotti (Jan. 2023a). “Chemical evolution of elliptical galaxies I: supernovae and AGN feedback”. In: 518.1, pp. 987–1001. DOI: [10.1093/mnras/stac3066](https://doi.org/10.1093/mnras/stac3066). arXiv: [2210.11851](https://arxiv.org/abs/2210.11851) [astro-ph.GA].
- Molero, Marta et al. (Aug. 2021a). “Evolution of neutron capture elements in dwarf galaxies”. In: 505.2, pp. 2913–2931. DOI: [10.1093/mnras/stab1429](https://doi.org/10.1093/mnras/stab1429). arXiv: [2105.06916](https://arxiv.org/abs/2105.06916) [astro-ph.GA].
- Molero, Marta et al. (Jan. 2021b). “Predicted rates of merging neutron stars in galaxies”. In: 500.1, pp. 1071–1086. DOI: [10.1093/mnras/staa3340](https://doi.org/10.1093/mnras/staa3340). arXiv: [2005.10226](https://arxiv.org/abs/2005.10226) [astro-ph.GA].
- Molero, Marta et al. (Aug. 2023b). “Origin of neutron-capture elements with the Gaia-ESO survey: the evolution of s- and r-process elements across the Milky Way”. In: 523.2, pp. 2974–2989. DOI: [10.1093/mnras/stad1577](https://doi.org/10.1093/mnras/stad1577). arXiv: [2304.06452](https://arxiv.org/abs/2304.06452) [astro-ph.GA].
- Mollá, Mercedes et al. (Aug. 2015). “Galactic chemical evolution: stellar yields and the initial mass function”. In: 451.4, pp. 3693–3708. DOI: [10.1093/mnras/stv1102](https://doi.org/10.1093/mnras/stv1102). arXiv: [1505.03341](https://arxiv.org/abs/1505.03341) [astro-ph.GA].
- Moriya, Takashi J., Elena I. Sorokina, and Roger A. Chevalier (Mar. 2018). “Superluminous Supernovae”. In: 214.2, 59, p. 59. DOI: [10.1007/s11214-018-0493-6](https://doi.org/10.1007/s11214-018-0493-6). arXiv: [1803.01875](https://arxiv.org/abs/1803.01875) [astro-ph.HE].
- Mösta, Philipp et al. (Sept. 2018). “r-process Nucleosynthesis from Three-dimensional Magnetorotational Core-collapse Supernovae”. In: 864.2, 171, p. 171. DOI: [10.3847/1538-4357/aad6ec](https://doi.org/10.3847/1538-4357/aad6ec). arXiv: [1712.09370](https://arxiv.org/abs/1712.09370) [astro-ph.HE].
- Müller, B. (Sept. 2016). “The Status of Multi-Dimensional Core-Collapse Supernova Models”. In: 33, e048, e048. DOI: [10.1017/pasa.2016.40](https://doi.org/10.1017/pasa.2016.40). arXiv: [1608.03274](https://arxiv.org/abs/1608.03274) [astro-ph.SR].
- Narayan, Ramesh, Bohdan Paczynski, and Tsvi Piran (Aug. 1992). “Gamma-Ray Bursts as the Death Throes of Massive Binary Stars”. In: 395, p. L83. DOI: [10.1086/186493](https://doi.org/10.1086/186493). arXiv: [astro-ph/9204001](https://arxiv.org/abs/astro-ph/9204001) [astro-ph].
- Nelson, Erica June et al. (Sept. 2016). “Where Stars Form: Inside-out Growth and Coherent Star Formation from HST H α Maps of 3200 Galaxies across the Main Sequence at $0.7 < z < 1.5$ ”. In: 828.1, 27, p. 27. DOI: [10.3847/0004-637X/828/1/27](https://doi.org/10.3847/0004-637X/828/1/27). arXiv: [1507.03999](https://arxiv.org/abs/1507.03999) [astro-ph.GA].
- Ness, Melissa and Dustin Lang (July 2016). “The X-shaped Bulge of the Milky Way Revealed by WISE”. In: 152.1, 14, p. 14. DOI: [10.3847/0004-6256/152/1/14](https://doi.org/10.3847/0004-6256/152/1/14). arXiv: [1603.00026](https://arxiv.org/abs/1603.00026) [astro-ph.GA].
- Nidever, David L. et al. (Nov. 2014). “Tracing Chemical Evolution over the Extent of the Milky Way’s Disk with APOGEE Red Clump Stars”. In: 796.1, 38, p. 38. DOI: [10.1088/0004-637X/796/1/38](https://doi.org/10.1088/0004-637X/796/1/38). arXiv: [1409.3566](https://arxiv.org/abs/1409.3566) [astro-ph.GA].
- Nidever, David L. et al. (Dec. 2015). “The Data Reduction Pipeline for the Apache Point Observatory Galactic Evolution Experiment”. In: 150.6, 173, p. 173. DOI: [10.1088/0004-6256/150/6/173](https://doi.org/10.1088/0004-6256/150/6/173). arXiv: [1501.03742](https://arxiv.org/abs/1501.03742) [astro-ph.IM].
- Nishimura, N. et al. (Feb. 2017). “The Intermediate r-process in Core-collapse Supernovae Driven by the Magneto-rotational Instability”. In: 836.2, L21, p. L21. DOI: [10.3847/2041-8213/aa5dee](https://doi.org/10.3847/2041-8213/aa5dee). arXiv: [1611.02280](https://arxiv.org/abs/1611.02280) [astro-ph.HE].

- Nishimura, Nobuya, Tomoya Takiwaki, and Friedrich-Karl Thielemann (Sept. 2015). “The r-process Nucleosynthesis in the Various Jet-like Explosions of Magnetorotational Core-collapse Supernovae”. In: 810.2, 109, p. 109. DOI: [10.1088/0004-637X/810/2/109](https://doi.org/10.1088/0004-637X/810/2/109). arXiv: [1501.06567](https://arxiv.org/abs/1501.06567) [astro-ph.SR].
- Noguchi, Masafumi (July 2018). “The formation of solar-neighbourhood stars in two generations separated by 5 billion years”. In: 559.7715, pp. 585–588. DOI: [10.1038/s41586-018-0329-2](https://doi.org/10.1038/s41586-018-0329-2). arXiv: [1809.02299](https://arxiv.org/abs/1809.02299) [astro-ph.GA].
- Nomoto, Ken’ichi, Chiaki Kobayashi, and Nozomu Tominaga (Aug. 2013). “Nucleosynthesis in Stars and the Chemical Enrichment of Galaxies”. In: 51.1, pp. 457–509. DOI: [10.1146/annurev-astro-082812-140956](https://doi.org/10.1146/annurev-astro-082812-140956).
- Obergaulinger, M. and M. Á. Aloy (May 2021). “Magnetorotational core collapse of possible GRB progenitors - III. Three-dimensional models”. In: 503.4, pp. 4942–4963. DOI: [10.1093/mnras/stab295](https://doi.org/10.1093/mnras/stab295). arXiv: [2008.07205](https://arxiv.org/abs/2008.07205) [astro-ph.HE].
- Obergaulinger, M., O. Just, and M. A. Aloy (Aug. 2018). “Core collapse with magnetic fields and rotation”. In: *Journal of Physics G Nuclear Physics* 45.8, p. 084001. DOI: [10.1088/1361-6471/aac982](https://doi.org/10.1088/1361-6471/aac982). arXiv: [1806.00393](https://arxiv.org/abs/1806.00393) [astro-ph.HE].
- O’Neill, J. K. and John Dubinski (Nov. 2003). “Detailed comparison of the structures and kinematics of simulated and observed barred galaxies”. In: 346.1, pp. 251–264. DOI: [10.1046/j.1365-2966.2003.07085.x](https://doi.org/10.1046/j.1365-2966.2003.07085.x). arXiv: [astro-ph/0305169](https://arxiv.org/abs/astro-ph/0305169) [astro-ph].
- Ortolani, Sergio et al. (Oct. 1995). “Near-coeval formation of the Galactic bulge and halo inferred from globular cluster ages”. In: 377.6551, pp. 701–704. DOI: [10.1038/377701a0](https://doi.org/10.1038/377701a0).
- Pagel, B. E. J. and B. E. Patchett (July 1975). “Metal abundances in nearby stars and the chemical history of the solar neighbourhood.” In: 172, pp. 13–40. DOI: [10.1093/mnras/172.1.13](https://doi.org/10.1093/mnras/172.1.13).
- Palla, M. et al. (Oct. 2020). “Chemical evolution of the Milky Way: constraints on the formation of the thick and thin discs”. In: 498.2, pp. 1710–1725. DOI: [10.1093/mnras/staa2437](https://doi.org/10.1093/mnras/staa2437). arXiv: [2008.07484](https://arxiv.org/abs/2008.07484) [astro-ph.GA].
- Palla, Marco (Feb. 2021). “The effects of different Type Ia SN yields on Milky Way chemical evolution”. In: DOI: [10.1093/mnras/stab293](https://doi.org/10.1093/mnras/stab293). arXiv: [2101.12679](https://arxiv.org/abs/2101.12679) [astro-ph.GA].
- Palla, Marco et al. (July 2022). “[Mg/Fe] ratios in the solar neighbourhood: Stellar yields and chemical evolution scenarios”. In: 663, A125, A125. DOI: [10.1051/0004-6361/202142645](https://doi.org/10.1051/0004-6361/202142645). arXiv: [2205.01558](https://arxiv.org/abs/2205.01558) [astro-ph.GA].
- Pan, Zhizheng, Xianzhong Zheng, and Xu Kong (Jan. 2017). “The Quenched Mass Portion of Star-forming Galaxies and the Origin of the Star Formation Sequence Slope”. In: 834.1, 39, p. 39. DOI: [10.3847/1538-4357/834/1/39](https://doi.org/10.3847/1538-4357/834/1/39). arXiv: [1611.04698](https://arxiv.org/abs/1611.04698) [astro-ph.GA].
- Perego, A., F. K. Thielemann, and G. Cescutti (2021). “r-Process Nucleosynthesis from Compact Binary Mergers”. In: *Handbook of Gravitational Wave Astronomy*, 13, p. 13. DOI: [10.1007/978-981-15-4702-7_13-1](https://doi.org/10.1007/978-981-15-4702-7_13-1).
- Peterken, Thomas et al. (Apr. 2021). “Size, shade, or shape? The contribution of galaxies of different types to the star formation history of the Universe from SDSS-IV MaNGA”. In: 502.3, pp. 3128–3143. DOI: [10.1093/mnras/stab268](https://doi.org/10.1093/mnras/stab268). arXiv: [2101.11945](https://arxiv.org/abs/2101.11945) [astro-ph.GA].

- Pian, E. et al. (Nov. 2017). “Spectroscopic identification of r-process nucleosynthesis in a double neutron-star merger”. In: 551.7678, pp. 67–70. DOI: [10.1038/nature24298](https://doi.org/10.1038/nature24298). arXiv: [1710.05858](https://arxiv.org/abs/1710.05858) [astro-ph.HE].
- Pignatari, M. et al. (Feb. 2010). “The Weak s-Process in Massive Stars and its Dependence on the Neutron Capture Cross Sections”. In: 710.2, pp. 1557–1577. DOI: [10.1088/0004-637X/710/2/1557](https://doi.org/10.1088/0004-637X/710/2/1557).
- Pignatari, Marco et al. (Apr. 2016). “The production of proton-rich isotopes beyond iron: The γ -process in stars”. In: *International Journal of Modern Physics E* 25.4, 1630003–232, pp. 1630003–232. DOI: [10.1142/S0218301316300034](https://doi.org/10.1142/S0218301316300034). arXiv: [1605.03690](https://arxiv.org/abs/1605.03690) [astro-ph.SR].
- Pipino, A. and F. Matteucci (Aug. 2008). “Are dry mergers of ellipticals the way to reconcile model predictions with downsizing?” In: 486.3, pp. 763–769. DOI: [10.1051/0004-6361:200809395](https://doi.org/10.1051/0004-6361:200809395). arXiv: [0805.0793](https://arxiv.org/abs/0805.0793) [astro-ph].
- Pipino, Antonio and Francesca Matteucci (Jan. 2004). “Photochemical evolution of elliptical galaxies - I. The high-redshift formation scenario”. In: 347.3, pp. 968–984. DOI: [10.1111/j.1365-2966.2004.07268.x](https://doi.org/10.1111/j.1365-2966.2004.07268.x). arXiv: [astro-ph/0310251](https://arxiv.org/abs/astro-ph/0310251) [astro-ph].
- Pipino, Antonio et al. (July 2002). “SNe heating and the chemical evolution of the intra-cluster medium”. In: 7.5, pp. 227–247. DOI: [10.1016/S1384-1076\(02\)00136-7](https://doi.org/10.1016/S1384-1076(02)00136-7). arXiv: [astro-ph/0204161](https://arxiv.org/abs/astro-ph/0204161) [astro-ph].
- Portail, Matthieu et al. (Sept. 2017). “Chemodynamical modelling of the galactic bulge and bar”. In: 470.1, pp. 1233–1252. DOI: [10.1093/mnras/stx1293](https://doi.org/10.1093/mnras/stx1293). arXiv: [1704.07821](https://arxiv.org/abs/1704.07821) [astro-ph.GA].
- Pozzi, F. et al. (Apr. 2015). “Are the Bulk of z > 2 Herschel Galaxies Proto-Spheroids?” In: 803.1, 35, p. 35. DOI: [10.1088/0004-637X/803/1/35](https://doi.org/10.1088/0004-637X/803/1/35). arXiv: [1502.03686](https://arxiv.org/abs/1502.03686) [astro-ph.GA].
- Prantzos, N., M. Hashimoto, and K. Nomoto (Aug. 1990). “The s-process in massive stars : yields as a function of stellar mass and metallicity.” In: 234, p. 211.
- Prantzos, N. et al. (May 2018). “Chemical evolution with rotating massive star yields - I. The solar neighbourhood and the s-process elements”. In: 476.3, pp. 3432–3459. DOI: [10.1093/mnras/sty316](https://doi.org/10.1093/mnras/sty316). arXiv: [1802.02824](https://arxiv.org/abs/1802.02824) [astro-ph.GA].
- Prantzos, N. et al. (Jan. 2020). “Chemical evolution with rotating massive star yields II. A new assessment of the solar s- and r-process components”. In: 491.2, pp. 1832–1850. DOI: [10.1093/mnras/stz315410.48550/arXiv.1911.02545](https://doi.org/10.1093/mnras/stz315410.48550/arXiv.1911.02545). arXiv: [1911.02545](https://arxiv.org/abs/1911.02545) [astro-ph.GA].
- Prantzos, Nikos et al. (Aug. 2023). “On the origin of the Galactic thin and thick discs, their abundance gradients and the diagnostic potential of their abundance ratios”. In: 523.2, pp. 2126–2145. DOI: [10.1093/mnras/stad1551](https://doi.org/10.1093/mnras/stad1551). arXiv: [2305.13431](https://arxiv.org/abs/2305.13431) [astro-ph.GA].
- Queiroz, A. B. A. et al. (May 2018). “StarHorse: a Bayesian tool for determining stellar masses, ages, distances, and extinctions for field stars”. In: 476.2, pp. 2556–2583. DOI: [10.1093/mnras/sty330](https://doi.org/10.1093/mnras/sty330). arXiv: [1710.09970](https://arxiv.org/abs/1710.09970) [astro-ph.IM].
- Queiroz, A. B. A. et al. (June 2020). “From the bulge to the outer disc: StarHorse stellar parameters, distances, and extinctions for stars in APOGEE DR16 and other spectroscopic surveys”. In: 638, A76, A76. DOI: [10.1051/0004-6361/201937364](https://doi.org/10.1051/0004-6361/201937364). arXiv: [1912.09778](https://arxiv.org/abs/1912.09778) [astro-ph.GA].

- Queiroz, A. B. A. et al. (Dec. 2021). “The Milky Way bar and bulge revealed by APOGEE and Gaia EDR3”. In: 656, A156, A156. DOI: [10 . 1051 / 0004 - 6361 / 202039030](https://doi.org/10.1051/0004-6361/202039030). arXiv: [2007 . 12915](https://arxiv.org/abs/2007.12915) [astro-ph.GA].
- Quillen, Alice C. et al. (Apr. 2018). “Migration in the shearing sheet and estimates for young open cluster migration”. In: 475.4, pp. 4450–4466. DOI: [10 . 1093 / mnras / sty125](https://doi.org/10.1093/mnras/sty125). arXiv: [1709 . 04801](https://arxiv.org/abs/1709.04801) [astro-ph.GA].
- Raha, N. et al. (Aug. 1991). “A dynamical instability of bars in disk galaxies”. In: 352.6334, pp. 411–412. DOI: [10 . 1038 / 352411a0](https://doi.org/10.1038/352411a0).
- Ramya, P., Bacham E. Reddy, and David L. Lambert (Oct. 2012). “Chemical compositions of stars in two stellar streams from the Galactic thick disc”. In: 425.4, pp. 3188–3200. DOI: [10 . 1111 / j . 1365 - 2966 . 2012 . 21677 . x](https://doi.org/10.1111/j.1365-2966.2012.21677.x). arXiv: [1207 . 0767](https://arxiv.org/abs/1207.0767) [astro-ph.GA].
- Randich, S. et al. (Oct. 2022). “The Gaia-ESO Public Spectroscopic Survey: Implementation, data products, open cluster survey, science, and legacy”. In: 666, A121, A121. DOI: [10 . 1051 / 0004 - 6361 / 202243141](https://doi.org/10.1051/0004-6361/202243141). arXiv: [2206 . 02901](https://arxiv.org/abs/2206.02901) [astro-ph.GA].
- Read, J. I. (June 2014). “The local dark matter density”. In: *Journal of Physics G Nuclear Physics* 41.6, 063101, p. 063101. DOI: [10 . 1088 / 0954 - 3899 / 41 / 6 / 063101](https://doi.org/10.1088/0954-3899/41/6/063101). arXiv: [1404 . 1938](https://arxiv.org/abs/1404.1938) [astro-ph.GA].
- Recchi, Simone, Francesca Matteucci, and Annibale D’Ercole (Apr. 2001). “Dynamical and chemical evolution of gas-rich dwarf galaxies”. In: 322.4, pp. 800–820. DOI: [10 . 1046 / j . 1365 - 8711 . 2001 . 04189 . x](https://doi.org/10.1046/j.1365-8711.2001.04189.x). arXiv: [astro - ph / 0002370](https://arxiv.org/abs/astro-ph/0002370) [astro-ph].
- Recio-Blanco, A. et al. (July 2014). “The Gaia-ESO Survey: the Galactic thick to thin disc transition”. In: 567, A5, A5. DOI: [10 . 1051 / 0004 - 6361 / 201322944](https://doi.org/10.1051/0004-6361/201322944). arXiv: [1403 . 7568](https://arxiv.org/abs/1403.7568) [astro-ph.GA].
- Reddy, B. E., D. L. Lambert, and C. A. Prieto (Sept. 2006). “VizieR Online Data Catalog: Elemental abundances for 176 stars (Reddy+, 2006)”. In: *VizieR Online Data Catalog*, J/MNRAS/367/1329, J/MNRAS/367/1329.
- Reddy, B. E. et al. (June 2003). “VizieR Online Data Catalog: [X/Fe] of Galactic disc F and G dwarfs (Reddy+, 2003)”. In: *VizieR Online Data Catalog*, J/MNRAS/340/304, J/MNRAS/340/304.
- Reichert, M. et al. (Sept. 2020). “Neutron-capture elements in dwarf galaxies. III. A homogenized analysis of 13 dwarf spheroidal and ultra-faint galaxies”. In: 641, A127, A127. DOI: [10 . 1051 / 0004 - 6361 / 201936930](https://doi.org/10.1051/0004-6361/201936930). arXiv: [2004 . 01195](https://arxiv.org/abs/2004.01195) [astro-ph.GA].
- Reichert, M. et al. (Mar. 2021). “Nucleosynthesis in magneto-rotational supernovae”. In: 501.4, pp. 5733–5745. DOI: [10 . 1093 / mnras / stab029](https://doi.org/10.1093/mnras/stab029). arXiv: [2010 . 02227](https://arxiv.org/abs/2010.02227) [astro-ph.HE].
- Reichert, M. et al. (Jan. 2023). “Magnetorotational supernovae: a nucleosynthetic analysis of sophisticated 3D models”. In: 518.1, pp. 1557–1583. DOI: [10 . 1093 / mnras / stac3185](https://doi.org/10.1093/mnras/stac3185). arXiv: [2206 . 11914](https://arxiv.org/abs/2206.11914) [astro-ph.HE].
- Rich, R. Michael (Mar. 1988). “Spectroscopy and Abundances of 88 K Giants in Baade’s Window”. In: 95, p. 828. DOI: [10 . 1086 / 114681](https://doi.org/10.1086/114681).
- Rizzuti, F. et al. (Nov. 2019). “The contribution from rotating massive stars to the enrichment in Sr and Ba of the Milky Way”. In: 489.4, pp. 5244–5255. DOI:

- [10.1093/mnras/stz250510.48550/arXiv.1909.04378](https://arxiv.org/abs/1909.04378). arXiv: 1909.04378 [astro-ph.GA].
- Rizzuti, F. et al. (Apr. 2021). “Constraints on stellar rotation from the evolution of Sr and Ba in the Galactic halo”. In: 502.2, pp. 2495–2507. DOI: [10.1093/mnras/stab158](https://doi.org/10.1093/mnras/stab158). arXiv: 2101.05345 [astro-ph.GA].
- Roberti, Lorenzo et al. (Sept. 2023). “The γ -process nucleosynthesis in core-collapse super-novae”. In: *European Physical Journal Web of Conferences*. Vol. 279. European Physical Journal Web of Conferences, 09002, p. 09002. DOI: [10.1051/epjconf/202327909002](https://doi.org/10.1051/epjconf/202327909002).
- Rojas-Arriagada, A. et al. (Feb. 2016). “The Gaia-ESO Survey: Separating disk chemical substructures with cluster models. Evidence of a separate evolution in the metal-poor thin disk”. In: 586, A39, A39. DOI: [10.1051/0004-6361/201526969](https://doi.org/10.1051/0004-6361/201526969). arXiv: 1512.03835 [astro-ph.GA].
- Rojas-Arriagada, A. et al. (May 2017). “The Gaia-ESO Survey: Exploring the complex nature and origins of the Galactic bulge populations”. In: 601, A140, A140. DOI: [10.1051/0004-6361/201629160](https://doi.org/10.1051/0004-6361/201629160). arXiv: 1704.03325 [astro-ph.GA].
- Rojas-Arriagada, A. et al. (June 2019). “The bimodal [Mg/Fe] versus [Fe/H] bulge sequence as revealed by APOGEE DR14”. In: 626, A16, A16. DOI: [10.1051/0004-6361/201834126](https://doi.org/10.1051/0004-6361/201834126). arXiv: 1905.01364 [astro-ph.GA].
- Rojas-Arriagada, Alvaro et al. (Nov. 2020). “How many components? Quantifying the complexity of the metallicity distribution in the Milky Way bulge with APOGEE”. In: 499.1, pp. 1037–1057. DOI: [10.1093/mnras/staa2807](https://doi.org/10.1093/mnras/staa2807). arXiv: 2007.13967 [astro-ph.GA].
- Romano, D. et al. (Feb. 2005). “Quantifying the uncertainties of chemical evolution studies. I. Stellar lifetimes and initial mass function”. In: 430, pp. 491–505. DOI: [10.1051/0004-6361:20048222](https://doi.org/10.1051/0004-6361:20048222).
- Romano, D. et al. (Nov. 2010). “Quantifying the uncertainties of chemical evolution studies. II. Stellar yields”. In: 522, A32, A32. DOI: [10.1051/0004-6361/201014483](https://doi.org/10.1051/0004-6361/201014483). arXiv: 1006.5863 [astro-ph.GA].
- Romano, Donatella and Else Starckenburg (Sept. 2013). “Chemical evolution of Local Group dwarf galaxies in a cosmological context - I. A new modelling approach and its application to the Sculptor dwarf spheroidal galaxy”. In: 434.1, pp. 471–487. DOI: [10.1093/mnras/stt1033](https://doi.org/10.1093/mnras/stt1033). arXiv: 1306.1722 [astro-ph.GA].
- Romano, Donatella, Monica Tosi, and Francesca Matteucci (Jan. 2006). “Formation and evolution of late-type dwarf galaxies - I. NGC1705 and NGC1569”. In: 365.3, pp. 759–778. DOI: [10.1111/j.1365-2966.2005.09684.x](https://doi.org/10.1111/j.1365-2966.2005.09684.x). arXiv: [astro-ph/0510113](https://arxiv.org/abs/astro-ph/0510113) [astro-ph].
- Romano, Donatella et al. (Aug. 2000). “The Mass Surface Density in the Local Disk and the Chemical Evolution of the Galaxy”. In: 539.1, pp. 235–240. DOI: [10.1086/309223](https://doi.org/10.1086/309223). arXiv: [astro-ph/0003130](https://arxiv.org/abs/astro-ph/0003130) [astro-ph].
- Romano, Donatella et al. (Feb. 2015). “Chemical enrichment in very low metallicity environments: Boötes I”. In: 446.4, pp. 4220–4231. DOI: [10.1093/mnras/stu2427](https://doi.org/10.1093/mnras/stu2427). arXiv: 1411.4508 [astro-ph.GA].
- Romano, Donatella et al. (Dec. 2019). “The evolution of CNO isotopes: the impact of massive stellar rotators”. In: 490.2, pp. 2838–2854. DOI: [10.1093/mnras/stz2741](https://doi.org/10.1093/mnras/stz2741). arXiv: 1907.09476 [astro-ph.GA].

- Romano, Donatella et al. (July 2023). “Modeling the Chemical Enrichment History of the Bulge Fossil Fragment Terzan 5”. In: 951.2, 85, p. 85. DOI: [10.3847/1538-4357/acd8ba](https://doi.org/10.3847/1538-4357/acd8ba). arXiv: [2305.15355](https://arxiv.org/abs/2305.15355) [astro-ph.GA].
- Rubele, S. et al. (Nov. 2015). “VizieR Online Data Catalog: VMC survey. XIV. SFR in SMC (Rubele+, 2015)”. In: *VizieR Online Data Catalog*, J/MNRAS/449/639, J/MNRAS/449/639.
- Russell, Henry Norris (June 1914). “Relations Between the Spectra and Other Characteristics of the Stars”. In: *Popular Astronomy* 22, pp. 331–351.
- Safarzadeh, Mohammadtaher and Evan Scannapieco (Oct. 2017). “Simulating neutron star mergers as r-process sources in ultrafaint dwarf galaxies”. In: 471.2, pp. 2088–2096. DOI: [10.1093/mnras/stx1706](https://doi.org/10.1093/mnras/stx1706). arXiv: [1707.01909](https://arxiv.org/abs/1707.01909) [astro-ph.GA].
- Safarzadeh, Mohammadtaher et al. (Feb. 2019). “r-process Enrichment of the Ultrafaint Dwarf Galaxies by Fast-merging Double-neutron Stars”. In: 872.1, 105, p. 105. DOI: [10.3847/1538-4357/aafe0e](https://doi.org/10.3847/1538-4357/aafe0e). arXiv: [1810.04176](https://arxiv.org/abs/1810.04176) [astro-ph.HE].
- Salpeter, Edwin E. (Jan. 1955). “The Luminosity Function and Stellar Evolution.” In: 121, p. 161. DOI: [10.1086/145971](https://doi.org/10.1086/145971).
- Salvadori, Stefania and Andrea Ferrara (May 2009). “Ultra faint dwarfs: probing early cosmic star formation”. In: 395.1, pp. L6–L10. DOI: [10.1111/j.1745-3933.2009.00627.x](https://doi.org/10.1111/j.1745-3933.2009.00627.x). arXiv: [0812.3151](https://arxiv.org/abs/0812.3151) [astro-ph].
- Sazonov, S. Yu. et al. (Mar. 2005). “Radiative feedback from quasars and the growth of massive black holes in stellar spheroids”. In: 358.1, pp. 168–180. DOI: [10.1111/j.1365-2966.2005.08763.x](https://doi.org/10.1111/j.1365-2966.2005.08763.x). arXiv: [astro-ph/0411086](https://arxiv.org/abs/astro-ph/0411086) [astro-ph].
- Scalo, J. M. (May 1986). “The Stellar Initial Mass Function”. In: 11, pp. 1–278.
- Scannapieco, C. et al. (Sept. 2006). “Feedback and metal enrichment in cosmological SPH simulations - II. A multiphase model with supernova energy feedback”. In: 371.3, pp. 1125–1139. DOI: [10.1111/j.1365-2966.2006.10785.x](https://doi.org/10.1111/j.1365-2966.2006.10785.x). arXiv: [astro-ph/0604524](https://arxiv.org/abs/astro-ph/0604524) [astro-ph].
- Scannapieco, Cecilia et al. (Sept. 2008). “Effects of supernova feedback on the formation of galaxy discs”. In: 389.3, pp. 1137–1149. DOI: [10.1111/j.1365-2966.2008.13678.x](https://doi.org/10.1111/j.1365-2966.2008.13678.x). arXiv: [0804.3795](https://arxiv.org/abs/0804.3795) [astro-ph].
- Schaller, G. et al. (Dec. 1992). “New Grids of Stellar Models from 0.8-SOLAR-MASS to 120-SOLAR-MASSSES at Z=0.020 and Z=0.001”. In: 96, p. 269.
- Schmidt, Maarten (Mar. 1959). “The Rate of Star Formation.” In: 129, p. 243. DOI: [10.1086/146614](https://doi.org/10.1086/146614).
- (Apr. 1963). “The Rate of Star Formation. II. The Rate of Formation of Stars of Different Mass.” In: 137, p. 758. DOI: [10.1086/147553](https://doi.org/10.1086/147553).
- Schönrich, Ralph and James Binney (June 2009). “Chemical evolution with radial mixing”. In: 396.1, pp. 203–222. DOI: [10.1111/j.1365-2966.2009.14750.x](https://doi.org/10.1111/j.1365-2966.2009.14750.x). arXiv: [0809.3006](https://arxiv.org/abs/0809.3006) [astro-ph].
- Schönrich, Ralph and Paul J. McMillan (May 2017). “Understanding inverse metallicity gradients in galactic discs as a consequence of inside-out formation”. In: 467.1, pp. 1154–1174. DOI: [10.1093/mnras/stx093](https://doi.org/10.1093/mnras/stx093). arXiv: [1605.02338](https://arxiv.org/abs/1605.02338) [astro-ph.GA].
- Shakura, N. I. and R. A. Sunyaev (June 1973). “Reprint of 1973A&A....24..337S. Black holes in binary systems. Observational appearance.” In: 500, pp. 33–51.
- Shen, Lu et al. (Oct. 2023). “NGDEEP Epoch 1: Spatially Resolved H α Observations of Disk and Bulge Growth in Star-Forming Galaxies at $z \sim 0.6$ -2.2 from JWST

- NIRISS Slitless Spectroscopy”. In: *arXiv e-prints*, arXiv:2310.13745, arXiv:2310.13745. DOI: [10.48550/arXiv.2310.13745](https://doi.org/10.48550/arXiv.2310.13745). arXiv: [2310.13745](https://arxiv.org/abs/2310.13745) [astro-ph.GA].
- Sheth, Kartik et al. (Mar. 2008). “Evolution of the Bar Fraction in COSMOS: Quantifying the Assembly of the Hubble Sequence”. In: 675.2, pp. 1141–1155. DOI: [10.1086/524980](https://doi.org/10.1086/524980). arXiv: [0710.4552](https://arxiv.org/abs/0710.4552) [astro-ph].
- Shibata, Masaru and Kenta Hotokezaka (Oct. 2019). “Merger and Mass Ejection of Neutron Star Binaries”. In: *Annual Review of Nuclear and Particle Science* 69, pp. 41–64. DOI: [10.1146/annurev-nucl-101918-023625](https://doi.org/10.1146/annurev-nucl-101918-023625). arXiv: [1908.02350](https://arxiv.org/abs/1908.02350) [astro-ph.HE].
- Siegel, Daniel M. and Brian D. Metzger (Dec. 2017). “Three-Dimensional General-Relativistic Magnetohydrodynamic Simulations of Remnant Accretion Disks from Neutron Star Mergers: Outflows and r -Process Nucleosynthesis”. In: 119.23, 231102, p. 231102. DOI: [10.1103/PhysRevLett.119.231102](https://doi.org/10.1103/PhysRevLett.119.231102). arXiv: [1705.05473](https://arxiv.org/abs/1705.05473) [astro-ph.HE].
- Silk, Joseph and Gary A. Mamon (Aug. 2012). “The current status of galaxy formation”. In: *Research in Astronomy and Astrophysics* 12.8, pp. 917–946. DOI: [10.1088/1674-4527/12/8/004](https://doi.org/10.1088/1674-4527/12/8/004). arXiv: [1207.3080](https://arxiv.org/abs/1207.3080) [astro-ph.CO].
- Silva Aguirre, V. et al. (Apr. 2018). “Confirming chemical clocks: asteroseismic age dissection of the Milky Way disc(s)”. In: 475.4, pp. 5487–5500. DOI: [10.1093/mnras/sty150](https://doi.org/10.1093/mnras/sty150). arXiv: [1710.09847](https://arxiv.org/abs/1710.09847) [astro-ph.GA].
- Simmerer, Jennifer et al. (Dec. 2004). “The Rise of the s-Process in the Galaxy”. In: 617.2, pp. 1091–1114. DOI: [10.1086/424504](https://doi.org/10.1086/424504). arXiv: [astro-ph/0410396](https://arxiv.org/abs/astro-ph/0410396) [astro-ph].
- Simon, Joshua D. (Aug. 2019). “The Faintest Dwarf Galaxies”. In: 57, pp. 375–415. DOI: [10.1146/annurev-astro-091918-104453](https://doi.org/10.1146/annurev-astro-091918-104453). arXiv: [1901.05465](https://arxiv.org/abs/1901.05465) [astro-ph.GA].
- Simonetti, Paolo et al. (June 2019). “A new delay time distribution for merging neutron stars tested against Galactic and cosmic data”. In: 486.2, pp. 2896–2909. DOI: [10.1093/mnras/stz991](https://doi.org/10.1093/mnras/stz991). arXiv: [1901.02732](https://arxiv.org/abs/1901.02732) [astro-ph.HE].
- Skúladóttir, Á. and S. Salvadori (Feb. 2020a). “Evidence for $\gtrsim 4$ Gyr timescales of neutron star mergers from Galactic archaeology”. In: 634, L2, p. L2. DOI: [10.1051/0004-6361/201937293](https://doi.org/10.1051/0004-6361/201937293). arXiv: [2001.03628](https://arxiv.org/abs/2001.03628) [astro-ph.GA].
- Skúladóttir, Á. et al. (Nov. 2019). “Neutron-capture elements in dwarf galaxies. I. Chemical clocks and the short timescale of the r-process”. In: 631, A171, A171. DOI: [10.1051/0004-6361/201936125](https://doi.org/10.1051/0004-6361/201936125). arXiv: [1908.10729](https://arxiv.org/abs/1908.10729) [astro-ph.GA].
- Skúladóttir, Á. et al. (Feb. 2020b). “Neutron-capture elements in dwarf galaxies. II. Challenges for the s- and i-processes at low metallicity”. In: 634, A84, A84. DOI: [10.1051/0004-6361/201937075](https://doi.org/10.1051/0004-6361/201937075). arXiv: [1912.06671](https://arxiv.org/abs/1912.06671) [astro-ph.GA].
- Smartt, S. J. et al. (Nov. 2017). “A kilonova as the electromagnetic counterpart to a gravitational-wave source”. In: 551.7678, pp. 75–79. DOI: [10.1038/nature24303](https://doi.org/10.1038/nature24303). arXiv: [1710.05841](https://arxiv.org/abs/1710.05841) [astro-ph.HE].
- Smith, Matthew C., Debora Sijacki, and Sijing Shen (July 2018). “Supernova feedback in numerical simulations of galaxy formation: separating physics from numerics”. In: 478.1, pp. 302–331. DOI: [10.1093/mnras/sty994](https://doi.org/10.1093/mnras/sty994). arXiv: [1709.03515](https://arxiv.org/abs/1709.03515) [astro-ph.GA].
- Snedden, C., J. J. Cowan, and R. Gallino (Sept. 2008). “Neutron-capture elements in the early galaxy.” In: 46, pp. 241–288. DOI: [10.1146/annurev.astro.46.060407.145207](https://doi.org/10.1146/annurev.astro.46.060407.145207).

- Somerville, Rachel S. and Joel R. Primack (Dec. 1999). “Semi-analytic modelling of galaxy formation: the local Universe”. In: 310.4, pp. 1087–1110. DOI: [10.1046/j.1365-8711.1999.03032.x](https://doi.org/10.1046/j.1365-8711.1999.03032.x). arXiv: [astro-ph/9802268](https://arxiv.org/abs/astro-ph/9802268) [astro-ph].
- Sormani, Mattia C. et al. (Aug. 2023). “Fuelling the nuclear ring of NGC 1097”. In: 523.2, pp. 2918–2927. DOI: [10.1093/mnras/stad1554](https://doi.org/10.1093/mnras/stad1554). arXiv: [2305.14437](https://arxiv.org/abs/2305.14437) [astro-ph.GA].
- Spina, L. et al. (May 2021). “The GALAH survey: tracing the Galactic disc with open clusters”. In: 503.3, pp. 3279–3296. DOI: [10.1093/mnras/stab471](https://doi.org/10.1093/mnras/stab471). arXiv: [2011.02533](https://arxiv.org/abs/2011.02533) [astro-ph.GA].
- Spina, Lorenzo, Laura Magrini, and Katia Cunha (Jan. 2022). “Mapping the Galactic Metallicity Gradient with Open Clusters: The State-of-the-Art and Future Challenges”. In: *Universe* 8.2, p. 87. DOI: [10.3390/universe8020087](https://doi.org/10.3390/universe8020087). arXiv: [2202.00463](https://arxiv.org/abs/2202.00463) [astro-ph.GA].
- Spitoni, E. and F. Matteucci (July 2011). “Effects of the radial flows on the chemical evolution of the Milky Way disk”. In: 531, A72, A72. DOI: [10.1051/0004-6361/201015749](https://doi.org/10.1051/0004-6361/201015749). arXiv: [1104.4881](https://arxiv.org/abs/1104.4881) [astro-ph.GA].
- Spitoni, E. et al. (Sept. 2009). “Effects of galactic fountains and delayed mixing in the chemical evolution of the Milky Way”. In: 504.1, pp. 87–96. DOI: [10.1051/0004-6361/200911768](https://doi.org/10.1051/0004-6361/200911768). arXiv: [0906.3400](https://arxiv.org/abs/0906.3400) [astro-ph.GA].
- Spitoni, E. et al. (Aug. 2019a). “2D chemical evolution model: The impact of Galactic disc asymmetries on azimuthal chemical abundance variations”. In: 628, A38, A38. DOI: [10.1051/0004-6361/201834665](https://doi.org/10.1051/0004-6361/201834665). arXiv: [1811.11196](https://arxiv.org/abs/1811.11196) [astro-ph.GA].
- Spitoni, E. et al. (Mar. 2019b). “Galactic Archaeology with asteroseismic ages: Evidence for delayed gas infall in the formation of the Milky Way disc”. In: 623, A60, A60. DOI: [10.1051/0004-6361/201834188](https://doi.org/10.1051/0004-6361/201834188). arXiv: [1809.00914](https://arxiv.org/abs/1809.00914) [astro-ph.GA].
- Spitoni, E. et al. (Mar. 2020). “Galactic archaeology with asteroseismic ages. II. Confirmation of a delayed gas infall using Bayesian analysis based on MCMC methods”. In: 635, A58, A58. DOI: [10.1051/0004-6361/201937275](https://doi.org/10.1051/0004-6361/201937275). arXiv: [1912.04312](https://arxiv.org/abs/1912.04312) [astro-ph.GA].
- Spitoni, E. et al. (Feb. 2023). “Beyond the two-infall model. I. Indications for a recent gas infall with Gaia DR3 chemical abundances”. In: 670, A109, A109. DOI: [10.1051/0004-6361/202244349](https://doi.org/10.1051/0004-6361/202244349). arXiv: [2206.12436](https://arxiv.org/abs/2206.12436) [astro-ph.GA].
- Spitoni, Emanuele et al. (Apr. 2015). “The Effect of Stellar Migration on Galactic Chemical Evolution: A Heuristic Approach”. In: 802.2, 129, p. 129. DOI: [10.1088/0004-637X/802/2/129](https://doi.org/10.1088/0004-637X/802/2/129). arXiv: [1407.5797](https://arxiv.org/abs/1407.5797) [astro-ph.GA].
- Starkenbourg, Else et al. (Feb. 2013). “The satellites of the Milky Way - insights from semi-analytic modelling in a Λ CDM cosmology”. In: 429.1, pp. 725–743. DOI: [10.1093/mnras/sts367](https://doi.org/10.1093/mnras/sts367). arXiv: [1206.0020](https://arxiv.org/abs/1206.0020) [astro-ph.GA].
- Stonkutė, E. et al. (July 2016). “The Gaia-ESO Survey: the selection function of the Milky Way field stars”. In: 460.1, pp. 1131–1146. DOI: [10.1093/mnras/stw1011](https://doi.org/10.1093/mnras/stw1011). arXiv: [1605.00515](https://arxiv.org/abs/1605.00515) [astro-ph.GA].
- Stratta, G. et al. (Jan. 2018). “THESEUS in the era of multi-messenger astronomy.” In: 89, p. 205. arXiv: [1802.01677](https://arxiv.org/abs/1802.01677) [astro-ph.IM].
- Suda, Takuma et al. (Oct. 2008). “Stellar Abundances for the Galactic Archeology (SAGA) Database — Compilation of the Characteristics of Known Extremely Metal-Poor Stars”. In: 60, p. 1159. DOI: [10.1093/pasj/60.5.1159](https://doi.org/10.1093/pasj/60.5.1159). arXiv: [0806.3697](https://arxiv.org/abs/0806.3697) [astro-ph].

- Suda, Takuma et al. (Apr. 2011). “The Stellar Abundances for Galactic Archaeology (SAGA) data base - II. Implications for mixing and nucleosynthesis in extremely metal-poor stars and chemical enrichment of the Galaxy”. In: 412.2, pp. 843–874. DOI: [10.1111/j.1365-2966.2011.17943.x](https://doi.org/10.1111/j.1365-2966.2011.17943.x). arXiv: [1010.6272](https://arxiv.org/abs/1010.6272) [astro-ph.GA].
- Suda, Takuma et al. (Oct. 2017). “Stellar Abundances for Galactic Archaeology Database. IV. Compilation of stars in dwarf galaxies”. In: 69.5, 76, p. 76. DOI: [10.1093/pasj/psx059](https://doi.org/10.1093/pasj/psx059). arXiv: [1703.10009](https://arxiv.org/abs/1703.10009) [astro-ph.GA].
- Tacchella, S. et al. (Apr. 2015). “Evidence for mature bulges and an inside-out quenching phase 3 billion years after the Big Bang”. In: *Science* 348.6232, pp. 314–317. DOI: [10.1126/science.1261094](https://doi.org/10.1126/science.1261094). arXiv: [1504.04021](https://arxiv.org/abs/1504.04021) [astro-ph.GA].
- Talbot Raymond J., Jr. and W. David Arnett (Nov. 1973). “The Evolution of Galaxies. II. Chemical Evolution Coefficients”. In: 186, pp. 51–67. DOI: [10.1086/152477](https://doi.org/10.1086/152477).
- Tantalo, Rosaria, Cesare Chiosi, and Alessandro Bressan (May 1998). “Ages and metallicities in elliptical galaxies from the H_β, <Fe>, and Mg₂ diagnostics”. In: 333, pp. 419–432. arXiv: [astro-ph/9710246](https://arxiv.org/abs/astro-ph/9710246) [astro-ph].
- Tarumi, Yuta, Naoki Yoshida, and Shigeki Inoue (May 2020). “R-process enrichment in ultrafaint dwarf galaxies”. In: 494.1, pp. 120–128. DOI: [10.1093/mnras/staa720](https://doi.org/10.1093/mnras/staa720). arXiv: [2002.06913](https://arxiv.org/abs/2002.06913) [astro-ph.GA].
- Tauris, T. M. et al. (Sept. 2017). “Formation of Double Neutron Star Systems”. In: 846.2, 170, p. 170. DOI: [10.3847/1538-4357/aa7e89](https://doi.org/10.3847/1538-4357/aa7e89). arXiv: [1706.09438](https://arxiv.org/abs/1706.09438) [astro-ph.HE].
- Taylor, Philip, Christoph Federrath, and Chiaki Kobayashi (Aug. 2017). “Star formation in simulated galaxies: understanding the transition to quiescence at $3 \times 10^{10} M_{\odot}$ ”. In: 469.4, pp. 4249–4257. DOI: [10.1093/mnras/stx1128](https://doi.org/10.1093/mnras/stx1128). arXiv: [1705.03173](https://arxiv.org/abs/1705.03173) [astro-ph.GA].
- Thielemann, F. K. et al. (Oct. 2017). “Neutron Star Mergers and Nucleosynthesis of Heavy Elements”. In: *Annual Review of Nuclear and Particle Science* 67, pp. 253–274. DOI: [10.1146/annurev-nucl-101916-123246](https://doi.org/10.1146/annurev-nucl-101916-123246). arXiv: [1710.02142](https://arxiv.org/abs/1710.02142) [astro-ph.HE].
- Thielemann, Friedrich-Karl, Benjamin Wehmeyer, and Meng-Ru Wu (Oct. 2020). “r-Process Sites, their Ejecta Composition, and their Imprint in Galactic Chemical Evolution”. In: *Journal of Physics Conference Series*. Vol. 1668. Journal of Physics Conference Series, 012044, p. 012044. DOI: [10.1088/1742-6596/1668/1/012044](https://doi.org/10.1088/1742-6596/1668/1/012044).
- Tinsley, B. M. (Jan. 1980). “Evolution of the Stars and Gas in Galaxies”. In: 5, pp. 287–388. DOI: [10.48550/arXiv.2203.02041](https://doi.org/10.48550/arXiv.2203.02041). arXiv: [2203.02041](https://arxiv.org/abs/2203.02041) [astro-ph.GA].
- Tolstoy, Eline, Vanessa Hill, and Monica Tosi (Sept. 2009). “Star-Formation Histories, Abundances, and Kinematics of Dwarf Galaxies in the Local Group”. In: 47.1, pp. 371–425. DOI: [10.1146/annurev-astro-082708-101650](https://doi.org/10.1146/annurev-astro-082708-101650). arXiv: [0904.4505](https://arxiv.org/abs/0904.4505) [astro-ph.CO].
- Tomisaka, Kohji and Satoru Ikeuchi (July 1988). “Starburst Nucleus: Galactic Scale Bipolar Flow”. In: 330, p. 695. DOI: [10.1086/166505](https://doi.org/10.1086/166505).
- Tosi, M. (May 1988). “Models of galactic chemical evolution - The problem of uniqueness”. In: 197.1-2, pp. 33–46.

- Travaglio, Claudia et al. (Feb. 2004). “Galactic Evolution of Sr, Y, And Zr: A Multiplicity of Nucleosynthetic Processes”. In: 601.2, pp. 864–884. DOI: [10.1086/380507](https://doi.org/10.1086/380507). arXiv: [astro-ph/0310189](https://arxiv.org/abs/astro-ph/0310189) [astro-ph].
- Treu, Tommaso et al. (Mar. 2005). “Keck Spectroscopy of Distant GOODS Spheroidal Galaxies: Downsizing in a Hierarchical Universe”. In: 622.1, pp. L5–L8. DOI: [10.1086/429374](https://doi.org/10.1086/429374). arXiv: [astro-ph/0502028](https://arxiv.org/abs/astro-ph/0502028) [astro-ph].
- Tsujimoto, Takuji and Kenji Bekki (Mar. 2012). “Two-component Galactic Bulge Probed with Renewed Galactic Chemical Evolution Model”. In: 747.2, 125, p. 125. DOI: [10.1088/0004-637X/747/2/125](https://doi.org/10.1088/0004-637X/747/2/125). arXiv: [1201.1019](https://arxiv.org/abs/1201.1019) [astro-ph.GA].
- Uttenthaler, S. et al. (Oct. 2012). “Constraining the structure and formation of the Galactic bulge from a field in its outskirts. FLAMES-GIRAFFE spectra of about 400 red giants around $(l, b) = (0^\circ, -10^\circ)$ ”. In: 546, A57, A57. DOI: [10.1051/0004-6361/201219055](https://doi.org/10.1051/0004-6361/201219055). arXiv: [1206.3469](https://arxiv.org/abs/1206.3469) [astro-ph.GA].
- Valentini, Milena, Simona Gallerani, and Andrea Ferrara (Oct. 2021). “Host galaxies of high-redshift quasars: SMBH growth and feedback”. In: 507.1, pp. 1–26. DOI: [10.1093/mnras/stab1992](https://doi.org/10.1093/mnras/stab1992). arXiv: [2107.05638](https://arxiv.org/abs/2107.05638) [astro-ph.GA].
- Valiante, Rosa et al. (Sept. 2011). “The origin of the dust in high-redshift quasars: the case of SDSS J1148+5251”. In: 416.3, pp. 1916–1935. DOI: [10.1111/j.1365-2966.2011.19168.x](https://doi.org/10.1111/j.1365-2966.2011.19168.x). arXiv: [1106.1418](https://arxiv.org/abs/1106.1418) [astro-ph.CO].
- Van den Hoek, L. B. and M. A. T. Groenewegen (June 1997). “New theoretical yields of intermediate mass stars”. In: 123, pp. 305–328. DOI: [10.1051/aas:1997162](https://doi.org/10.1051/aas:1997162).
- Van der Swaelmen, M. et al. (Feb. 2023). “The Gaia-ESO survey: Placing constraints on the origin of r-process elements”. In: 670, A129, A129. DOI: [10.1051/0004-6361/202243764](https://doi.org/10.1051/0004-6361/202243764). arXiv: [2207.14747](https://arxiv.org/abs/2207.14747) [astro-ph.GA].
- Varma, Vishnu, Bernhard Müller, and Fabian R. N. Schneider (Jan. 2023). “3D simulations of strongly magnetized non-rotating supernovae: explosion dynamics and remnant properties”. In: 518.3, pp. 3622–3636. DOI: [10.1093/mnras/stac3247](https://doi.org/10.1093/mnras/stac3247). arXiv: [2204.11009](https://arxiv.org/abs/2204.11009) [astro-ph.HE].
- Venn, K. A. et al. (Jan. 2004). “Stellar Abundances in Dwarf Irregular Galaxies”. In: *Origin and Evolution of the Elements*. Ed. by Andrew McWilliam and Michael Rauch, 58, p. 58. arXiv: [astro-ph/0305188](https://arxiv.org/abs/astro-ph/0305188) [astro-ph].
- Vescovi, Diego et al. (July 2020). “Magnetic-buoyancy-induced Mixing in AGB Stars: Presolar SiC Grains”. In: 897.2, L25, p. L25. DOI: [10.3847/2041-8213/ab9fa1](https://doi.org/10.3847/2041-8213/ab9fa1). arXiv: [2006.13729](https://arxiv.org/abs/2006.13729) [astro-ph.SR].
- Vincenzo, F. et al. (July 2014). “Chemical evolution of classical and ultra-faint dwarf spheroidal galaxies”. In: 441.4, pp. 2815–2830. DOI: [10.1093/mnras/stu710](https://doi.org/10.1093/mnras/stu710). arXiv: [1404.2476](https://arxiv.org/abs/1404.2476) [astro-ph.GA].
- Vincenzo, F. et al. (May 2015). “The IGIMF and other IMFs in dSphs: the case of Sagittarius”. In: 449.2, pp. 1327–1339. DOI: [10.1093/mnras/stv357](https://doi.org/10.1093/mnras/stv357). arXiv: [1502.05221](https://arxiv.org/abs/1502.05221) [astro-ph.GA].
- Vincoletto, L. et al. (Apr. 2012). “Cosmic star formation rate: a theoretical approach”. In: 421.4, pp. 3116–3126. DOI: [10.1111/j.1365-2966.2012.20535.x](https://doi.org/10.1111/j.1365-2966.2012.20535.x). arXiv: [1201.1751](https://arxiv.org/abs/1201.1751) [astro-ph.CO].
- Viscasillas Vázquez, C. et al. (Apr. 2022a). “The Gaia-ESO survey: Age-chemical-clock relations spatially resolved in the Galactic disc”. In: 660, A135, A135. DOI: [10.1051/0004-6361/202142937](https://doi.org/10.1051/0004-6361/202142937). arXiv: [2202.04863](https://arxiv.org/abs/2202.04863) [astro-ph.GA].

- (Apr. 2022b). “The Gaia-ESO survey: Age-chemical-clock relations spatially resolved in the Galactic disc”. In: 660, A135, A135. DOI: [10.1051/0004-6361/202142937](https://doi.org/10.1051/0004-6361/202142937). arXiv: [2202.04863](https://arxiv.org/abs/2202.04863) [astro-ph.GA].
- Volonteri, Marta and Priyamvada Natarajan (Dec. 2009). “Journey to the $M_{BH-\sigma}$ relation: the fate of low-mass black holes in the Universe”. In: 400.4, pp. 1911–1918. DOI: [10.1111/j.1365-2966.2009.15577.x](https://doi.org/10.1111/j.1365-2966.2009.15577.x). arXiv: [0903.2262](https://arxiv.org/abs/0903.2262) [astro-ph.CO].
- Walker, Matthew G. et al. (Oct. 2009). “A Universal Mass Profile for Dwarf Spheroidal Galaxies?” In: 704.2, pp. 1274–1287. DOI: [10.1088/0004-637X/704/2/1274](https://doi.org/10.1088/0004-637X/704/2/1274). arXiv: [0906.0341](https://arxiv.org/abs/0906.0341) [astro-ph.CO].
- Wanajo, Shinya (2006). “The r-Process in Proto-Neutron Star Winds with Anisotropic Neutrino Emission”. In: *The Astrophysical Journal* 650.1, pp. L79–L82. DOI: [10.1086/508568](https://doi.org/10.1086/508568). URL: <https://doi.org/10.1086/508568>.
- Wanajo, Shinya, Yutaka Hirai, and Nikos Prantzos (Aug. 2021). “Neutron star mergers as the astrophysical site of the r-process in the Milky Way and its satellite galaxies”. In: 505.4, pp. 5862–5883. DOI: [10.1093/mnras/stab165510.48550](https://doi.org/10.1093/mnras/stab165510.48550) / arXiv: [2106.03707](https://arxiv.org/abs/2106.03707). arXiv: [2106.03707](https://arxiv.org/abs/2106.03707) [astro-ph.GA].
- Wanderman, David and Tsvi Piran (Apr. 2015). “The rate, luminosity function and time delay of non-Collapsar short GRBs”. In: 448.4, pp. 3026–3037. DOI: [10.1093/mnras/stv123](https://doi.org/10.1093/mnras/stv123). arXiv: [1405.5878](https://arxiv.org/abs/1405.5878) [astro-ph.HE].
- Watson, Darach et al. (Oct. 2019). “Identification of strontium in the merger of two neutron stars”. In: *Nature* 574, pp. 497–500. DOI: [10.1038/s41586-019-1676-3](https://doi.org/10.1038/s41586-019-1676-3).
- Wegg, Christopher and Ortwin Gerhard (Nov. 2013). “Mapping the three-dimensional density of the Galactic bulge with VVV red clump stars”. In: 435.3, pp. 1874–1887. DOI: [10.1093/mnras/stt1376](https://doi.org/10.1093/mnras/stt1376). arXiv: [1308.0593](https://arxiv.org/abs/1308.0593) [astro-ph.GA].
- Wegg, Christopher, Ortwin Gerhard, and Matthieu Portail (July 2015). “The structure of the Milky Way’s bar outside the bulge”. In: 450.4, pp. 4050–4069. DOI: [10.1093/mnras/stv745](https://doi.org/10.1093/mnras/stv745). arXiv: [1504.01401](https://arxiv.org/abs/1504.01401) [astro-ph.GA].
- Wehmeyer, B., M. Pignatari, and F. K. Thielemann (Sept. 2015). “Galactic evolution of rapid neutron capture process abundances: the inhomogeneous approach”. In: 452.2, pp. 1970–1981. DOI: [10.1093/mnras/stv1352](https://doi.org/10.1093/mnras/stv1352). arXiv: [1501.07749](https://arxiv.org/abs/1501.07749) [astro-ph.GA].
- Weiland, J. L. et al. (Apr. 1994). “COBE Diffuse Background Experiment Observations of the Galactic Bulge”. In: 425, p. L81. DOI: [10.1086/187315](https://doi.org/10.1086/187315).
- Weinberger, Rainer et al. (Oct. 2017). “Simulating the interaction of jets with the intracluster medium”. In: 470.4, pp. 4530–4546. DOI: [10.1093/mnras/stx1409](https://doi.org/10.1093/mnras/stx1409). arXiv: [1703.09223](https://arxiv.org/abs/1703.09223) [astro-ph.GA].
- Winteler, C. et al. (May 2012). “Magnetorotationally Driven Supernovae as the Origin of Early Galaxy r-process Elements?” In: 750.1, L22, p. L22. DOI: [10.1088/2041-8205/750/1/L22](https://doi.org/10.1088/2041-8205/750/1/L22). arXiv: [1203.0616](https://arxiv.org/abs/1203.0616) [astro-ph.SR].
- Woosley, S. E. and J. S. Bloom (Sept. 2006a). “The Supernova Gamma-Ray Burst Connection”. In: 44.1, pp. 507–556. DOI: [10.1146/annurev.astro.43.072103.150558](https://doi.org/10.1146/annurev.astro.43.072103.150558). arXiv: [astro-ph/0609142](https://arxiv.org/abs/astro-ph/0609142) [astro-ph].
- Woosley, S. E. and A. Heger (Feb. 2006b). “The Progenitor Stars of Gamma-Ray Bursts”. In: 637.2, pp. 914–921. DOI: [10.1086/498500](https://doi.org/10.1086/498500). arXiv: [astro-ph/0508175](https://arxiv.org/abs/astro-ph/0508175) [astro-ph].

- Wu, Meng-Ru et al. (Dec. 2016). “Production of the entire range of r-process nuclides by black hole accretion disc outflows from neutron star mergers”. In: 463.3, pp. 2323–2334. DOI: [10.1093/mnras/stw2156](https://doi.org/10.1093/mnras/stw2156). arXiv: [1607.05290](https://arxiv.org/abs/1607.05290) [astro-ph.HE].
- Wu, Xue-Bing and J. L. Han (Dec. 2001). “On black hole masses, radio-loudness and bulge luminosities of Seyfert galaxies”. In: 380, pp. 31–39. DOI: [10.1051/0004-6361:20011429](https://doi.org/10.1051/0004-6361:20011429). arXiv: [astro-ph/0110219](https://arxiv.org/abs/astro-ph/0110219) [astro-ph].
- Yamada, Shimako et al. (Dec. 2013). “The Stellar Abundances for Galactic Archaeology (SAGA) Database - III. Analysis of enrichment histories for elements and two modes of star formation during the early evolution of the Milky Way”. In: 436.2, pp. 1362–1380. DOI: [10.1093/mnras/stt1652](https://doi.org/10.1093/mnras/stt1652). arXiv: [1309.3430](https://arxiv.org/abs/1309.3430) [astro-ph.GA].
- Yoshii, Y. and N. Arimoto (Dec. 1987). “Spheroidal systems as a one-parameter family of mass at their birth.” In: 188, pp. 13–23.
- Yuan, Feng et al. (Apr. 2018). “Active Galactic Nucleus Feedback in an Elliptical Galaxy with the Most Updated AGN Physics. I. Low Angular Momentum Case”. In: 857.2, 121, p. 121. DOI: [10.3847/1538-4357/aab8f8](https://doi.org/10.3847/1538-4357/aab8f8). arXiv: [1712.04964](https://arxiv.org/abs/1712.04964) [astro-ph.HE].
- Zhang, Haopeng, Yuqin Chen, and Gang Zhao (Sept. 2021). “Radial Migration from the Metallicity Gradient of Open Clusters and Outliers”. In: 919.1, 52, p. 52. DOI: [10.3847/1538-4357/ac0e92](https://doi.org/10.3847/1538-4357/ac0e92). arXiv: [2106.12841](https://arxiv.org/abs/2106.12841) [astro-ph.GA].
- Zoccali, M. et al. (July 2008). “The metal content of bulge field stars from FLAMES-GIRAFFE spectra. I. Stellar parameters and iron abundances”. In: 486.1, pp. 177–189. DOI: [10.1051/0004-6361:200809394](https://doi.org/10.1051/0004-6361:200809394). arXiv: [0805.1218](https://arxiv.org/abs/0805.1218) [astro-ph].
- Zoccali, M. et al. (Feb. 2014). “The GIRAFFE Inner Bulge Survey (GIBS). I. Survey description and a kinematical map of the Milky Way bulge”. In: 562, A66, A66. DOI: [10.1051/0004-6361/201323120](https://doi.org/10.1051/0004-6361/201323120). arXiv: [1401.4878](https://arxiv.org/abs/1401.4878) [astro-ph.GA].
- Zoccali, M. et al. (Mar. 2017). “The GIRAFFE Inner Bulge Survey (GIBS). III. Metallicity distributions and kinematics of 26 Galactic bulge fields”. In: 599, A12, A12. DOI: [10.1051/0004-6361/201629805](https://doi.org/10.1051/0004-6361/201629805). arXiv: [1610.09174](https://arxiv.org/abs/1610.09174) [astro-ph.GA].